

**CHARACTERIZING THE DIELECTRIC PROPERTIES OF
GEOLOGIC AND ASTEROID REGOLITH ANALOGUE
MATERIAL FOR IMPROVED PLANETARY RADAR
INTERPRETATION**

DYLAN C. HICKSON

A DISSERTATION SUBMITTED TO
THE FACULTY OF GRADUATE STUDIES
IN PARTIAL FULFILLMENT OF THE REQUIREMENTS
FOR THE DEGREE OF
DOCTOR OF PHILOSOPHY

GRADUATE PROGRAM IN
EARTH & SPACE SCIENCE
YORK UNIVERSITY
TORONTO, ONTARIO
MAY 2019

© Dylan Hickson, 2019

Abstract

Planetary radar has provided an increasingly growing number of datasets on the inner terrestrial planets and near-Earth and main-belt asteroid populations in our solar system. Physical interpretation of radar data for inference of surface properties requires constraints on the constitutive parameters of the material making up a given surface. For many planetary surfaces, the response to electromagnetic radiation is described by the complex permittivity. In this thesis, the dielectric response of several geologic materials as a function of frequency and porosity was characterized to supplement radar data interpretation. Using the coaxial transmission line method, the complex permittivity of seven powdered mineral samples was measured. The samples were characterized for their composition and structure using a variety of laboratory techniques. A detailed review of the theory and use of electromagnetic mixing equations was presented to introduce the range of models available to describe the experimental permittivity measurements. A thorough analysis of the experiments was performed which showed that the Looyenga-Landau-Lifshitz and Bruggeman (Symmetric) mixing models described the experimental results with the highest accuracy. Measurement bias in the coaxial transmission line method highlighted in previous research due to inhomogeneities at the sample/conductor interface was modelled using these mixing theories, providing a way to correct for these effects post-measurement. The variation in the permittivity of the solid mineral grains between different minerals was characterized based on the grain density of the minerals, as well as the chemical composition. The experimentally verified mixing models were incorporated into an existing asteroid radar model and were used to calculate the porosity in the near-surface of seven asteroids visited by robotic spacecraft. Comparing with bulk porosity estimates, the asteroid radar model indicated the presence of a porous regolith covering on each asteroid that is similar in porosity to the upper 30 cm of the Moon. The results from this research are important for future radar studies, and the model predictions for asteroid surface properties will be tested with results from upcoming space missions visiting asteroids, such as NASA's *OSIRIS-REx* and JAXA's *Hayabusa2* missions.

Dedication

I dedicate this thesis to my family, without whom I would never have pursued graduate studies. Your encouragement, patience, understanding, support, and love have enabled me to expand my horizons and explore how far my curiosity will take me. Thank you for everything.

Acknowledgements

I am forever grateful for the opportunity from, and continued support by, my Ph.D. supervisor Dr. Michael Daly, and would like to acknowledge his guidance and mentoring that has greatly helped me complete this thesis. As I am something of a late academic bloomer, Dr. Daly's patience and dedication to my research efforts allowed me to grow both in confidence and research proficiency. I am also eternally grateful for the support of Dr. Rebecca Ghent, who, as an unofficial co-supervisor, has offered her guidance, support, expertise, and the use of facilities at the University of Toronto throughout my Ph.D. studies. I am also thankful for the opportunity to work with, and learn from, the Solar System Exploration Group at the University of Toronto, particularly Alexandre Boivin, Alister Cunje, and Brian Tsai for their help and suggestions in completing the permittivity measurements in this thesis. I would like to thank all of the members of the Planetary Instrumentation Laboratory at York University for making graduate studies enjoyable, and for helping me work through difficult research problems. Dr. Emmanuel Lalla and Kristen Cote especially helped me work through some of the electromagnetic theory. The staff at the Royal Ontario Museum, specifically Dr. Kim Tait, Ian Nicklin, and Veronica DiCecco, were very supportive and helpful in my research efforts and I thank you deeply. I would also like to thank Jerry Gresch from the Machine Shop at York University for helping me design the custom machined components in this thesis. I would like to acknowledge and thank Dr. Pamela Burnley from the University of Nevada, Las Vegas for providing the synthetic fayalite sample used in this thesis. Lastly, I would like to thank my family and friends for their support. Without the support of my parents and grandparents I would not have had the opportunity to pursue post-secondary education, and for that I am forever grateful. My wife filled the roles of therapist, editor, and life partner throughout my Ph.D. studies; you're the love of my life and I couldn't have done this without you.

Contents

Abstract	ii
Dedication	iii
Acknowledgements	iv
Table of Contents	v
List of Tables	x
List of Figures	xii
Preface	xx
1 Introduction	1
1.1 Motivation	1
1.2 Purpose and structure of thesis	3
1.3 Asteroid Planetary Radar	4
1.3.1 Radar Polarimetry	6
1.3.2 Radar Scattering Laws	8
1.4 Electromagnetic Theory	11
1.4.1 Electromagnetic Wave Propagation: The Wave Equation	11
1.4.2 Propagation, Phase, and Attenuation constants	15
1.4.3 Dielectric Permittivity	16
1.4.4 Magnetic Permeability	20
1.4.5 Electric Conductivity	21
1.4.6 Electromagnetic Wave Polarization	21
1.4.7 Reflection and Transmission	22
1.4.8 Theoretical Assumptions	23
1.5 Geologic Description of Powders	24

2	Electromagnetic Mixing Equations Review	25
2.1	Introduction	25
2.2	Matrix/Inclusions Mixing Theories	27
2.2.1	Maxwell Garnett (MG)	27
2.2.2	Bruggeman (Non Symmetric) (BGNS)	36
2.2.3	Coherent Potential (CP)	38
2.3	Statistical/Aggregate Mixing Theories	39
2.3.1	Bruggeman Symmetric (BG)	39
2.3.2	General Power Law Mixing Theory: β	43
2.3.3	Linear (LIN), $\beta = 1$	44
2.3.4	Complex Refractive Index Model (CRIM), $\beta = 1/2$	45
2.3.5	Looyenga-Landau-Lifshitz Formula (LLL), $\beta = 1/3$	46
2.3.6	Lichtenecker Formula (LI), $\beta = 0$	49
2.4	Particle Shape: Depolarization Factor	52
2.5	Mixing Theory: Bounds	53
2.6	Summary	55
3	Experimental Setup and Methodology	62
3.1	Introduction	62
3.2	Coaxial Transmission Line Method	63
3.2.1	Overview of Coaxial Transmission/Reflection Method	63
3.2.2	Calculating constitutive parameters from S-parameters	69
3.3	Equipment	70
3.3.1	Network Analyzer	70
3.3.2	Coaxial Airlines, Cables, and Adapters	70
3.3.3	Custom Filling Funnel	71
3.3.4	Teflon [®] Washers	73
3.4	Environment Chamber	74
3.5	Heating Mechanism	77
3.6	Silica Aerogel	80
3.7	Software	83
3.7.1	METAS VNA Tools II	83

3.7.2	<i>permittivitycalc</i>	84
3.8	Calibration	85
3.9	Uncertainty in the Complex Permittivity	86
3.9.1	Type A and Type B Uncertainty	86
3.9.2	Type A Uncertainty for Powder Samples	87
3.10	Basic Workflow	91
4	Sample Characterization and Preparation	93
4.1	Techniques to Characterize and Prepare Samples	93
4.1.1	Sample Comminution	93
4.1.2	Mass Balance	94
4.1.3	Particle Size Distribution	94
4.1.4	Scanning Electron Microscope (SEM) / Electron Dispersive Spectroscopy (EDS)	99
4.1.5	Particle Density	100
4.1.6	X-ray Diffraction (XRD)	101
4.1.7	Fines Removal	102
4.1.8	Magnetite Removal	103
4.2	Samples	103
4.2.1	Overview	103
4.2.2	Aluminium Oxide (Al_2O_3)	105
4.2.3	Forsterite (Mg_2SiO_4)	106
4.2.4	Fayalite (Fe_2SiO_4)	108
4.2.5	Antigorite ($Mg_3Si_2O_5(OH)_4$)	110
4.2.6	Lizardite ($Mg_3Si_2O_5(OH)_4$)	112
4.2.7	Dolomite ($CaMg(CO_3)_2$)	113
4.2.8	Labradorite ($(Ca, Na)(Al, Si)_4O_8$)	114
4.2.9	Samples Summary	116
4.3	Oven Drying Samples prior to Permittivity Measurements	116
5	Boundary Conditions Model	120
5.1	Overview	120
5.2	Abstract	121

5.3	Introduction	121
5.4	Experimental Procedure	123
5.4.1	Sample Preparation	123
5.4.2	Measurement Results	124
5.5	Revised Mixing Model	125
5.5.1	Boundary Conditions	125
5.5.2	Modelling and Mixing	126
5.6	Application of Model to Measured Data	129
5.7	Conclusion	134
5.8	Acknowledgements	135
5.9	Appendix	135
5.9.1	Maxwell Garnett	135
5.9.2	Inverse Maxwell Garnett	135
5.9.3	Coherent Potential	137
5.9.4	Lichtenecker	137
5.9.5	Looyenga	137
5.10	Summary	139
6	Permittivity Measurements and Mixing Theory Analysis	140
6.1	Permittivity Measurement Results	140
6.1.1	Aluminium Oxide Dispersion	149
6.2	Fitting mixing theories to data	153
6.3	Comparison to the literature	157
6.3.1	Comparison to Resonant Cavity Measurements	165
6.4	Modelling Permittivity of Solid Mineral Samples (Solid Permittivity)	166
6.4.1	Additivity Rule of Ionic/Molecular Polarizability	169
6.5	Empirical Methods	172
6.6	Summary	176
7	Applications to Asteroid Radar Modelling	181
7.1	Incorporating mixing analysis into asteroid radar model	181
7.2	Modelling Asteroid Regolith Porosity	183

8	Conclusions and Future Work	188
8.1	Conclusion	188
8.2	Future Work	190
9	References	192
A	Appendix	214
A.1	Landau & Lifshitz Derivation	214
A.2	Looyenga Derivation	220

List of Tables

2.1	Two-phase mixing equations considered in this study. ϵ_{eff} is the effective permittivity of the mixture, ϵ_e and ϵ_i refer to the permittivities of the first and second phase with volume fractions $(1 - f)$ and f respectively.	55
2.2	Summary of various studies exploring the use of mixing theory. Each study is characterized by the type of mixture considered, the frequency range applicable for the analysis (by orders of magnitude), and the mixing theory that was determined to be the most accurate in that study.	56
2.3	Summary from Table 2.2 continued.	57
2.4	Summary from Table 2.3 continued.	58
4.1	Average particle size determined through Gaussian fitting to PSD's compared with those reported in Sotodeh (2014). Particle sizes taken as the sieve sizes for regular Gaussian fit, and particle sizes taken as average between bin sizes for adjusted Gaussian fit.	96
4.2	Summary of the samples used in this research.	117
5.1	Permittivity of alumina: results from this study (spherical particle shapes) compared to results in the literature	134
6.1	Frequency-averaged permittivities, $\langle \epsilon'_r \rangle$, of aluminium oxide, dolomite, and labradorite measurements.	148
6.2	Frequency-averaged permittivities, $\langle \epsilon'_r \rangle$, of forsterite, fayalite, and antigorite measurements	149
6.3	Fitting parameters for Havriliak-Negami and Cole-Cole model fits to aluminium oxide data from Figures 6.10 and 6.11 (Maximum value of $\tau = 5.0 \times 10^{-7}$ s applied). Note the samples were measured at different bulk densities.	153
6.4	Solid aluminium oxide permittivity measurements from the literature.	159
6.5	Solid dolomite permittivity measurements from the literature.	159

6.6	Solid fayalite permittivity measurements from the literature.	160
6.7	Solid forsterite permittivity measurements from the literature.	160
6.8	Solid labradorite permittivity measurements from the literature.	160
6.9	Solid serpentine permittivity measurements from the literature. There were not enough experiments found differentiating between the types of serpentine, and so the analysis of the lizardite and antigorite samples was combined.	161
6.10	Mean solid permittivity from the literature with t-distribution 95% confidence intervals.	162
6.11	Regression analysis of <i>Apollo</i> 15, 16, and 17 mission lunar regolith sample permit- tivity measurements presented in Carrier et al. (1991).	175
6.12	Solid density (g/cm^3) measurements of regolith samples returned in <i>Apollo</i> missions 15, 16, and 17 with references.	175
6.13	Calculated solid permittivity for lunar regolith returned during the <i>Apollo</i> 15, 16, and 17 missions using the data in Tables 6.11 and 6.12. The solid permittivity is calculated using the Olhoeft and Strangway (1975) equation ($\epsilon_s = a^{\rho_s}$), equation (6.4) ($\epsilon_s = (\rho_s \alpha + 1)^3$), and the linear equation $\epsilon_s = 1.85\rho_s + 1$ defined in section 6.4.	176
7.1	Asteroids for which the asteroid radar model (equations (7.3) and (7.4)) are applied with required input data and references.	184

List of Figures

1.1	<i>Figure taken from (Benner et al., 2015) with following caption: Number of near-Earth asteroid radar detections through the end of 2014. The increase in cumulative detections in 1999-2000 was caused in part by a surge of discoveries by LINEAR and by the order-of-magnitude increase in sensitivity at Arecibo after the upgrade. The increase in 2012 was the result of increased funding for Arecibo and greater access to telescope time at Arecibo and Goldstone. (The upgrade here refers to the installation of the 1 MW 12.6 cm radar system).</i>	5
1.2	Hagfor’s scattering law for rms slope angles of $\theta_{\text{rms}} = 1^\circ, 2^\circ$, and 8° , as well as the diffuse scattering law for incident angles from $\phi = 0 - 60^\circ$. The quasi-specular radar cross section is given in units of decibels ($\sigma_{\text{qs}}(\text{dB}) = 10\log_{10}(\sigma_{\text{qs}})$) and is seen to drop off sharply as the incident angle increases from nadir ($\phi = 0$), and decreases gradually with increasing ϕ . Increasing surface roughness (θ_{rms}) decreases the sharpness of the nadir peak. The diffuse radar cross section drops off less dramatically with incident angle, and becomes more important for high ϕ and high θ_{rms} . In this figure the exponent assumed in equation (1.7) is $n = 1.5$, and the radar reflectivity is calculated from the Fresnel reflectivity at normal incidence on a loss-less material with $\epsilon'_r = 4$	10
1.3	Polarization mechanisms in dielectrics adapted from (Stillman, 2006; Olhoeft, 1981; Balanis, 1989). Interfacial polarization is sometimes referred to as Maxwell-Wagner polarization, and in this figure is represented by charge build-up at the boundaries of an individual mineral grain.	18
2.1	Spatially uniform electric field, $\mathbf{E}_0 = E_0\hat{\mathbf{z}}$, in some medium with permittivity ϵ_e	28
2.2	Dielectric sphere with permittivity ϵ_i embedded in the medium.	29
2.3	Field lines of \mathbf{E}_0 and \mathbf{E}_i for a dielectric sphere with permittivity ϵ_i embedded in the medium.	29
2.4	Effective permittivity of a mixture.	31

2.5	Empty cavity with same shape as inclusion to calculate Lorentz field contribution to \mathbf{E}_L .	32
2.6	Lorentz sphere.	33
2.7	BG model assumes each inclusion is embedded in an already homogenized medium, and so must have zero polarization.	40
2.8	Wiener and Hashin-Shtrikman bounds for the effective permittivity of two mixtures with dielectric contrast of 4 and 10.	54
2.9	Mixing theories for a dielectric contrast of $\frac{\epsilon_i}{\epsilon_e} = 4$.	59
2.10	Mixing theories for a dielectric contrast of $\frac{\epsilon_i}{\epsilon_e} = 10$.	60
2.11	Mixing theories for a dielectric contrast of $\frac{\epsilon_i}{\epsilon_e} = 100$.	61
3.1	Cross-sectional view of the GR900-LZ coaxial airline filled with a powder sample. Electric field lines are the green arrows, and magnetic field lines the orange arrows.	63
3.2	Cutoff frequency of the GR900-LZ coaxial airlines as a function of the permittivity of the sample being measured.	65
3.3	Illustration of the effect of the cutoff frequency on permittivity measurements (here a measurement of the labradorite sample).	66
3.4	<i>(Adapted from Figure 4.1 (Chen et al., 2004))</i> Depiction of the VNA circuit, including the VNA, coaxial cables, and sample filled coaxial airline. This circuit is broken down into the corresponding diagram depicting a forward (S_{11}, S_{21}) measurement, made up of regions I, II, and III, where region II represents the sample filled airline. The z-axis is chosen to be along the length of the airline.	67
3.5	<i>(Adapted from Figure 3.2-2. (Adam and Packard, 1969))</i> Flow graph depiction of the 2-port VNA network.	68
3.6	10 cm length GR 900-LZ coaxial airline with inner conductor removed from airline and Teflon [®] washers.	71
3.7	Custom funnel filling device designed and manufactured by RobotWorks Corp. based on the designs from Sotodeh (2014).	72
3.8	Annotated image of the environment chamber used for the permittivity measurements in this research.	74
3.9	Custom aluminium plate used for environment chamber	75
3.10	KJLC 300 Series pressure gauge.	76

3.11	Annotated heating mechanism incorporated into permittivity measurement setup. The wire leads were eventually soldered to sub-D connectors.	79
3.12	<i>Figure taken from (Boivin et al., 2018) with the following caption:</i> Measurements of the empty transmission line in vacuum at different temperatures. A very slight increase in ϵ'_r can be seen with increasing temperature attributed to error due to thermal expansion of the brass transmission line. Note the log scale on the frequency axis.	80
3.13	Measured permittivity and loss tangent for silica aerogel used in this study. Note the pronounced measurement spikes at resonant frequencies due to the very low loss of the material.	82
3.14	<i>Figure taken from (Hickson et al., 2018) with the following caption:</i> a) Powdered dunite with silica aerogel prior to mixing. b) Resulting dunite/silica aerogel mixture.	83
3.15	Raw forsterite sample data set (un-normalized) (average standard deviation of 0.193).	88
3.16	Forsterite dataset normalized to a bulk density of $\rho_{bd} = 1.60 \text{ g/cm}^3$ using the Olhoeft and Strangway (1975) equation (average standard deviation of 0.025).	89
3.17	Forsterite dataset normalized to a bulk density of $\rho_{bd} = 1.60 \text{ g/cm}^3$ using the LLL equation, with the input parameter ϵ_i optimized through non-linear least squares regression to fit the dataset (average standard deviation of 0.014).	90
3.18	Workflow for the permittivity measurements.	91
4.1	Gaussian distribution fit to PSD from Kramer Industries, Inc. for #120 mesh alumina sample.	95
4.2	Adjusted Gaussian distribution fit to PSD from Kramer Industries, Inc. for #120 mesh alumina grit.	96
4.3	ANSI B74.12.2001 size grading standard particle size ranges compared to average particle size estimates from Sotodeh (2014) and using the adjusted Gaussian fit. . . .	97
4.4	Gaussian (not-adjusted) function plotted as PDF and CDF for #100 mesh alumina sample.	98
4.5	Tescan VEGA3 SEM with Bruker Quantax EDS detector at York University.	100
4.6	Micromeritics [®] Instrument Corporation Accucyc [®] II 1340 Gas Displacement Pycnometer at York University.	101

4.7	Lizardite before and after decanting process was applied (for a small batch of overall sample).	102
4.8	Labradorite sample viewed through the petrographic microscope before and after decanting the sample (same magnification).	103
4.9	The setup used to remove magnetite from the samples. The upper weight boat has several magnets taped to its bottom, and can be seen capturing magnetite grains. . .	104
4.10	Dunite sample provided by the University of Toronto (provenance unknown) that was used in this research.	106
4.11	Raman spectrum of the dunite sample compared with the RRUFF database ID X050088 processed San Carlos forsterite spectrum.	107
4.12	XRD spectrum (Dylan.raw) of dunite sample with matching mineral spectrum from PDF database.	107
4.13	EDS spectrum for elemental mapping of roughly 3 mm ² area of solid dunite sample. Energy levels expected for common elements found in rocks and minerals are indicated.	108
4.14	Fayalite sample as viewed by petrographic microscope.	108
4.15	XRD spectrum of fayalite sample with matching mineral spectrum from ICDD PDF database.	109
4.16	EDS spectrum for elemental mapping of roughly 3 mm ² area of pelletized fayalite sample.	109
4.17	Silica inclusions identified in BSE image and EDS spectral mapping of pelletized fayalite sample.	110
4.18	XRD spectrum of antigorite sample with attempted matching of mineral spectrum from ICDD PDF database.	111
4.19	EDS point spectra of pelletized antigorite sample, differentiated by colour and overlapped.	111
4.20	XRD spectrum of lizardite sample with matching mineral spectrum from RRUFF database (RRUFF ID R060006).	112
4.21	BSE image of annotated inclusion in lizardite sample with corresponding EDS point spectra taken in different brightness zones of the BSE image.	113
4.22	XRD spectrum of dolomite sample (labelled marble in the plot) with matching mineral spectrum from ICDD PDF database.	114

4.23	BSE image of inclusion in dolomite sample with corresponding EDS point spectra taken in different brightness zones of the BSE image.	115
4.24	XRD spectrum of labradorite sample with matching mineral spectrum from ICDD PDF database.	115
4.25	EDS spectrum of pelletized labradorite sample.	116
4.26	Colour change in fayalite sample after heating to 250° C.	117
4.27	Loss on ignition test to determine oven drying time required at 115° C.	118
5.1	Effective (real) permittivity of alumina measured with 7 mm and 14 mm airlines at 7.5 GHz ($\Delta\epsilon_r \approx 0.015$, $\Delta\phi \approx 0.001$). Annotated text refers to average grain size of measured sample (Sotodeh, 2014).	124
5.2	Geometry for spherical particles of powder in airline at conductor interface.	125
5.3	Cross section of coaxial airline showing the sample region (C_2) and boundary regions (C_1, C_3). For ‘7 mm’ airline $D_1 = 0.30404$ cm and $D_4 = 0.69926$ cm. For ‘14 mm’ airline $D_1 = 0.62052$ cm and $D_4 = 1.42824$ cm. The values for D_2 and D_3 are dependent on the average grain size of the sample being measured as discussed in section 3.1.	127
5.4	Cross section of coaxial airline with radial component cross section for a) Classical Mixing Scenario b) Model Mixing Scenario.	128
5.5	Output of model mixing scenario and classical mixing scenario results plotted vs. average grain size of sample measurement (data grouped by coaxial airline used). Smaller grain sizes (76 μm , 102 μm , 165 μm)	130
5.6	Output of model mixing scenario and classical mixing scenario results plotted vs. porosity of sample measurement (data grouped by coaxial airline used)	131
5.7	76 μm (left) and 305 μm (right) alumina grain shapes (Sotodeh, 2014)	132
5.8	Output of model mixing scenario and classical mixing scenario results plotted vs. average grain size of sample measurement (data grouped by coaxial airline used). Smaller grain sizes (76 μm , 102 μm , 165 μm) modelled as needles.	132
5.9	Study Results (Figure 5.5) derived using the Maxwell-Garnett equation.	136
5.10	Study Results (Figure 5.5) derived using the Inverse Maxwell Garnett equation.	136
5.11	Study Results (Figure 5.5) derived using the Coherent Potential equation.	137
5.12	Study Results (Figure 5.5) derived using the Lichtenecker equation.	138

5.13	Study Results (Figure 5.5) derived using the Looyenga-Landau-Lifshitz equation. . .	138
6.1	Dataset of permittivity measurements of the aluminium oxide sample.	141
6.2	Dataset of permittivity measurements of the forsterite sample.	142
6.3	Dataset of permittivity measurements of the lizardite sample.	143
6.4	Dataset of permittivity measurements of the fayalite sample.	144
6.5	Dataset of permittivity measurements of the antigorite sample.	145
6.6	Dataset of permittivity measurements of the dolomite sample.	146
6.7	Dataset of permittivity measurements of the labradorite sample.	147
6.8	Permittivity measurements of two 76 μm average grain size aluminium oxide, one oven dried at 250° C and the other not oven dried.	150
6.9	Permittivity measurements of two 76 μm average grain size aluminium oxide, one oven dried at 250° C and the other not oven dried. Data normalized to a bulk density of $\rho_{\text{bd}} = 1.60 \text{ g/cm}^3$ using the fitted LLL equation.	151
6.10	Permittivity measurements of two 76 μm average grain size aluminium oxide, one oven dried at 250° C and the other oven dried at 115° C fitted with the Havriliak-Negami relaxation model (Maximum value of $\tau = 5.0 \times 10^{-7}$ s applied).	154
6.11	Permittivity measurements of two 76 μm average grain size aluminium oxide, one oven dried at 250° C and the other oven dried at 115° C fitted with the Cole-Cole relaxation model.	155
6.12	Frequency-averaged permittivity as a function of bulk density.	156
6.13	Frequency-averaged permittivity as a function of volume fraction ($1 - \phi$).	156
6.14	Regression of mixing models for fayalite and aluminium oxide datasets. The data points are the frequency-averaged permittivity, $\langle \epsilon'_r \rangle$, for each measurement.	158
6.15	Regression of mixing models for fayalite and aluminium oxide datasets. Mean solid permittivity from the literature measurements are plotted at 100% volume fraction (ideal zero porosity) with the t-distribution 95% confidence intervals as error bars. The data points are the frequency-averaged permittivity, $\langle \epsilon'_r \rangle$, for each measurement.	163
6.16	WRMSE (equation (6.1)) for each mixing theory prediction compared with literature values across all samples.	164

6.17	Regression of mixing models for labradorite dataset compared with mean literature value and resonant cavity solid sample measurement from Brian Tsai.	166
6.18	Solid permittivities used to fit the BG mixing model (with boundary conditions) to the sample permittivity measurements plotted against the grain density of each sample. The data is fitted with a linear model.	167
6.19	Pearson correlation coefficient for linear fits derived from solid permittivities used for each mixing model (with and without boundary conditions applied).	168
6.20	Solid permittivities used to fit the BG mixing model (with boundary conditions) to the sample permittivity measurements compared with the sample permittivity measurements and results from Ulaby et al. (1988) separated by rock type.	169
6.21	Ionic polarizabilities (\AA^3) derived in Shannon (1993).	170
6.22	a) Solid permittivities for the samples predicted using the theoretical ARIP and CM models (ARIP/CM Predictions) compared to the mean values from the literature (Literature Values). b) Solid permittivities for the samples predicted by the LLL fit to the sample permittivity measurements (LLL Mixing Predictions) compared to the mean values from the literature (Literature Values). The error bars for the mixing predictions are the WRMSE for the LLL mixing model predictions compared with the mean literature values. c) Solid permittivities for the samples predicted by the the ARIP and CM theories (ARIP/CM Predictions) compared to the those predicted by the LLL fit to the sample permittivity measurements (LLL Mixing Predictions). $R^2 = 0.87$	171
6.23	Ulaby et al. (1990) empirical equation, $\epsilon'_r = 1.96\rho_{bd}$, plotted with the frequency-averaged mineral powder permittivity measurements, $\langle \epsilon'_r \rangle$, from the current research.	173
6.24	<i>Figure taken from Hickson et al. (2017a)</i> $\epsilon_{eff} \equiv \epsilon'_r$. Olhoeft and Strangway (1975) empirical equation, $\epsilon'_r = a\rho_{bd}$, and equation (6.4) fit to lunar regolith permittivity measurements from Carrier et al. (1991).	174
6.25	Comparison of measured permittivities across all samples with permittivities predicted from measured grain densities using $\epsilon_s = 1.85\rho_{bd} + 1$ to predict solid permittivities, and then using these as inputs to the LLL model (with boundary conditions). R^2 for 1:1 line is 0.85.	177

6.26	Comparison of measured permittivities across all samples with permittivities predicted from the Ulaby et al. (1990) equation $\epsilon'_r = 1.96^{\rho_{bd}}$. R^2 for 1:1 line is 0.71.	178
6.27	The accurate modelling of the permittivity of the mineral samples in this research is dependent on the length-scale considered: at high porosity (e.g a bulk powder of that mineral) the LLL mixing model was shown to be accurate, and at low porosity (e.g a single mineral grain) the ARIP/CM theories were shown to be accurate. This describes a hierarchical system depending on the length-scale and type of material (single grain or bulk powder) considered. This figure is a graphical depiction of these different models for the forsterite mineral.	179
7.1	Near-surface porosity of asteroids visited by robotic spacecraft calculated using two asteroid radar models (this thesis, and (Magri et al., 1999)) compared with the bulk porosity for the entire asteroid. The dashed line is 50% porosity.	186

Preface

Sections of this thesis have been adapted from previously published peer reviewed papers:

Hickson, D., Boivin, A., Daly, M.G., Ghent, R., Nolan, M.C., Tait, K., Cunje, A. and Tsai, C.A. Near surface bulk density estimates of NEAs from radar observations and permittivity measurements of powdered geologic material. *Icarus* 306, 16-24 (2018).

Hickson, D., Sotodeh, S., Daly, M.G., Ghent, R., and Nolan, M.C. Improvements on effective permittivity measurements of powdered alumina: Implications for bulk permittivity properties of asteroid regoliths. *Advances in Space Research* 59(1), 472–482 (2017).

Results from this thesis research were also incorporated into the following published peer reviewed paper:

Boivin, A.L., Hickson, D., Tsai, C-A., Cunje, A., Ghent, R.R., and Daly, M. Broadband measurements of the complex permittivity of carbonaceous asteroid regolith analog materials. *Journal of Geophysical Research: Planets* 123(12), 3088-3104 (2018).

Chapter 1

Introduction

1.1 Motivation

Knowledge of our solar system has increased greatly in recent decades as a result of technological advances, and renewed interest in, and funding support for, robotic exploration missions. Planetary bodies close to Earth, such as the Moon and Mars, have been studied extensively by robotic orbiters, landers, and rovers by various governmental space organizations. The Moon was the first and (at the time of writing) only solar system body to be visited by humans as part of the United States (US) National Aeronautics and Space Administration (NASA) *Apollo* missions throughout the 1970's. These missions, along with the Soviet Space Program's *Luna* missions, acquired the largest selection of pristine extraterrestrial geologic samples, consisting primarily of lunar regolith, or the fine-grained geologic material covering the upper layer of the lunar surface. Analysis of these samples and data collected from lunar robotic exploration missions have resulted in the current understanding of regolith evolution on airless bodies. For airless bodies further from Earth, the vast majority of data have been collected from Earth-based remote sensing observations and by studying meteorites. Spectral and chemical properties of meteorites are used to link them to the known properties of parent bodies such as the Moon, Mars, asteroids and comets. Much of the current knowledge base of asteroids and their taxonomy is based on the analysis of meteorites. This is biased by an uneven distribution of the types of asteroidal meteorites discovered on Earth, as well as contamination of samples by interaction with Earth's atmosphere and biosphere. As a result, asteroids and comets remain some of the most mysterious objects in our solar system.

Asteroids are of significant interest for research in planetary science as they are generally acknowledged as being relatively unaltered material created during the formation of the solar system. Primitive asteroids that have not undergone metamorphism or significant alteration post forma-

tion have been shown to be compositionally similar to the Sun, and thus the material present in the early solar nebula. Asteroids and comets have been proposed as possible carriers of water and organic material to the early Earth, and may hold information about the formation of life in our solar system. Due to their scientific importance, and our lack of understanding, asteroids and comets have been the focus of many recent and current space missions. The first robotic exploration mission to encounter an asteroid was NASA's *Galileo* mission, which performed flybys of S-complex asteroids 951 Gaspra and 243 Ida in 1991 and 1993 respectively while en route to Jupiter (Chapman, 1996). S-complex refers to the spectral taxonomic complex that the two asteroids belong to, which is a function of the asteroid composition and surface weathering. The *Galileo* flybys confirmed the link between S-complex asteroids and ordinary chondrite meteorites (Chapman, 1996). There are different taxonomic classification schemes that differentiate asteroid complexes into different classes; however, all agree on the main three complexes: the siliceous S-complex, the (most common) low-albedo carbonaceous C-complex, and the metallic X-complex asteroids (DeMeo et al., 2009; Bus and Binzel, 2002; Demeo et al., 2015). In 1997, NASA's *NEAR* spacecraft performed a flyby of 253 Mathilde, providing the first close look at a C-type asteroid (Yeomans et al., 1997). *NEAR* then continued on to orbit and investigate the large S-complex asteroid 433 Eros from 2000 - 2001 (Yeomans et al., 2000). In 2005 the Japan Aerospace Exploration Agency (JAXA) mission *Hayabusa* was the first robotic exploration mission to land on an asteroid, S-complex near-Earth asteroid (NEA) 25143 Itokawa, confirming a rubble-pile structure and composition matching that of LL chondrites (Fujiwara et al., 2006). *Hayabusa* returned pristine regolith samples from 25143 Itokawa, although the sampling mechanism did not function properly and the quantity of returned sample was low. The first X-complex asteroids to be encountered by a spacecraft were 2867 Steins and 21 Lutetia in 2008 and 2010 respectively, observed through flybys during the European Space Agency (ESA) *Rosetta* mission (Keller et al., 2010; Pätzold et al., 2011). NASA's *Dawn* mission orbited the large NEA 4 Vesta 3 times in 2011, confirming 4 Vesta as the likely parent body for Howardite-Eucarite-Diogenite (HED) achondrite meteorites (Russell et al., 2015; McSween Jr et al., 2013). *Dawn* proceeded to orbit the dwarf-planet and first object ever observed in the asteroid belt 1 Ceres, revealing interesting icy features (Russell et al., 2016). The China National Space Administration (CNSA) performed a flyby of the S-complex asteroid 4179 Toutatis in 2012 as part of the *Chang'e-2* mission, confirming the accuracy of the previously derived radar shape model and complex structure (Huang et al., 2013). At the time of writing, in an unprecedented effort to study asteroids, two robotic exploration missions are currently or-

biting and analyzing NEAs. JAXA's *Hayabusa2* mission is orbiting 162173 Ryugu and NASA's Origins, Spectral Interpretation, Resource Identification, Security, Regolith Explorer, or *OSIRIS-REx*, mission is orbiting 101955 Bennu (Lauretta et al., 2017; Watanabe et al., 2017). Both of these asteroids are C-complex asteroids, representing some of the most primitive asteroidal material, with potentially significant quantities of organic carbon and volatile content. These missions also intend to return pristine regolith samples for detailed analysis in Earth-based laboratories. It truly has never been a more interesting time to study asteroids, and the future is filled with data collection and insights to be gained from current missions, such as *Hayabusa2* and *OSIRIS-REx*, and from future planned missions such as NASA's *Lucy*, *DART*, and *Psyche* missions. In support of on-going investigations of 101955 Bennu by the *OSIRIS-REx* mission, the research presented in this thesis focuses on furthering our knowledge of asteroids by ascertaining correlations observed in laboratory dielectric experiments to inform interpretations of asteroid radar observation datasets. With the *OSIRIS-REx* and *Hayabusa2* missions targeting carbonaceous asteroids, as well as the general scientific interest in these types of asteroids, this research will focus the discussion when possible on this asteroid taxonomy.

1.2 Purpose and structure of thesis

The purpose of this thesis is to support the study of asteroids, specifically using radar observations, through increasing our understanding of the responses of materials to radar waves by performing laboratory experiments and modelling the experimental results. The processing, analysis, and modelling of planetary radar data yields properties of the regolith material within the radar penetration depth. These properties, such as the constitutive parameters, can be related to the fundamental response of a material to the electric and magnetic fields which electromagnetic (EM) radiation is comprised of. The constitutive parameters of different materials can be measured in laboratory experiments to see how these change as a function of composition and environmental parameters, such as temperature and water content. These relationships can then be applied to planetary radar data to surmise such environmental parameters of the planetary surfaces. This area of research is broad, as there are numerous environmental parameters that can be varied experimentally. In this thesis, the aim is to use laboratory microwave measurements of the complex permittivity of different geologic powders to understand radar propagation through a particulate regolith layer.

The environmental parameter that is examined is the porosity of the powder, or the amount of void space between solid mineral grains. The derived function relating the permittivity and porosity for a geologic powder is then be applied to some asteroid radar data to calculate the porosity within the radar penetration depth. The structure of the thesis is as follows. Chapter 1 introduces the motivation behind this research and provides the necessary theoretical background in planetary radar and electromagnetic theory to establish context for the remainder of the thesis. Chapter 2 reviews the existing theories, termed generally as electromagnetic mixing equations, relating permittivity and porosity for a material. Then a summary of the body of literature that exists regarding experimental measurements of the permittivity of geologic materials as a function of porosity is given. Chapter 3 discusses the experimental setup and methodology used to perform the permittivity measurements. Chapter 4 discusses the samples that were used in this study, as well as the ways in which they were characterized. Chapter 5 focuses on the results of modelling efforts in correcting measurement bias observed in the permittivity measurement technique used in this thesis. Chapter 6 discusses the permittivity measurements, and the results of modelling these measurements with mixing theories. Chapter 7 discusses the application of this modelling to asteroid radar data. Finally, chapter 8 summarizes the major contributions and findings of this thesis, and provides a brief discourse on the possible future directions that can expand on this work.

1.3 Asteroid Planetary Radar

Visiting asteroids, or any planetary body, with robotic spacecraft remains the best way to obtain the most scientific information. As can be surmised from the above discussion, these visits are relatively few and far between owing to their complexity, orbital constraints, and funding requirements. One of the most-used Earth-based remote sensing techniques to observe asteroids at a fraction of the price of a space mission is planetary radar. Large radio telescopes, like the Arecibo Observatory and the Goldstone Solar System Radar, can transmit microwave signals with enough power and receiver sensitivity to measure the reflected signal from an asteroid surface. From these observations, many properties of asteroids can be determined, such as shape, spin state, generic composition, and surface roughness. Recent funding support for asteroid radar studies and technological advances have significantly increased the number of radar observed NEAs (Figure1.1) (Benner et al., 2015). Radar was developed for military applications concurrently by several countries during World War II for the detection of naval ships and aircraft. The first extraterrestrial target probed by radar

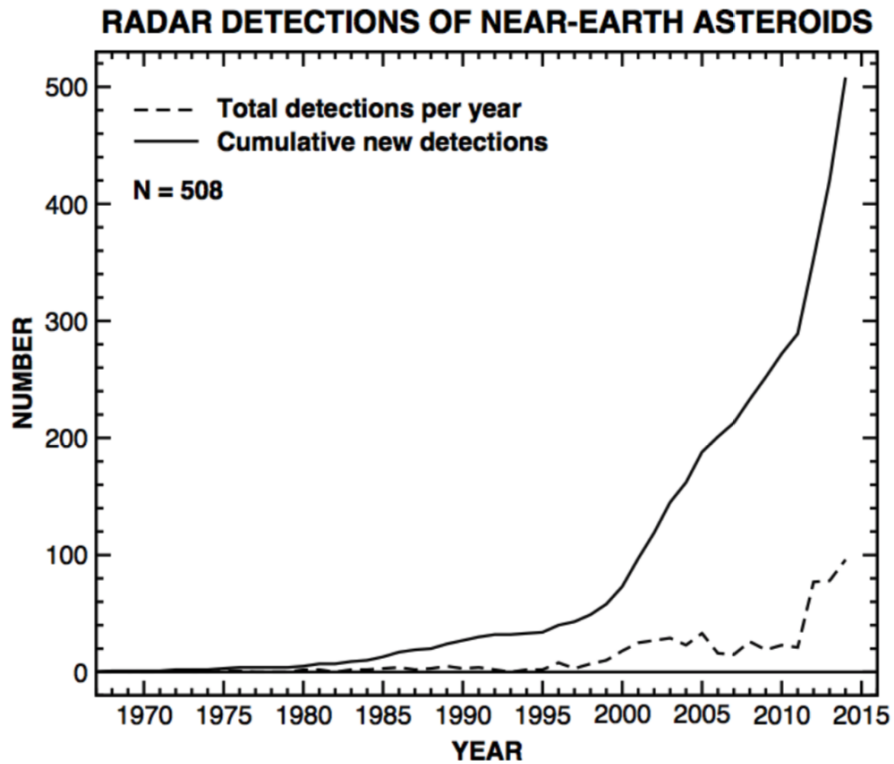


Figure 1.1: *Figure taken from (Benner et al., 2015) with following caption:* Number of near-Earth asteroid radar detections through the end of 2014. The increase in cumulative detections in 1999-2000 was caused in part by a surge of discoveries by LINEAR and by the order-of-magnitude increase in sensitivity at Arecibo after the upgrade. The increase in 2012 was the result of increased funding for Arecibo and greater access to telescope time at Arecibo and Goldstone. (The upgrade here refers to the installation of the 1 MW 12.6 cm radar system).

was the Moon, followed by Venus, Mercury and Mars. The power of a radar echo, or the signal that reflects from a target and is received by the antenna, is determined by the following equation, termed the ‘‘Radar Equation’’ (Ostro, 1993):

$$P_{\text{rcv}} = \frac{P_{\text{tx}} G_{\text{ant}}^2 \lambda^2 \sigma}{(4\pi)^3 r^4} \quad (1.1)$$

In the Radar Equation (1.1), P_{rcv} is the power of the received signal, P_{tx} is the power of the transmitted signal, λ is the signal wavelength, G_{ant} is the antenna’s gain (equal to $\frac{4\pi}{\lambda^2} A_{\text{eff}}$, where A_{eff} is the effective aperture of the antenna), σ is the radar cross-section of the target, and r is the distance to the target. The signal-to-noise (SNR) ratio is a limiting factor for radar detections (the received power must be higher than the receiver noise power), and is dependent on the specific antenna properties. The SNR is dependent on the integration time, which increases with the number of independent estimates of P_{rcv} for a given target (i.e the more observations of a target, the higher the SNR). A radar signal emitted from the transmitting antenna will decay in power according to the inverse of the squared distance from the transmitter, which means that for the two-way travel of a transmitted and then reflected echo, the power will depend on the inverse of the fourth power of distance, or r in the Radar Equation. This means that the received power is strongly limited by the distance to the target, which bounds the possible regions of the solar system observable from Earth-based radar systems.

1.3.1 Radar Polarimetry

In early radar studies of the Moon, it was observed that the Earth’s ionosphere induces Faraday rotation of a linear-polarized signal, so that the angle of polarization is altered with propagation (Campbell, 2016). As a result, most radar signals that propagate through Earth’s atmosphere are intentionally circularly polarized, termed left-handed circularly polarized or right-handed circularly polarized depending on whether the angle of polarization is rotating in a counter-clockwise or clockwise orientation with respect to the direction of propagation. The polarization of the received signal, relative to the polarization of the transmitted signal, contains information about the target surface properties. To make use of this information, most modern radar systems can receive polarimetric signals in two orthogonal polarizations simultaneously, so that the full polarization of the signal is known (Carter et al., 2011). The polarization of the signal is described by the Stokes vector, \mathbf{S} , which can be broken down into the four Stokes parameters, S_{1-4} , all described by the

relative amount of signal received in either circular polarization channel and their relative phase (Campbell, 2016):

$$\mathbf{S} = \begin{bmatrix} S_1 \\ S_2 \\ S_3 \\ S_4 \end{bmatrix} = \begin{bmatrix} \langle V_L^2 \rangle + \langle V_R^2 \rangle \\ 2 \langle V_L V_R \cos \delta \rangle \\ 2 \langle V_L V_R \sin \delta \rangle \\ \langle V_L^2 \rangle - \langle V_R^2 \rangle \end{bmatrix} \quad (1.2)$$

In equation (1.2), V_L and V_R are the voltages measured for the polarized channels in the left- and right- handed sense respectively, δ is their relative phase, and $\langle \rangle$ represents a time average. S_1 is the total average power of the echo received in both left- and right- handed circular polarizations, S_2 and S_3 represent the linearly polarized state of the wave, and S_4 describes the handedness and magnitude of the circularly polarized state of the wave (Carter et al., 2011). Rather than describing the received signal in terms of left- and right-handed circular polarizations, the circular polarization is typically described relative to that transmitted, so that an echo received in the same direction of circular polarization as transmitted is termed same sense circularly polarized (SC), and an echo received in the opposite direction is termed opposite sense circularly polarized (OC). Planar specular reflection of a circularly polarized signal reverses the direction of circular polarization, so that the reflected signal would be in the OC polarization (Ostro et al., 1985; Ostro, 1993; Carter et al., 2011; Campbell, 2016). Received signals that are SC polarized are comprised mostly of diffuse scattering such as multiple scattering, single scattering from curved surfaces, or subsurface volume scattering (Ostro, 1993; Carter et al., 2011). The radar cross section, σ , is labelled for the portion of the radar echo received in SC and OC polarizations as σ_{SC} and σ_{OC} . The radar albedo, $\hat{\sigma}$, for a given circular polarization state is defined as the radar cross section divided by the mean projected area, $\langle A_{\text{proj}} \rangle$, of the radar target, which for the OC signal reads: $\hat{\sigma}_{\text{OC}} \equiv \sigma_{\text{OC}} / \langle A_{\text{proj}} \rangle$ (Magri et al., 2001; Ostro, 1993). The ratio of the radar albedo (or equivalently the radar cross section) in either circular polarization is termed the circular polarization ratio (CPR), μ_C :

$$\mu_C = \frac{\hat{\sigma}_{\text{SC}}}{\hat{\sigma}_{\text{OC}}} = \frac{S_1 - S_4}{S_1 + S_4} \quad (1.3)$$

Since the radar albedo is higher in SC polarization for rougher surfaces, and is higher in OC polarization for smoother surfaces, the CPR is used as an indication of the wavelength-scale surface roughness of the radar target. The wavelength scale dependence is important, as regolith features

can appear smooth or rough on different length scales (i.e particle grain size, surface topology). The CPR will also increase with the incident angle, since more of the reflected signal is comprised of diffuse scattering for large incident angles (Carter et al., 2011). For asteroid observations from Earth-based radar telescopes, the reflected signal is virtually entirely in the backscatter direction and the incident angle can be taken as nadir, or $\approx 0^\circ$. Circularly polarized waves are ideal cases of the general elliptical polarization, which is a combination of circular polarization and linear polarization components at the same frequencies and fixed phase relationship (Carter et al., 2011). Linear polarization is sensitive to transmission through an interface, and can be used as an indication of scattering from subsurface material. The degree of linear polarization, m_l , is calculated from the Stokes vector as (Carter et al., 2011):

$$m_l = \frac{\sqrt{S_2^2 + S_3^2}}{S_1} \quad (1.4)$$

The degree of linear polarization increases with incident angle and is zero at normal incidence, and therefore is not often used for Earth-based radar observations of asteroids (Carter et al., 2011).

1.3.2 Radar Scattering Laws

The scattering of radar signals from planetary surfaces depends on many factors, such as surface roughness, composition, and angle of incidence. Initial radar studies of the Moon did not take these dependencies into consideration until the 1960's, when it was determined that radar scattering was wavelength dependent and varied across the lunar surface (Simpson and Tyler, 1982). The power in the OC polarization of the reflected echo from planetary surfaces, indicating that this is the quasi-specular component of the reflection, was observed to be highest at the subradar point (McCullom and Jakosky, 1993; Ostro, 1993). The subradar point is the intersection of a line connecting the radar receiver and the planet's centre of mass with the surface of the planet (Campbell, 2016). Radar echo power decreases from the subradar point to the limbs, or edges of the target planet, since the reflections from the limb are mostly diffuse in nature. The variation in quasi-specular reflections across a planetary surface is thought to arise from smooth, tilted facets perpendicular to the incident signal, and can be related to the surface slope at wavelength scales. The wavelength scale dependence of the quasi-specular scattering of a planetary surface can then be used to determine changes in surface slope at relevant length scales.

Radar scattering laws have been developed primarily from an empirical perspective to be mathematical descriptions relating the reflection characteristics of a particular surface roughness to the received radar echo power (in the OC polarization for quasi-specular reflection). Several laws have been applied and can be fit to radar data for a given surface, resulting in varying estimates of surface roughness. Each scattering law is described as a function of the incident angle, ϕ , the radar reflectivity, R , and the roughness parameter, C (Mitchell et al., 1996; Ostro, 1993; McCollom and Jakosky, 1993). When not considering diffuse scattering, the roughness parameter is related to the adirectional root-mean-square (rms) slope, s_0 , by the following equation (Simpson and Tyler, 1982):

$$s_0 = \langle \tan^2 \theta_{\text{rms}} \rangle^{1/2} = \left[\int_0^{2\pi} \tan^2 \theta p_p(\theta) \sin \theta d\theta \right]^{1/2} = C^{-1/2} \quad (1.5)$$

In equation (1.5) θ_{rms} is the rms slope angle of a given tilted facet with respect to the mean surface normal, not to be confused with the incident angle, ϕ , and $p_p(\theta)$ is the slope probability distribution, sometimes referred to as Parker’s density function (Simpson and Tyler, 1982; Parker, 1973). If there is no diffuse component to the scattering, the radar cross section as a function of incident angle, $\sigma_{\text{qs}}(\phi)$, is most commonly calculated using the Hagfor’s scattering law, assuming a “smoothly undulating surface” with flat, tilted facets on the wavelength scale (Hagfors, 1964; McCollom and Jakosky, 1993; Ostro, 1993; Campbell, 2002):

$$\sigma_{\text{qs}}(\phi) = \left(\frac{RC}{2} \right) (\cos^4 \phi + C \sin^2 \phi)^{-3/2} \quad (1.6)$$

For the radar cross section resulting from diffuse scattering as a function of incident angle, σ_{diff} , a cosine power law is often assumed:

$$\sigma_{\text{diff}}(\phi) = \rho \cos^n(\phi) \quad (1.7)$$

The exponent, n , in equation (1.7) is fit to a radar spectrum, and usually falls between unity for the scattering observed on the Moon and 2 for Lambertian scattering (Ostro, 1993). ρ is related to the radar brightness, but is not necessarily equivalent to the Fresnel reflectivity (Mitchell et al., 1996; Hudson and Ostro, 1994). The amount of diffuse scattering from a surface is determined by the rms slope at relevant wavelength scales, and increases with increasing incident angle (increasing distance from the subradar point). In some studies, combinations of quasi-specular and diffuse

radar scattering laws are used to derive the rms slope for planetary surfaces (Ostro, 1993; Harmon and Ostro, 1985; Thompson et al., 2011). For asteroid radar studies, typically a radar scattering law similar to equation (1.7) is assumed (Mitchell et al., 1996; Hudson and Ostro, 1994). Figure 1.2 shows the radar cross section calculated by equations (1.6) and (1.7) for a range of incident angles and rms slope angles. The radar albedo due to quasi-specular reflection alone is typically assumed

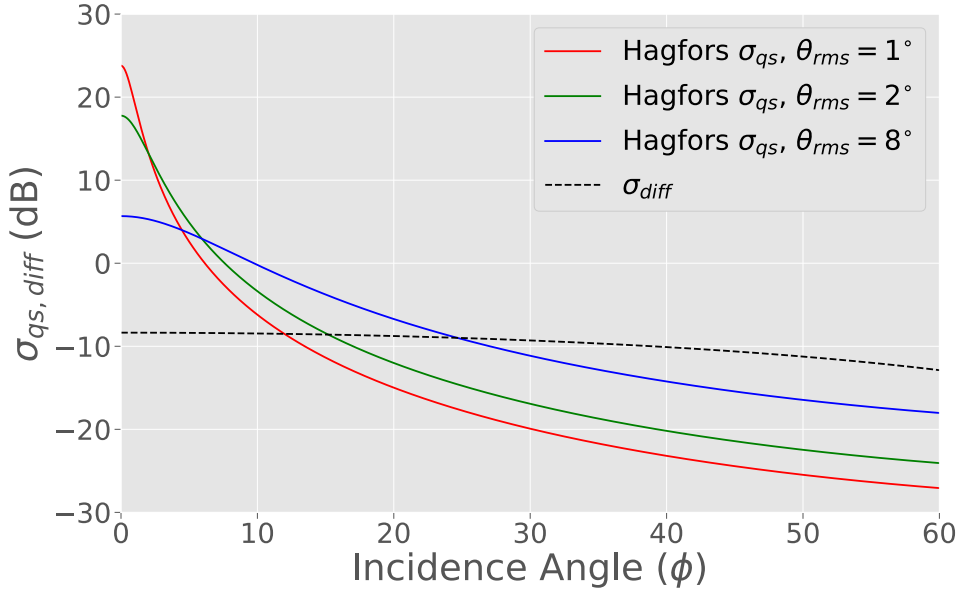


Figure 1.2: Hagfor’s scattering law for rms slope angles of $\theta_{rms} = 1^\circ, 2^\circ,$ and 8° , as well as the diffuse scattering law for incident angles from $\phi = 0 - 60^\circ$. The quasi-specular radar cross section is given in units of decibels ($\sigma_{qs}(\text{dB}) = 10\log_{10}(\sigma_{qs})$) and is seen to drop off sharply as the incident angle increases from nadir ($\phi = 0$), and decreases gradually with increasing ϕ . Increasing surface roughness (θ_{rms}) decreases the sharpness of the nadir peak. The diffuse radar cross section drops off less dramatically with incident angle, and becomes more important for high ϕ and high θ_{rms} . In this figure the exponent assumed in equation (1.7) is $n = 1.5$, and the radar reflectivity is calculated from the Fresnel reflectivity at normal incidence on a loss-less material with $\epsilon'_r = 4$.

equal to $\hat{\sigma}_{OC}$, and is related to the Fresnel power reflection coefficient, R_{fp} , by the backscatter gain, g (Ostro, 1993; Magri et al., 2001; Mitchell et al., 1996):

$$g = \frac{\hat{\sigma}_{OC}}{R_{fp}} \approx 1 + \frac{1}{2}s_0^2 \quad (1.8)$$

To the second order, radar scattering theories generally agree in the equivalency between g and s_0

in equation (1.8) for a spherical target, where $g < 1.5$ (increasing g from unity indicates increased surface roughness) is observed for most surfaces, corresponding to an adirectional rms slope of $\theta_{\text{rms}} = 45^\circ$ (Ostro et al., 1985). By applying a radar scattering law to fit the observed radar spectrum of a planetary surface, the surface roughness and Fresnel reflectivity can be determined.

1.4 Electromagnetic Theory

1.4.1 Electromagnetic Wave Propagation: The Wave Equation

The propagation of electromagnetic radiation through a vacuum is described by Maxwell's equations, which in differential form and in the time domain are (Balanis, 1989) (all subsequent derivations in this section are based on (Balanis, 1989), with any deviations indicated by another citation. Vectors are indicated by bold characters.):

$$\nabla \times \mathbf{E} = -\mathbf{M}_i - \frac{\partial \mathbf{B}}{\partial t} \quad (1.9)$$

$$\nabla \times \mathbf{H} = \mathbf{J}_i + \mathbf{J}_c + \frac{\partial \mathbf{D}}{\partial t} \quad (1.10)$$

$$\nabla \cdot \mathbf{D} = \rho_e \quad (1.11)$$

$$\nabla \cdot \mathbf{B} = \rho_m \quad (1.12)$$

In equations (1.9) - (1.12), the variables are defined as:

\mathbf{E} = electric field intensity (V/m)

\mathbf{H} = magnetic field intensity (A/m)

\mathbf{D} = electric flux density (C/m²)

\mathbf{B} = magnetic flux density (T)

\mathbf{J}_i = impressed (source) electric current density (A/m²)

\mathbf{J}_c = conduction electric current density (A/m²)

\mathbf{M}_i = impressed (source) magnetic current density (V/m²)

ρ_e = electric charge density (C/m³)

ρ_m = magnetic charge density (T/m)

So far there have been no magnetic monopoles, or magnetic charge carriers, discovered in nature, and the magnetic charge density, ρ_m , and impressed magnetic current density, \mathbf{M}_i , are not physi-

cally reasonable. In the formulation of Maxwell's equations presented in equations (1.9) - (1.12), these terms are included to provide symmetry between the electric and magnetic phenomena and for mathematical descriptions of different electromagnetic problems; however, they are typically assumed to be equal to zero in most references, and will be treated so for the purpose of this thesis. The constitutive equations are used to further describe the interaction between the variables introduced in equations (1.9) - (1.12), specifically in the interaction of electric and magnetic fields with matter:

$$\mathbf{D} = \epsilon^* \mathbf{E} \quad (1.13)$$

$$\mathbf{B} = \mu^* \mathbf{H} \quad (1.14)$$

$$\mathbf{J}_c = \sigma_s \mathbf{E} \quad (1.15)$$

The charged particles that matter consists of (electrons and protons), and inherent magnetic or electric dipoles present in different materials, interact with the electric and magnetic fields of an electromagnetic wave, and will alter the propagation properties of the wave. The multiplication in equations (1.13) - (1.15) is for the variables in the frequency domain, where in the time domain the multiplication is a convolution. The variables ϵ^* , μ^* , and σ_s are called the constitutive parameters and determine how a material responds to electromagnetic radiation. EM radiation consists of electric and magnetic fields alternating with time, thus the response of the charges within a material will be a function of the frequency of the oscillation of the fields. The constitutive parameters are generally complex quantities, termed the (complex) dielectric permittivity, ϵ^* , the (complex) magnetic permeability, μ^* , and the (real-valued) static electric conductivity, σ_s . In 3-dimensional (3D) space the constitutive parameters can also be a function of position within a material, and are then in general 3×3 tensors relating the x , y and z components of the associated vectors, which for \mathbf{E} and \mathbf{D} would read:

$$\mathbf{D} = \begin{bmatrix} D_x \\ D_y \\ D_z \end{bmatrix} = \begin{bmatrix} \epsilon_{xx}^* & \epsilon_{xy}^* & \epsilon_{xz}^* \\ \epsilon_{yx}^* & \epsilon_{yy}^* & \epsilon_{yz}^* \\ \epsilon_{zx}^* & \epsilon_{zy}^* & \epsilon_{zz}^* \end{bmatrix} \begin{bmatrix} E_x \\ E_y \\ E_z \end{bmatrix} \quad (1.16)$$

Combining Maxwell's equations (1.9) - (1.12) with the constitutive equations (1.13) - (1.15) results in:

$$\nabla \times \mathbf{E} = -\mu^* \frac{\partial \mathbf{H}}{\partial t} \quad (1.17)$$

$$\nabla \times \mathbf{H} = \mathbf{J}_i + \sigma_s \mathbf{E} + \epsilon^* \frac{\partial \mathbf{E}}{\partial t} \quad (1.18)$$

$$\nabla \cdot \mathbf{E} = \frac{1}{\epsilon^*} \rho_e \quad (1.19)$$

$$\nabla \cdot \mathbf{H} = 0 \quad (1.20)$$

Equation (1.10) can be rewritten by considering the EM fields as time harmonic with a $e^{j\omega t}$ dependence (i.e $\mathbf{D}(x, y, z, t) = \mathbf{D}(x, y, z)e^{j\omega t}$), where $j^2 = -1$, and $\omega = 2\pi f$, and computing the derivative $\frac{\partial \mathbf{D}}{\partial t}$ (Knoll, 1996; Plonus, 1978):

$$\nabla \times \mathbf{H} = \mathbf{J}_i + \mathbf{J}_c + j\omega \mathbf{D} \quad (1.21)$$

Substituting equations (1.13) and (1.15) into (1.21) results in:

$$\nabla \times \mathbf{H} = \mathbf{J}_i + \sigma_s \mathbf{E} + j\omega(\epsilon' - j\epsilon'')\mathbf{E} \quad (1.22)$$

ϵ' refers to the real part of the complex dielectric permittivity, and ϵ'' the imaginary part (i.e, $\epsilon^* = \epsilon' - j\epsilon''$). The remainder of this thesis will use the same notation for real and imaginary components of complex numbers. Equation (1.22) can be rewritten in terms of an effective, or equivalent conductivity $\sigma_e = \sigma_s + \omega\epsilon'' = \sigma_s + \sigma_a$:

$$\nabla \times \mathbf{H} = \mathbf{J}_i + (\sigma_s + \omega\epsilon'')\mathbf{E} + j\omega\epsilon'\mathbf{E} = \mathbf{J}_i + \sigma_e \mathbf{E} + j\omega\epsilon'\mathbf{E} \quad (1.23)$$

The complex nature of ϵ^* and μ^* accounts for the frequency dependent properties of the permittivity and permeability. Now with the definition of an effective conductivity, σ_e , with a static, σ_s , and an alternating field, σ_a , component, the frequency dependent conductivity behaviour of a material is also accounted for.

The total electric current density, \mathbf{J}_t , of a material is a combination of the impressed electric current density, \mathbf{J}_i , the effective electron conduction current density, $\mathbf{J}_{ce} = \sigma_e \mathbf{E}$, and the effective displacement current density, $\mathbf{J}_{de} = j\omega\epsilon'\mathbf{E}$:

$$\mathbf{J}_t = \mathbf{J}_i + \sigma_e \mathbf{E} + j\omega\epsilon' \mathbf{E} \quad (1.24)$$

Equation (1.24) can be rearranged to:

$$\mathbf{J}_t = \mathbf{J}_i + j\omega\epsilon' \left(1 - j\frac{\sigma_e}{\omega\epsilon'}\right) \mathbf{E} = \mathbf{J}_i + j\omega\epsilon' (1 - j \tan \delta_e) \mathbf{E} \quad (1.25)$$

In equation (1.25), the effective loss tangent, $\tan \delta_e = \frac{\sigma_s}{\omega\epsilon'} + \frac{\sigma_a}{\omega\epsilon'}$, the static electric loss tangent, $\tan \delta_s = \frac{\sigma_s}{\omega\epsilon'}$, and the alternating current electric loss tangent, $\tan \delta_a = \frac{\sigma_a}{\omega\epsilon'} = \frac{\epsilon''}{\epsilon'}$, have been defined, where $\tan \delta_s$ and $\tan \delta_a$ represent energy loss in the electric field strength due to DC conduction and AC conduction.

The symmetry between the electric and magnetic components of EM radiation allow a complementary derivation to arrive at a similar expression to describe the total magnetic current density, \mathbf{M}_t :

$$\mathbf{M}_t = \mathbf{M}_i + j\omega\mu' (1 - j \tan \delta_m) \mathbf{H} \quad (1.26)$$

In equation (1.26), $\tan \delta_m = \frac{\mu''}{\mu'}$ is the alternating magnetic loss tangent (since there is no static case as a result of no magnetic monopoles). Substituting in equations (1.13) and (1.15) into (1.10), and (1.14) into (1.9), along with the definitions of σ_e and ϵ^* , results in:

$$\nabla \times \mathbf{E} = -\mathbf{M}_i - \mu^* \frac{\partial \mathbf{H}}{\partial t} \quad (1.27)$$

$$\nabla \times \mathbf{H} = \mathbf{J}_i + \sigma_e \mathbf{E} + \epsilon' \frac{\partial \mathbf{E}}{\partial t} \quad (1.28)$$

To uncouple these two first order differential equations, the medium is assumed homogeneous and the curl of each side of equations (1.27) and (1.28) is taken to arrive at:

$$\nabla^2 \mathbf{E} = \nabla \times \mathbf{M}_i + \mu^* \frac{\partial \mathbf{J}_i}{\partial t} + \frac{1}{\epsilon'} \nabla \rho_{ve} + \mu^* \sigma_e \frac{\partial \mathbf{E}}{\partial t} + \mu^* \epsilon' \frac{\partial^2 \mathbf{E}}{\partial t^2} \quad (1.29)$$

$$\nabla^2 \mathbf{H} = -\nabla \times \mathbf{J}_i + \sigma_e \mathbf{M}_i + \frac{1}{\mu^*} \nabla \rho_{vm} + \epsilon' \frac{\partial \mathbf{M}_i}{\partial t} + \mu^* \sigma_e \frac{\partial \mathbf{H}}{\partial t} + \mu^* \epsilon' \frac{\partial^2 \mathbf{H}}{\partial t^2} \quad (1.30)$$

If it is further assumed that there are no sources near the region in consideration, $\mathbf{J}_i = \rho_{ve} = 0$ and $\mathbf{M}_i = \rho_{vm} = 0$ (even though $\mathbf{M}_i = \rho_{vm} = 0$ is already true due to the lack of magnetic monopoles), equations (1.29) and (1.30) can be written in the form that is termed the Wave Equation:

$$\nabla^2 \mathbf{E} = \mu^* \sigma_e \frac{\partial \mathbf{E}}{\partial t} + \mu^* \epsilon' \frac{\partial^2 \mathbf{E}}{\partial t^2} \quad (1.31)$$

$$\nabla^2 \mathbf{H} = \mu^* \sigma_e \frac{\partial \mathbf{H}}{\partial t} + \mu^* \epsilon' \frac{\partial^2 \mathbf{H}}{\partial t^2} \quad (1.32)$$

The Wave Equation describes the propagation of EM waves through a material. The dominant constitutive parameter for a given material will then largely determine the EM properties of that material. For materials with free charges, such as metals, or with significant $\tan \delta_e$, the first term on the right hand side of either equation will dominate. Similarly, for materials with no free charges, such as insulators or dielectrics with low $\tan \delta_e$, the second term on the right hand side of either equation will dominate. The propagation of radar signals, which are EM waves, through a material is described by the Wave Equation, where the variation of propagation/scattering properties of EM waves within/from different materials is due to the differences in constitutive parameters.

1.4.2 Propagation, Phase, and Attenuation constants

The Wave Equation (equations (1.31) & (1.32)) can be written in time harmonic form, similar to the derivation of equation (1.21) by assuming each field varies in time according to $e^{j\omega t}$. In this way, the operators $\partial/\partial t$ and $\partial^2/\partial t^2$ can be rewritten as $j\omega$ and $-\omega^2$ ($(j\omega)^2 = -\omega^2$, since $j^2 = -1$). Under the same assumptions that there are no sources, the Wave Equation (equations (1.31) & (1.32)) can be rewritten as:

$$\nabla^2 \mathbf{E} = j\omega \mu^* \sigma_e \mathbf{E} - \omega^2 \mu^* \epsilon' \mathbf{E} = \gamma^2 \mathbf{E} \quad (1.33)$$

$$\nabla^2 \mathbf{H} = j\omega \mu^* \sigma_e \mathbf{H} - \omega^2 \mu^* \epsilon' \mathbf{H} = \gamma^2 \mathbf{H} \quad (1.34)$$

In the time harmonic Wave Equation (equations (1.33) & (1.34)) the propagation constant, γ , has been introduced:

$$\gamma^2 = j\omega \mu^* \sigma_e - \omega^2 \mu^* \epsilon' \quad (1.35)$$

Writing γ as a complex number, $\gamma = \alpha + j\beta$, squaring the result, $\gamma^2 = \alpha^2 + j2\alpha\beta - \beta^2$, and comparing with equation (1.35), equating the real and imaginary parts, expressions for α and β can be written as:

$$\alpha = \omega\sqrt{\mu^*\epsilon'} \left\{ \frac{1}{2} \left[\sqrt{1 + \tan^2 \delta_e} - 1 \right] \right\}^{1/2} \quad (\text{Np/m}) \quad (1.36)$$

$$\beta = \omega\sqrt{\mu^*\epsilon'} \left\{ \frac{1}{2} \left[\sqrt{1 + \tan^2 \delta_e} + 1 \right] \right\}^{1/2} \quad (\text{rad/m}) \quad (1.37)$$

β in equation (1.37) is called the phase-propagation constant, which defines the phase velocity at which the EM wave propagates. The sinusoidal wave form of \mathbf{E} and \mathbf{H} means that the strength of either field is determined by the phase angle, which is constant at a phase velocity defined by β (Plonus, 1978). α in equation (1.36) is called the attenuation constant, and describes the attenuation of an EM wave during propagation through a medium with appreciable σ_e , otherwise known as a lossy material. The attenuation constant is commonly expressed in units of decibels (dB), which can be calculated from units of (Np/m) by:

$$\alpha(\text{dB}) = 20\log_{10} \left(e^{\alpha(\text{Np/m})} \right) = 8.686\alpha(\text{Np/m}) \quad (1.38)$$

The attenuation of an EM wave decreases the energy of that wave as it propagates through a material. The distance travelled when the wave energy reaches $e^{-1} = 0.368$ of it's initial energy is termed the skin depth, δ :

$$\delta = \frac{1}{\alpha} \quad (1.39)$$

The skin depth is generally considered the penetration depth of an EM wave into a lossy medium. In the context of radar remote sensing, the penetration depth is $\delta = \frac{1}{2\alpha}$, since the wave that propagates through the material must be reflected (and thus travels a distance in the material twice in opposite directions) in the subsurface in order for a reflected wave to be detected.

1.4.3 Dielectric Permittivity

As was introduced in section 1.4.2, materials that do not contain free charges are termed dielectric, or insulating, materials. Since there are no free charges, when an electric field is externally applied to such a material, there is no static conduction current ($\sigma_s = 0$). Instead, the electric field exerts

a force that shifts the distribution of charges within the material that depends on the frequency, strength, and direction of the electric field, as well as the material properties. When a positive and negative charge, with total charge Q , are displaced a distance \mathbf{d} from one another, a dipole moment, \mathbf{p} , is established:

$$\mathbf{p} = Q\mathbf{d} \quad (1.40)$$

The accumulation of n dipole moments (assuming all dipoles are of the same magnitude and direction for simplicity) within a dielectric in the presence of an applied electric field summed over a given volume defines the electric polarization, \mathbf{P} :

$$\mathbf{P} = n\mathbf{p} = \epsilon_0\chi_e\mathbf{E} \quad (1.41)$$

In equation (1.41), χ_e is the electric susceptibility:

$$\chi_e = \frac{1}{\epsilon_0} \frac{|\mathbf{P}|}{|\mathbf{E}|} \quad (1.42)$$

In equation (1.42) the permittivity of free space (vacuum), $\epsilon_0 = 8.85 \times 10^{-12}$ (F/m), has been introduced. The electric polarization interacts with the applied electric field, \mathbf{E} , to change the electric flux density, \mathbf{D} :

$$\mathbf{D} = \epsilon_0\mathbf{E} + \mathbf{P} = \epsilon^*\mathbf{E} \quad (1.43)$$

Typically, the complex permittivity of a material is reported relative to the permittivity of free space, and is termed the relative complex permittivity, ϵ_r^* :

$$\epsilon_r^* = \frac{\epsilon^*}{\epsilon_0} = \epsilon_r' - j\epsilon_r'' = 1 + \chi_e \quad (1.44)$$

There are different types of charge separation, and thus dipole moments, that can manifest in a material in the presence of an applied electric field. These depend on the atomic, molecular, and polar properties, as well as the frequency of the applied electric field. Since the length scale for each polarization mechanism is different, the frequency of the oscillation in the electric field for an EM wave determines whether there is enough time for the dipole to establish itself before the field direction is inverted. The polarization mechanisms for dielectric materials are summarized in

Figure 1.3. As an example, the length scale of an atom's electron cloud is relatively small, and so

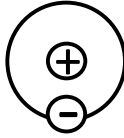
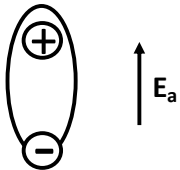
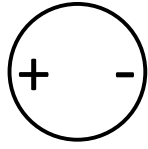
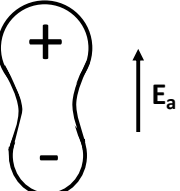
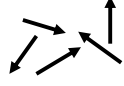

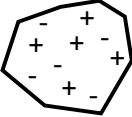
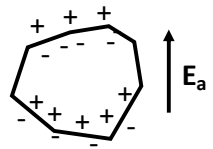
Polarization Mechanism	Frequency (Hz)	Description	No applied field	Applied Field
Electronic Polarization	$< 10^{24}$	An atom's electron cloud is distorted in the presence of an applied electric field.		
Molecular Polarization	$< 10^{14}$	An entire molecule is distorted in response to an applied electric field.		
Ionic Polarization	$< 10^{14}$	Ions are redistributed in a material in response to an applied electric field.		
Orientation Polarization	$< 10^{12}$	Polar molecules are reoriented in the presence of an applied electric field.		
Interfacial Polarization	$< 10^6$	Charge accumulations at the boundary of electrical properties in a material in the presence of an applied electric field.		

Figure 1.3: Polarization mechanisms in dielectrics adapted from (Stillman, 2006; Olhoef, 1981; Balanis, 1989). Interfacial polarization is sometimes referred to as Maxwell-Wagner polarization, and in this figure is represented by charge build-up at the boundaries of an individual mineral grain.

this type of dipole can be established very quickly and persists to high frequencies ($< 10^{24}$ Hz). The length scale of an entire mineral grain is much larger than this, so the dipole associated with interfacial polarization is only established for lower frequencies ($< 10^6$ Hz). If the direction of the electric field is inverted too quickly, the charges cannot move the required distance in time. The bound charges in a dielectric want to resist the separation of charges to maintain the lowest energy state. Therefore when polarization mechanisms establish electric dipoles in a material, there is electric potential energy stored in the dipoles. This is described by the real part of the relative complex permittivity. The rotation and movement of permanent dipoles and charges in a dielectric material during polarization consumes energy, and represents energy lost in the material, which is described by the imaginary part of the relative complex permittivity. The polarization of charges within a dielectric is distinct from the polarization of an EM wave, although the same term is used to describe both phenomena. If the frequency of oscillation of the electric field of an EM wave is in resonance with the rotation rate of the dipoles in a dielectric, significant energy is lost, causing

a peak in the effective loss tangent ($\tan \delta_e$) of the material at that frequency, termed a relaxation peak. The relaxation refers to how long it takes for the dipoles to reorient themselves.

Frequency Dependence

The frequency dependence of polarization mechanisms in dielectrics has already been introduced, but also implies that the real and imaginary parts of the relative complex permittivity are related. When the dipoles in a material are establishing themselves by rotating and moving charges in space, potential energy is converted to kinetic energy and the real part of the relative complex permittivity (hereafter just referred to as permittivity for simplicity) decreases as the imaginary part of the permittivity increases. This interdependency has been derived mathematically for determining ϵ'_r as a function of ϵ''_r and vice-versa, termed the Kramers-Kronig relations (also referred to as the Hilbert transform of a complex function):

$$\epsilon'_r(\omega) = 1 + \frac{2}{\pi} \int_0^\infty \frac{\omega' \epsilon''_r(\omega')}{(\omega')^2 - \omega^2} d\omega' \quad (1.45)$$

$$\epsilon''_r(\omega) = \frac{2\omega}{\pi} \int_0^\infty \frac{1 - \epsilon'_r(\omega')}{(\omega')^2 - \omega^2} d\omega' \quad (1.46)$$

In (1.45) and (1.46), $\omega = 2\pi f$ is the angular frequency of the applied electric field. Several models describing the real and imaginary parts of the permittivity as a function of frequency, typically in the form of angular frequency, have been derived by various researchers. One of the most commonly used models, the Debye model, was derived by considering the response of pure polar molecules in the presence of an applied electric field (Sihvola, 1999):

$$\epsilon_r^*(\omega) = \epsilon'_r(\omega) - j\epsilon''_r(\omega) = \epsilon'_{r,\infty} + \frac{\epsilon'_{r,s} - \epsilon'_{r,\infty}}{1 + j\omega\tau} \quad (1.47)$$

Equation (1.47) introduces the static permittivity, $\epsilon'_{r,s}$, the high-frequency limit for the permittivity, $\epsilon'_{r,\infty}$, and the relaxation time constant, τ , which refers to the relaxation time for a given resonant frequency, $\omega_{res} = \frac{1}{\tau}$, for a local maximum ϵ''_r in a material as described earlier. The real and imaginary parts of the permittivity can be solved for individually from the general Debye equation as:

$$\epsilon'_r(\omega) = \epsilon'_{r,\infty} + \frac{\epsilon'_{r,s} - \epsilon'_{r,\infty}}{1 + (\omega\tau)^2} \quad (1.48)$$

$$\epsilon''_r(\omega) = \frac{(\epsilon'_{r,s} - \epsilon'_{r,\infty})\omega\tau}{1 + (\omega\tau)^2} \quad (1.49)$$

Multiple polarization mechanisms can occur at different frequencies within a material, so in general there are N relaxation time constants to describe N polarization mechanisms:

$$\epsilon_r^*(\omega) = \epsilon'_r(\omega) - j\epsilon''_r(\omega) = \epsilon'_{r,\infty} + \sum_{n=1}^N \frac{\epsilon'_{r,s} - \epsilon'_{r,\infty}}{1 + j\omega\tau_n} \quad (1.50)$$

Several variations of (1.50) have been proposed to explain experimentally observed data, which in the most general form is the Havriliak-Negami (HN) relaxation equation (Tsai et al., 2019):

$$\epsilon_r^*(\omega) = \epsilon'_r(\omega) - j\epsilon''_r(\omega) = \epsilon'_{r,\infty} + \sum_{n=1}^N \frac{\epsilon'_{r,s} - \epsilon'_{r,\infty}}{(1 + (j\omega\tau_n)^{\alpha_n})^{\beta_n}} \quad (1.51)$$

In equation (1.51), α_n and β_n are parameters that control the broadness and asymmetry of a given relaxation peak. Some names for special cases of the HN relaxation are the Cole-Cole relaxation ($\beta = 1$), the Cole-Davidson relaxation ($\alpha = 1$), and the Debye relaxation ($\alpha = \beta = 1$).

1.4.4 Magnetic Permeability

The magnetic permeability of a material relates the magnetic flux density, \mathbf{B} , and the magnetic field intensity, \mathbf{H} (see equation (1.14)), in an analogous way that the dielectric permittivity relates the electric flux density, \mathbf{D} , and electric field intensity, \mathbf{E} . Similar to the permittivity, the magnetic permeability is complex, and often reported relative to the magnetic permeability of free space, $\mu_0 = 4\pi \times 10^{-7}$ (henries/m):

$$\mu_r^* = \frac{\mu^*}{\mu_0} = \mu'_r - j\mu''_r \quad (1.52)$$

Magnetic dipoles in a material are formed by the angular momentum of electrons as they spin and orbit atomic nuclei (Balanis, 1989; Stillman, 2006). For some minerals, such as magnetite, the inherent magnetic dipoles in the molecules will interact with an applied magnetic field. In most cases, there are not significant magnetic dipoles present, and the mineral in question has little interaction with an applied magnetic field. For the purposes of the work presented in thesis, the

minerals studied are considered non-magnetic, and to have a magnetic permeability equal to that of free space (μ_0). This assumption can be tested and verified for each material experimentally, and is also assumed by similar studies in the literature (Campbell and Ulrichs, 1969; Robinson and Friedman, 2003; Telford et al., 1990). As such, there will not be extensive discussion on the magnetic properties of materials throughout this thesis.

1.4.5 Electric Conductivity

As opposed to dielectric materials with no free charges, conductive materials contain significant amounts of free electrons that are loosely bound to their parent atom, permitting movement of electrons. In the absence of an applied electric field, these charges move in random directions resulting in zero net conduction current. In the presence of an applied electric field, the charges will migrate to the surface of a conductor, establishing an electric current as described in equation (1.15). The amount of bound and free charges in a material determines if that material behaves more like a conductor, or an insulator. Metals contain many free electrons and behave almost like perfect conductors, whereas minerals often contain more bound electrons and behave like dielectrics. The magnitude of the effective electric loss tangent, $\tan \delta_e$, gives an indication of whether there is appreciable conductive current flow in a material. Water, especially salt water or water with ionic impurities, is a good conductor and can therefore drastically influence whether a geologic powder will behave according to a conductive or dielectric material. This is why differences in water saturation in natural settings can be readily observed by electromagnetic methods. On Earth, this is an important parameter to consider; however, in the vacuum of space and for small, airless bodies, water cannot exist in liquid form. Planetary radar studies of asteroids will not likely encounter (liquid) water saturated geologic material. For this reason, the work presented in this thesis assumes that there is negligible static conductivity in the mineral samples considered. To justify this assumption, steps were taken to ensure minimal water saturation of samples during measurements.

1.4.6 Electromagnetic Wave Polarization

The polarization of an EM wave is arbitrarily defined as the magnitude and direction of the electric field vector over time, where specific polarizations refer to patterns in these properties. If the tip of the electric field vector stays within a straight line in the plane perpendicular to the direction of wave propagation, the wave is linearly polarized. In general, the polarization of any wave can

be described by a combination of orthogonal linear polarizations in the plane perpendicular to the direction of wave propagation. If the orthogonal (often termed H for horizontal and V for vertical) polarizations have equal magnitude and are exactly $\pi/2$ radians (or integer multiples of $\pi/2$) out of phase, the tip of the electric field vector will trace a circle in the plane perpendicular to the direction of propagation, which is referred to as circular polarization. The direction of the rotation of the electric field vector with time is determined by which orthogonal polarization is leading in phase, where the naming convention of left- and right-handed circular polarization has already been defined. Elliptically polarized waves are composed of both left- and right-handed polarization components.

1.4.7 Reflection and Transmission

When an EM wave encounters a boundary where the constitutive parameters of the medium in which the wave propagates are changed, a portion of the wave is reflected from, and a portion transmitted through, the boundary. The angle of the incident (wave 1) and transmitted waves (wave 2) with respect to the surface normal vector are given by Snell's law:

$$n_1 \sin \theta_1 = n_2 \sin \theta_2 \quad (1.53)$$

In Snell's law (1.53) the index of refraction, n , for the mediums 1 and 2 has been introduced. The index of refraction of a material is the ratio of the speed of light in vacuum, $c = \frac{1}{\sqrt{\epsilon_0 \mu_0}}$, to the phase velocity of a wave, $v_p = \frac{\omega}{\beta}$, travelling in that medium:

$$n = \frac{c}{v_p} = \frac{1}{\frac{\omega}{\beta \sqrt{\epsilon_0 \mu_0}}} \approx \sqrt{\epsilon'_r} \quad (1.54)$$

In (1.54), the term on the right side has been equated with the index of refraction by assuming that the material is loss-less and non-magnetic. The electric and magnetic field amplitudes of the reflected and transmitted EM waves are derived by applying boundary conditions at the interface of contrasting n , or $\sqrt{\epsilon'_r}$ for the loss-less and non-magnetic assumptions. For the general case of normal incidence of an EM wave to some interface, the Fresnel amplitude reflection coefficient, R_f (Fresnel power reflection coefficient, $R_{fp} = |R_f|^2$), which defines the fraction of the wave reflected, is calculated according to:

$$R_f = \frac{\sqrt{\epsilon'_{r,2}} - \sqrt{\epsilon'_{r,1}}}{\sqrt{\epsilon'_{r,2}} + \sqrt{\epsilon'_{r,1}}} \quad (1.55)$$

The transmission coefficient, T , defining the fraction of the wave transmitted, is then $T = 1 - R_f$, or $T = (2\sqrt{\epsilon'_{r,2}}) / (\sqrt{\epsilon'_{r,1}} + \sqrt{\epsilon'_{r,2}})$. The Fresnel reflection and transmission coefficients depend on the angle of incidence, as well as the polarization, of the incident wave. In general the index of refraction is a complex quantity. Lossy materials will also require different considerations for their reflection and transmission properties. The derivations of these equations are beyond the scope of this thesis, but can be found in most EM textbooks (Griffiths, 1999; Balanis, 1989).

1.4.8 Theoretical Assumptions

In the EM discussion just presented, several assumptions about material properties have been made to justify the use of certain equations. To clarify the interpretation of this thesis, the main assumptions about the material properties of the geologic samples considered in this thesis are summarized in this section. All of the constitutive parameters of the samples are considered linear functions of the applied field strength, which is valid for most materials. The constitutive parameters are also considered to be constant, or homogeneous, with respect to the position within a sample, which is valid for geologic powders randomly mixed with grain sizes much smaller than the observing wavelength. Similarly, due to the random orientation of individual powder grains, the samples are considered isotropic, which means that the constitutive parameters are independent of the direction of the applied field. The dependence of the constitutive parameters on the frequency of the applied field is termed dispersion. In general, the samples from this study are characterized as low-loss materials and have little dispersion. This low-loss assumption validates the use of (1.54) and equations (1.55) in describing EM reflection properties for these materials. The samples are also considered non-magnetic, which is true for the dominant minerals identified in each sample. Lastly, the samples are considered to have negligible static conductivity due to the low values of the loss tangent measured for each sample at low frequencies. These assumptions are commonly applied in similar dielectric experiments and radar modelling. The focus is on the real part of the permittivity throughout this thesis, as this has the greatest impact on the reflectance properties of most dry geologic materials, including the samples used in this thesis.

1.5 Geologic Description of Powders

This thesis is predominantly concerned with mineral and rock samples in a particulate, or powder, form. Therefore it is necessary to define some parameters that are commonly used to describe the properties of geologic samples in both solid and powder form. The density of a geologic sample can refer to the bulk density, ρ_{bd} , or the grain (solid) density, ρ_{s} . The bulk density refers to the mass density within a specified volume, and can include micro- and macro-porosity. Porosity, ϕ , is defined as the proportion of empty space, or voids, in the sample. Micro-porosity refers to the void space on very small scales in a sample, typically in microcracks between crystal grains. Macro-porosity refers to void space on a larger scale, such as fractures and the voids between particulate grains (composed of many crystals). The grain density refers to the zero-porosity density of a geologic sample. In practice, the grain density of a sample is determined through experimental techniques that cannot identify certain types of micro-porosity in a sample, like isolated voids, and so in truth is not representative of the zero-porosity state of the sample. This bias is relatively insignificant, and for the rest of this thesis the grain density will be considered representative of the zero-porosity sample. When the term “solid permittivity” is used, this is referring to the permittivity of the zero-porosity sample. The porosity can be calculated from the bulk density and grain density of a sample according to:

$$\phi = 1 - \frac{\rho_{\text{bd}}}{\rho_{\text{s}}} \quad (1.56)$$

Chapter 2

Electromagnetic Mixing Equations

Review

2.1 Introduction

The intricacies of natural systems makes modelling their properties difficult, and has motivated extensive studies into the description of such systems by macroscopic effective properties. The powdered samples used in the presented research, and the regolith material on the surfaces of planetary bodies, can be viewed as heterogeneous mixtures. For the powdered mineral samples analyzed in this research, this mixture is comprised of the solid mineral grains and air in the pore space between grains. For actual regolith material, this mixture is made up of a variety of minerals, lithic fragments, glasses, voids, and in some cases, possibly adhered water or other volatiles as well. In both the cases of radar remote sensing of planetary bodies and laboratory permittivity measurements of powders, some or all of the information extracted from a given target/sample by a microwave signal is the effective material properties averaged over the observing wavelength. When the heterogeneities of a material are on a similar length scale as the wavelength of incident EM radiation, Mie and Rayleigh scattering occur. For heterogeneities at smaller length scales (typical threshold is 1/10th of the EM wavelength), the propagation of the EM wave can be approximated by the propagation through an equivalent material whose properties are described by spatial averages of the true material properties (Sihvola, 1999). In the case of a heterogeneous mixture of dielectric materials, the averaged relative complex permittivity is labelled the effective permittivity, $\epsilon_{r,eff}^*$, of the mixture. Based on the assumptions introduced in chapter 1, the following discussion will assume low-loss materials, where the permittivity can be adequately described by, and will refer to, the real part of the relative complex permittivity. To simplify the interpretation of symbols in this chapter, the subscript r and superscript $*$ will be dropped from all mentions of permittivity, and

it is implied that the permittivity is referring to the real part of the relative complex permittivity unless otherwise stated (i.e, $\epsilon'_{eff,r} \equiv \epsilon_{eff}$, the use of the term permittivity to describe the real part of the permittivity will be assumed throughout this thesis as well). The effective permittivity, representing the contributions from the entire volume within the sample holder, is the parameter that is measured by the laboratory permittivity experiments presented in this research. To extract the solid sample permittivity, or the permittivity of just the rock/mineral phase of this mixture, requires a method of characterizing how the permittivities of the materials in the sample holder relate to ϵ_{eff} . Electromagnetic mixing equations have been derived over the years for modelling this homogenization. The method of homogenization is complicated by a variety of factors including the micro-structure of the mixture, the frequency of the incident electric field, and the contrast between constituent permittivities. At the frequencies measured in the presented experiments, the mixture is assumed to be quasi-static since the wavelength of the incident electric field is much larger than the scale of the inhomogeneities in the mixture, based on the average measured grain size of the mineral samples. The micro-structure of the mixture can be taken into account with some mixing theories, while others attempt to average the properties such that small fluctuations do not impact the effective permittivity.

The range and complexity of the micro-structure and material chemistry of different materials has motivated the derivation of many mixing theories. In mixtures of conducting and insulating components, the structure becomes increasingly important as connecting pathways between phases can dramatically change the effective conductivity or permittivity, creating percolating pathways. The percolation threshold, f_c , is defined as the volume fraction at which a given phase dominates the effective properties of the mixture, and in some cases has been calculated for different mixing theories. The percolation behaviour predicted by some mixing theories limits the types of mixtures which those theories can be applied to, based on the experimentally observed percolation behaviour of different mixtures. Similar effects are possible with insulating mixtures when the dielectric contrast (ratio of the permittivities of each component) between components is large. Of particular importance to the geologic context is the consideration of liquid phases in a mixture. The conductivity and permittivity of a liquid vary not only with temperature and frequency, but also with the intermolecular forces acting on a given molecule, which for example will be different for bound water and free water. The presence and distribution of water within a rock or mineral will change the way in which each component contributes to the effective material properties. Ex-

tensive literature reviews on mixing theories have been published throughout the decades in which this field of research has been active (Brosseau, 2006; Landauer, 1978; Reynolds and Hough, 1957; Sihvola, 1999). This chapter will provide a similar review of mixing theory as it pertains to permittivity, but will also discuss the applications of mixing theory to explain laboratory permittivity measurements. The mixing theories discussed are separated into two general groups based on their properties, which are the matrix/inclusions group and the statistical/aggregate group. The focus in the current research is on two-phase mixtures that can model powdered mineral samples. While the range in mineralogy of a given regolith is diverse, the mixing problem is simplified in the laboratory experiments from this research by using samples made up of predominantly one mineral. The thermodynamic conditions are unfavourable for liquid water to exist on most airless bodies, and so this research is focused on dry materials in both the analysis and measurements. In the context of a mineral powder, the two mixture phases can be thought of as air and solid mineral grains, but in the following discussion the two mixture phases will be generally labelled as an inclusion phase with permittivity ϵ_i and an environment, or background, phase with permittivity ϵ_e . The volume fraction of inclusions will be labelled f , and the volume fraction of the environment is then $(1 - f)$. These labels are arbitrary, but will help in the discussion of the matrix/inclusions mixing theories, and follows the nomenclature of Sihvola (1999).

2.2 Matrix/Inclusions Mixing Theories

This group of mixing equations is defined by the asymmetry with respect to the mixture phases. In other words, each phase contributes differently to the effective permittivity, and the definition of which mixture component is inclusion (phase 1) or environment (phase 2) will change the behaviour of the model. The general structural assumptions in these theories is that phase 1 is embedded as inclusions in some background matrix composed of phase 2. In the following discussion the inclusions are assumed to be spherical, but it will later be shown how this assumption can be dropped and general ellipsoidal inclusions can be modelled. Each matrix/inclusions mixing theory considered in this thesis will be introduced in individual sections.

2.2.1 Maxwell Garnett (MG)

(Otherwise known as the Clausius-Mossotti, Lorenz-Lorentz, or Rayleigh equation (Sihvola, 1999)).

$$\epsilon_{eff} = \epsilon_e + 3f\epsilon_e \frac{\epsilon_i - \epsilon_e}{\epsilon_i + 2\epsilon_e - f(\epsilon_i - \epsilon_e)} \quad (2.1)$$

Equation (2.1) is one of the oldest and most commonly applied mixing theories. It was derived by James Clerk Maxwell Garnett in 1904 to explain the observed properties of metal spheres embedded in a liquid, which was then extended to the general dielectric case (Maxwell Garnett, 1904). This equation is fundamental to the origin and development of mixing theories, and therefore will be derived from classical electrodynamics to provide context for its application to experimental measurements.

Derivation

Consider a spatially uniform electric field, $\mathbf{E}_0 = E_0\hat{\mathbf{z}}$, in some medium with permittivity ϵ_e (Figure 2.1). Next, introduce a linear, homogeneous, and isotropic dielectric sphere with permittivity ϵ_i

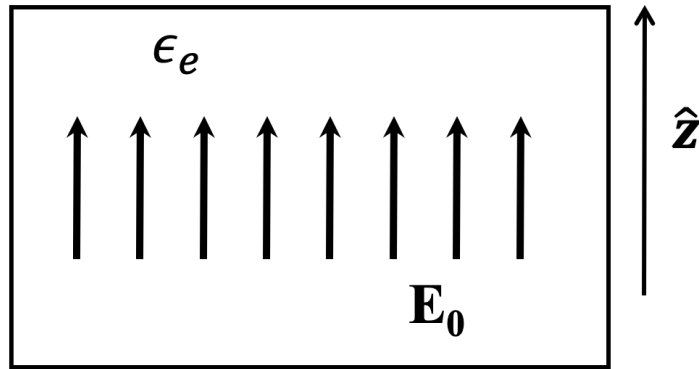


Figure 2.1: Spatially uniform electric field, $\mathbf{E}_0 = E_0\hat{\mathbf{z}}$, in some medium with permittivity ϵ_e .

into the medium (Figure 2.2). \mathbf{E}_0 will induce a polarization in the sphere, which can be modelled as an electric dipole linearly proportional to \mathbf{E}_0 :

$$\mathbf{p} = \alpha\mathbf{E}_0 \quad (2.2)$$

Here α is the polarizability of the spherical inclusion. The dipole moment can be written in terms of the difference in permittivity between the inclusion and environment, the internal electric field in the inclusion, \mathbf{E}_i , and the volume of the inclusion, V (Sihvola, 1999):

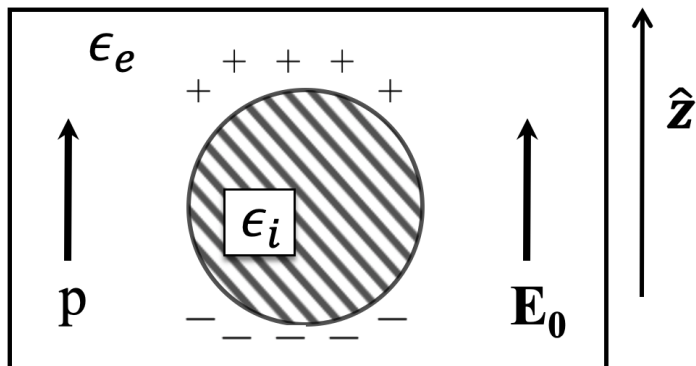


Figure 2.2: Dielectric sphere with permittivity ϵ_i embedded in the medium.

$$\mathbf{p} = \int_V (\epsilon_i - \epsilon_e) \mathbf{E}_i dV \quad (2.3)$$

In order to write a useable expression for the dipole moment, the internal field \mathbf{E}_i relative to the external field \mathbf{E}_0 (Figure 2.3) needs to be calculated to express the dipole moment in terms of known fields.

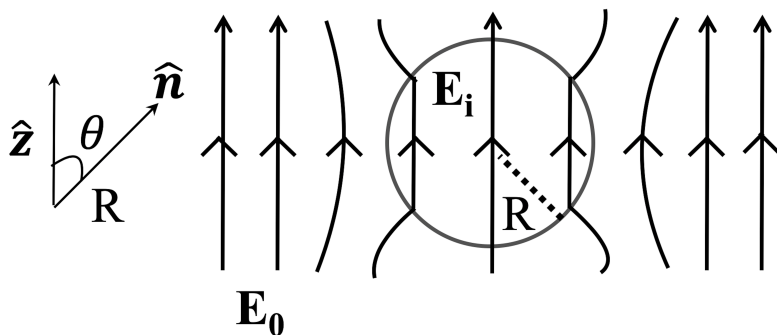


Figure 2.3: Field lines of \mathbf{E}_0 and \mathbf{E}_i for a dielectric sphere with permittivity ϵ_i embedded in the medium.

Here \mathbf{E}_i is a result of \mathbf{E}_0 and not the polarization induced by \mathbf{p} . The solution to this problem is to solve for the electric potential, $V(r, \theta)$, (not to be confused with the volume of the sphere, despite the same symbol) both inside the sphere ($r \leq R$) and outside the sphere ($r \geq R$) using Laplace's equation (since there are no free charges within $r \leq R$, $r \geq R$) in spherical coordinates (sphere is centered at the origin of the coordinate system). The solution is constrained by three boundary conditions (Griffiths, 1999):

1. Potential must be continuous at $r = R$:

$$V_{in} = V_{out} \text{ at } r = R$$

2. Normal ($\hat{\mathbf{n}}$) components of electric flux, \mathbf{D} , must be continuous at surface (no free charge at surface):

$$\epsilon_i \frac{\partial V_{in}}{\partial r} = \epsilon_e \frac{\partial V_{out}}{\partial r} \text{ at } r = R$$

3. Far from the sphere the contribution to the potential from the perturbing field of the sphere should vanish:

$$V_{out} \rightarrow -E_0 r \cos \theta \text{ at } r \gg R$$

The general solution to Laplace's equation in spherical coordinates is written:

$$V(r, \theta) = \sum_l^{\infty} \left(A_l r^l + \frac{B_l}{r^{(l-1)}} \right) P_l \cos \theta \quad (2.4)$$

Here P_l are the Legendre polynomials. As $r \rightarrow 0$ (inside sphere), $B_l = 0$ and the potential inside the sphere can be written:

$$V_{in}(r, \theta) = \sum_l A_l r^l P_l \cos \theta$$

As $r \rightarrow \infty$ (outside sphere) $A_l r^l \rightarrow \infty$ and the potential outside the sphere can be written (including boundary condition 3):

$$V_{out}(r, \theta) = -E_0 r \cos \theta + \sum_l \frac{B_l}{r^{(l+1)}} P_l \cos \theta$$

Applying the boundary conditions and solving for A and B when $l = 1$ ($A = B = 0$ for $l \neq 1$) yields:

$$\mathbf{E}_i = \frac{3\epsilon_e}{\epsilon_i + 2\epsilon_e} \mathbf{E}_0 \quad (2.5)$$

Equation (2.5) can also be derived by considering the Lorentz field, which will be discussed later. Now that \mathbf{E}_i is expressed in terms of \mathbf{E}_0 , this result can be substituted into equation (2.3) after integrating over the volume of the spherical inclusion, V :

$$\mathbf{p} = (\epsilon_i - \epsilon_e) \frac{3\epsilon_e}{\epsilon_i + 2\epsilon_e} \mathbf{E}_0 V \quad (2.6)$$

Using the definition of a dipole moment (2.2), the polarizability of the dielectric sphere can be expressed as:

$$\alpha = V(\epsilon_i - \epsilon_e) \frac{3\epsilon_e}{\epsilon_i + 2\epsilon_e} \quad (2.7)$$

Here it is worth noting that the expression for polarizability is independent of the field that excited the sphere, \mathbf{E}_0 . Now there are expressions to relate the dipole moment of the spherical dielectric inclusion to the permittivity of the sphere relative to the background medium. The case of multiple random spherical inclusions of permittivity ϵ_i embedded in an environment with permittivity ϵ_e is shown in Figure 2.4. The macroscopic behaviour of the two phase composite can be approximated by a homogenized effective medium with permittivity ϵ_{eff} . Here, ϵ_{eff} is defined as the relation

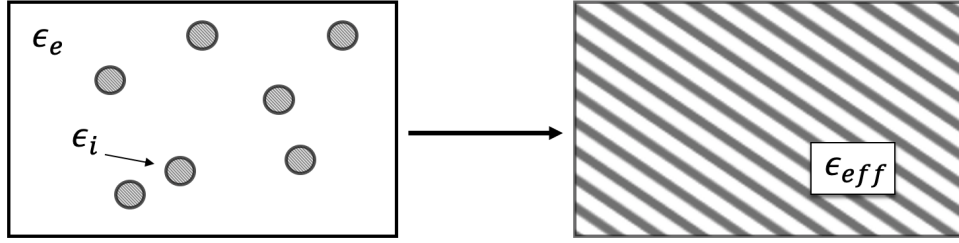


Figure 2.4: Effective permittivity of a mixture.

between the volume averaged electric field and flux density:

$$\langle \mathbf{D} \rangle = \epsilon_{eff} \langle \mathbf{E} \rangle \quad (2.8)$$

$$\langle \mathbf{D} \rangle = f\epsilon_i \mathbf{E}_i + (1 - f)\epsilon_e \mathbf{E}_0 \quad (2.9)$$

$$\langle \mathbf{E} \rangle = f\mathbf{E}_i + (1 - f)\mathbf{E}_0 \quad (2.10)$$

With equation (2.10), the Maxwell Garnett formula can actually be derived macroscopically using the result for the electric field in a dielectric sphere (2.5). For a microscopic description of the homogenization, the dipole moment and polarizability is used to arrive at the same result. When in terms of the polarizability of the inclusions, the resulting equation is often termed the Clausius-Mossotti equation. The constitutive equation (2.8) can be expanded to:

$$\langle \mathbf{D} \rangle = \epsilon_{eff} \langle \mathbf{E} \rangle = \epsilon_e \langle \mathbf{E} \rangle + \langle \mathbf{P} \rangle \quad (2.11)$$

$$\langle \mathbf{P} \rangle = n\mathbf{p} \quad (2.12)$$

Here $\langle \mathbf{P} \rangle$ represents the average electric polarization and assumes all dipole moments (inclusions) to be of equal strength with $n =$ number density of \mathbf{p} . The field that excites a given inclusion, called the local electric field \mathbf{E}_L , is a combination of the average electric field and the average polarization from the other inclusions in the mixture. The contribution of the average polarization from the other inclusions is especially relevant at higher volume fractions of inclusions. To account for field contributions from other inclusions, the field that excites a given inclusion, \mathbf{E}_L , is calculated from an empty cavity with the same shape as the inclusion embedded in a background neighbourhood that has the average polarization, $\langle \mathbf{P} \rangle$, resulting from all other inclusions (Figure 2.5). This empty

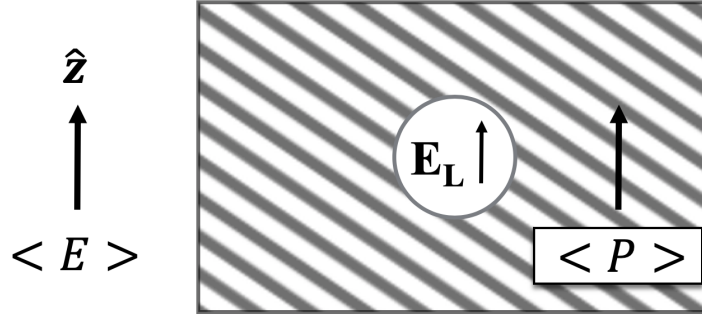


Figure 2.5: Empty cavity with same shape as inclusion to calculate Lorentz field contribution to \mathbf{E}_L .

cavity in which \mathbf{E}_L is determined takes on the shape of the inclusion, and in this case represents a Lorentz sphere where:

$$\mathbf{E}_L = \langle \mathbf{E} \rangle + \text{contribution from } \langle \mathbf{P} \rangle$$

The field contribution from $\langle \mathbf{P} \rangle$ is often called the Lorentz field, $\mathbf{E}_{\text{Lorentz}}$, arising from the bound surface charge along the cavity wall resulting from $\langle \mathbf{P} \rangle$. Looking into the sphere of radius r (Figure 2.6), the bound surface charge, σ_b is determined by the normal component of $\langle \mathbf{P} \rangle$:

$$\sigma_b = \langle \mathbf{P} \rangle \cdot \hat{\mathbf{n}} = \langle \mathbf{P} \rangle \cos \theta$$

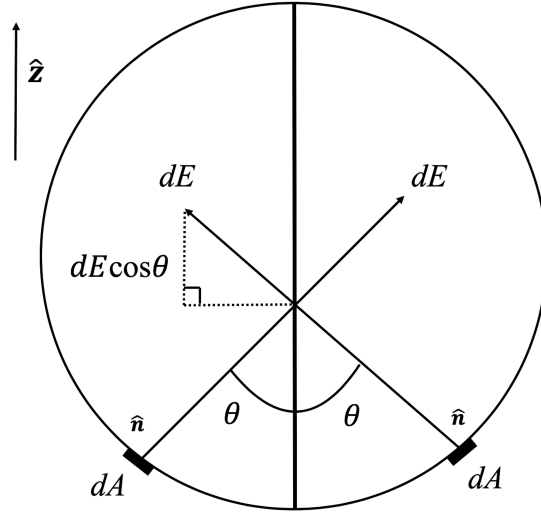


Figure 2.6: Lorentz sphere.

$$dA = 2\pi r^2 \sin \theta d\theta$$

Due to symmetry, horizontal components cancel and vertical components do not. A single charge contribution from the surface charge can be written:

$$dq = \sigma_b dA$$

$$dq = \langle \mathbf{P} \rangle \cos \theta 2\pi r^2 \sin \theta d\theta$$

Using Coulomb's Law and only the vertical components:

$$dE_{\text{Lorentz}} = \frac{1}{4\pi\epsilon_e} \frac{dq \cos \theta}{r^2}$$

Summing up all charge elements along the sphere (integral from $0 \rightarrow \pi$ due to symmetry):

$$\mathbf{E}_{\text{Lorentz}} = \frac{1}{4\pi\epsilon_e} \int_0^\pi \frac{\langle \mathbf{P} \rangle \cos^2 \theta}{r^2} 2\pi r^2 \sin \theta d\theta$$

$$\mathbf{E}_{\text{Lorentz}} = \frac{\langle \mathbf{P} \rangle}{2\epsilon_e} \int_0^\pi \cos^2 \theta \sin \theta d\theta$$

$$\mathbf{E}_{\text{Lorentz}} = \frac{1}{3\epsilon_e} \langle \mathbf{P} \rangle \quad (2.13)$$

The Lorentz field, $\mathbf{E}_{\text{Lorentz}}$, is the contribution from the bound surface charge at the cavity walls induced by $\langle \mathbf{P} \rangle$. Now the local exciting field of a given inclusion, including the contribution from the average polarization, is written as:

$$\mathbf{E}_{\mathbf{L}} = \langle \mathbf{E} \rangle + \frac{1}{3\epsilon_e} \langle \mathbf{P} \rangle \quad (2.14)$$

The dipole moment resulting from the local exciting electric field, \mathbf{p}_{mix} (the subscript differentiates this dipole moment from the dipole moment for an isolated dielectric sphere (2.3)), and average electric polarization, $\langle \mathbf{P} \rangle$, can be expressed as:

$$\begin{aligned} \mathbf{p}_{\text{mix}} &= \alpha \mathbf{E}_{\mathbf{L}} \\ \langle \mathbf{P} \rangle &= n \mathbf{p}_{\text{mix}} = n \alpha \mathbf{E}_{\mathbf{L}} \end{aligned}$$

Substituting this into equation (2.14):

$$\begin{aligned} \mathbf{E}_{\mathbf{L}} &= \langle \mathbf{E} \rangle + \frac{n \alpha \mathbf{E}_{\mathbf{L}}}{3\epsilon_e} \\ \langle \mathbf{E} \rangle &= \mathbf{E}_{\mathbf{L}} \left(1 - \frac{n \alpha}{3\epsilon_e}\right) \end{aligned}$$

Substituting this result for the average electric field back into the constitutive equation yields:

$$\begin{aligned} \epsilon_{eff} \langle \mathbf{E} \rangle &= \epsilon_e \langle \mathbf{E} \rangle + \langle \mathbf{P} \rangle \\ \epsilon_{eff} \mathbf{E}_{\mathbf{L}} \left(1 - \frac{n \alpha}{3\epsilon_e}\right) &= \epsilon_e \mathbf{E}_{\mathbf{L}} \left(1 - \frac{n \alpha}{3\epsilon_e}\right) + n \alpha \mathbf{E}_{\mathbf{L}} \\ \epsilon_{eff} &= \epsilon_e + \frac{n \alpha}{1 - \frac{n \alpha}{3\epsilon_e}} \\ \frac{\epsilon_{eff} - \epsilon_e}{\epsilon_{eff} + 2\epsilon_e} &= \frac{n \alpha}{3\epsilon_e} \quad (2.15) \end{aligned}$$

This last result (2.15) is one form of the Clausius-Mossotti (CM) mixing equation. This is used if microscopic quantities of a mixture are understood; however, generally the macroscopic quantities are what can be measured experimentally and most practically used. Often the variable n is

excluded in equation (2.15) in favour of the molar volume of some substance. The Clausius-Mossotti equation can be transformed into the Maxwell Garnett (MG) equation by substituting the expression for the polarizability of an inclusion (2.7) and the volume fraction of inclusions $f = nV$:

$$\epsilon_{eff} = \epsilon_e + 3f\epsilon_e \frac{\epsilon_i - \epsilon_e}{\epsilon_i + 2\epsilon_e - f(\epsilon_i - \epsilon_e)}$$

The spherical inclusions in the mixture need to be small when compared to the wavelength of the external electric field in order to be modelled as dipole moments; however, they do not all need to be of the same size (Sihvola, 1999). The MG equation satisfies the limiting cases $f \rightarrow 0$ and $f \rightarrow 1$, where in the latter case the size of the spheres in the mixture are such that smaller spheres fill the pore space of larger spheres. The MG equation for ϵ_{eff} becomes an increasingly non-linear function of f for higher dielectric contrasts ϵ_i/ϵ_e . Inherent in the derivation of the MG equation is the assumption that the local electric field acting on any inclusion is a combination of the average external electric field and the average polarization electric field caused by neighbouring inclusions. An assumption is made that the spheres must be well separated such that the contribution from other dipoles can be averaged by their far fields (Jylhä, 2008). The perturbation field of a scatterer falls off with $1/r^3$ justifying this assumption for sparse mixtures (Sihvola, 1989). The MG equation is asymmetric, i.e the inclusion phase and environment phase do not contribute on an equal basis to the effective permittivity of a mixture (Sihvola, 1999). The difference between using the MG equation or the inverse MG (IMG) ($\epsilon_{i,IMG} = \epsilon_e, \epsilon_{e,IMG} = \epsilon_i$) is greater for larger dielectric contrasts. Mathematically, the percolation threshold for the MG equation is calculated to be $f_c \approx 1$ (Sihvola, 1999). The host, or environment, phase of the mixture is considered continuous (and therefore within the percolation regime) with inclusions assumed to be separated islands (Sihvola et al., 2013). Therefore for any two phase mixture, the limiting bounds on effective permittivity through extreme percolation of either phase is given through the MG and IMG equations. At high dielectric contrasts in a mixture the MG equation breaks down for high inclusion volume fractions since the environment permittivity dominates until the percolation threshold. This is a result of the derivation being based on isolated dielectric spheres with no multi-pole interactions (Calame et al., 1996).

Use in the literature

One of the most influential studies investigating the dielectric properties of rocks for interpretation of planetary radar was by Campbell and Ulrichs (1969). The complex permittivity of numerous solid and powder samples of natural rocks was measured at 450 MHz in a re-entrant cavity and at 35 GHz in a waveguide. The error was estimated as 3% and 10% in the permittivity and loss tangents respectively when compared to accepted measurements of standard materials. Using the known permittivity of the solid phase for the powder measurements, the MG formula (labelled as the Rayleigh formula in the original paper) was shown to fit both the real and imaginary parts of the measured permittivity well for most samples. Variations with composition in the permittivity of solid rocks was observed, which could be observed in the powdered rocks if viewed at a common porosity. At a bulk density of 1 g/cm³, the permittivity of the powdered rocks was generally around 2. The authors highlight the theoretical limitations of the MG theory for anything but dilute mixtures, but do not discuss the fact that the MG theory was able to fit their measurements for denser mixtures regardless. Robinson and Friedman (2003) determined the solid (zero-porosity) permittivity of glass beads at 300 MHz using the liquid immersion technique in a coaxial waveguide. This technique consists of measuring the effective permittivity of a particulate substance immersed in liquid mixtures of known permittivity. Successive measurements in various liquids allows determination of the permittivity of the particulate substance (once the effective permittivity of the substance/liquid mixture equals that of the liquid mixture permittivity alone). The effective permittivity of the different mixtures was best predicted by the MG equation, with the inclusion volume fraction fixed at roughly 0.6, although below a fluid permittivity of 10 the differences between the investigated models seemed negligible. There are numerous studies that employ the MG equation for modelling the effective permittivity of a mixture simply due to its legacy and fundamental electrodynamic theoretical considerations. Due to the dilute mixture limit for the MG theory, its accuracy in predicting laboratory permittivity measurements is typically lower than for other mixing theories.

2.2.2 Bruggeman (Non Symmetric) (BGNS)

(Otherwise known as Sen-Scala-Cohen, Bruggeman-Hanai-Sen, and Hanai-Bruggeman equation).

$$\frac{\epsilon_i - \epsilon_{eff}}{\epsilon_i - \epsilon_e} = (1 - f) \left(\frac{\epsilon_{eff}}{\epsilon_e} \right)^{1/3} \quad (2.16)$$

Equation (2.16), or its complement (same as inverse, as defined for the MG equation) (Sihvola, 1999), has been derived independently in the literature in several studies over the years (Bruggeman, 1935; Hanai, 1960; Sen et al., 1981). It is a transcendental equation with no closed-form solution, and must be solved numerically for the effective permittivity. As shown by Sihvola (1999), (2.16) agrees with the Unified Mixing Theory introduced in Sihvola (1989) with the constant $\nu = 1$ up to the second order. The research presented in this thesis uses this approximation for the solution to (2.16) and its complement. In the extensive derivation by Sen et al. (1981), the complement of the BGNS equation (2.16) is arrived at by the differential application of the Bruggeman (Symmetric) (BG, which will be introduced in the next section) equation to a fractal system of coated spheres. Each sphere is considered coated with some effective medium made up of other coated spheres, and by incrementally adding coated spheres up to some volume fraction and differentiating, the complement to the BGNS equation, often termed the Sen-Scala-Cohen equation (after the authors), is arrived at. Merrill et al. (1999) showed that the the dilute mixture approximation of several mixing theories diverged to the BGNS equation by applying the same iterative approach as Sen et al. (1981). Semenov (2018) argued that the BGNS equation is only applicable in the dilute mixture limit, since each incremental addition to the effective permittivity in the iterative derivation is considered equivalent. Semenov (2018) opposed this assumption by noting the effects of each incremental addition would depend on the current effective permittivity, which is a viewpoint also supported by Merrill et al. (1999).

Use in the literature

Böttcher and Bordewijk (1978) found the BGNS equation to model effective permittivity measurements from the literature of mixtures of metallic inclusions in insulating matrices better than other tested mixing theories. In this study it was highlighted that conductor-insulator mixtures need to be prepared in either waxy mediums or with an applied velocity gradient to resist the clumping of particles, which would drastically change the percolation behaviour. Sen et al. (1981) derived the BGNS (its complement) equation to model permittivity measurements made in a 1.1 GHz resonant cavity of fused glass beads embedded in water and air. Banhegyi (1988) found the BGNS equation to model permittivity measurements of water-in-oil emulsion mixtures taken from the literature better than other mixing theories, noting that the mixture phases cannot be in direct contact (which is actually inherent in the Sen et al. (1981) derivation). Olhoeft (1987) found the BGNS equation to model permittivity measurements of sand/clay/water mixtures in a coaxial transmis-

sion line well at frequencies above 100 MHz. According to Olhoeft (1987), above this frequency, the mixture phases were deemed non-interacting; however, below 100 MHz, chemical interactions between the mixture phases, especially the clay surfaces, caused the experimental results to deviate from the BGNS predictions. Johnson and Poeter (2005) measured the complex permittivity of water saturated sand (silica) mixtures using the coaxial transmission line method from 20 - 200 MHz. The BGNS formula matched dry sand/air mixtures well with a sand permittivity taken to be that measured by Olhoeft (1981) at 1 MHz ($\epsilon_{\text{quartz}} = 4.5$). The three phase mixtures of sand/air/water were best modelled with an iterative application of the BGNS formula, using a weighted average of the calculated effective permittivity assuming an air/sand matrix composition and a water/sand matrix composition. Pervin (2015) performed permittivity measurements of porous NaCl and KCl salts using an open ended coaxial probe from 10 MHz - 3 GHz at very low porosity and found the MG and BGNS theories to model the measurements best out of the discussed mixing theories, although it was noted that the fit was still poor. Pervin (2015) noted the difficulty in comparing the accuracies of the mixing theories when the differences between them for the given dielectric contrasts of the samples was on the order of the measurement uncertainty. This is especially a result of the low volume fraction of the mixtures Pervin (2015) considered, since most mixing theories agree in this regime. In general, the BGNS theory has seen success in modelling the effective permittivity of conductor-insulator mixtures, particularly when the conducting phase is the background, or matrix.

2.2.3 Coherent Potential (CP)

$$\epsilon_{eff} = \epsilon_e + f(\epsilon_i - \epsilon_e) \frac{3\epsilon_{eff}}{3\epsilon_{eff} + (1-f)(\epsilon_i - \epsilon_e)} \quad (2.17)$$

The Coherent Potential (CP) equation as written in (2.17) is taken from Sihvola (1999); however, the name Coherent Potential is often used throughout the literature as a synonym for the Bruggeman Symmetric (BG) equation (Sihvola, 1999). The predictions of the CP equation are very similar to the BG equation, which explains the interchanging of the names throughout the literature. As a result, there are not any studies that could be found making use of the CP equation, and the discussion of this equation will be limited.

2.3 Statistical/Aggregate Mixing Theories

In contrast to the matrix/inclusions mixing theories, the statistical/aggregate mixing theories are defined by the symmetry with respect to the mixture phases. In this way, the mixture micro-geometry and topology is considered in the form of statistical averages, and the mixture can be considered as roughly homogeneous throughout. Generally these theories do not consider the polarizability of a given inclusion, and are thus independent of particle shape for powder mixtures. When individual inclusions are considered, they will be treated as spherical, and the definition of a mixture phase as being labelled inclusion (ϵ_i) or environment (ϵ_e) is arbitrary and invertible with no consequences for the model behaviour.

2.3.1 Bruggeman Symmetric (BG)

(Otherwise known as the Effective Medium Approximation (EMA), Böttcher equation, de Loor equation, Polder-van Santen, and Coherent Potential equation (Sihvola, 1999)).

$$(1 - f) \frac{\epsilon_e - \epsilon_{eff}}{\epsilon_e + 2\epsilon_{eff}} + f \frac{\epsilon_i - \epsilon_{eff}}{\epsilon_i + 2\epsilon_{eff}} = 0 \quad (2.18)$$

The Bruggeman Symmetric (BG) equation (2.18) was first introduced by Bruggeman (1935), and has seen extensive use in mixing problems in the literature as it overcomes some of the limitations of the MG equation. The BG equation is one of the most fundamental symmetrical mixing theories, and highlights the difference in the homogenization approach taken by mixing theories in the statistical/aggregate group compared to the matrix/inclusions group. The derivation of the BG equation follows from the MG equation derivation for spherical inclusions and will be discussed further.

Derivation

Consider the definition of ϵ_{eff} developed earlier in the derivation of the Maxwell Garnett equation (2.11) (Figure 2.4):

$$\langle \mathbf{D} \rangle = \epsilon_{eff} \langle \mathbf{E} \rangle = \epsilon_e \langle \mathbf{E} \rangle + \langle \mathbf{P} \rangle$$

Using the same logic as in the MG derivation, the expression for the local exciting electric field for a given spherical inclusion is re-written as before (2.14):

$$\mathbf{E}_L = \langle \mathbf{E} \rangle + \frac{1}{3\epsilon_e} \langle \mathbf{P} \rangle$$

The critical aspect of the BG theory is that the polarization of a given phase is measured with respect to the effective permittivity of the homogenized mixture (Figure 2.7). The polarizations induced by other inclusions are taken to be included in the effective material properties. As a result, when calculating the polarization of a given particle, the overall contribution must be zero to maintain the effective material properties relative to other inclusions (self-consistency requirement). In other words, the exciting electric field must be equivalent to the average electric field, $\mathbf{E}_L = \langle \mathbf{E} \rangle$. This consideration implies that there is a polarization associated with the environment phase of a mixture as well as the inclusion phase (for a 2-phase mixture), where each phase is equally weighted.

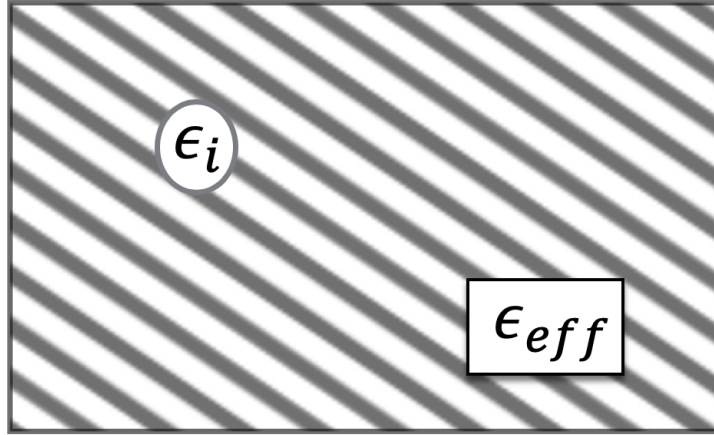


Figure 2.7: BG model assumes each inclusion is embedded in an already homogenized medium, and so must have zero polarization.

For a two phase mixture the visualization of the inclusion phase from the BG perspective is shown in Figure 2.7. Mathematically, this is a change of variables from $\epsilon_e \rightarrow \epsilon_{eff}$:

$$\mathbf{E}_L = \langle \mathbf{E} \rangle + \frac{1}{3\epsilon_{eff}} \langle \mathbf{P} \rangle \quad (2.19)$$

Using $\mathbf{E}_L = \langle \mathbf{E} \rangle$, $\langle \mathbf{P} \rangle = n\mathbf{p}_{mix}$, $\mathbf{p}_{mix} = \alpha\mathbf{E}_L$, (2.7), and the effective constitutive parameters from the MG derivation the following can be substituted:

$$\langle \mathbf{P} \rangle = n\mathbf{p}_{mix} = nV(\epsilon_i - \epsilon_{eff}) \frac{3\epsilon_{eff}}{\epsilon_i - \epsilon_{eff}} \mathbf{E}_L, \text{ where } f = nV$$

$$\langle \mathbf{E} \rangle = \langle \mathbf{E} \rangle + f \frac{\epsilon_i - \epsilon_{eff}}{3\epsilon_{eff}} \frac{3\epsilon_{eff}}{\epsilon_i + 2\epsilon_{eff}} \langle \mathbf{E} \rangle$$

Since $\langle \mathbf{E} \rangle \neq 0$, the i^{th} phase in an N phase mixture can be written:

$$\sum_{i=1}^N f \frac{\epsilon_i - \epsilon_{eff}}{\epsilon_i + 2\epsilon_{eff}} = 0$$

Specifically for the 2-phase mixture under consideration, the BG equation introduced at the beginning of this section is arrived at (2.18):

$$(1 - f) \frac{\epsilon_e - \epsilon_{eff}}{\epsilon_e + 2\epsilon_{eff}} + f \frac{\epsilon_i - \epsilon_{eff}}{\epsilon_i + 2\epsilon_{eff}} = 0$$

In the case of the MG theory, the permittivity outside a scatterer is approximately ϵ_e for sparse mixtures. As described in the BG derivation, polarizations due to each phase arise in a mixture and are treated equally. Therefore, unlike the MG theory, the environment and inclusion phase of a 2-phase mixture are treated symmetrically in the BG theory (Sihvola, 1999). The BG equation is widely used as its solution for the effective permittivity of a mixture is more theoretically valid than the MG theory for a wider range of volume fractions of the inclusion phase (useful when there is no particular dominating phase of the mixture) (Jylhä, 2008). The solution for the effective permittivity using the BG equation requires finding the roots to a polynomial, or for a 2-phase composite the roots to a quadratic equation (Calame et al., 1996). In the case of a two-phase mixture the correct root represents a positive, physically realistic value for ϵ_{eff} (Calame et al., 1996). Due to the symmetrical nature of the BG theory, at small volume fractions of the inclusion phase the equation tends to overestimate the effective permittivity. The BG approach maximizes the interactions between phases of a mixture where the effects of *all* neighbouring inclusions are considered in the polarization of a given inclusion, thereby representing an extreme case in which all inclusions interact with one another (Cosenza et al., 2009). The BG assumption that each inclusion is surrounded by a medium with permittivity ϵ_{eff} breaks down when the dielectric contrast between mixture phases increases, since local changes in the effective permittivity will be more substantial (Adams et al., 1996; Dube and Parshad, 1970; Goncharenko, 2003). Mathematically the percolation threshold is calculated to be $f_c \approx 0.33$ for the BG equation (Sihvola, 1999). Due to the symmetry between the phases in the BG formulation, the components form a three dimensional continuum with connectivity between all phases at the percolation threshold. For a 2-phase mixture, at

and above the percolation threshold the macroscopic permittivity will be closer to the inclusion permittivity. As in the case of the MG formula, percolation behaviour is enhanced for higher dielectric contrasts in the mixture.

Use in the literature

Dube and Parshad (1970) performed permittivity measurements of several loss-free and lossy powders at 20 MHz using a commercial Q -meter and at 9.375 GHz using a rectangular waveguide. The BG equation predicted a solid permittivity for the powder in agreement with values from the literature, and was less accurate for particle sizes less than 30 μm in diameter, as well as for predicting the imaginary part of the permittivity, where the loss mechanisms of a dielectric material were proposed to be different in solid and powder form for a given material. Larger grain sizes were also discussed as introducing non-uniformity in the powder samples, breaking the homogeneous assumption in the BG theory. Benadda et al. (1982) measured the effective permittivity of powder mixtures of the polar compound 1-cyanoadamantane from 1 kHz - 1 GHz in an open coaxial cell and found the BG theory to match the experimental data most accurately above volume fractions of $f > 0.75$ (corresponding to a porosity of $\phi < 0.25$). The authors discuss the viable use of mixing theories derived under quasi-static assumptions for the dynamic case in the frequency range considered (1 kHz - 1 GHz). Adams et al. (1996) found the BG formula to predict the most accurate solid permittivity, when compared with other mixing theories, from powdered granite and two basalt samples (first measured as solid samples to constrain analysis) in a short circuited slotted rectangular waveguide from 4 - 19 GHz. The LLL equation (introduced later) was also shown to calculate similar solid permittivity values for the three samples. Kärkkäinen et al. (2000) performed thousands of 2D Finite Difference Time Domain (FDTD) simulations, initially developed by Pekonen et al. (1999), to explore the adherence to mixing boundary theories, and found all measurements fall between the Wiener bounds and most within the Hashin-Shtrikman bounds (Wiener and Hashin-Shtrikman bounds discussed in section 2.5). The BG model matched the simulations best, similar to the results of Pekonen et al. (1999). Kärkkäinen et al. (2001) extended the simulation to 3D and found that the BG model fits the results best when inclusion clustering is allowed and that the MG model fits for non-clustering systems. However, these models only worked well for dilute mixtures, and as the volume fraction of inclusions was increased the results tended to fall between the BG and MG predictions. A hybrid mixing formula, matching closer to the MG model for low volume fractions of inclusions and the BG model for high volume

fractions of inclusions, was derived by Jylhä and Sihvola (2007). It is assumed in this derivation that the contrast between the permittivities of the mixture phases is large, and the model predicts a similar percolation threshold to the BG model. The formula fit numerical FDTD simulations of effective permittivities of large contrast mixtures by Kärkkäinen et al. (2001) and effective conductivity measurements by Mamunya et al. (2001). Calame (2008) found the BG model predicted an effective permittivity close to finite difference numerical simulations, although the simulations did not match the functional form of the BG predictions. Oguchi et al. (2009) measured the permittivity of volcanic ash powder samples with particle diameters $< 170 \mu\text{m}$ in a 7 mm coaxial airline from 3 - 13 GHz. The solid permittivity of the samples extracted using the BG equation was in agreement with those found by similar studies. Scattering effects were observed for samples with larger grain sizes, at a diameter of roughly 0.5 mm and in the GHz frequency regime. Rogers et al. (2011) used a quasi-optical free space permittivity measurement technique to measure the permittivity of loose and pelletized volcanic ash powder samples from 65 - 110 GHz. By using the measured permittivity of the pelletized samples as the permittivity of the solid phase of the loose mixtures, the loose samples were fit well with the BG model. Similar values for the solid permittivity of volcanic ash were derived when compared with Adams et al. (1996) and Oguchi et al. (2009). The samples were ground to small particle sizes; however, no particle size metrics were provided, nor a discussion of possible scattering effects that would be relevant at the higher frequency range of the permittivity measurements. The BG equation has generally been shown to be accurate in calculating the effective permittivity of low dielectric contrast mixtures with relatively equal mixture phases by volume. In studies that also considered the LLL equation, it was observed that the BG and LLL equations predict similar effective permittivities, and are exactly equal for a volume fraction of $f = 0.43$ (Tuhkala et al., 2013).

2.3.2 General Power Law Mixing Theory: β

(Otherwise known as the Lichtenecker-Rother equation (Knoll, 1996; Lichtenecker and Rother, 1931)).

$$\epsilon_{eff}^{\beta} = f\epsilon_i^{\beta} + (1 - f)\epsilon_e^{\beta} \quad (2.20)$$

A group of mixing equations exist that in general describe the effective permittivity by averaging the contribution of volume weights of different powers of the permittivity of the mixture components

Sihvola (1999). Equation (2.20) is the generalized form of this group of equations to relate a two component mixture. Different values of β used in the above equation result in a different physical model for the mixture. A consistent feature in this group of mixing equations is that the geometrical shape of a given phase (particle shape of inclusions) in a mixture is generally not taken into consideration. Since the polarization of an isolated inclusion is not considered, this family of mixing equations tends to overestimate the value of the effective permittivity of a mixture at low volume fractions of inclusions. It has been shown by Zakri et al. (1998) that (2.20) can be derived through application of the self-consistent effective medium theory (used to arrive at the BG equation from the MG equation) and the assumption of a beta distribution of depolarization coefficients (a measure of particle shape, as will be discussed further) of inclusions (if only spheres are considered, derivation results in BG equation). In the Zakri et al. (1998) model, the variable β is comprised of the three angles made between an ellipsoid's three principal axes and the applied electric field.

2.3.3 Linear (LIN), $\beta = 1$

(Otherwise known as the Silberstein formula, Browns formula, and the Wiener upper bound (Sihvola, 1999; Birchak et al., 1974)).

$$\epsilon_{eff} = f\epsilon_i + (1 - f)\epsilon_e \quad (2.21)$$

Equation (2.21) represents the maximum effective permittivity attainable for a mixture bounded by the permittivities of the components for a given volume fraction. Physically this is represented by the mixture phases represented as layers that are parallel to the direction of electric flux. Inversely if the layers are perpendicular to the direction of electric flux, the resulting equation is the lower limit of the Wiener bounds.

Use in the literature

In most applications of homogenization, the structure of a mixture will be more complex than that associated with the linear law. As such this equation acts as the extreme end of possibilities in approximating the effective permittivity of a mixture and is not used to model most physical systems. Brouet et al. (2014) and Brouet et al. (2015) make use of a linear relationship to describe the change in the effective permittivity of various cometary analogue material powders with bulk

density. This is not a true application of the LIN equation, since the mixture was not described in terms of volume fraction (or inversely, porosity). Rust et al. (1999) found the LIN equation to model experimental permittivity measurements of various volcanic rocks from 0.01 - 10 MHz well, possibly due to parallel layering in samples. Kameyama and Miyamoto (2008) similarly used the LIN equation to model permittivity measurements of terrestrial soils made with a time domain reflectometry (TDR) probe at an unspecified frequency, making note of the implied parallel geometry of the samples. ElShafie and Heggy (2013) measured the permittivity of volcanic basalts in a dielectric capacitive cell from 100 - 1000 MHz and found a linear relationship to exist between the permittivity and density of the samples.

2.3.4 Complex Refractive Index Model (CRIM), $\beta = 1/2$

(Otherwise known as the Time-Propagation model (Martinez and Brynes, 2001; Knoll, 1996)).

$$\sqrt{\epsilon_{eff}} = f\sqrt{\epsilon_i} + (1 - f)\sqrt{\epsilon_e} \quad (2.22)$$

Equation (2.22) was developed for use in optical physics to describe the refractive index of a mixture of non-magnetic gases (Sihvola, 1999). The same result has been derived in certain models depicting plane wave propagation through a heterogeneous dielectric medium (Nelson, 1992). Birchak et al. (1974) proposed a mixing model of this form derived from the optical path length of a single EM wave in a heterogeneous medium. In general, the CRIM equation describes the refractive index of non-magnetic mixtures as being a simple volume average of the component refractive indices.

Use in the literature

Gladstone and Dale (1863) have applied this formula with success in approximating the refractive index of a mixture of liquids. Birchak et al. (1974) found this equation to be a better model for the measured complex permittivity (greater discrepancy in imaginary permittivity due to ionic conduction) of bentonite clay mixed with water at 4 GHz in a coaxial transmission line when compared with a linear mixing model. When compared with an extensive set of mixing equations, the refractive mixing model showed the best correlation with experimental data of the complex permittivity of soil as a function of volumetric water content in a study by Shutko and Reutov (1982). In the Feng and Sen (1985) study of partially water/oil saturated clay-free sedimentary rocks, the CRIM and BGNS models compared well with experimental permittivity data from the

literature at high frequency, but deviated from some of the results due to the lack of consideration of grain shape. Similarly Shen et al. (1985) found good agreement with the CRIM and BGNS models and permittivity measurements made using a coaxial transmission line on saturated sedimentary rocks. The models deviated from the measurements at higher salinity values in the water, as was similarly found by Feng and Sen (1985), likely due to increased chemical interactions between mixture phases. Knoll (1996) found the CRIM equation to model permittivity measurements of dry sand/clay mixtures well, extrapolating a solid permittivity for the powder grains consistent with values from the literature. Martinez and Brynes (2001) used the CRIM equation to model GPR surveys of water saturated soils, and despite not testing any other mixing theories, found the CRIM equation to fit experimental data from the literature well. Leão et al. (2015) used a 50 MHz impedance sensor to measure the permittivity of several saturated soil samples. The generic form of the power law mixing model was fitted to the data using least squares regression, where the solid phase permittivity and power law exponent were used as fitting parameters. Due to this over-parameterization, many soil measurements could not be fitted properly and the resulting discussion is questionable. The CRIM model was found to fit measurements of glass beads well, although the solid permittivity used was found by least squares fitting and not constrained by other means. As a result of the lack of constraints on the fitting of the different mixing models analyzed in Leão et al. (2015), the conclusions are vague at best. The CRIM equation has typically been applied in mixtures with liquid phases, and predicts a similar effective permittivity to the BGNS equation for high frequencies and simpler mixtures.

2.3.5 Looyenga-Landau-Lifshitz Formula (LLL), $\beta = 1/3$

$$\epsilon_{eff}^{\frac{1}{3}} = f\epsilon_i^{\frac{1}{3}} + (1-f)\epsilon_e^{\frac{1}{3}} \quad (2.23)$$

The LLL equation was derived independently by Looyenga (1965) and Landau and Lifshitz (1960) for the effective permittivity of a mixture. In either derivation (see appendix A.1 and A.2 for more detail), the basic premise consists of a system made of two components with slightly higher $\epsilon_{eff} + \delta\epsilon$ and lower $\epsilon_{eff} - \delta\epsilon$ permittivities than the effective permittivity of the whole mixture. The effective permittivity of the overall mixture is then considered a volume average of these two components, which are in themselves mixtures. In either derivation it is assumed that the dielectric contrast between the mixture phases is small. In addition the particle shape is not considered for either derivation, for which the resulting equations are independent of particle shape or structure.

Since the structure and positioning of the mixture components with respect to one another is not considered, and the dielectric contrast is assumed small, there is no percolation threshold for the LLL equation.

Use in the literature

Looyenga (1965) tested the validity of their equation against measurements of the effective permittivity of glass spheres dispersed in carbon tetrachloride from van Beek (1967), and found it to fit the measurements better than other mixing laws, especially at higher volume fractions of the inclusion phase. At low volume fractions the BG equation predicted the effective permittivity of the mixture more precisely. Dube (1970) estimated the solid permittivity of various minerals from bulk powder permittivity measurements using the Böttcher (BG) and LLL formulas. Measurements at 20 MHz were made from pressed discs of material using a commercial Q -meter and at 9.375 GHz using a rectangular waveguide. Nearly identical values for low dielectric constant minerals were predicted by both equations, however for higher (9 and above) dielectric constant minerals, the LLL formula resulted in more accurate dielectric values. Böttcher and Bordewijk (1978) found the BG and LLL (LLL deemed slightly more accurate) equations to accurately model effective permittivity measurements of dry non-conducting powders taken from the literature. The authors noted the lack of either of these mixing theories to account for conduction mechanisms in materials. In the Benadda et al. (1982) study that found the BG model to match experimental permittivity measurements of mixtures of 1-cyanoadamantane from 1 kHz - 1 GHz in an open coaxial cell above $f > 0.75$, the authors concluded that the LLL equation matched the data sets below $f < 0.35$. Banhegyi (1988) compared the LLL, BG, and BGNS formulas through numerical modelling and fits to experimental data from various permittivity studies in the literature. In general, the LLL formula was found to behave similarly to the BG equation in situations with no clear distinction between mixture components, such as for powders, but lacked the ability to predict percolation behaviour in conductor-dielectric and high dielectric contrast mixtures. Malik et al. (1988) used the LLL equation to estimate the solid permittivity of various dried marble powders from effective permittivity measurements made at 100 kHz and 10 MHz in a universal R.F. bridge. The solid permittivity was in agreement with other measurements from the literature. Merrill et al. (1999) presented the metallic inclusion limit for a variety of mixing equations and noted that the LLL formula is only valid for low permittivity contrast mixtures. The authors showed that an iterative application of the MG and BG equations resulted in the BGNS equation, whereas an iterative ap-

plication of the LLL equation resulted in itself due to the iterative approach in the LLL equation's original derivation. Gershon et al. (2001) performed resonant cavity measurements between 1 - 4 GHz of the complex permittivity of porous and densified (sintered) alumina. The solid permittivity was extrapolated from the densified measurements using the MG, BG, and LLL mixing models, and subsequently used to predict the porous measurements according to the respective models (three phase, with water content measured at $< 0.2\%$). The LLL model predicted the real part within 8-12%, the BG model to slightly worse accuracy, and the MG model with the worst fit. The imaginary part in all cases was severely underestimated, which was attributed to an inability of the analytical models to describe micro-structure and the distribution of water throughout the samples. Finite difference quasi-electrostatic simulations predicted similar complex permittivities, but when the water content was restricted to contact points between alumina grains the simulations predicted accurate effective imaginary permittivities. The numerous studies into the effective permittivity of dried mineral and agricultural powders and standard plastics by Stuart Nelson using a variety of measurement techniques in the GHz range all concluded that the LLL equation modelled the effective permittivity the most accurately (Nelson et al., 1989; Nelson, 1992; Nelson and Bartley, 1998; Nelson, 2005). The error in the model fit increased with the powder particle size, and it was noted that the BG equation gave similar results. Plug et al. (2006) tested the predictions of several mixing theories against 3D Finite Element Model (FEM) and Finite Difference Model (FDM) numerical simulation results for heterogeneous material and found that for low dielectric contrasts the LLL and BG equations were in the most agreement with the simulations. Stillman et al. (2010) measured the low frequency (1 mHz - 1 MHz) complex permittivity of several sand, ice, and saline liquid ($CaCl_2$) mixtures using a capacitively coupled three-electrode sample holder. The static limit for the real part of the permittivity was modelled well with the general power law equation with an exponent $1/\beta$, with $\beta = 2.7 \pm 0.3$, which is consistent with the LLL equation. Tuhkala et al. (2013) used an open ended resonant cavity to measure the effective permittivity of several oxide powders at 4.5 GHz. Various mixing equations were fit to the measurements, and the LLL and BG were found to fit the data with a solid permittivity closest to those found in the literature for the samples. It was noted that both equations predict similar effective permittivities for a given solid permittivity, and are exactly equal at a volume fraction of $f = 0.43$. Throughout the literature, the LLL equation has been successfully applied to low dielectric contrast powder mixtures and found to predict similar effective permittivities as the BG equation. The similar assumptions in either equation's derivation explains their similar predictive abilities.

2.3.6 Lichtenecker Formula (LI), $\beta = 0$

$$\epsilon_{eff} = \epsilon_i^f \epsilon_e^{1-f} \quad (2.24)$$

This formula was first proposed by Lichtenecker (1926) and is considered semi-empirical, as the original derivation lacked a strong theoretical foundation. Zakri et al. (1998) derived the LI formula as a special case of a uniform particle distribution in their broader derivation of the general power law equations (for which inclusion shapes follow a beta function distribution). Recently, Simpkin (2010) was able to derive the LI formula directly from Maxwell's equations and the principle of charge conservation for a random spatial distribution of inclusions. Based on this derivation, the effectiveness of applying the LI formula relies on how well the mixture in question satisfies the condition of having a random spatial distribution of inclusions. It was also shown that the MG and BG equations can be derived from this model for special model parameters, and thus each equation is valid for first-order interactions between mixture phases and represent approximations of the LI formula. Through the derivation of the spectral density function (which describes the micro-geometry of a mixture) of the LI formula, Goncharenko et al. (2000) showed that the topology associated with the LI model is that of randomly oriented spheroids with uniform shape distributions. Considering that $\beta = +1$ and $\beta = -1$ represent geometries where mixture components are contained in flat planes parallel and perpendicular to the applied electric field, it is intuitive that a value of $\beta = 0$ corresponds to mixture components in random orientations. Neelakantaswamy et al. (1985) proposed a modified form of the Lichtenecker formula derived in Lichtenecker (1926) that takes into consideration the shape of particle inclusions and thus can be considered an extension of the fundamental Lichtenecker formula. Kiley et al. (2012) highlighted that no peak in the loss tangent of a mixture considered by the LI approximation exists, and as such the model fails to predict a percolation threshold. In Kiley et al. (2012), the LI and BG models predicted the effective permittivities (both real and imaginary) of metal powders better than the MG model for volume fractions below the observed percolation threshold.

Use in the literature

Saint-Amant (1968) measured the complex permittivity of various rock samples using a variety of techniques, albeit with questionable procedures and accuracies. Of relevance in this study was the determination of the solid, and subsequently effective powder permittivities of a basalt, granite, and olivine sample. The LI and BG formulas were used with the solid sample permittivity measurement

to predict the effective powder permittivity for each sample. For the granite and olivine samples, the LI and BG equations underestimated and overestimated the measured permittivity at room temperature, respectively. The LI equation predicted the closest value to the measured permittivity for the basalt sample. In each case the powder measurement was only completed at one porosity. Olhoeft and Strangway (1975) compiled 92 measurements of the complex permittivity of lunar regolith samples returned from NASA’s *Apollo* missions and found that a function of the form $\epsilon_{eff} = a^{\rho_{bd}}$ with $a = 1.93 \pm 0.17$ fit measurements of the real part of the permittivity well. The imaginary part did not follow such a strong correlation with density, but was better explained by the TiO_2 and FeO weight percent oxide (wt. % oxide) concentrations in the samples. It was shown that the empirical exponential equation fitted to the real part of the permittivity was equivalent to the LI equation assuming an average solid permittivity of 7.7 and solid density of 3.1 g/cm^3 for the lunar regolith (which are reasonable values (Carrier et al., 1991)). The value of the constant, a , is in good agreement with the value of $1.9 - 2.1$ for normalized (to a bulk density of $\rho_{bd} = 1 \text{ g/cm}^3$ using the MG equation) rock powder permittivity measurements by Campbell and Ulrichs (1969). Drawing from such a large database of permittivity measurements on lunar regolith samples, this relationship, or slight variations of it (i.e (Palmer et al., 2015; Bussey, 1979; Garvin et al., 1985; Carrier et al., 1991; Campbell, 2002; Barmatz et al., 2012; Brouet et al., 2016)), has been used predominantly in planetary radar inversion efforts. Neelakantaswamy et al. (1983) used least squares regression to show that the LI equation fits the data from Benadda et al. (1982) better than the BG and LLL equations suggested by the original authors. This comparison isn’t very valuable, since the BG and LLL equations were not also fit by least squares regression. Ulaby et al. (1988) and Ulaby et al. (1990) measured the complex permittivity of 80 dry solid rock samples in resonant cavities from 1 - 16 GHz. All of the samples were found to be essentially dispersionless within this frequency range, and their permittivities were fit well with an exponential equation similar to that from Olhoeft and Strangway (1975) with the constant $a = 1.96$. A chemical analysis of the various wt. % oxides in the samples found that after accounting for the correlation of the real part of the permittivity with density, the chemical composition could explain most of the remaining variance in the dataset. Similar to Olhoeft and Strangway (1975), the imaginary part of the permittivity showed no obvious correlation with density, and was more dependent on the chemical composition. The real part of the permittivity was also fitted with the linear equation $\epsilon_{eff} = 1.86\rho_{bd} + 1$, which was found to be statistically as significant as the exponential fit. Zheng et al. (2005) used the resonant cavity perturbation method at 9.37 GHz to measure

the complex permittivity of a variety of reference materials, rocks, and minerals. In addition to directly measuring solid samples, mixtures of samples with polythene were created, where the sample permittivity was derived assuming the LI mixing model. The latter method was validated by comparing the derived sample permittivities to values found in the literature, as well as to values measured directly. In the calculation of the sample permittivity from the resonant frequency shift in the cavity, small perturbation theory is assumed, and the range in sample permittivities that can be accurately measured by the system is limited (highest direct measurement is 8.11 for the real part of the permittivity). The mixtures are composed of polythene with a real part of the permittivity of 2.35. These mixtures can be compared to mixtures of rock samples with air by looking at the contrast in the mixture component permittivities. A measurement of a sample with a permittivity of 5 mixed with polythene has an equivalent contrast in permittivity to a sample with a permittivity of 2.13 mixed with air. Similarly, a measurement of a sample with a permittivity of 8 with polythene would correspond to a sample with a permittivity of 3.40 mixed with air. At such low contrasts in permittivity, most mixing theories will predict similar effective permittivities and could be shown to adequately model the measured data. For instance, at a permittivity contrast of 3.40 the upper and lower Hashin-Shtrikman bounds differ in the predicted effective permittivity by an average of only 7%. Since Zheng et al. (2005) did not attempt to calculate sample permittivities based on any mixing model other than the LI model, this fact is not discussed. Ebara et al. (2006) measured the effective permittivity of powdered silica and ferrite in a Teflon[®]-capped open waveguide from 4.0 - 5.8 GHz at various porosities and extracted the solid silica permittivity by fitting the data with the LI formula. The derived solid permittivity was compared to a measurement of solid silica using a cylindrical cavity resonator and it was found that the solid permittivity of silica extracted from the powder measurements using the LI equation was roughly 6.5% higher (3.97) than that measured in the cylindrical cavity resonator (3.71). Of note in this study is that the uncertainty of the measurements was not quantified, and there was no consideration for the moisture content in any samples. The LI equation has been used as an accurate empirical mixing theory to fit experimental data, but has been criticized in the literature for lacking strong theoretical validation.

2.4 Particle Shape: Depolarization Factor

So far the inclusion phase of a given mixture, or what can be thought of as the solid particles in a mineral powder, have been considered perfect spheres in mixing theories that depend on inclusion shape. This assumption can be extended to general ellipsoids by using the depolarization factors N_x , N_y , and N_z of an ellipsoid for 3D Cartesian space. The depolarization factor in the $\hat{\mathbf{x}}$ direction, N_x , for an ellipse with semi-axes a_x , a_y , and a_z is (Sihvola, 1999):

$$N_x = \frac{a_x a_y a_z}{2} \int_0^\infty \frac{ds}{(s + a_x^2) \sqrt{(s + a_x^2)(s + a_y^2)(s + a_z^2)}} \quad (2.25)$$

The term outside the square root in the denominator within the integral is specific to the direction of the depolarization factor, and for N_y and N_z the a_x is replaced by a_y and a_z respectively. The three depolarization factors must add to one: $N_x + N_y + N_z = 1$. The depolarization factors for three special ellipsoids are perfect spheres (1/3, 1/3, 1/3), discs (1, 0, 0) and needles (0, 1/2, 1/2). General solutions to the integral in (2.25) can be found in Sihvola (1999). The depolarization factors are used to calculate the polarizability, α , of the ellipsoidal inclusion, which for the $\hat{\mathbf{x}}$ direction reads (Sihvola, 1999):

$$\alpha_x = \frac{4\pi a_x a_y a_z}{3} (\epsilon_i - \epsilon_e) \frac{\epsilon_e}{\epsilon_e + N_x (\epsilon_i - \epsilon_e)} \quad (2.26)$$

The lowest polarizability for an inclusion is for a spherical shape. In the case of an ellipsoidal inclusion, the polarizability is anisotropic and is a 3×3 tensor. The effective permittivity is then also anisotropic, except for the case of randomly oriented ellipsoidal inclusions, since in this case the average deviations in any one direction will be zero. The MG equation for randomly oriented ellipsoidal inclusions is (Sihvola, 1999):

$$\epsilon_{eff} = \epsilon_e + \epsilon_e \frac{\frac{f}{3} \sum_{j=x,y,z} \frac{\epsilon_i - \epsilon_e}{\epsilon_e + N_j (\epsilon_i - \epsilon_e)}}{1 - \frac{f}{3} \sum_{j=x,y,z} \frac{N_j (\epsilon_i - \epsilon_e)}{\epsilon_e + N_j (\epsilon_i - \epsilon_e)}} \quad (2.27)$$

The BG equation for randomly oriented ellipsoidal inclusions is (Sihvola, 1999):

$$\epsilon_{eff} = \epsilon_e + \frac{f}{3} (\epsilon_i - \epsilon_e) \sum_{j=x,y,z} \frac{\epsilon_{eff}}{\epsilon_{eff} + N_j (\epsilon_i - \epsilon_{eff})} \quad (2.28)$$

Boyle (1985) extended the BGNS equation by incorporating a depolarization factor, N , so that

particle shape can be considered:

$$\frac{\epsilon_{eff} - \epsilon_i}{\epsilon_e - \epsilon_i} \left(\frac{\epsilon_e}{\epsilon_{eff}} \right)^N = (1 - f) \quad (2.29)$$

It is not clear in the study how to account for the depolarization factors in each direction. Boyle (1985) also provided a revised form of the LLL equation making use of a depolarization factor; however, this is not appropriate since there is no assumed particle shape in the original derivation. Consideration of the depolarization factor is important for mixtures where there is information known about the particle shape and when the polarizability of individual particles is required.

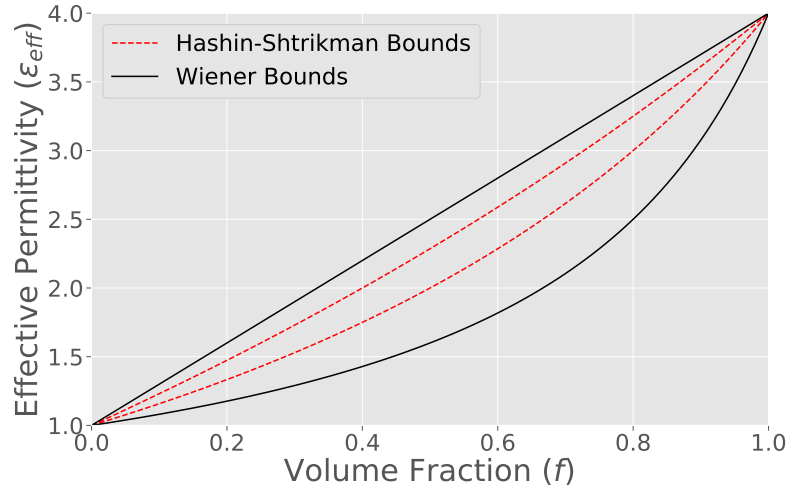
2.5 Mixing Theory: Bounds

There are two sets of generally accepted bounds for the effective permittivity of a mixture: the Wiener bounds, and the Hashin-Shtrikman bounds. The Wiener bounds are the most general, and represent the maximum and minimum bounds for any mixture as completely connected layers in series (parallel to applied electric field) and in parallel (perpendicular to applied electric field) (Sihvola, 1999):

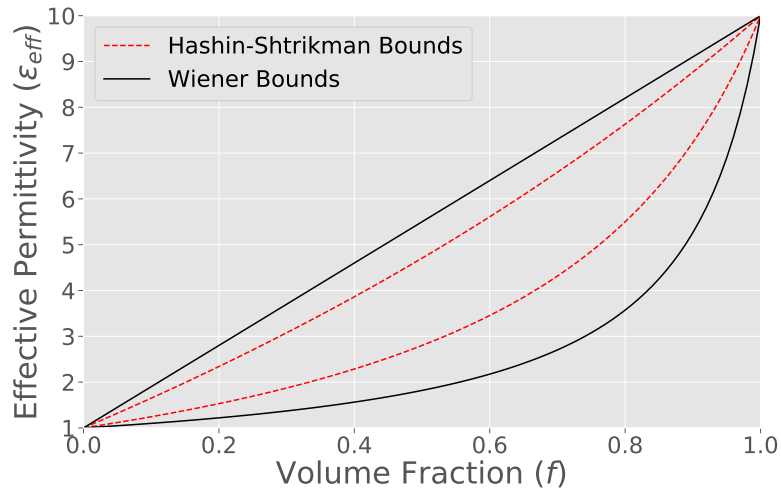
$$\epsilon_{eff,max} = f\epsilon_i + (1 - f)\epsilon_e \quad (2.30)$$

$$\epsilon_{eff,min} = \frac{\epsilon_i\epsilon_e}{f\epsilon_e + (1 - f)\epsilon_i} \quad (2.31)$$

The Wiener bounds represent an anisotropic mixture that has the extreme structure to maximize and minimize the possible effective permittivity. Hashin and Shtrikman (1962) developed bounds, termed the Hashin-Shtrikman bounds, for the maximum and minimum effective permittivity of an isotropic mixture, which have been shown to be identical to the MG and IMG equations (Sihvola, 1999). Figure 2.8 shows the Wiener and Hashin-Shtrikman bounds for a dielectric contrast of 4 and 10. For both the Wiener and Hashin-Shtrikman bounds, the difference between the maximum and minimum effective permittivity increases with the dielectric contrast in the mixture. These mixing theory bounds are useful for constraining the possible effective permittivity of a mixture where not much information is known. They have been used at times for a more conservative analysis of the mixing problem of planetary radar inversion (Kofman et al., 2015; Hérique et al., 2017).



(a) Dielectric contrast $\frac{\epsilon_i}{\epsilon_e} = 4$.



(b) Dielectric contrast $\frac{\epsilon_i}{\epsilon_e} = 10$.

Figure 2.8: Wiener and Hashin-Shtrikman bounds for the effective permittivity of two mixtures with dielectric contrast of 4 and 10.

2.6 Summary

Due to the complexity at microscopic scales in heterogeneous mixtures, it is not a simple task to choose which equation best represents a system macroscopically. Inherent in all mixing models is the generalization of the structure of a mixture. While some equations have obvious constraints on applicability, many behave very similarly for a given mixture. Numerous studies have been undertaken to characterize the effectiveness of mixing equations for a variety of situations, some of which have been introduced. Numerical methods such as FDTD and Monte Carlo simulations are sometimes used to solve for the effective permittivity of a mixture, for which results can be compared to predictions from analytical mixing equations. Furthermore experimental permittivity measurements of different material mixtures have also been conducted to test the validity of mixing equations. Table 2.1 summarizes the mixing theories that have been discussed in this chapter (the Sen-Scala-Cohen (SSC) equation is the inverse, or complement, to the Bruggeman (Non-Symmetric) equation). Tables 2.2 - 2.4 summarize the usage of these equations in the literature (SSC and BGNS equations are considered as one (BGNS), similar to the MG and IMG equations (MG)). The studies

Table 2.1: Two-phase mixing equations considered in this study. ϵ_{eff} is the effective permittivity of the mixture, ϵ_e and ϵ_i refer to the permittivities of the first and second phase with volume fractions $(1 - f)$ and f respectively.

Matrix/Inclusions Mixing Equations	
Maxwell Garnett (MG)	$\epsilon_{eff} = \epsilon_e + 3f\epsilon_e \frac{\epsilon_i - \epsilon_e}{\epsilon_i + 2\epsilon_e - f(\epsilon_i - \epsilon_e)}$
Inverse Maxwell Garnett (IMG)	$\epsilon_{eff} = \epsilon_i + 3(1 - f)\epsilon_i \frac{\epsilon_e - \epsilon_i}{\epsilon_e + 2\epsilon_i - (1 - f)(\epsilon_e - \epsilon_i)}$
Coherent Potential (CP)	$\epsilon_{eff} = \epsilon_i + f(\epsilon_i + \epsilon_e) \frac{3\epsilon_{eff}}{3\epsilon_{eff} + (1 - f)(\epsilon_i - \epsilon_e)}$
Bruggeman (Non-Symmetric) (BGNS)	$\frac{\epsilon_i - \epsilon_{eff}}{\epsilon_i - \epsilon_e} = (1 - f) \left(\frac{\epsilon_{eff}}{\epsilon_e} \right)^{\frac{1}{3}}$
Sen-Scala-Cohen (SSC)	$\frac{\epsilon_{eff} - \epsilon_e}{\epsilon_i - \epsilon_e} = f \left(\frac{\epsilon_{eff}}{\epsilon_i} \right)^{\frac{1}{3}}$
Statistical/Aggregate Mixing Equations	
Lichtenecker (LI)	$\epsilon_{eff} = \epsilon_i^f \epsilon_e^{1-f}$
Looyenga-Landau-Lifshitz (LLL)	$\epsilon_{eff}^{\frac{1}{3}} = f\epsilon_i^{\frac{1}{3}} + (1 - f)\epsilon_e^{\frac{1}{3}}$
Complex Refractive Index Model (CRIM)	$\sqrt{\epsilon_{eff}} = f\sqrt{\epsilon_i} + (1 - f)\sqrt{\epsilon_e}$
Bruggeman (Symmetric) (BG)	$(1 - f) \frac{\epsilon_e - \epsilon_{eff}}{\epsilon_e + 2\epsilon_{eff}} + f \frac{\epsilon_i - \epsilon_{eff}}{\epsilon_i + 2\epsilon_{eff}} = 0$

included in this summary span a wide range of research fields, are performed on numerous materials under different experimental conditions, and derived conclusions on the appropriateness of a given mixing theory in a variety ways. Tables 2.2 - 2.4 represent a summary of the essential findings of each study; however, for more thorough information on each study the reader is encouraged to refer to the original publication. The consideration of a large, diverse research base contained in

Table 2.2: Summary of various studies exploring the use of mixing theory. Each study is characterized by the type of mixture considered, the frequency range applicable for the analysis (by orders of magnitude), and the mixing theory that was determined to be the most accurate in that study.

Reference	Type of Mixture	Frequency Range	Mixing Model Used
(Adams et al., 1996)	dielectric	1 - 10 GHz	BG
(Banhegyi, 1988)	liquid saturated	1 MHz	BGNS
(Banhegyi, 1988)	dielectric	10 GHz	LLL
(Barmatz et al., 2012)	dielectric	1 GHz	LI
(Benadda et al., 1982) ($f > 0.75$)	dielectric	1 kHz - 1 GHz	BG
(Benadda et al., 1982) ($f < 0.35$)	dielectric	1 kHz - 1 GHz	LLL
(Birchak et al., 1974)	liquid saturated	1 GHz	CRIM
(Böttcher and Bordewijk, 1978)	dielectric	10 MHz, 10 GHz	LLL
(Böttcher and Bordewijk, 1978)	conductive/dielectric	10 MHz, 10 GHz	BGNS
(Brouet et al., 2014)	dielectric	> 20 GHz	LIN
(Brouet et al., 2015)	dielectric	100 MHz, > 20 GHz	LIN
(Brouet et al., 2016)	dielectric (ice/rock)	10 MHz - 1 GHz	LI
(Calame et al., 1996)	dielectric	1 GHz	Custom/Empirical
(Calame, 2008)	numerical simulation	-	Custom/Empirical
(Campbell and Ulrichs, 1969)	dielectric	100 MHz, > 20 GHz	MG
(Dobson et al., 1985)	liquid saturated	1 - 10 GHz	Custom/Empirical
(Dube and Parshad, 1970)	dielectric	10 MHz, 10 GHz	BG
(Dube, 1970)	dielectric	10 MHz, 10 GHz	LLL
(Ebara et al., 2006)	dielectric	1 GHz	LI

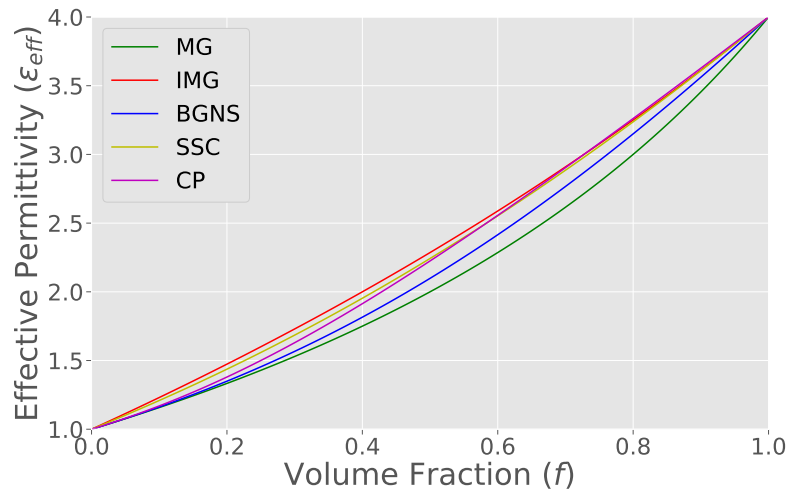
Table 2.3: Summary from Table 2.2 continued.

Reference	Type of Mixture	Frequency Range	Mixing Model Used
(ElShafie and Heggy, 2013)	dielectric	100 MHz - 1 GHz	LIN
(Fensler et al., 1962)	dielectric	100 MHz - 1 GHz	LIN
(Gershon et al., 2001)	dielectric	1 GHz	LLL
(Gladstone and Dale, 1863)	liquid saturated	> 20 GHz	CRIM
(Heggy et al., 2001)	dielectric	1 MHz	Custom/Empirical
(Heggy et al., 2012)	dielectric (ice/rock)	1 - 10 MHz	Custom/Empirical
(Johnson and Poeter, 2005)	liquid saturated	10 - 100 MHz	BGNS
(Kameyama and Miyamoto, 2008)	dielectric	1 - 10 MHz	LIN
(Kenyon, 1984)	liquid saturated	100 kHz - 1 GHz	Custom/Empirical
(Knight and Nur, 1987)	liquid saturated	10 kHz - 1 MHz	Custom/Empirical
(Knoll, 1996)	dielectric	100 kHz - 10 MHz	CRIM
(Malik et al., 1988)	dielectric	100 kHz, 10 MHz	LLL
(Martinez and Brynes, 2001)	dielectric	100 MHz - 1 GHz	CRIM
(Neelakantaswamy et al., 1983)	dielectric	1 kHz - 1 GHz	LI
(Nelson et al., 1989)	dielectric	1 - 10 GHz	LLL
(Nelson, 1992)	dielectric	1 - 10 GHz	LLL
(Nelson and Bartley, 1998)	dielectric	1 - 10 GHz	LLL
(Nelson, 2005)	dielectric	1 - 10 GHz	LLL
(Oguchi et al., 2009)	dielectric	1 - 10 GHz	BG
(Olhoeft and Strangway, 1975)	dielectric	100 kHz - 1 MHz, 100 MHz, 10 GHz	LI
(Olhoeft, 1987)	liquid saturated	100 MHz	BGNS
(Park et al., 2017)	liquid saturated	10 MHz, 1 - 10 GHz	Custom/Empirical
(Pekonen et al., 1999)	numerical simulation	-	BG
(Penn et al., 1997)	dielectric	10 GHz	Custom/Empirical

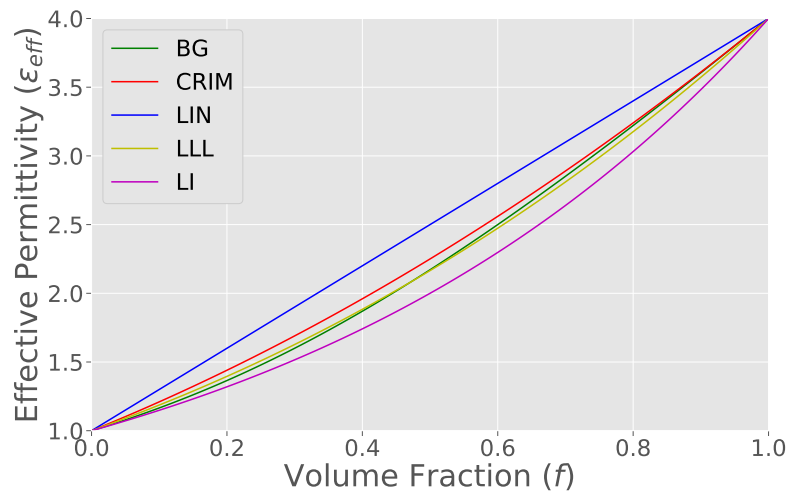
Table 2.4: Summary from Table 2.3 continued.

Reference	Type of Mixture	Frequency Range	Mixing Model Used
(Pervin, 2015)	dielectric	10 MHz - 1 GHz	BGNS
(Plug et al., 2006)	numerical simulation	-	LLL
(Robinson and Friedman, 2003)	liquid saturated	10 MHz - 1 GHz	MG
(Robinson and Friedman, 2003)	dielectric	10 MHz - 1 GHz	LI
(Robinson and Friedman, 2005)	liquid saturated	10 MHz - 1 GHz	Custom/Empirical
(Rogers et al., 2011)	dielectric	> 20 GHz	BG
(Rust et al., 1999)	dielectric	10 MHz	LIN
(Sen et al., 1981)	liquid saturated	1 GHz	BGNS
(Sharif, 1995)	dielectric	10 GHz	LLL
(Sheen et al., 2010) $f < 0.25$	dielectric	10 GHz	LIN
(Sheen et al., 2010) $f > 0.25$	dielectric	10 GHz	LLL
(Shen et al., 1985)	liquid saturated	100 MHz - 1 GHz	CRIM
(Stillman et al., 2010)	dielectric (ice/rock)	< 1 kHz - 1 MHz	LLL
(Tuhkala et al., 2013)	dielectric	1 GHz	LLL
(Ulaby et al., 1990)	dielectric	100 MHz - 10 GHz	LI
(Zheng et al., 2005)	dielectric	10 GHz	LI

Tables 2.2 - 2.4 allows for some general analysis of the frequency of use of each mixing theory in the literature. It was noted in several of the studies that the LLL model and the BG model predicted similar effective permittivities, especially at relatively equal mixtures (50% phase 1, 50% phase two), where the two model predictions are equivalent at $f = 0.43$ (or 43% of phase 1) (Tuhkala et al., 2013; Dube, 1970; Plug et al., 2006; Nelson, 2005). From Tables 2.2 - 2.4, roughly 35% of the studies found the LLL and BG models to describe their dataset the best, followed by custom/empirical models (17%) and the LI model (13%). If the studies considered are restricted to those on dry materials in the GHz frequency range (corresponding to S- and X- band radar), these percentages change to 56% for the LLL and BG models, 6% for the custom/empirical models, and 20% for the LI model. The following plots illustrate how each mixing theory that has been discussed predicts the effective permittivity of a mixture as a function of the volume fractions of either phase, for given dielectric contrasts. In Figure 2.9 it is evident that for low dielectric contrast, the mixing theories are generally not that different from one another. As the dielectric contrast increases (Figure 2.10), the differences between the mixing theories become greater. A dielectric contrast of 100 (Figure 2.11) is not reasonable for typical non-metallic geologic material, but is useful in illustrating the percolation behaviour of each mixing theory. The percolation threshold can be visually identified in Figure 2.11 as the point where the slope of the curve increases dramatically.

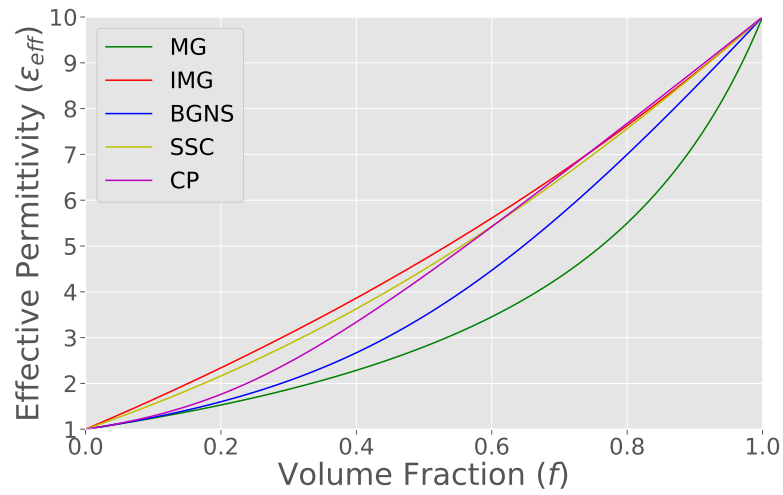


(a) Matrix/Inclusion Group.

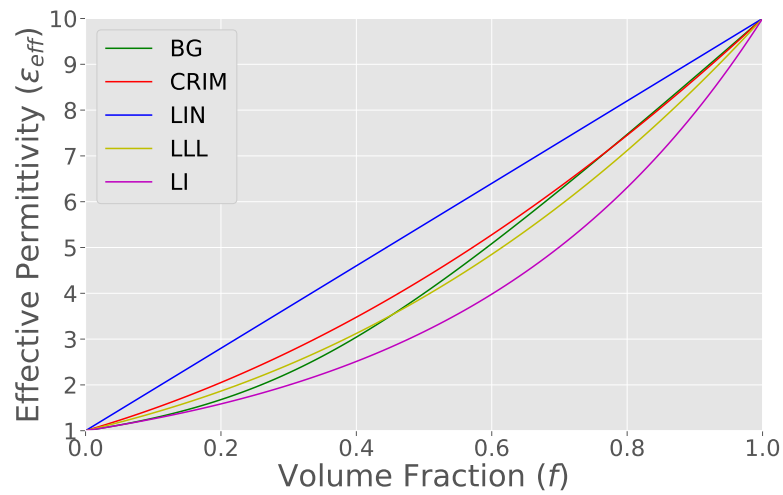


(b) Statistical/Aggregate Group.

Figure 2.9: Mixing theories for a dielectric contrast of $\frac{\epsilon_i}{\epsilon_e} = 4$.

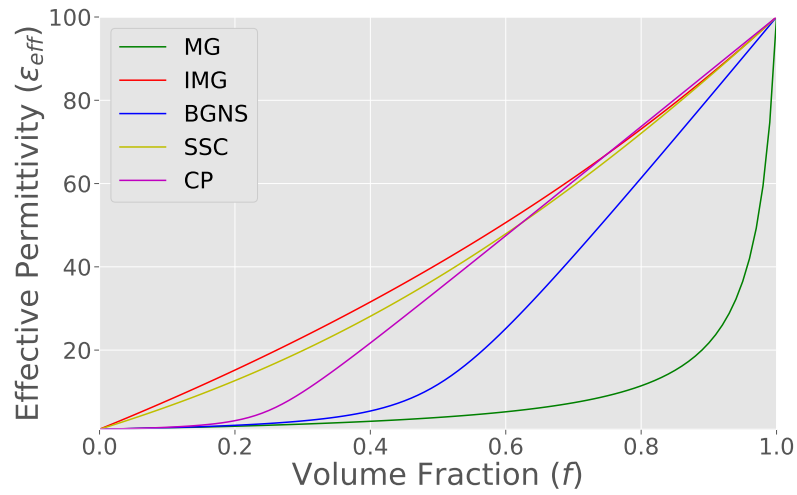


(a) Matrix/Inclusion Group.

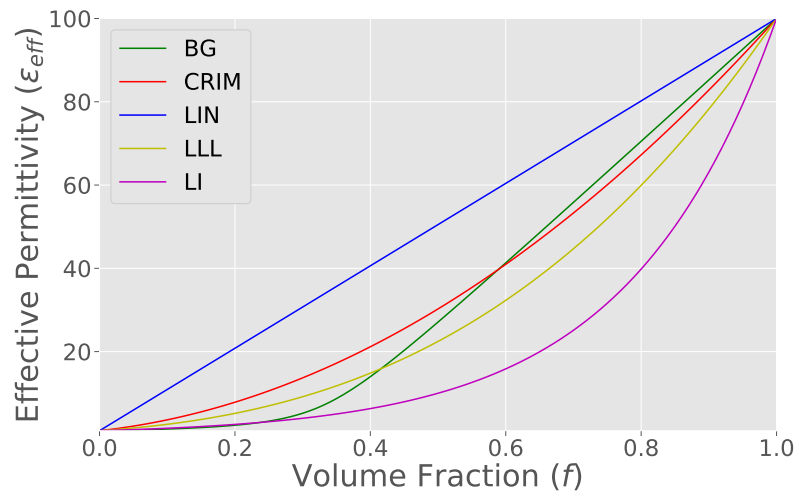


(b) Statistical/Aggregate Group.

Figure 2.10: Mixing theories for a dielectric contrast of $\frac{\epsilon_i}{\epsilon_e} = 10$.



(a) Matrix/Inclusion Group.



(b) Statistical/Aggregate Group.

Figure 2.11: Mixing theories for a dielectric contrast of $\frac{\epsilon_i}{\epsilon_e} = 100$

Chapter 3

Experimental Setup and Methodology

3.1 Introduction

The experimental work in the presented research consists of geologic powder sample preparation and characterization, which will be discussed in chapter 4, and complex permittivity measurements of those samples. This chapter will describe the experimental setup and the methodology that was followed to measure the complex permittivity of powder samples. The coaxial transmission line method was used for the complex permittivity measurements of the powder samples, utilizing coaxial airlines, coaxial cables, and a vector network analyzer (VNA). A VNA is a device that transmits a voltage wave, or signal, (over a range of possible frequencies) through some device under test (DUT) and measures the signal as received at each port of the electrical network. For 2-port VNA, for example, a signal is transmitted from port 1 and the signal's amplitude and phase is measured at both port 1 (reflected) and port 2 (transmitted) (the reverse, from port 2 to 1, is also executed). The magnitude and phase of the measured signals are used to derive the scattering parameters, or S-parameters, of the DUT, which can then be used to determine the constitutive parameters, such as permittivity, for that DUT. With the application to powder samples in this research, the powder sample contained within a coaxial airline is the DUT, and the measured permittivity is thus the permittivity (more specifically, the effective permittivity) of that sample. The foundation for the specific methodology used in this research was established in Sotodeh (2014), and has since been expanded as reported in this work in cooperation with several collaborators at the University of Toronto. The major contributions reported in this work towards the methodology are the design, construction, and incorporation of an environment chamber and a heating mechanism for the setup, as well as the introduction of the use of silica aerogel for high porosity measurements. To a lesser extent this work contributed in the development of the software used to analyze the raw outputs from the network analyzer, with the majority of the software written by Alexandre Boivin,

a graduate student in the Solar System Exploration Group (SSXG) at the University of Toronto. When applicable, this chapter will be explicit in delineating any research efforts made by others that were made use of in this research.

3.2 Coaxial Transmission Line Method

3.2.1 Overview of Coaxial Transmission/Reflection Method

The constitutive parameters for a material are determined using the coaxial transmission line method by measuring the scattering parameters from a sample filled coaxial airline inserted into a transmission line that is connected to a network analyzer. As opposed to resonance based methods, the coaxial transmission line method has the advantage of being relatively cheap, can be readily adapted for measurements of powder samples, and measures the scattering parameters over a broad frequency range. A coaxial airline is essentially the same as a coaxial transmission line, consisting of a solid cylindrical inner conductor with diameter b surrounded by a hollow cylindrical outer conductor with diameter a (Figure 3.1). The space between the inner and outer conductors is filled

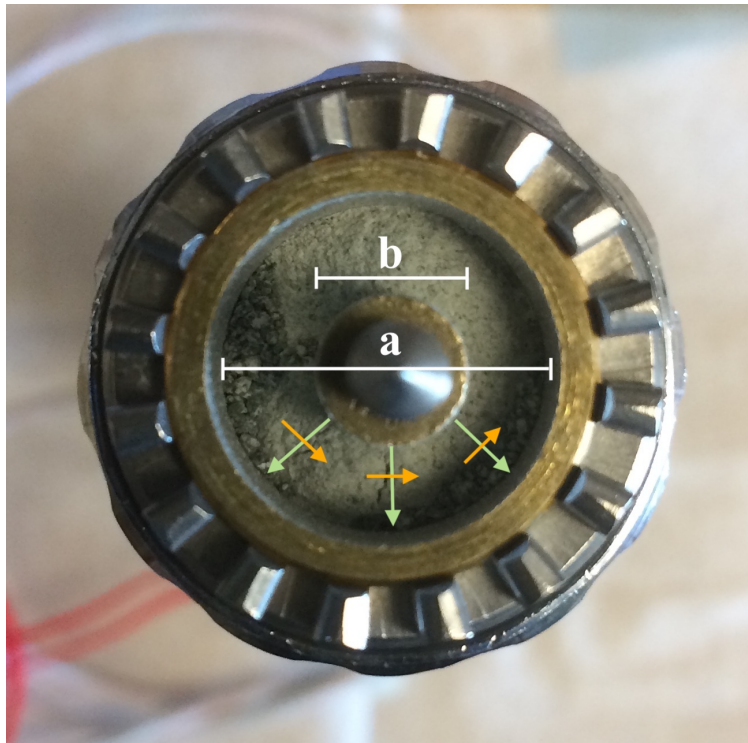


Figure 3.1: Cross-sectional view of the GR900-LZ coaxial airline filled with a powder sample. Electric field lines are the green arrows, and magnetic field lines the orange arrows.

with whatever material is being tested in the coaxial airline. A voltage wave is transmitted through

the inner conductor, which creates a potential difference with the grounded outer conductor. The result is an electric field directed radially outward from the inner conductor, perpendicular to both the inner and outer conductors and the direction of propagation of the wave. Since the voltage wave oscillates at some frequency of interest dictated by the network analyzer, the electric field also changes with time, in turn inducing a magnetic field that is perpendicular to the electric field and propagation direction (Figure 3.1). This describes a transverse electric/magnetic wave (TEM), which is the fundamental mode in coaxial airlines (Chen et al., 2004). Transverse electric (TE) and transverse magnetic (TM) higher order wave modes are also supported in coaxial airlines, but occur at higher frequencies than the fundamental TEM mode. The frequency where TE and TM modes manifest themselves is often described in terms of wavelength, or the cutoff wavelength, λ_c (Adam and Packard, 1969):

$$\lambda_c = \pi \left(\frac{a+b}{2} \right) \sqrt{\epsilon_r^* \mu_r^*} \quad (3.1)$$

For the GR900-LZ coaxial airlines used in this research the inner and outer conductor dimensions are roughly the same, and for the 15 cm length airline used for most of the measurements the dimensions are $b = 0.62052 \pm 0.00025$ cm and $a = 1.42824 \pm 0.00025$ cm. The cutoff frequency for the empty airline is then ≈ 9.32 GHz according to (3.1). This is in agreement with the manufacturer listed upper frequency limit of 8.5 GHz, since the cutoff frequency is often defined just below the theoretical limit to account for defects in the airline. Under the assumption that $\mu_r^* = 1 - 0j$ for all of the samples in this research and that the materials are low loss, the cutoff frequency as a function of the real part of the permittivity is plotted in Figure 3.2. For the typical range in the measured sample permittivity in this research, the cutoff wavelength occurs at roughly 5 - 6 GHz. An example of the effect that this has on the data is shown in Figure 3.3 for a labradorite/silica aerogel mixture. The frequency-averaged permittivity for this sample measurement is 3.16, corresponding to a cutoff frequency of 5.2 GHz. Highlighted in Figure 3.3 is the cutoff frequency in the spectrum, where the higher order TE and TM modes can be seen to add spurious deviations, or sharp spikes as a function of frequency, in the solution for ϵ_r^* above this frequency. This is due to the random constructive and destructive interference of these wave modes with the fundamental TEM mode. The interference caused by these higher order modes is more significant for the measured imaginary part of the permittivity, and relatively less important for the measured real part of the permittivity. Although the frequency-averaged real part of the permittivity is calculated including frequencies

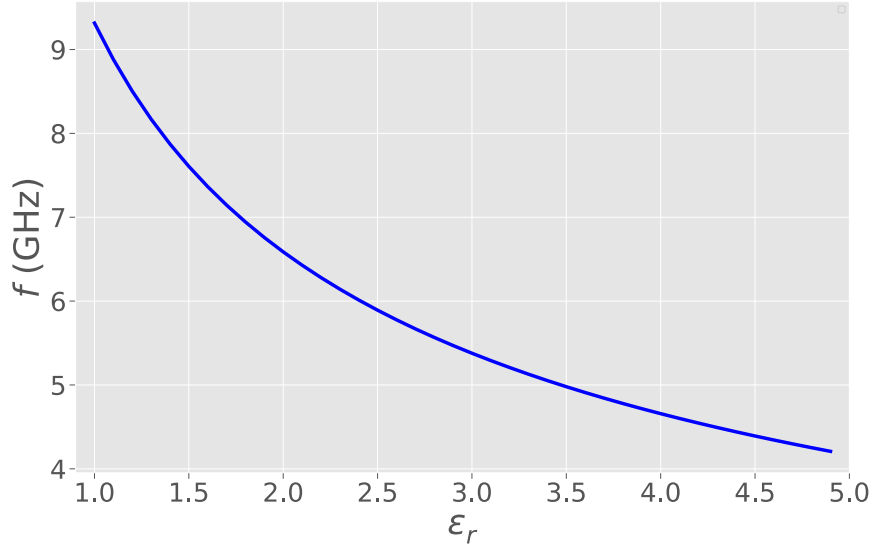
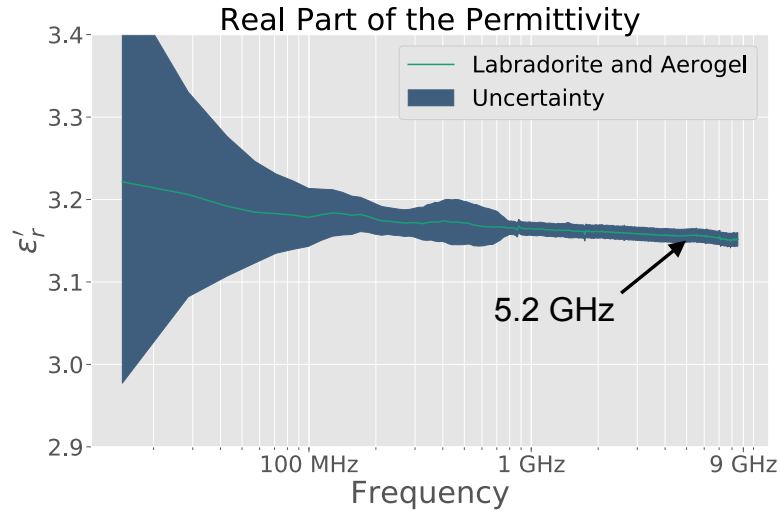
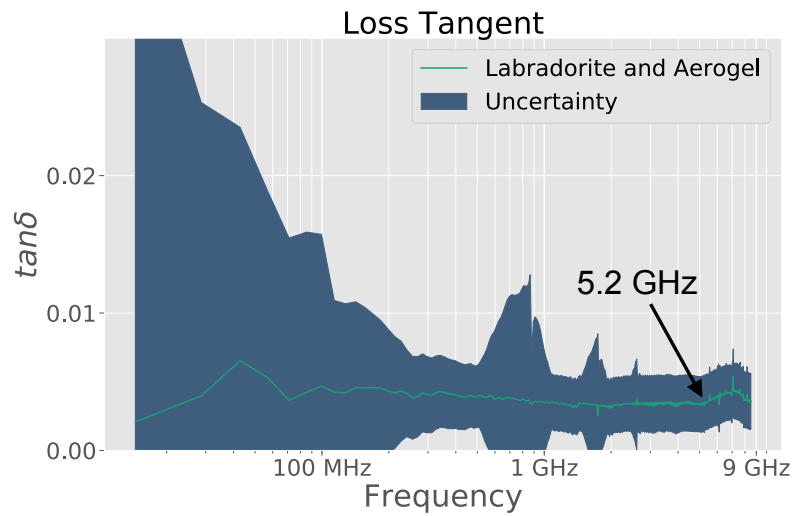


Figure 3.2: Cutoff frequency of the GR900-LZ coaxial airlines as a function of the permittivity of the sample being measured.

above the cutoff frequency, the standard deviation of this average is typically less than the Type A measurement uncertainty for powder samples (see section 3.9.2). Care must be taken to consider this interference, however, when analyzing the high frequency component of the imaginary part of the permittivity. The cutoff wavelength for a guided wave in a coaxial airline changes the calculation of the propagation constant, γ , of the wave. The propagation constant as written in (1.35) can be rewritten in terms of a complex permittivity with zero static conductivity (substituting $\sigma_e = \sigma_s + \omega\epsilon''$): $\gamma = j\omega\sqrt{\mu^*\epsilon^*}$. Here it is worth noting that in many applications, the AC conductivity is considered inherently in the imaginary part of the permittivity. Instead of including an effective conductivity term that encompasses static conductivity, the static conductivity is included in the definition of the complex permittivity: $\epsilon^* = \epsilon' - j(\frac{\sigma_s}{\omega} + \epsilon'')$. In this case, the permittivity is often called the effective permittivity, which can be confusing in this thesis given the definition of effective permittivity with regards to mixtures (Baker-Jarvis et al., 2005; Knoll, 1996). The definition of the static conductivity is arbitrary, and is inherently measured as part of the effective loss tangent in the coaxial transmission line method, and so can be considered part of the complex permittivity. The propagation constant for a guided wave is $\gamma = j\sqrt{k^2 - k_c^2}$, where $k = \omega\sqrt{\mu^*\epsilon^*}$ and $k_c = 2\pi/\lambda_c$



(a) Real part of the measured effective permittivity.



(b) (Effective) loss tangent of the measured effective permittivity.

Figure 3.3: Illustration of the effect of the cutoff frequency on permittivity measurements (here a measurement of the labradorite sample).

(Baker-Jarvis et al., 2005). The propagation constant for a guided wave can then be written for a given material γ and for free space γ_0 as (Baker-Jarvis et al., 1993):

$$\gamma = j\sqrt{\frac{\omega^2\mu_r^*\epsilon_r^*}{c^2} - \left(\frac{2\pi}{\lambda_c}\right)^2} \quad (3.2)$$

$$\gamma_0 = j\sqrt{\left(\frac{\omega}{c}\right)^2 - \left(\frac{2\pi}{\lambda_c}\right)^2} \quad (3.3)$$

Here the speed of light, $c = \frac{1}{\sqrt{\epsilon_0\mu_0}}$, has been introduced. These propagation constants will determine the electric field of an EM wave that is incident on, reflected from, and transmitted through a material in a coaxial airline. In Figure 3.4 a schematic of a sample filled coaxial airline in the VNA

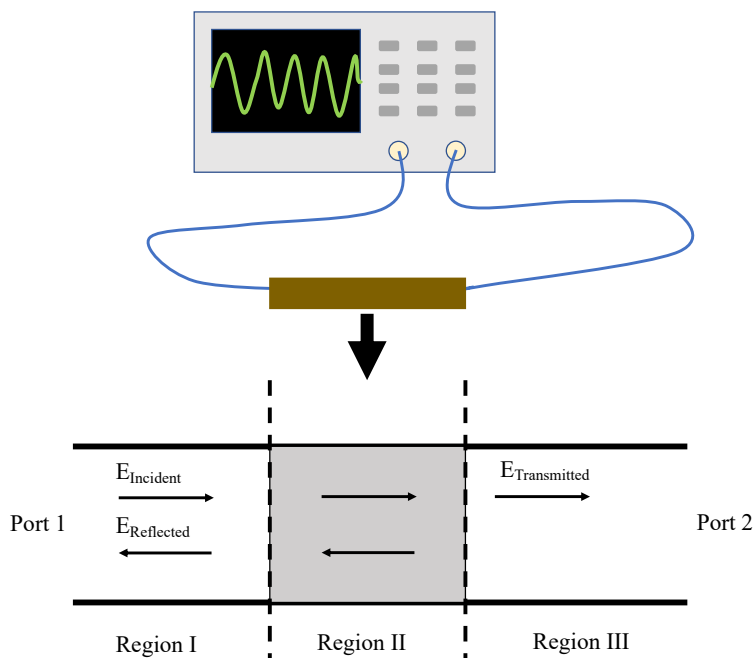


Figure 3.4: (Adapted from Figure 4.1 (Chen et al., 2004)) Depiction of the VNA circuit, including the VNA, coaxial cables, and sample filled coaxial airline. This circuit is broken down into the corresponding diagram depicting a forward (S_{11}, S_{21}) measurement, made up of regions I, II, and III, where region II represents the sample filled airline. The z-axis is chosen to be along the length of the airline.

circuit is given, dividing the area into regions I, II, and III. The normalized electric fields in each region are defined by (Chen et al., 2004; Baker-Jarvis et al., 1993):

$$E_I = e^{-\gamma_0 z} + C_1 e^{\gamma_0 z} \quad (3.4)$$

$$E_{II} = C_2 e^{-\gamma z} + C_3 e^{\gamma z} \quad (3.5)$$

$$E_{III} = C_4 e^{-\gamma_0 z} \quad (3.6)$$

For a typical 2-port network analyzer, like the one used in the research presented in this thesis, each port is described by an incident (or input) node, a , and a reflected (or output) node, b (Chen et al., 2004; Adam and Packard, 1969). The incident nodes for port 1, a_1 , and port 2, a_2 , measure the magnitude and phase of the source voltage wave, and the reflected nodes for port 1, b_1 , and port 2, b_2 , measure the magnitude and phase of the reflected (S_{11} or S_{22}) and transmitted voltage wave (S_{21} or S_{12}) (Figure 3.5). The relationship between the input and output waves are described by

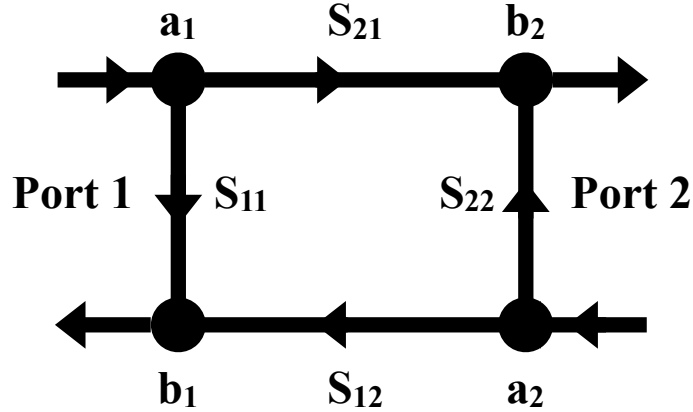


Figure 3.5: (Adapted from Figure 3.2-2. (Adam and Packard, 1969)) Flow graph depiction of the 2-port VNA network.

the 2×2 scattering matrix \mathbf{S} with S-parameters, S_{ij} , which are complex parameters with magnitude and phase:

$$\begin{bmatrix} b_1 \\ b_2 \end{bmatrix} = \begin{bmatrix} S_{11} & S_{12} \\ S_{21} & S_{22} \end{bmatrix} \begin{bmatrix} a_1 \\ a_2 \end{bmatrix} \quad (3.7)$$

The S-parameters for a given measurement are determined by the ratios of the complex signals measured at each node ($a_{1,2}$ and $b_{1,2}$) and are related to the electric fields E_I , E_{II} , and E_{III} . The

constants in equations (3.4) - (3.6) can be determined by applying boundary conditions at the interfaces of regions I, II, and III requiring that the tangential electric and magnetic fields must be equal (Baker-Jarvis et al., 1993). With equations (3.4) - (3.6) solved, the measured S-parameters can be written in terms of the reflection coefficient, Γ , and the transmission coefficient, T :

$$S_{11} = S_{22} = \frac{\Gamma(1 - T^2)}{1 - \Gamma^2 T^2} \quad (3.8)$$

$$S_{21} = \frac{T(1 - \Gamma^2)}{1 - \Gamma^2 T^2} \quad (3.9)$$

$$T = e^{-\gamma d} \quad (3.10)$$

$$\Gamma = \frac{\frac{\mu^*}{\gamma} - \frac{\mu_0}{\gamma_0}}{\frac{\mu^*}{\gamma} + \frac{\mu_0}{\gamma_0}} \quad (3.11)$$

In equation (3.8), it is assumed that the scattering matrix (and thus the sample) is symmetric. With knowledge of the sample length, d , and the measured S-parameters of the DUT, equations (3.8) - (3.11) represent an over-determined system of equations that can be solved for the constitutive parameters ϵ^* and μ^* (Baker-Jarvis et al., 1993).

3.2.2 Calculating constitutive parameters from S-parameters

A direct calculation of the constitutive parameters from the S-parameters was discovered by Nicolson and Ross (1970) and Weir (1974), aptly called the Nicolson-Ross-Weir (NRW) algorithm. This algorithm has been used extensively in the literature as it is relatively easy to implement, solves for both ϵ^* and μ^* , and can be applied to coaxial airlines or rectangular waveguides (Boughriet et al., 1997). The significant drawback to the NRW algorithm is in the numerical instabilities that occur at integral multiples of one-half wavelength in the sample (Baker-Jarvis et al., 1993; Boughriet et al., 1997). At these intervals, the magnitude of S_{11} is small and there is a large uncertainty in the phase of S_{11} . This instability causes large spikes in the calculated values of ϵ^* and μ^* which makes it difficult to ascertain the broadband frequency dependence of these parameters. Stillman (2006) provided an equation that allows the determination of the frequencies, f_r , up to n harmonics at which these spikes occur in the NRW solution as a function of the constitutive parameters (since the spikes are wavelength dependent):

$$f_r = \frac{\sqrt{2}c}{\frac{2d}{n} \sqrt{\sqrt{(\mu_r' \epsilon_r' - \epsilon_r'' \mu_r'')^2 + (\mu_r'' \epsilon_r' + \mu_r' \epsilon_r'')^2} + \epsilon_r' \mu_r' - \epsilon_r'' \mu_r''}} \quad (3.12)$$

To overcome this issue, Baker-Jarvis et al. (1990) developed an iterative technique that provides a stable solution for ϵ_r^* assuming $\mu_r^* = 1$. This method can be accurate, but also requires specific tuning (initial guesses for ϵ_r^*) for a given sample and can be computationally intensive. Another stable solution for ϵ_r^* was derived in Boughriet et al. (1997) that is non-iterative and also assumes $\mu_r^* = 1$. The Boughriet et al. (1997) algorithm is the one chosen to calculate ϵ_r^* from the measured S-parameters in the current research, as the samples are considered non-magnetic and the algorithm can be easily applied for any sample. The resonant frequency instabilities are still present to some extent in the data, and are especially strong for low-loss materials. The uncertainty in the constitutive parameters are derived in Boughriet et al. (1997) as a propagation of the uncertainty in the length of the sample and the measured S-parameters, where the latter can be extracted directly from the network analyzer. This method only requires the S-parameters from one orientation with respect to the sample, i.e either S_{11} and S_{21} , or S_{22} and S_{12} . As a result, two separate calculations for the complex permittivity of the sample can be made making use of either pair of S-parameters. If the sample is truly homogeneous, then the two calculations would be equal. This provides a method of quantifying the homogeneity of the sample filled coaxial airline post-measurement.

3.3 Equipment

3.3.1 Network Analyzer

A 2-port Keysight (previously Agilent) E5071C ENA Vector Network Analyzer (VNA) operating from 300 kHz - 12 GHz was used to measure the S-parameters for all of the permittivity measurements in this research. The ports are fitted with standard 3.5 mm coaxial connectors. The VNA was controlled using a built in Windows operating system, external buttons, and the METAS VNA Tools II software package (see section 3.7.1).

3.3.2 Coaxial Airlines, Cables, and Adapters

The coaxial airlines used for all of the measurements in this study are from the General Radio Reference Airline Set consisting of different lengths of the 14 mm diameter General Radio GR 900-LZ 50 Ω model coaxial airline (Figure 3.6). It was shown in Sotodeh (2014) that the measurement



Figure 3.6: 10 cm length GR 900-LZ coaxial airline with inner conductor removed from airline and Teflon[®] washers.

uncertainty decreases with increasing airline length. The largest airline is 30 cm in length and was too large to fit inside of the environment chamber used for the measurements, so the second largest airline at 15 cm length was predominantly used. Some of the samples used in the current research did not consist of enough material to completely fill the 15 cm length airline, which is required based on the homogeneous and symmetrical assumptions in the derivation of the constitutive parameters. The 7.5 cm and 10 cm length airlines were used for these samples. The cables connecting the VNA to the coaxial airlines were Maury Microwave SC-35-MM-36-TVAC cables, which were chosen for their low-outgassing properties and thermal stability over a wide range of temperature (-55°C to $+125^{\circ}\text{C}$). To connect the 14 mm GR connectors on either end of the GR 900-LZ coaxial airlines to the cables, GR900-QMMJ 3.5 mm - 14 mm adapters were used. The GR 14 mm connectors have good repeatability between connections and are hand tightened (Sotodeh, 2014). The 3.5 mm connectors can potentially be over-tightened, and were therefore tightened with a 12 in-lb precision HP 1250-1874 torque wrench for all connections made.

3.3.3 Custom Filling Funnel

To fill the coaxial airlines with powder samples, the custom filling funnel from Sotodeh (2014) was utilized. This setup consists of an aluminium funnel to which the coaxial airline is attached vertically (both the inner and outer conductor), which is then attached to a Gilson Performer III Sieve Shaker (Figure 3.7). The powder sample is poured into the top of the funnel and redirected to the space

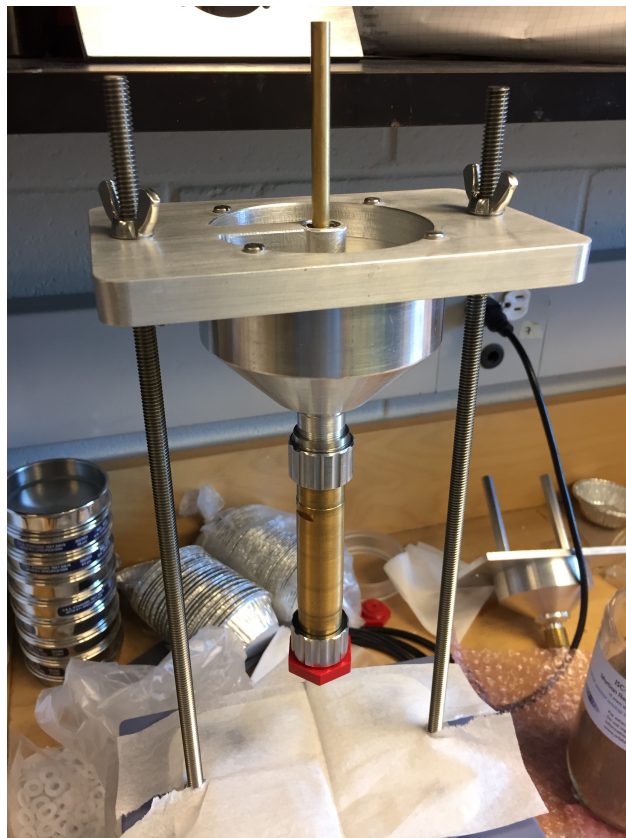


Figure 3.7: Custom funnel filling device designed and manufactured by RobotWorks Corp. based on the designs from Sotodeh (2014).

between the inner and outer conductor of the coaxial airline. To ensure homogeneous packing of the powder, the sieve shaker was set to vibrate during the packing procedure and the coaxial airline was periodically tapped by hand, which has been shown to help with the packing process (Dube, 1970). The original funnel from Sotodeh (2014) was used for most of the measurements, but eventually degraded in quality from continued use. A similar funnel was then designed and fabricated by RobotWorks Corp. for the remaining measurements.

3.3.4 Teflon[®] Washers

One of the difficulties in containing a powder sample in the coaxial airlines was in stopping the powder grains from spilling into the GR 14 mm connectors, and keeping the powder sample/connector interface perfectly perpendicular to the length of the airline. To achieve these ends the use of Teflon[®] washers was incorporated into the measurement setup, as established in Sotodeh (2014). Teflon[®] is a brand of polytetrafluoroethylene (PTFE) and is considered a standard dielectric material with a low permittivity (real and imaginary) of $\epsilon_r^* \approx 2.1 - j0.0007$. The Teflon[®] washers were machined to have an inner and outer diameter matching the GR 900-LZ coaxial airlines and were made as thin as possible, while maintaining structural integrity (Figure 3.6). Alister Cunje, a graduate student in the SSXG lab at the University of Toronto, characterized (using a digital caliper) an average width of 1.7 mm for the large batch of Teflon[®] washers machined at the University of Toronto that were used in the measurements presented in this research. The washers can be cleaned and re-used in some cases, and in others are deformed in the process of removing them from the airline and are discarded after one use. To use the washers, a washer is attached at one end of the coaxial airline with the inner conductor in place prior to filling the airline with a powder sample, ensuring that the washer is flush with the connection surface. The airline is then filled using the custom filling funnel until the level of powder nearly reaches the end of the airline (with roughly 1.7 mm of space). The airline is then removed and the second washer is attached to the “top” of the airline, thereby sealing the powder sample and ensuring that it maintains its correct orientation during measurement. This last step proved to be difficult, and required some intuition from the experimenter. With practice, it became easier to judge when the airline was “full”.

3.4 Environment Chamber

To accurately measure the permittivity of a geologic sample, the volume within the coaxial airline needs to be devoid of all other substances, especially water. Water has a high complex (both real and imaginary) permittivity, especially with increased salinity and ionic concentrations, and will drastically affect the effective permittivity measured. Air, at low relative humidity, has essentially the same permittivity as that of free space, $\epsilon_{r,\text{air}} = \epsilon_{\text{air}}/\epsilon_0 = 1$, and will be accounted for in the post-processing of the data (modelling effective permittivity with mixing equations). To ensure that there is minimal water in the sample it is necessary to oven dry the powder samples prior to measurements, which will be discussed in the next chapter. In the time that the sample is removed from the oven, packed into the coaxial airline, and connected to the network analyzer, the sample will adsorb some amount of water. For minerals with low permittivities, such as silicates and carbonates, this small amount of water can significantly alter the effective permittivity. In an effort to reduce this contribution to the permittivity measurements, an environment chamber was incorporated into the experimental setup (Figure 3.8). The aim of this chamber was to isolate the

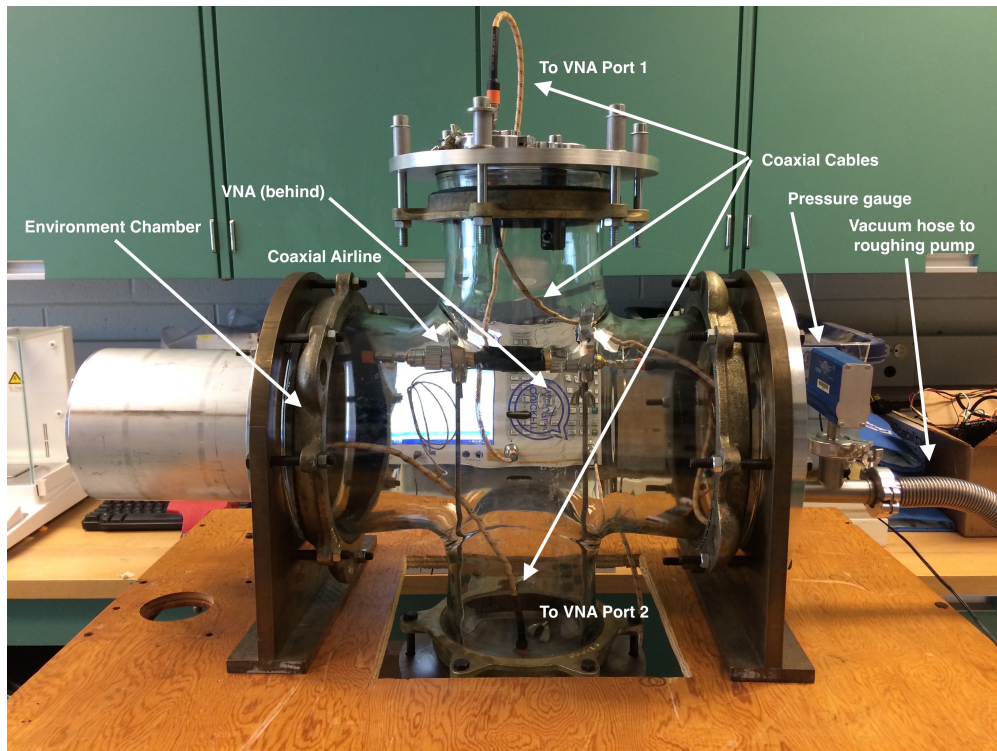
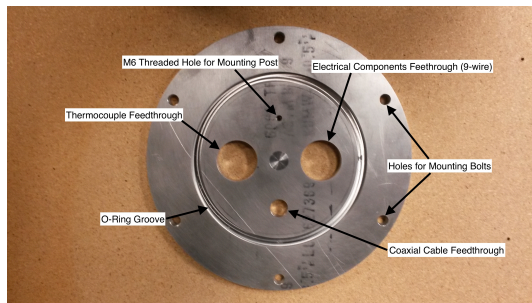
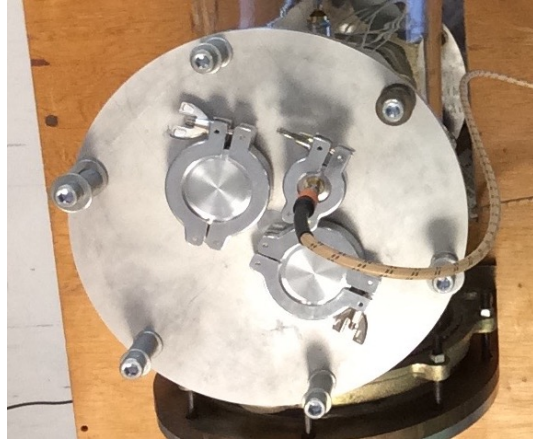


Figure 3.8: Annotated image of the environment chamber used for the permittivity measurements in this research.

coaxial airline from the ambient laboratory atmosphere with appropriate feedthrough components



(a) Upper aluminium plate prior to attaching feedthroughs.



(b) Upper aluminium plate incorporated into chamber.

Figure 3.9: Custom aluminium plate used for environment chamber

for the coaxial cables, vacuum hoses, and electrical wiring. The glass chamber that was used for the environment chamber was salvaged from a previous experiment in the Centre for Earth and Space Science at York University. To adapt the chamber to the requirements of the experiments in this research, two custom aluminium plates were designed and fabricated at the Machine Shop in the Faculty of Science at York University (Figure 3.9). The aluminium plates were designed to line up with the existing O-ring grooves and mounting bolt positions. Holes were cut in either plate to attach the necessary feedthrough components (Figure 3.9). In the upper plate, two QF40 half nipples, for a thermocouple and sub-D electrical connector, were attached to the appropriate holes using vacuum epoxy. In both plates, a QF16 vacuum half nipple was attached to the appropriate hole for the MPF Products Inc. SMA 50 Ω coaxial connector feedthrough. Figure 3.9 (b) shows the upper plate with QF40 plugs and the QF16 coaxial connector feedthrough attached with appropriate O-rings and vacuum clamps. The upper plate also had a shallow M6 threaded hole that was meant to house a threaded rod to which the coaxial airline could be attached. This was for intended use with an HP (Agilent) 85051B Verification Kit 50 Ω reference airline with a 7 mm outer diameter and 10 cm length. The original design was for the 7 mm airline to be attached in the vertical position with retort stand clamps. As the experimental design progressed, it became apparent that the 7 mm airline was too small to incorporate the desired heating components, and the 7 mm airline was set aside in favour of the larger 14 mm outer diameter, 15 cm length GR900-LZ airline. To accommodate the 14 mm airline, two shallow M6 threaded holes were added to the bottom aluminium plate. Two M6 threaded aluminium rods of equal length were fabricated and screwed

into the threaded holes. A QF25 vacuum clamp with an M6 threaded hole was attached to the end of each threaded rod. It was observed that the diameter of these clamps roughly matched the exterior diameter (slightly larger than 14 mm) of the 14 mm airline, and were a simple solution to attaching the airline to the threaded rods. Figure 3.8 shows the 14 mm outer diameter, 15 cm length GR900-LZ coaxial airline secured in the environment chamber. The horizontal positioning of the coaxial airline during measurement is commonly used in similar studies (i.e (Stillman, 2006)), and the perpendicular orientation of the powder/connector interface was deemed to be maintained with the incorporation of the Teflon[®] washers. The aluminium cylinder on the left of the chamber (Figure 3.8) is remnant from a previous experiment that made use of the chamber, and was mainly used to allow easy access to install the coaxial airline and relevant components prior to a permittivity measurement. The aluminium plate on the right side of the chamber (Figure 3.8) already had a QF25 half nipple attached from the previous experimenter. This was used to attach a QF25 tee nipple that connected a Kurt J. Lesker[®] Company (KJLC) 300 Series pressure gauge (Convection Enhanced Pirani method) and the vacuum hose to the roughing pump (Figure 3.10). This pressure

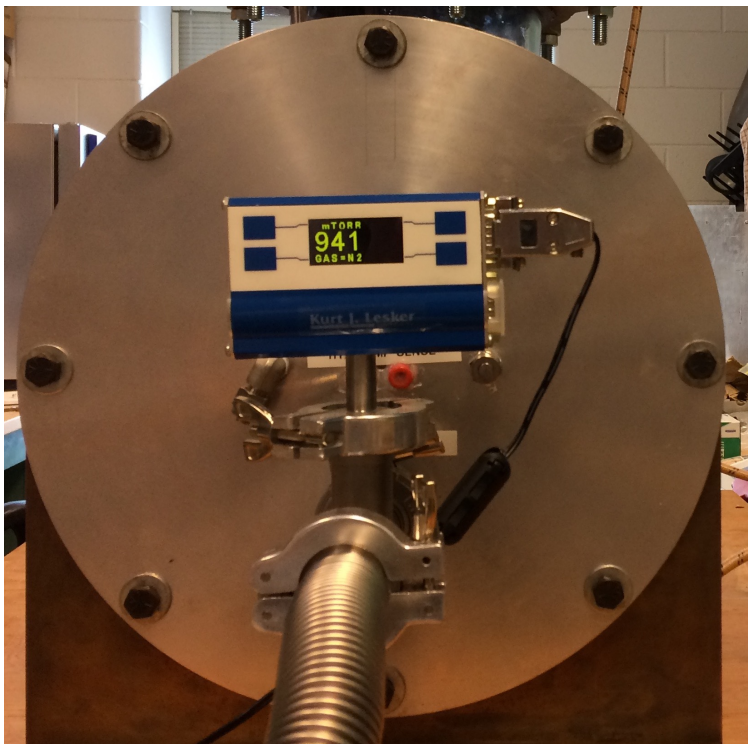


Figure 3.10: KJLC 300 Series pressure gauge.

gauge is factory calibrated for nitrogen gas, and was used to determine the pressure in the chamber during a permittivity measurement. The vacuum hose attached to the same QF25 tee nipple was

then attached to an nXDS10i Edwards rotary scroll pump that was used to evacuate the air in the sealed chamber. All vacuum connections were periodically cleaned and lubricated with vacuum grease. The lowest pressure that was reached over the course of the use of the environment chamber was roughly 400 mTorr. Atmospheric pressure is roughly 760 Torr, so a pressure of 400 mTorr is greater than three orders of magnitude reduction in the air pressure inside the chamber. The highest pressures in the chamber during a permittivity measurement were roughly 950 mTorr. According to the phase diagram for water, at pressures below 950 mTorr water exists in a vapour state above 0.01° C (Lemmon et al., 2017). By this logic, any water that has adsorbed to the sample inside the coaxial airline will be removed as the gases inside the chamber are pumped out through the roughing pump. Capillary water is subject to stronger intermolecular forces and may stay in a liquid phase at lower pressures. The change in relative humidity between the ambient laboratory atmosphere and the evacuated chamber was not directly measured. Regardless of how much water was removed from the sample in the environment chamber, it is likely that there was no further adsorption of water to the sample as long as the roughing pump was turned on. It was observed for all permittivity measurements conducted in the environment chamber that the real part of the permittivity decreased with increasing time in the low pressure atmosphere. In tests conducted on oven dried serpentine samples by Alexandre Boivin it was observed that the decrease in the permittivity levelled off after approximately 2 hours under vacuum, and that this time was sufficient in removing adsorbed water from the sample (Boivin et al., 2018). A duration of 2 hours was then adopted as the standard time required to remove adsorbed moisture from the samples prior to a permittivity measurement. For permittivity measurements of oven dried aluminium oxide samples that were performed in the chamber, the difference between the permittivity of the sample under low pressure for 1 hour and two hours were within the estimated uncertainty of either measurement. As such, permittivity measurements on samples in low pressure for 1 hour were considered identical to those in low pressure for 2 hours.

3.5 Heating Mechanism

The polarization mechanisms responsible for the storage and loss of electrical energy in a medium are temperature dependent, since the thermal motion of the particles and dipoles will change with temperature. This dependency varies with the thermal behaviour of different materials. The real and imaginary parts of the permittivity can increase or decrease with increasing temperature; how-

ever, most of the change seems to occur at low frequencies (< 1 MHz) (Chen and Hunter, 2004; Nelson and Bartley Jr, 2000; Napijalo et al., 1998). To model the permittivity as a function of temperature, the time constant of relaxation, τ , is often described with a Boltzmann temperature dependence (Stillman, 2006; Brouet et al., 2019). From the perspective of planetary radar astronomy, surface regolith of airless bodies can exhibit a wide range of surface temperatures over a diurnal cycle. As a result, the received radar echoes from a given surface can change depending on the surface temperature at the time of observation. For NEA (101955) Bennu, the target of NASA's *OSIRIS-REx* mission, surface temperatures can reach as high as 117° C in its current orbit, and may have been as high as 227° C in the recent past (Lauretta et al., 2015). A heating and temperature control mechanism was then desired in the permittivity measurement methodology established in this research in order to characterize the dependence of sample permittivity on temperature.

In the preliminary design of this heating mechanism it was identified that the simplest setup would consist of heating tape and a temperature sensor attached to the coaxial airline, which could then be controlled by a temperature controller. Restrictions on the size of available heating tape, as well as the minimum allowed bending radius, constrained the use of heating tape to the 14 mm outer diameter, 15 cm length GR900-LZ coaxial airline. Kapton[®] flexible heating tape capable of reaching temperatures of $+120^\circ$ C were used. Originally, self-adhesive versions were applied, but it was immediately obvious that the curvature of the outside of the coaxial airline was such that the corners of the heating tape were repeatedly peeling off. Thermal epoxy was then applied to non-self-adhesive heating tape to maintain contact with the airline. A self-adhesive Omega SA1-RTD-4W resistance temperature detector (operable from -70° C to $+260^\circ$ C) was attached to the airline opposite the heating tape, also using thermal epoxy. To control the heating tape, an Omega CNi8 series temperature controller was utilized. The heating tape was connected to the output of the temperature controller, and the RTD connected to the input. The temperature controller utilizes proportional-integral-derivative (PID) control that can be auto-tuned to control how much current is supplied to the heating tape, and thus controlling what temperature the sample is maintained at, as read by the RTD. The basic heating mechanism, assembled outside of the environment chamber but using the sub-D connection electrical feedthrough, is shown in Figure 3.11. The same 14 mm outer diameter, 15 cm length GR900-LZ coaxial airline was used by Alister Cunje in permittivity measurements conducted in a freezer at low temperatures, since the attached RTD was capable

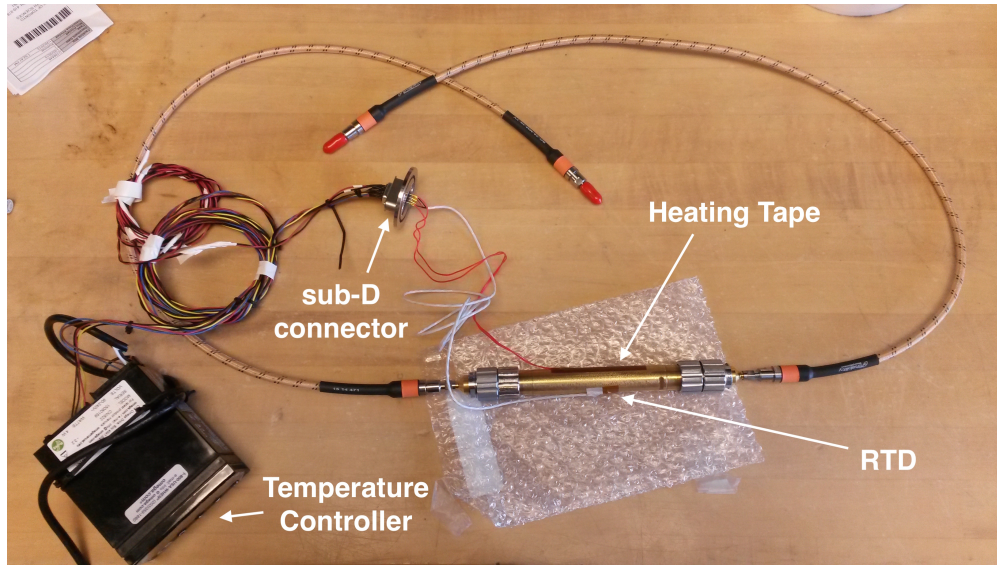


Figure 3.11: Annotated heating mechanism incorporated into permittivity measurement setup. The wire leads were eventually soldered to sub-D connectors.

of measuring the airline temperature during measurement. After repeated use of the airline, the wires connected to the RTD broke. A second RTD was then attached, but this time thermal epoxy was not used, as the old epoxy was not easily removable and the available surface area with which to attach temperature components was limited. Instead, the heating tape and RTD were both attached to the exterior of the airline using a layer of aluminium tape and then duct tape. At the temperatures that the airline was expected to be subjected to, these tapes are sufficient. Furthermore, the tape was able to secure the wires connected to both the heating tape and the RTD to reduce strain on the connections to the actual resistive elements, prolonging the life of the system.

As this research project evolved, the focus was aimed at investigating the usefulness of different mixing equations at room temperature, and did not further explore the use of the heating mechanism for measurements. The setup was utilized by Alexandre Boivin to remove adsorbed water from temperature-sensitive samples that could not be oven dried at high temperatures. By placing the sample in the airline in the environment chamber at low pressure, the airline was subjected to a lower temperature of 40°C using the heating mechanism, which was adequate in removing water from the sample (Boivin et al., 2018). The permittivity of the samples in Boivin et al. (2018) were measured at room temperature and at 40°C , and so it was necessary to determine if the permittivity measurement process itself was affected by elevated temperatures. A simple experiment was performed to determine if this would pose an issue. First, based on the thermal

properties of the airline (composed of brass) and the airline volume, the expected volume expansion of the airline at 120° C was calculated to be less than 1%. Next, the permittivity of air was measured from room temperature to 90° C at 10° C increments, which should be stable, to see if there were any effects on the rest of the equipment. Figure 3.12 shows the results of these measurements, where the maximum standard deviation (between the room temperature and 90° C measurement) was 0.005, which was within the measurement uncertainty of the setup. From both of these conclusions, it

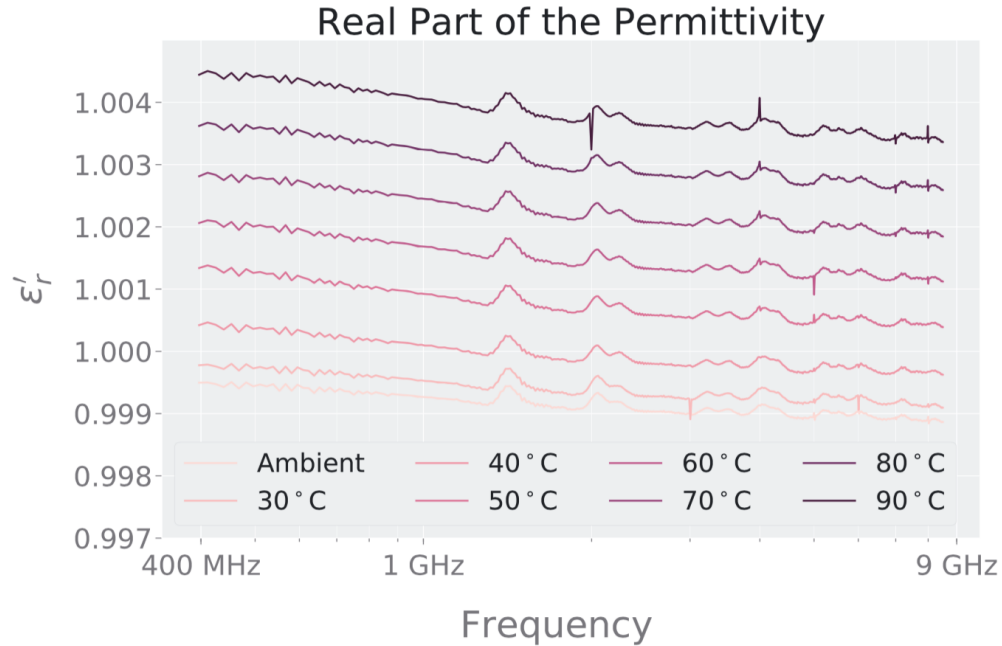


Figure 3.12: *Figure taken from (Boivin et al., 2018) with the following caption:* Measurements of the empty transmission line in vacuum at different temperatures. A very slight increase in ϵ_r' can be seen with increasing temperature attributed to error due to thermal expansion of the brass transmission line. Note the log scale on the frequency axis.

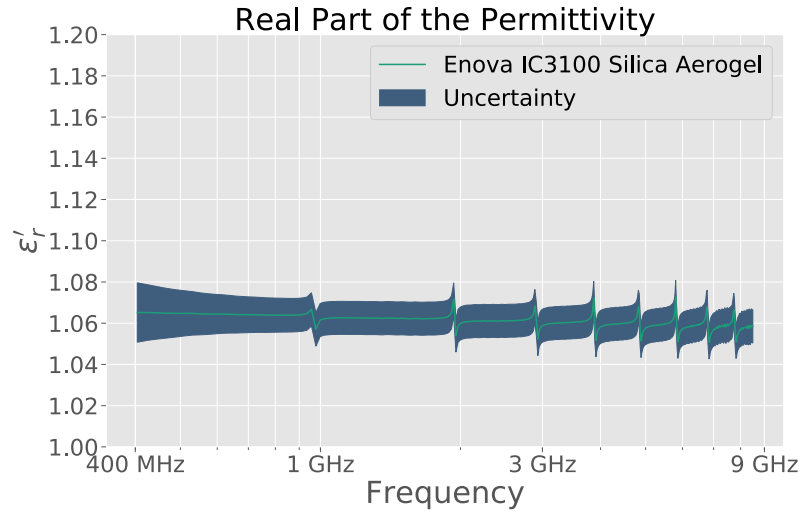
was decided that the elevated temperatures did not adversely affect the permittivity measurement setup, and that changes in the permittivity measured at elevated temperatures were indicative of the sample properties.

3.6 Silica Aerogel

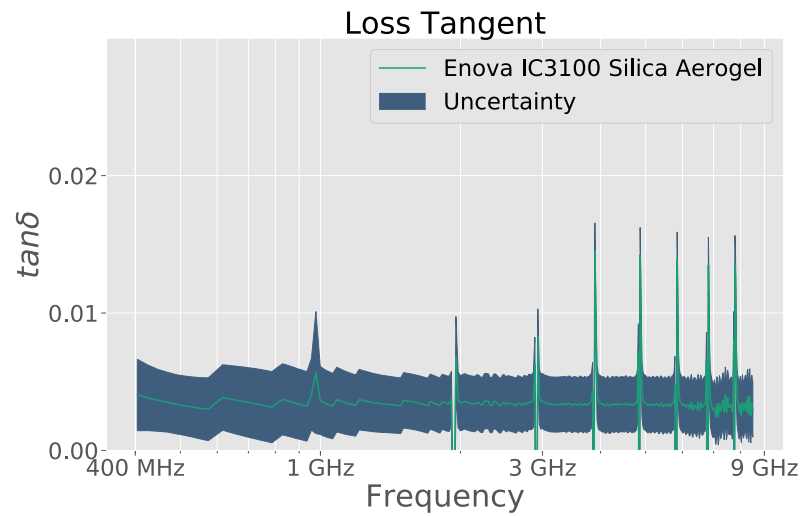
In order to compare the accuracy of the mixing theories considered in this research, it was necessary to measure the permittivity of each sample as a function of porosity. Tests performed in Sotodeh (2014) using the custom filling funnel to pack powder samples in the coaxial airline showed that the sample reaches an asymptotic limit of porosity within a few minutes of vibration, which is within

the amount of time it takes to completely fill the airline. As a result, repeated measurements of the same powder sample, with a given particle size distribution, result in very similar porosities. Dr. Michael Daly offered the idea of incorporating silica aerogel particles into the powder samples to artificially increase the void space, and thus the porosity. Silica aerogel is a synthetic polymer composed of silica (SiO_4) that is highly porous, consisting of 95 - 99% empty space (Soleimani Dorcheh and Abbasi, 2008). This extremely high porosity gives silica aerogel unique material properties, such as low thermal and acoustic conductivity, and low complex permittivity (Gurav et al., 2010). Silica aerogel has a legacy of use in space applications, being a key component of NASA's *Stardust* mission to capture small hypervelocity particles from a cometary tail, and in use as thermal insulation on NASA's *Mars Pathfinder* mission (Jones, 2006).

The extremely low complex permittivity of silica aerogel is due to the amount of empty space that makes up the bulk material, since silica has a real part of the permittivity of ≈ 4.5 (Soleimani Dorcheh and Abbasi, 2008; Olhoeft, 1981). This can be seen from the application of any mixing theory to a two-phase silica aerogel composite that is made up of silica and air with a conservative porosity of 95%. Hrubesh and Pekala (1994) performed measurements of the complex permittivity of silica aerogel and found the material to behave electrically as a gas, and its effective permittivity was dominated by the pore spaces. The measurements were made on both oven dried and ambient (left in regular atmosphere) samples in a resonant cavity from 2 GHz - 40 GHz. It was found that the real part of the permittivity varied linearly with density from 0.01 g/cm^3 to 0.6 g/cm^3 with slopes of 1.60 and 1.48 for the ambient and oven dried samples respectively, and that water contributed to 70% of the measured loss tangent. The silica aerogel that was used in the current research is Enova IC3100 particles ranging in size from 2 - 40 μm with a particle density of $0.12 - 0.15 \text{ g/cm}^3$ (Cabot Corporation, 2017). Using the linear model from Hrubesh and Pekala (1994), at this density the solid permittivity of the aerogel is estimated as $\epsilon'_r \approx 1.2$. A permittivity measurement of the ambient silica aerogel particles was carried out to verify this (Figure 3.13). From the measured bulk density, the porosity of the sample was roughly 75%. The reason that this is lower than the expected porosity is likely due to water retained by the sample, since the sample was not oven dried. From Figure 3.13 it can be seen that the silica aerogel is dispersionless, and the frequency-averaged real part of the permittivity and loss tangent are $\epsilon'_{r,\text{aerogel}} = 1.059 \pm 0.008$ and $\tan \delta = 0.003 \pm 0.003$. From this measurement and the results from Hrubesh and Pekala (1994), it was concluded that the addition of the silica aerogel to a powdered mineral sample to increase the void space was valid,



(a) Real part of the permittivity.



(b) Loss tangent.

Figure 3.13: Measured permittivity and loss tangent for silica aerogel used in this study. Note the pronounced measurement spikes at resonant frequencies due to the very low loss of the material.

and the silica aerogel would behave the same as the air filled voids. By making use of the silica aerogel in repeated measurements of the samples, the total range in porosity across all measured samples was from 30% - 70%. The silica aerogel was added in small increments to each sample over the course of the permittivity measurements (Figure 3.14). The aerogel was mixed with mineral

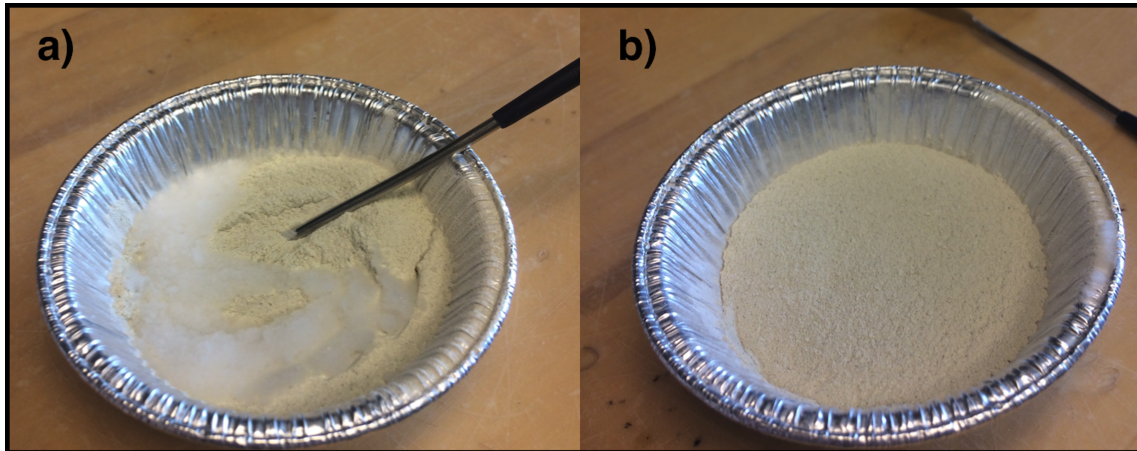


Figure 3.14: *Figure taken from (Hickson et al., 2018) with the following caption: a) Powdered dunite with silica aerogel prior to mixing. b) Resulting dunite/silica aerogel mixture.*

samples by mechanical stirring. The resulting sample was not mixed well if the mineral grain size was significantly larger than the aerogel (effect was observed for $\approx 200 \mu\text{m}$ average grain size). This did not pose an issue for the samples in this research, since the grain size of the mineral samples was kept low to reduce boundary effects in the coaxial airline at the sample conductor interface.

3.7 Software

To collect, process, and analyze the data used in this research, several software packages were used, both commercial and developed throughout the research. This section will discuss the major software packages that were used.

3.7.1 METAS VNA Tools II

The VNA can be controlled by external buttons and built in software. For better control of the VNA, Alexandre Boivin incorporated the METAS VNA Tools II software package for use with the permittivity measurement methodology, which was then used for the measurements presented in this thesis (Boivin et al., 2018; Wollensack et al., 2012). This is advantageous as it can track sources of uncertainty, log operations, and provides alternate calibration techniques. The settings

and calibration data that were input to METAS VNA Tools II were established by Alexandre Boivin.

3.7.2 *permittivitycalc*

Several programmed scripts were developed over the course of this research and by collaborators for the processing of the raw data (measured S-parameters and uncertainties) output by the VNA and METAS VNA Tools II software. These scripts were based off of the original MATLAB[®] code used in Sotodeh (2014), and were expanded on and consolidated into the open source Python package *permittivitycalc* (Boivin and Hickson, 2018). Contributions to developing the initial scripts were made by Alister Cunje, Brian Tsai (from the Department of Physics at the University of Toronto), and Alexandre Boivin. Alexandre Boivin then developed the majority of the *permittivitycalc* package, with some minor contributions resulting from the current research. This package includes many functions and tools for analyzing the raw data, and for processing the data in different ways. At the time of writing this thesis, the package can apply the NRW algorithm and the Boughriet et al. (1997) algorithm to the S-parameters measured by the VNA. When applying these algorithms, *permittivitycalc* calculates the complex permittivity from both the forward $S_{11,21}$ and reverse $S_{22,12}$ S-parameters and compares the results to check for the homogeneity of the sample in the airline. If the results are significantly different from one another, the sample is not homogeneous and the software will give some simple statistics regarding this difference and corresponding degree of heterogeneity. Corrections can be applied to the data that account for the boundary effects of the coaxial airline, the influence of the teflon washers on the measured effective permittivity (de-embedding), and for the specific dimensions of the coaxial airline used for a given measurement. The package includes functions that create publishable plots and figures from the data, which can include multiple permittivity measurements of different samples. *permittivitycalc* can normalize a permittivity measurement to some bulk density using standard techniques for comparison between measurements made at different densities. The software also automatically calculates the frequency-averaged real part of the permittivity, imaginary part of the permittivity, and loss tangent from roughly 1 GHz - 9 GHz (for the GR900-LZ coaxial airlines from the current research). To avoid the influence of the resonance spikes in this averaging, the values for the parameter of interest are taken from the nearest midpoint frequency between resonant frequencies (calculated from (3.12), where median values used as estimates for ϵ'_r and ϵ''_r). These midpoint values are taken past the first two resonant frequencies, which roughly corresponds to the 1 GHz - 9 GHz frequency range.

Depending on the dispersion of a given sample, these frequency-averaged values are possibly valid at lower frequencies. The *permittivitycalc* package was used to analyze all of the data presented in this research, as well as to create all of the plots of permittivity measurements.

3.8 Calibration

The coaxial transmission line method is subject to three general sources of measurement error, termed systematic error, random error, and drift error (KeysightTechnologies, 2014a). Random error, or VNA instrument noise, cannot be removed with any calibration and is inherent to a given VNA. Systematic errors are defined as predictable, arising from minor defects in the coaxial cables, coaxial adapters, and VNA used for a measurement. This bias can be removed from the final measurement if it is initially characterized for a given set of equipment by calibrating that equipment prior to measurement. The systematic error in a two-port VNA measurement is typically described by a 12-term error model, with each term representing a source of systematic error for a given measurement direction (forward or reverse S-parameters) (Rytting, 2001). A full 2-port calibration of the VNA, coaxial cables, and coaxial adapters will determine the values for these terms so that the error model can be applied to correct a subsequent material measurement. The SOLT technique, or Short, Open, Through, and Load method is widely used and was implemented in Sotodeh (2014), and so was initially used to correct measurements performed in the current research (KeysightTechnologies, 2014a). In this calibration, a Short (out of phase 180°) and Open (in phase) calibration standard are measured for each port, representing an ideal perfect reflection of the source signal. A Load ($50\ \Omega$) calibration standard that matches the characteristic impedance of the VNA and cables ($50\ \Omega$) is measured for each port as well, representing ideal zero reflection. Finally a measurement is made with port 1 connected to port 2 (Through), representing ideal transmission. The METAS VNA Tools II software then uses these measurements to solve for the error terms in the error model, which is then applied to calibrate any further measurements. Alexandre Boivin implemented the use of the Through-Reflect-Match (TRM) calibration into the measurement setup, since the TRM calibration requires fewer calibration measurements (fewer standards) and is comparable if not improved in accuracy compared to the SOLT calibration (Pulido-Gaytán et al., 2015; KeysightTechnologies, 2014a). The TRM calibration requires a measurement of a Short and Load standard for each port, and one Through measurement. The calibration standards used in this research were included in the General Radio 900-LZ series Reference-Airline set. The cali-

bration standard definitions, and input parameters to the METAS VNA Tools II software required for TRM calibration, were implemented by Alexandre Boivin. The TRM calibration was applied prior to all permittivity measurements in this research unless otherwise stated. After calibration, the measurement plane where the S-parameters are recorded is at the coaxial adapter/coaxial air-line connection interface. Ideally the measurement plane is at the interface with the sample under measurement, not the Teflon[®] washer. The measurement plane can be artificially moved to this interface post-measurement in a step called de-embedding (KeysightTechnologies, 2014b). Alexandre Boivin implemented this correction in the *permittivitycalc* package, which was then applied to all of the measurements in the current research (Boivin and Hickson, 2018).

3.9 Uncertainty in the Complex Permittivity

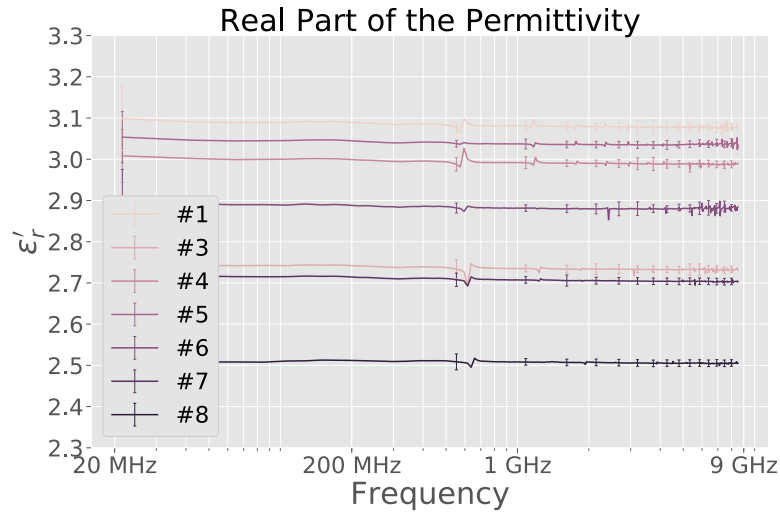
3.9.1 Type A and Type B Uncertainty

The uncertainty in the measured S-parameters is output from the METAS VNA Tools II software after the calibration is applied to the raw data. The sources of this uncertainty can be tracked in the METAS VNA Tools II software, and is made up of error associated with connector repeatability, VNA noise, VNA linearity, VNA drift, and cable stability (Boivin et al., 2018). Alexandre Boivin performed a series of measurements to characterize each of these sources of error for the permittivity measurement setup (including the environment chamber), and then used these to define the errors in the METAS VNA Tools II software that are applied to all other measurements. This uncertainty is then propagated in the calculation of the complex permittivity according to the error propagation equations in Boughriet et al. (1997) and Baker-Jarvis et al. (1993) for the Boughriet et al. (1997) and NRW algorithms respectively. Alexandre Boivin characterized the total error in a permittivity measurement as combinations of Type A and Type B uncertainties as defined by the ISO Guide to the Expression of Uncertainty in Measurements (Boivin et al., 2018; ISO/IEC GUIDE 98-3, 2008). The propagated error in calculating the complex permittivity from the S-parameters is the Type B error. Type A error for the real and imaginary parts of the permittivity is defined as the maximum standard deviation between 10 separate measurements (performed by Alexandre Boivin) of a solid Rexolite[®] sample across all measured frequencies. Rexolite[®] is a standard dielectric material, and as a solid sample should yield high precision results. The total uncertainty is then the Type A and Type B uncertainties added in quadrature. The Type A uncertainty in the real part of the permittivity was found to be 0.008, and for the loss tangent was defined in two regions: below 100

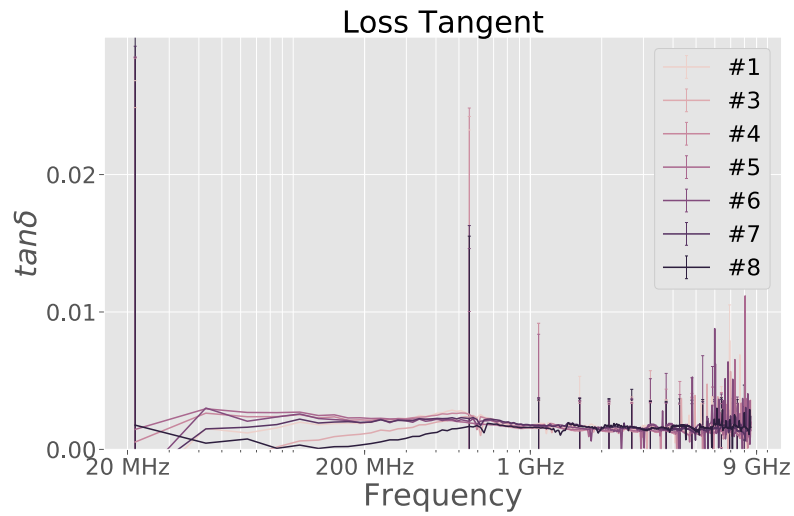
MHz the uncertainty is 0.009, above 100 MHz the uncertainty is 0.002. The Type A error was found to be higher than the Type B error for all measurements, so that the lowest error achieved was 0.008 and 0.002 in the real part of the permittivity and loss tangent.

3.9.2 Type A Uncertainty for Powder Samples

The Type A uncertainty described above was derived from repeated measurements of a solid standard dielectric sample, and is therefore applicable to measurements of similar samples for which you can expect similar repeatability. The repeatability of a powder sample measurement is lower than for a solid sample, since there will be a greater change in the homogeneity and distribution of the sample between measurements. These different distributions will cause the bulk density to change slightly, which will change the measured permittivity. Assuming that the difference between any two measurements is only due to the change in the density of the samples, all repeated measurements of a given powder sample should be able to be normalized to the same bulk density and permittivity. The standard deviation between a normalized set of measurements for a given sample thus represents the repeatability due to influences such as changes in moisture content, particle packing, and Teflon[®] washer positioning. The Olhoeft and Strangway (1975) equation ($\epsilon_{eff} = (1.93 \pm 0.17)^{\rho^{bd}}$) is most often used to normalize measurements with respect to density (Olhoeft and Strangway, 1975; Stillman, 2006; Stillman and Olhoeft, 2008; Boivin et al., 2018). In the current research it was found that if instead, the normalization is carried out using a mixing equation that has been optimized to fit that particular set of measurements, the convergence to a common permittivity value is improved and the standard deviation decreases (Figures 3.15 - 3.17). As will be illustrated later, most of the mixing theories discussed in this thesis can model a set of permittivity measurements equally well. By adjusting the solid permittivity input to a given mixing theory, that theory can be forced to fit the measurements, in some cases with unrealistic values that deviate from the literature. The Type A uncertainty assumed for a given powder sample measured in this research is defined as the averaged (across frequency) standard deviation between the normalized set of measurements for that sample, where the mixing equation used to normalize the measurements is the LLL equation that has been optimized to fit the data.

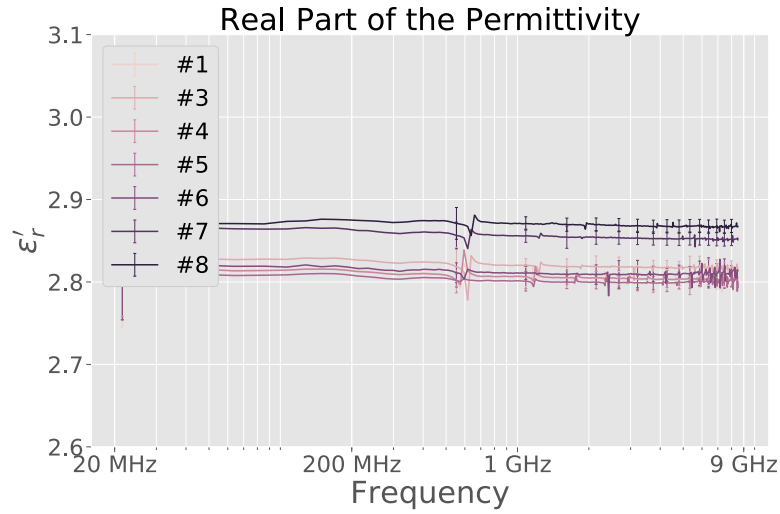


(a) Real part of the permittivity.

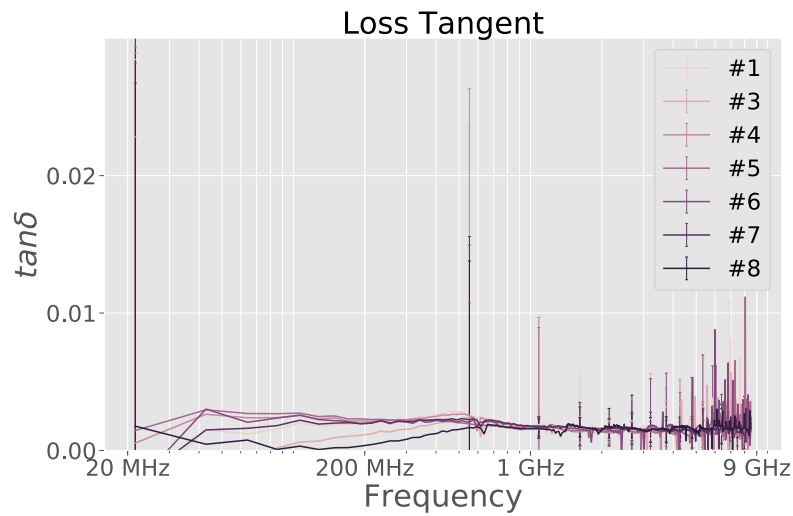


(b) Loss tangent.

Figure 3.15: Raw forsterite sample data set (un-normalized) (average standard deviation of 0.193).

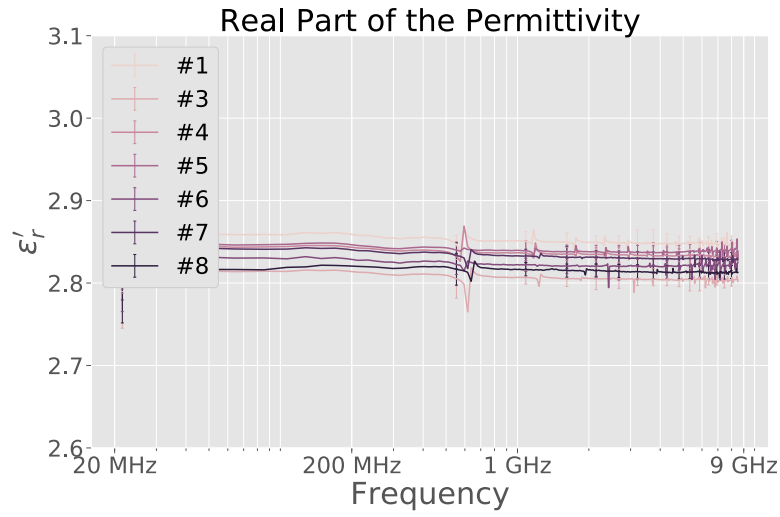


(a) Real part of the permittivity.

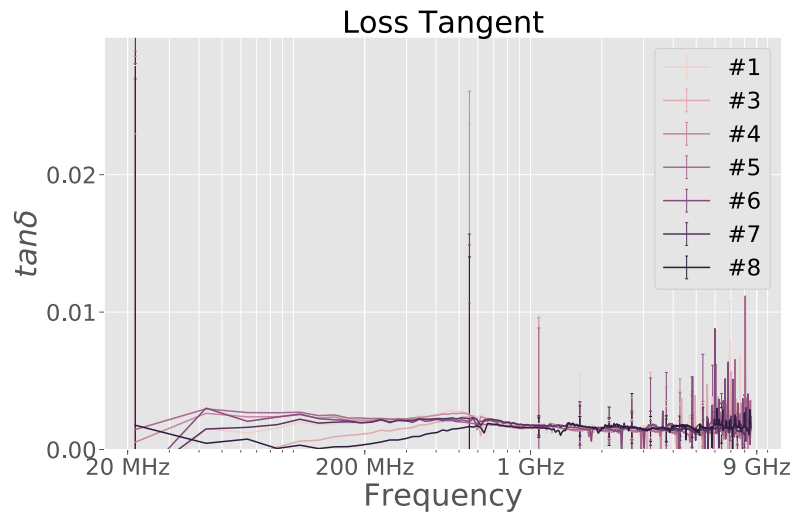


(b) Loss tangent.

Figure 3.16: Forsterite dataset normalized to a bulk density of $\rho_{\text{bd}} = 1.60 \text{ g/cm}^3$ using the Olhoeft and Strangway (1975) equation (average standard deviation of 0.025).



(a) Real part of the permittivity.



(b) Loss tangent.

Figure 3.17: Forsterite dataset normalized to a bulk density of $\rho_{bd} = 1.60 \text{ g/cm}^3$ using the LLL equation, with the input parameter ϵ_i optimized through non-linear least squares regression to fit the dataset (average standard deviation of 0.014).

3.10 Basic Workflow

The general procedure that was followed for the permittivity measurement experiments carried out in the current research is outlined in Figure 3.18. The VNA was turned on at least 1 hour prior to

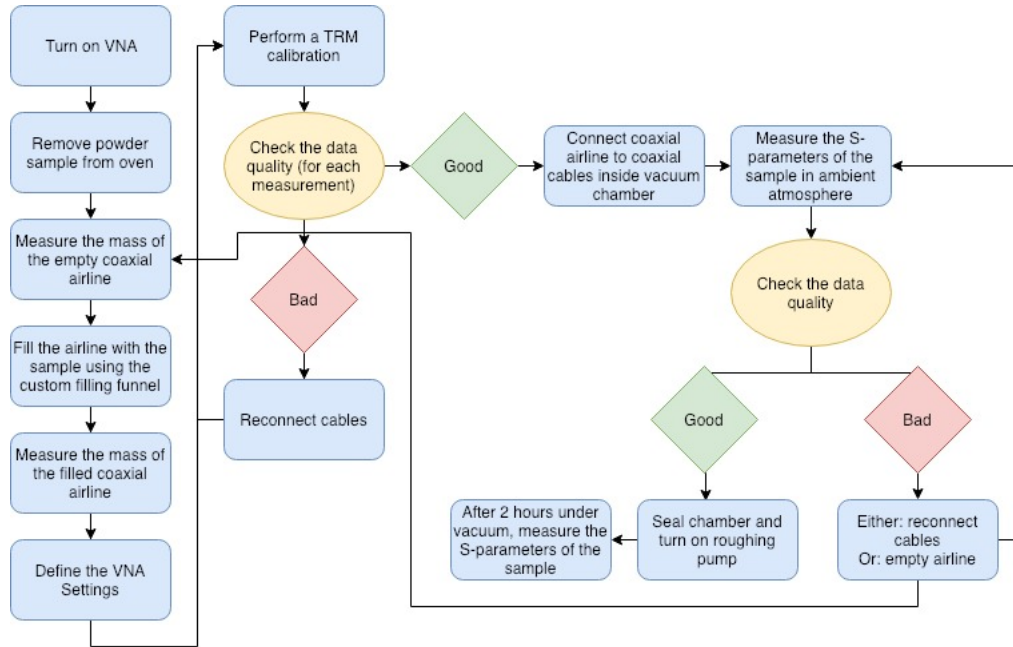


Figure 3.18: Workflow for the permittivity measurements.

its use to allow the internal electrical components to heat up to a constant temperature. The mass of the empty and filled airline is used to calculate the mass of the sample, which with the known volume of the coaxial airline allows the calculation of the bulk density of the sample. The VNA settings were kept constant for the permittivity measurements in this research. The intermediate-frequency bandwidth was set to 10 Hz for detailed spectral information. The power was chosen as -10 dB, as this results in the highest accuracy in the measured S-parameters for the VNA used (KeysightTechnologies, 2016). The recorded S-parameters were an average of five measurement sweeps of the sample. The highest frequency for the sweep was 8.5 GHz, corresponding to the highest frequency in the coaxial airline. Lastly, the number of frequency points for the recorded S-parameters was chosen as 601, being a trade off between frequency resolution and measurement time. The TRM calibration was performed with the environment chamber incorporated into the VNA circuit. The METAS VNA Tools II software displays the result of each measurement of a calibration standard performed. If the measurement showed obvious signs of error, often in the form of erroneous spikes due to an improper connection, the connection was re-established and

the measurement was repeated. Once the TRM calibration was completed successfully, the coaxial airline was connected to the coaxial cables in the environment chamber. An initial measurement in ambient atmospheric conditions was completed to check the overall quality of the data. If the data quality was poor, the connections were re-established and the measurement repeated. If the data was still poor, this was likely a result of improper washer placement, or some other filling error, and the airline was emptied of the sample and the process started over again. If the data quality was good, the environment chamber was sealed and the roughing pump left on for two hours before the final permittivity measurement was completed.

Chapter 4

Sample Characterization and Preparation

4.1 Techniques to Characterize and Prepare Samples

The powdered geologic samples used in the research presented in this thesis were analyzed using a variety of instrumentation and then prepared for measurement of their complex permittivity. This analysis was necessary to determine the composition, particle size distribution, and particle density for each sample. These parameters are used to understand and model correlations observed in the permittivity measurements.

4.1.1 Sample Comminution

The initial state of the samples used in this study varied from manufactured powder to natural cohesive rocks. For some samples it was necessary to comminute the samples to the desired powder particle size. This particle size was determined to be $20 \mu\text{m} < x < 200 \mu\text{m}$ by the boundary effects in the airline, which will be discussed in chapter 5, and the homogeneous mixing criteria with silica aerogel. At this size the particles are small enough that boundary effects are minimized and homogeneous mixing with silica aerogel is possible, while the particles are large enough to not pose a significant health hazard during handling (a dust mask or respirator was used for all handling of samples regardless).

Some of the samples were obtained as large, cohesive rocks that needed to be broken down into smaller pieces in order for further processing into powders. A Metkon[®] Instruments Inc. Geocut Petrographic Cutter was used to cut small pieces from the overall sample for the larger samples. The necessary particle size for use of the ball mill was roughly a few centimetres in diameter, so

these small pieces of samples were further broken down using a petrographic rock hammer. Care was taken to clean the surfaces of the cutter and hammer with isopropyl alcohol before and after use.

Once the sample grains were in the centimetre size range, they were further pulverized to the desired $20 \mu\text{m} < x < 200 \mu\text{m}$ particle size range. For the softer samples, such as the dunite and dolomite samples, an aluminium oxide ceramic mortar and pestle was used for this purpose. The aluminium oxide composition was desired as a metal mortar and pestle might contaminate the sample with metal particles which would significantly affect the effective permittivity of the sample. Harder samples, such as the labradorite, were pulverized using a Retsch[®] PM100 Planetary Ball Mill, with aluminium oxide grinding balls and grinding jar. Each sample was pulverized using either the mortar and pestle or ball mill in increments, with the resulting particle size analyzed in between. Once the particle size was close to the desired range of $20 \mu\text{m} < x < 200 \mu\text{m}$, the process was complete.

4.1.2 Mass Balance

Throughout the presented research it was necessary to accurately measure the mass of the samples and experimental apparatus used. This was completed using two identical Sartorius MSA524P-100 DI Cubis Precision Balances, one at the University of Toronto and one at York University, which is accurate to $\pm 0.0001 \text{ g}$ and $\pm 0.0005 \text{ g}$, depending on the total mass being weighed (the higher the mass, the lower the accuracy).

4.1.3 Particle Size Distribution

The particle size distribution (PSD) of each sample was determined by separating the sample by particle diameters with a Gilson Performer III Sieve Shaker and corresponding sieve screens. The sieve sizes were ASTM size #60, #100, #170, #325, and #500, corresponding to mesh screen sizes of $250 \mu\text{m}$, $150 \mu\text{m}$, $90 \mu\text{m}$, $45 \mu\text{m}$, and $25 \mu\text{m}$. The sieves were assembled on the Gilson Performer III Sieve Shaker, with the sample poured in small batches and left to vibrate for roughly 10 minutes at a time. The mass of the sample retained by each sieve was then used to determine the PSD.

The average particle diameter of a sample was of interest in this research for studying boundary effects at the sample/conductor interface during a permittivity measurement. Permittivity measurements of aluminium oxide grit from Kramer Industries, Inc. taken from Sotodeh (2014) were

used to model these boundary effects. In Sotodeh (2014), different aluminium oxide samples with varying average particle sizes were used, and it was observed that there was a correlation between the porosity and grain size of the samples. Unfortunately, it was not specified in Sotodeh (2014) how the average particle size was determined. The PSD of each different aluminium oxide sample is defined by Kramer Industries, Inc. according to ANSI Testing Methods (ANSI B74.12.2001). This size grading standard is commonly used for abrasive materials, and defines a range in particle diameters for which 65-75% of the sample conforms to, including the median particle size (Unified Abrasives Manufacturers' Association, 2018). This analysis gives some metric for the range expected for the average particle size, but does not coincide with the specific values from Sotodeh (2014). Instead it was found in the current research that the average particle sizes from Sotodeh (2014) matched well with the average value of a Gaussian distribution fit to the PSD of a test batch of a given aluminium oxide sample provided by Kramer Industries, Inc (fitting performed using the Python package *LMFIT* (Newville et al., 2014)). Figure 4.1 shows the Gaussian fit for the #120 mesh test batch aluminium oxide sample from Kramer Industries, Inc., where the values chosen for the particle sizes in the PSD are taken as the size of the sieves used in the analysis (the left side of the bins in Figure 4.1). The average grain sizes reported in Sotodeh (2014) are compared with

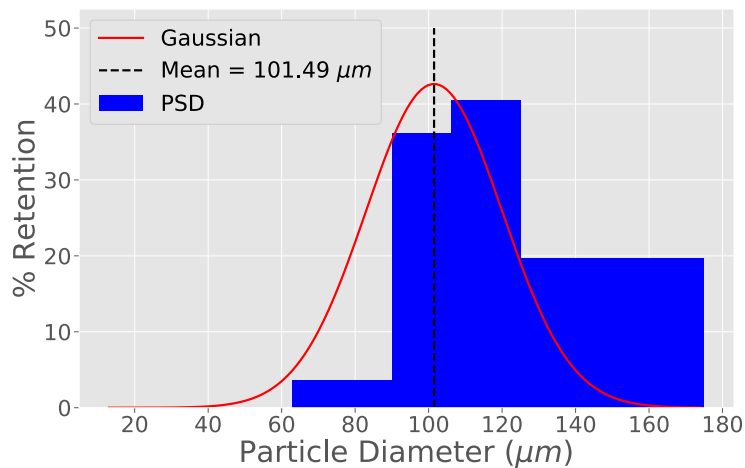


Figure 4.1: Gaussian distribution fit to PSD from Kramer Industries, Inc. for #120 mesh alumina sample.

the averages calculated from fitting Gaussian distributions to the Kramer Industries, Inc. PSD in Table 4.1. Since the particles retained by a given sieve will span the range in sizes permitted by

the bounds of the upper and lower sieve (i.e. the samples retained in the 90 μm sieve will range from this size to the size of the sieve in which they passed through, which for the 150 μm sieve results in particles in size ranging from 90 μm - 150 μm), it is more physically realistic instead to fit the Gaussian distribution to the average particle size between the sieve sizes. The results

Table 4.1: Average particle size determined through Gaussian fitting to PSD's compared with those reported in Sotodeh (2014). Particle sizes taken as the sieve sizes for regular Gaussian fit, and particle sizes taken as average between bin sizes for adjusted Gaussian fit.

Kramer Industries, Inc. Sample	Sotodeh (2014) avg. particle size (μm)	Gaussian fit avg. particle size (μm)	Adjusted Gaussian fit avg. particle size (μm)
#180 mesh	76	no fit	no fit
#120 mesh	102	101.5	118.4
#80 mesh	165	168.4	185.3
#54 mesh	305	303.6	328.6
#36 mesh	483	484.1	520.6
#24 mesh	686	715.1	756.7
#20 mesh	940	963.9	1029.1

of these fits will be called adjusted Gaussian fits and are also shown in Table 4.1. The adjusted Gaussian fit for the #120 mesh alumina sample is shown in Figure 4.2. Figure 4.3 shows a com-

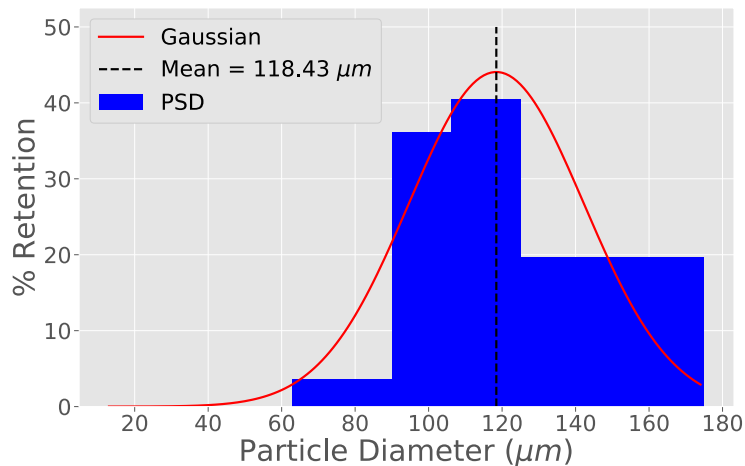


Figure 4.2: Adjusted Gaussian distribution fit to PSD from Kramer Industries, Inc. for #120 mesh alumina grit.

parison of the ANSI B74.12.2001 size grading standard particle size ranges and the average particle

size estimated in Sotodeh (2014) and the adjusted Gaussian fitting method used in the current research. The particle size estimates from Table 4.1 (the Sotodeh (2014) and adjusted Gaussian

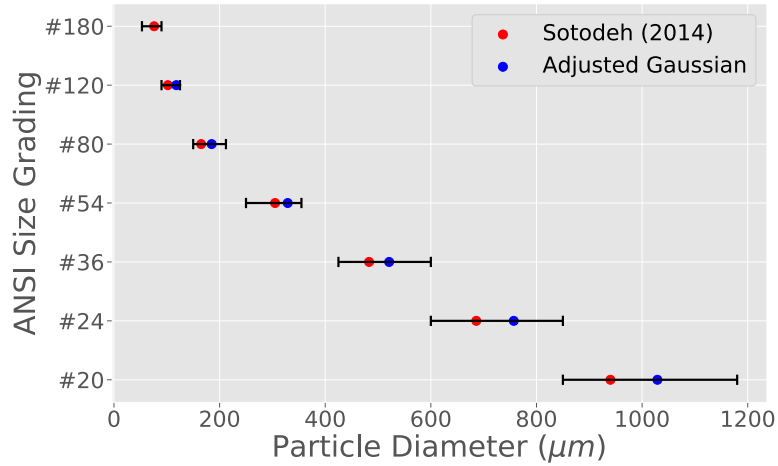


Figure 4.3: ANSI B74.12.2001 size grading standard particle size ranges compared to average particle size estimates from Sotodeh (2014) and using the adjusted Gaussian fit.

fits) fall within the ANSI B74.12.2001 size grading standard particle size ranges, validating the equivalency between the different methods. The PSDs of the samples in this research are fitted with an adjusted Gaussian distribution to estimate the average particle size. The significance of any Gaussian fit is questionable since the number of data points, or sieve sizes, is low. On the other hand, the correspondence with the average particle sizes from Sotodeh (2014) makes this method a way to characterize the average particle sizes of other samples and apply the same boundary effects model that was developed from the Sotodeh (2014) dataset. Carrier et al. (1991) used the following equation for calculating the mean particle size, \bar{x} , from a cumulative frequency distribution (CDF) of particle sizes for a sample:

$$\bar{x} = \frac{\sum pm(\phi)}{100} \approx \frac{\phi_{16} + \phi_{50} + \phi_{84}}{3} \quad (4.1)$$

In equation (4.1) p is the percent fraction of a sample for a size interval whose midpoint is $m(\phi)$, where ϕ is dependent on the particle size. Figure 4.4 shows the Gaussian probability distribution function (PDF) plotted along with the cumulative distribution function CDF for the Gaussian function fitted to the #100 mesh alumina sample. In Figure 4.4, the size interval for particle

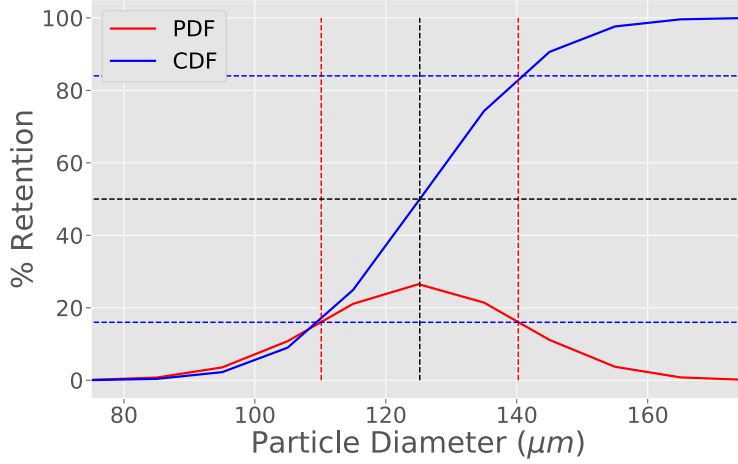


Figure 4.4: Gaussian (not-adjusted) function plotted as PDF and CDF for #100 mesh alumina sample.

diameter is 10 μm , which is significantly smaller than the intervals for the sieve sizes actually used, but allows comparison of the CDF and PDF. The 16% and 84% cumulative retention lines are plotted as blue dotted lines, and the one sigma particle diameter lines are plotted as red dotted lines. Equation (4.1) from Carrier et al. (1991) is equivalent to fitting the PSD with a Gaussian distribution and calculating the average particle size, assuming the particle sizes follow a normal distribution. If ϕ_{16} and ϕ_{84} in equation (4.1) are considered the one sigma interval for the PDF average the following can be written:

$$\bar{x} = \frac{\sum pm(\phi)}{100} \approx \frac{(x_{gauss}^- - \sigma) + x_{gauss}^- + (x_{gauss}^- + \sigma)}{3} = x_{gauss}^- \quad (4.2)$$

Using equations (4.1) and (4.2) on the CDF and PDF calculated from the fitted Gaussian parameters used to make Table 4.1, the results are generally in good agreement across all samples. This test is considered further justification for the use of the adjusted Gaussian distribution to determine average particle size for the samples used in this research.

The statistical significance of the average particle sizes calculated in this way is questionable, as previously mentioned. Regardless, it is a metric that is consistent between the relative average particle sizes between samples, and provides a general idea of the average particle size. The average

particle size is only used in the boundary effects modelling, and as will be shown, this effect is already small for the range in particle sizes for the samples considered, so the inaccuracy of the calculated average particle size will have a small effect on the results of the modelling. For some samples, a smaller quantity of material resulted in very narrow PSDs with material only retained in the #170 and #325 (90 μm and 45 μm) sieves. In these cases the average particle size was determined as a mass average of the amount retained in each sieve:

$$\bar{x} = p_{120}(120 \mu\text{m}) + p_{67.5}(67.5 \mu\text{m}) \quad (4.3)$$

In (4.3), p_{120} and $p_{67.5}$ are the percent (by mass) of the sample retained in the 90 μm and 45 μm sieves respectively, and these are then multiplied with the average grain size between these sieves and the upper sieve used in the grain size sorting (150 μm and 90 μm respectively).

4.1.4 Scanning Electron Microscope (SEM) / Electron Dispersive Spectroscopy (EDS)

The composition of the samples was generally known at the time the samples were acquired. For the aluminium oxide sample from Kramer Industries, Inc., for instance, the chemical purity of the sample is listed from the manufacturer's website. The compositions of the natural rock samples, however, were not known with the same certainty. The bulk chemical composition for each sample was thus determined using a Tescan VEGA3 SEM equipped with a Bruker Quantax EDS detector in the Planetary Instrumentation Laboratory at York University (Figure 4.5). The EDS detector was calibrated using a copper standard, and was periodically tested with standards such as nickel and copper. Images and spectra were obtained of the original cohesive rock sample for the natural rock samples, and images and spectra were also obtained for all powder samples. For the solid samples, point by point EDS analysis was used to determine the composition of distinct mineral phases observed in SEM images with a backscattered electron (BSE) detector. This was useful in identifying minor mineral phases, but was inadequate at quantifying the amount of these minor phases. A small amount of the powder samples was compacted into pellets for measurement in the SEM. Since a given powder sample may be composed of several mineral phases, the contextual information regarding these phases is lost in the pelletized samples, and so the EDS spectra were obtained over a large area and were interpreted as representing the bulk composition. The EDS spectra are comprised of characteristic X-ray emissions from different elements that have been en-



Figure 4.5: Tescan VEGA3 SEM with Bruker Quantax EDS detector at York University.

energized by the SEM electron beam. Characteristic X-ray emissions for elements can result from several electron orbital energy levels, and in some cases are very close to one another for different elements. In addition, the geometry of the sample relative to the electron beam and EDS detector can skew the obtained spectra, further complicating the analysis of EDS spectra (Lymer, 2017). EDS spectra can be quantified into elemental abundances, albeit with low accuracy, and are considered a semi-quantitative data product. ESPIRIT 2.1 software was used to collect and quantify all EDS spectra using the standardless P/B-ZAF QUANTAX analysis strategy (Bruker Nano GmbH, 2011). From this semi-quantitative analysis, it was possible to constrain mineralogies present in the different samples.

4.1.5 Particle Density

To calculate the porosity of a powder sample contained in a coaxial airline, it is necessary to know both the bulk density and particle (grain, or solid) density. The bulk density of a sample is measured directly for a given permittivity measurement from the known volume of the coaxial airline and the mass of the coaxial airline before and after filling with the sample. The particle density for each sample was determined using a Micromeritics[®] Instrument Corporation Accupyc[®] II 1340 Gas Displacement Pycnometer (Figure 4.6). The pycnometer was used with helium gas, which allows the determination of the skeletal volume of samples down to connected microporosity



Figure 4.6: Micromeritics[®] Instrument Corporation AccuPyc[®] II 1340 Gas Displacement Pycnometer at York University.

as small as a helium gas molecule. Measuring the mass of the sample whose volume was measured, the particle density of the sample was calculated. A capped sample holder was used that permitted measurement of powder samples in the pycnometer. All samples were oven dried at 115° C and kept in a dessicator prior to measurement in the pycnometer, since small amounts of adsorbed water can alter the volume measurement. The pycnometer was calibrated with manufacturer provided calibration standards prior to each measurement.

4.1.6 X-ray Diffraction (XRD)

XRD measurements were carried out for every sample, except the aluminium oxide sample, by the staff at the Royal Ontario Museum (ROM). This process consists of radiating the samples with fixed frequency X-rays over a range of incident angles and measuring the angle of reflection from the sample. The amount of radiation reflected in certain geometries is characteristic of the unique crystal structure of different minerals, and allows the identification of mineral phases present in the sample. The XRD system at the ROM is a Bruker D8 Advance with a Cu source operating at 40 kV and 40 mA with a Linx-eye detector. It is equipped with a twin primary motorized slit of 0.6 mm, nickel filter, and a twin secondary motorized slit of 5.5 mm. The XRD data can be compared with databases containing XRD spectra of known mineral samples to search for the closest matching

spectra. The XRD data from the current research was compared with the RRUFF project database for these purposes (Lafuente et al., 2015). Long XRD acquisition can increase the signal-to-noise ratio (SNR) of the data to the point that mineral quantification is possible from the data; however, this was not applied to any of the samples. XRD data presented in this thesis was collected for the samples by Veronica DiCecco, a technician in the mineralogy department at the ROM.

4.1.7 Fines Removal

The resulting powder for a sample pulverized in the ball mill contained a very fine grained component that was not observed for samples pulverized using the mortar and pestle. This made the sample clump together and then difficult to measure the PSD or to pack into the coaxial airlines. The fines were removed from these samples by a decanting process. In this process, powder samples are immersed in small batches into a beaker filled with isopropyl alcohol. The bottom of the beaker is then immersed several centimetres into a water bath in a vibrating ultrasonic cleaner to mobilize the finest particles in the sample. The fines can then be removed by slowly draining the liquid from the beaker and recovering the sample and letting it dry. Figures 4.7 and 4.8 show the lizardite and labradorite samples before and after the decanting process. EDS spectra collected

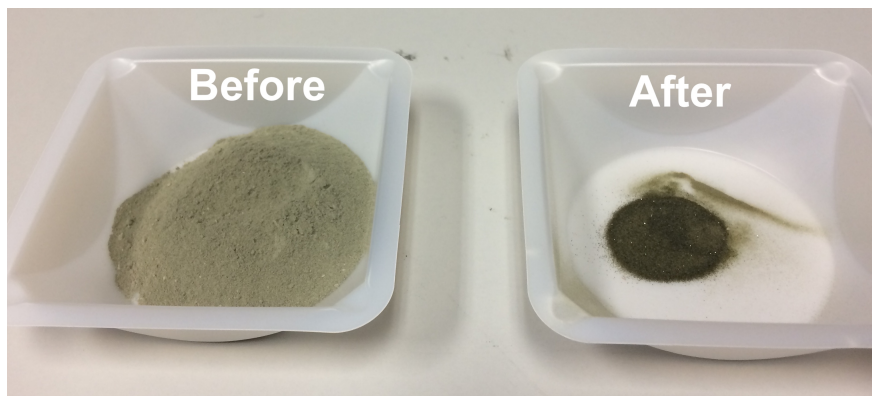


Figure 4.7: Lizardite before and after decanting process was applied (for a small batch of overall sample).

on pelletized labradorite samples before and after the decanting process was applied showed no change, confirming that the process does not preferentially remove any one mineral present in the sample.

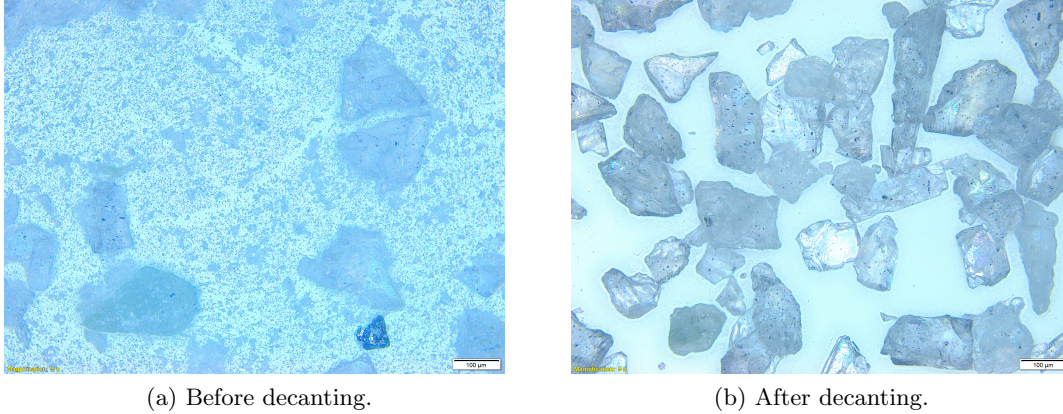


Figure 4.8: Labradorite sample viewed through the petrographic microscope before and after decanting the sample (same magnification).

4.1.8 Magnetite Removal

Some of the samples were found to contain magnetite, which is a mineral with appreciable magnetic permeability that would violate assumptions in the permittivity measurements. Several magnets were used to remove the magnetite component of these samples. The magnets were taped to the bottom of a plastic weight boat, and the sample was then poured into the weight boat in small batches. The magnets attracted the magnetite, and the rest of the sample was poured into a separate weight boat. The magnetite was brushed into another weight boat and the process was repeated until all of the magnetite was separated from the sample. Figure 4.9 shows the setup used to do this.

4.2 Samples

4.2.1 Overview

A total of seven different geologic samples were studied in the current research. Each was chosen for a specific reason with relevance to either the analysis of mixing theory or planetary radar observations. Aluminium oxide was chosen as a standard dielectric material, as it was a pure (> 99%) sample provided by Kramer Industries Inc. and has been studied extensively for its dielectric properties. A dolomite and labradorite sample provided by the Department of Earth Sciences at the University of Toronto (provenance unknown) were incorporated into this research to enhance the analysis of mixing theory. Brian Tsai measured the complex permittivity of either of these samples, in solid form, using a Keysight Technologies 85072A 10 GHz Split Cylinder Resonator



Figure 4.9: The setup used to remove magnetite from the samples. The upper weight boat has several magnets taped to its bottom, and can be seen capturing magnetite grains.

in a previous study. These measurements provide a constraint on the permittivity of the solid phase of the powdered dolomite and labradorite samples used in this research, which can then be used as an input in various mixing theories to test the correspondence with effective permittivity measurements of the powdered samples. With the focus of applying this research to radar surveys of carbonaceous asteroids, some samples were included that are representative of the dominant mineralogy for such asteroids. The visible (VIS)/near-infrared (NIR) spectra of C-complex asteroids is similar to those for carbonaceous chondrite meteorites, hinting that carbonaceous asteroids are the parent bodies of carbonaceous chondrites (Demeo et al., 2015). The petrologic types of carbonaceous chondrites range from 1-6, where types 1-3 are representative of varying degrees of aqueous alteration and types 3-6 of thermal metamorphism (Demeo et al., 2015; Hutchison, 2004). Early electron microprobe studies of carbonaceous chondrites revealed that serpentine mineral content increased with increasing degrees of aqueous alteration in CM chondrites, and that serpentine composition increased in Mg content (Tomeoka and Buseck, 1985; Zolensky et al., 1993). Browning et al. (1996) proposed the Mineralogical Alteration Index (MAI) for CM chondrites that classifies the degree of aqueous alteration by the progressive alteration of Fe-rich serpentine (cronstedtite) to Mg-rich serpentine (antigorite). Similar alteration scales and geochemical and petrologic studies have shown that this correlation generally holds true (Rubin et al., 2007; Howard et al., 2009; Takir

et al., 2013). The silicate mineral olivine is a possible precursor for serpentinization reactions and is common in carbonaceous chondrites. The distribution of Fe-rich olivine (fayalite) to Mg-rich olivine (forsterite) is varied among ordinary chondrites, and has been linked to petrologic types 3.1-3.9 showing correlation with thermal metamorphism (Huss et al., 2006; McCoy et al., 1991). Based on this mineralogical analysis, the current work focuses on observing the change in dielectric properties between Fe-rich and Mg-rich endmembers of the serpentine and olivine mineral groups, and whether there exists a dielectric contrast strong enough for discrimination between endmember compositions in analysis of asteroid radar data. A dunite sample from the University of Toronto (provenance unknown) was used as a sample in the presented research, being representative of the Mg-rich olivine endmember forsterite. Due to the rarity in natural samples on Earth, a synthetic fayalite sample created at the University of Nevada Las Vegas High Pressure Science and Engineering Center was used in this research, representing the Fe-rich olivine endmember. To represent the Mg-rich endmember of the serpentine mineral group, two serpentinite samples, one predominantly antigorite and one predominantly lizardite, were acquired from the UCF/DSI-CI-2 Deep Space Industries CI carbonaceous chondrite regolith simulant and the ROM respectively. The antigorite sample is labelled as such in the CI carbonaceous chondrite regolith simulant ensemble; however, at the time of writing there is little additional information available regarding the sample. The serpentinite (lizardite) sample from the ROM is originally from the Mt. Genevre Massif, France. The Fe-rich endmember of the serpentine mineral group, cronstedtite, was not available for use in this study in the necessary quantities.

4.2.2 Aluminium Oxide (Al_2O_3)

This sample was obtained from Kramer Industries, Inc. and has already been described somewhat previously. Two different samples with $> 99\%$ purity, #150 and #120 mesh, with average grain sizes of $76 \mu\text{m}$ and $102 \mu\text{m}$ were used, with these averages taken from Sotodeh (2014). Since the Gaussian fitting method was not successful for the PSD of the #150 mesh sample, the average grain sizes from Sotodeh (2014) were assumed instead. Some of the modelling in the presented research is based off of other aluminium oxide samples from Kramer Industries, Inc. that were measured by Sotodeh (2014). To minimize the boundary effects on the measured permittivity, only the #150 and #120 mesh samples were measured directly in the current work. Kramer Industries, Inc. list the specific gravity of the aluminium oxide to be 3.8 (irrespective of grain size). The grain density of the sample was measured with the pycnometer to be $3.948 \pm 0.002 \text{ g/cm}^3$.

4.2.3 Forsterite (Mg_2SiO_4)

The dunite sample used in this research is pictured in Figure 4.10. The provenance of this sample



Figure 4.10: Dunite sample provided by the University of Toronto (provenance unknown) that was used in this research.

was unknown, but was previously identified as dunite by Brian Tsai for prior research conducted on the sample. To confirm the mineralogy of the sample, it was taken to the ROM for an XRD measurement. While at the ROM, Veronica DiCecco collected a Raman spectrum of the sample using the Horiba LabRAM 532 nm (1300 nm spot size) Raman instrument at the ROM (Figure 4.11). The Raman spectrum compares well with the Raman spectrum (RRUFF ID X050088) for a forsterite sample from San Carlos, Arizona, USA. The XRD spectrum collected for the sample was in correspondence with a forsterite sample in the International Centre for Diffraction DATA (ICDD) Powder Diffraction File (PDF) database, as well as showing possible trace minerals present (Figure 4.12). An EDS spectrum of the dunite sample was also acquired (10 kV beam voltage due to sample charging), confirming the dominant *O*, *Si*, and *Mg* elemental composition expected for the forsterite mineralogy (Figure 4.13). Based on the Raman, XRD, and EDS data it was concluded that the dunite sample is predominantly forsterite, with some possible antigorite (from localized serpentinization) and chromite inclusions. The dunite sample will hereafter just be referred to as forsterite. The grain density of the forsterite was measured using the pycnometer to be $3.326 \pm 0.001 \text{ g/cm}^3$. The solid sample as depicted in Figure 4.10 was pulverized using the rock hammer and mortar and pestle to two samples with average grain sizes of $146 \mu\text{m}$ and $152 \mu\text{m}$ using

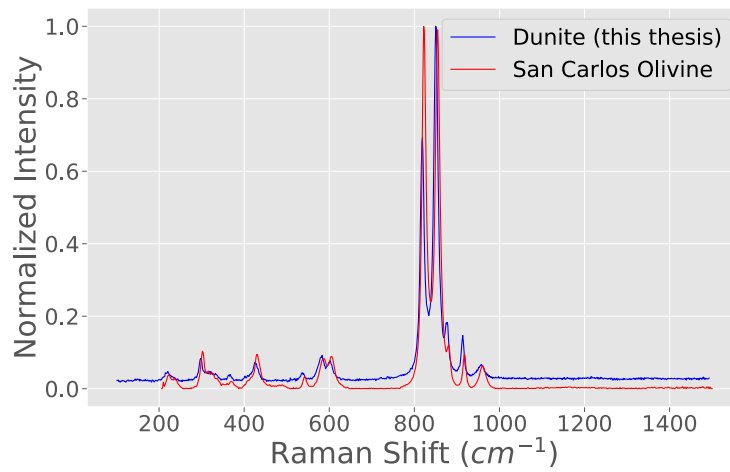


Figure 4.11: Raman spectrum of the dunite sample compared with the RRUFF database ID X050088 processed San Carlos forsterite spectrum.

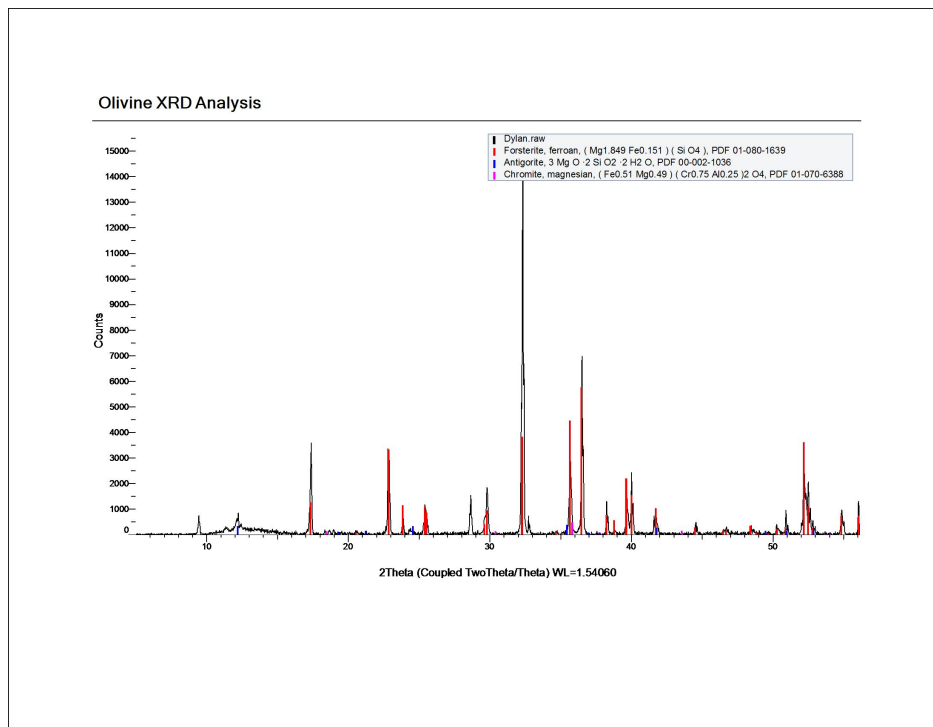


Figure 4.12: XRD spectrum (Dylan.raw) of dunite sample with matching mineral spectrum from PDF database.

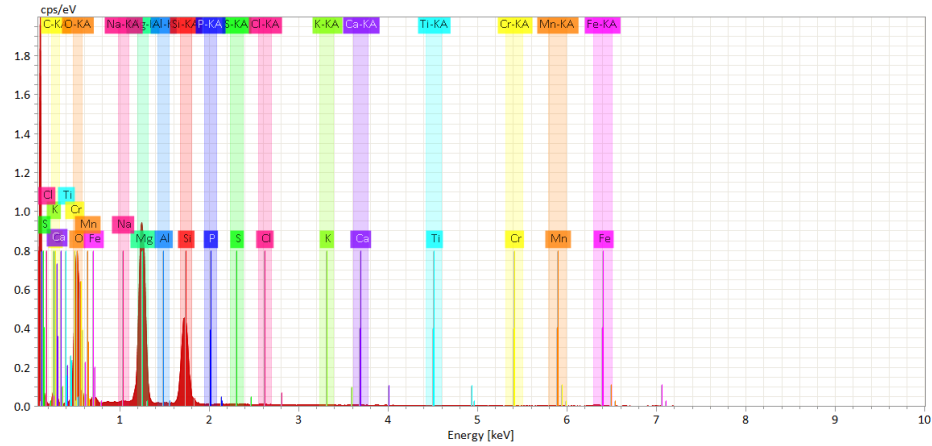
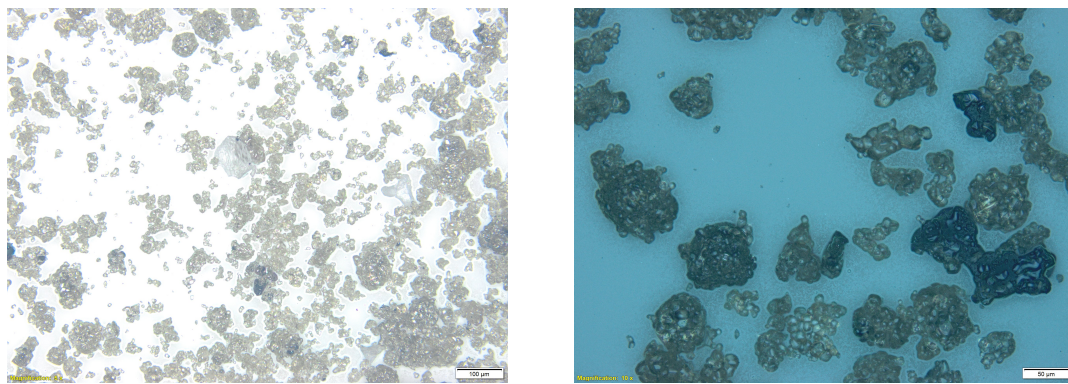


Figure 4.13: EDS spectrum for elemental mapping of roughly 3 mm² area of solid dunite sample. Energy levels expected for common elements found in rocks and minerals are indicated.

the (adjusted) Gaussian fit to the PSD. Two samples were made from the solid sample because the original powder sample was dropped during experimentation, and it was necessary to powder the solid sample further, resulting in a slightly different average grain size.

4.2.4 Fayalite (Fe_2SiO_4)

Synthetic fayalite produced in the University of Nevada Las Vegas High Pressure Science and Engineering Center was provided for use in this research by Dr. Pamela Burnley. The fayalite sample was acquired as a fine grain powder that was too small for the typical grain size sorting using mechanical sieves applied to the other samples. The fayalite sample was imaged using an Olympus BX-53P petrographic microscope, resulting in a visual classification of the average grain size as $\approx 20 \mu\text{m}$ (Figure 4.14). Trace amounts of magnetite were identified in the sample. The



(a) 5x magnification.

(b) 10x magnification.

Figure 4.14: Fayalite sample as viewed by petrographic microscope.

magnetite was removed using the methods outlined in section 4.1.8. XRD data was collected for the sample, confirming the fayalite composition (and removal of magnetite) by matching the spectrum with a fayalite spectrum from the ICDD PDF database (Figure 4.15). An EDS spectrum (15 kV

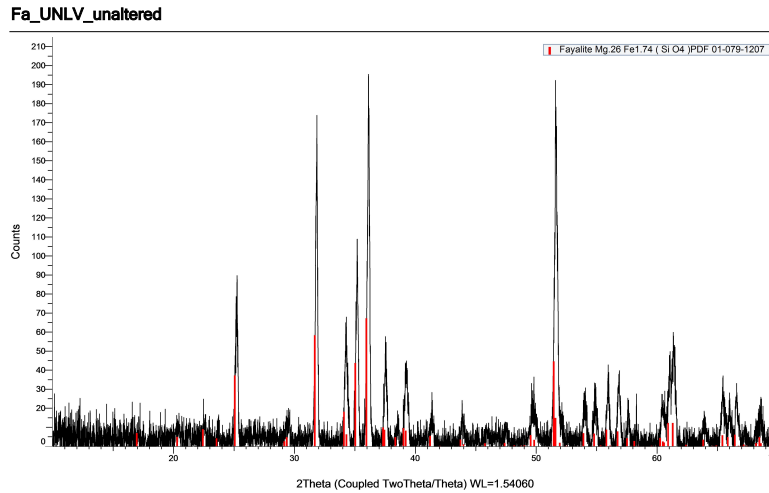


Figure 4.15: XRD spectrum of fayalite sample with matching mineral spectrum from ICDD PDF database.

beam voltage) was collected for a pellet made from the sample over a roughly 3 mm² area (Figure 4.16). In this EDS spectral map, small inclusions of silica were identified (Figure 4.17). The grain

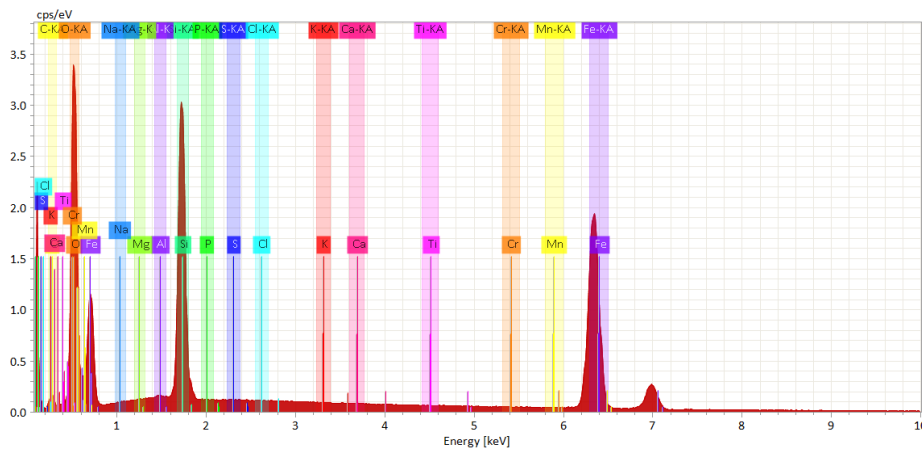


Figure 4.16: EDS spectrum for elemental mapping of roughly 3 mm² area of pelletized fayalite sample.

density of the fayalite was determined using the pycnometer to be 4.347 ± 0.003 g/cm³.

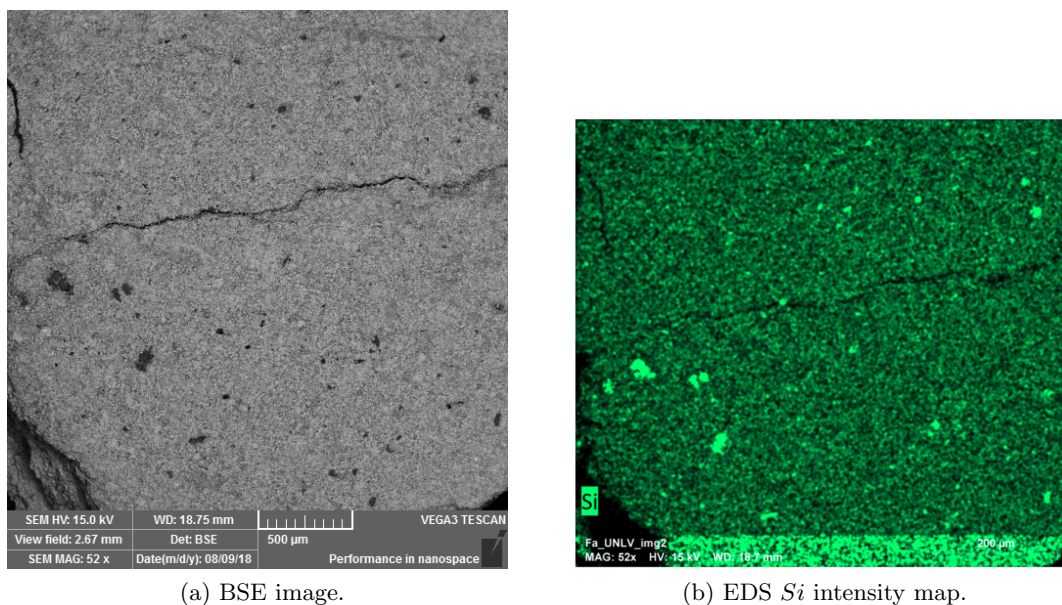


Figure 4.17: Silica inclusions identified in BSE image and EDS spectral mapping of pelletized fayalite sample.

4.2.5 Antigorite ($Mg_3Si_2O_5(OH)_4$)

The antigorite sample is the serpentine component from the UCF/DSI CI carbonaceous chondrite asteroid regolith simulant, which was obtained in powder form. On the safety datasheet for this simulant, the composition is listed as antigorite/lizardite, non-asbestiform. Covey et al. (2018) identify the simulant component as antigorite from Northfil Resources in Ontario, with roughly 5 % *Fe*. Covey et al. (2018) describe the sample processing procedure, and that average particle sizes of 75 μm were targeted in the comminution process. Metzger et al. (2019) list this component as antigorite in their work, and noted that in XRD analysis minor impurities of dolomite were identified. Veronica DiCecco collected XRD data for the antigorite sample at the ROM, and for the SNR of the data it was difficult to discern the major minerals besides antigorite present in the sample (Figure 4.18). EDS spectra (10 kV beam voltage) were collected at various points across a pellet made from the antigorite sample, with *Mg*, *Si*, and *O* being the predominant elements identified (Figure 4.19). Several inclusions containing *Na*, *Al*, *Fe*, and *Ca* were also identified. The *Ca* corresponds with the dolomite that was identified in Metzger et al. (2019). From the EDS and XRD analysis, there are clearly other minerals than antigorite present in the sample, some of which were not distinguished. The sample PSD could not be fit with a Gaussian distribution due to a considerable amount of particles larger than $> 250 \mu\text{m}$ skewing the distribution from normal. Particles larger than 250 μm were removed from the sample, and the PSD was then fit

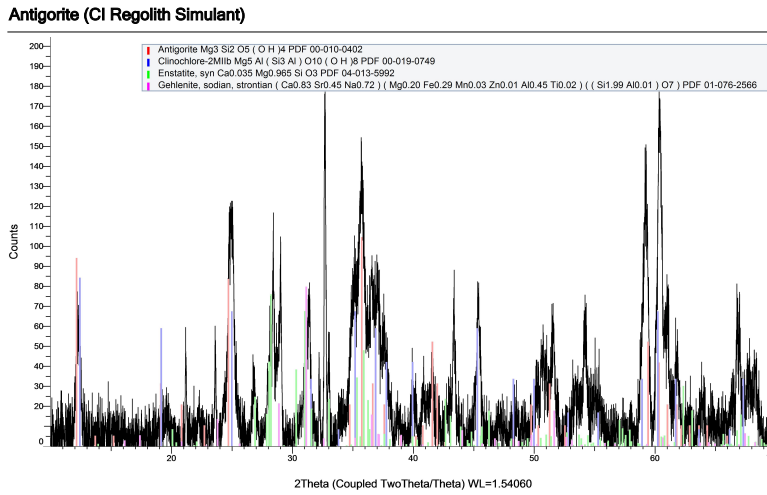


Figure 4.18: XRD spectrum of antigorite sample with attempted matching of mineral spectrum from ICDD PDF database.

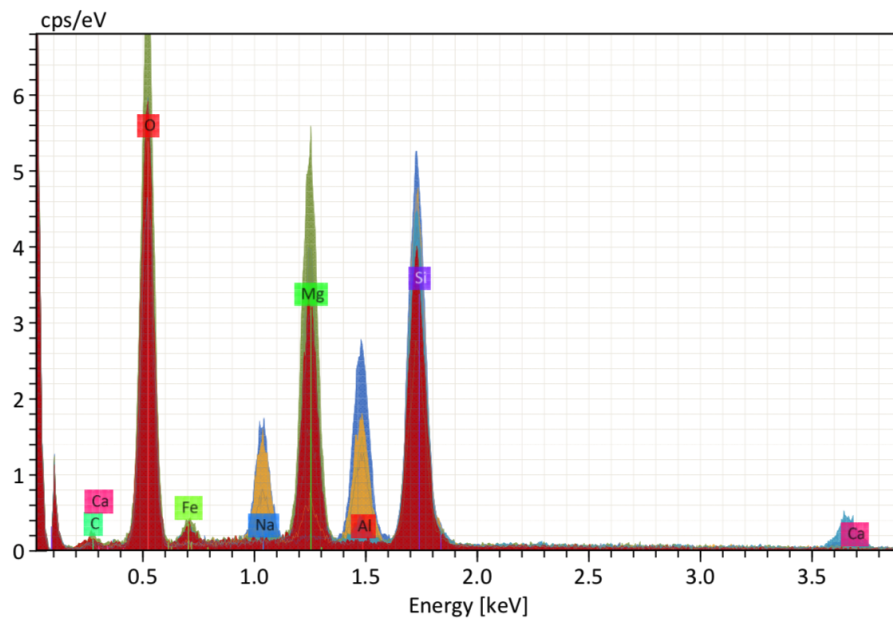


Figure 4.19: EDS point spectra of pelletized antigorite sample, differentiated by colour and overlapped.

with a (adjusted) Gaussian distribution with an average particle size of $121 \mu\text{m}$. Some permittivity measurements were performed before these large particles were removed, which through a mass weighted average the average particle size for these measurements was calculated to be $164 \mu\text{m}$. How the PSD affects the boundary effects model that was applied to the permittivity measurements is uncertain, and so the effect that the unique PSD for the antigorite sample has is also uncertain. The average (since this sample contains several minerals, the measurement in the pycnometer represents an average of their properties, which is technically true of all samples) grain density for the sample was measured by the pycnometer to be $2.763 \pm 0.001 \text{ g/cm}^3$.

4.2.6 Lizardite ($Mg_3Si_2O_5(OH)_4$)

This sample was provided by the ROM, originally from the Mt. Genevre Massif, France, in the form of a solid rock. Prior research conducted on the sample at the ROM and York University included the collection of XRD data, which compared well with XRD spectra for lizardite from the RRUFF database (Figure 4.20). Since the sample was in a solid form, it was possible to use the

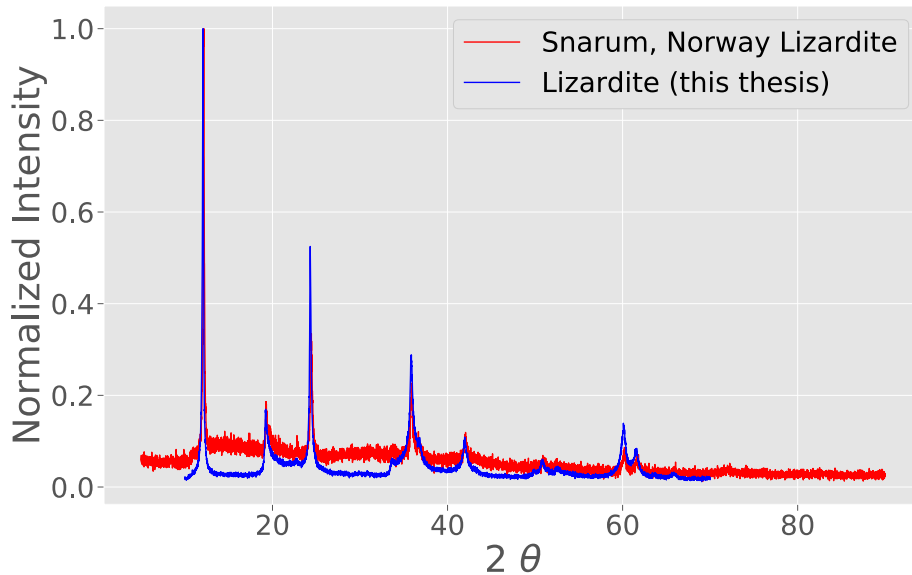


Figure 4.20: XRD spectrum of lizardite sample with matching mineral spectrum from RRUFF database (RRUFF ID R060006).

SEM to look at contextual information about the sample (Figure 4.21). The BSE image revealed a

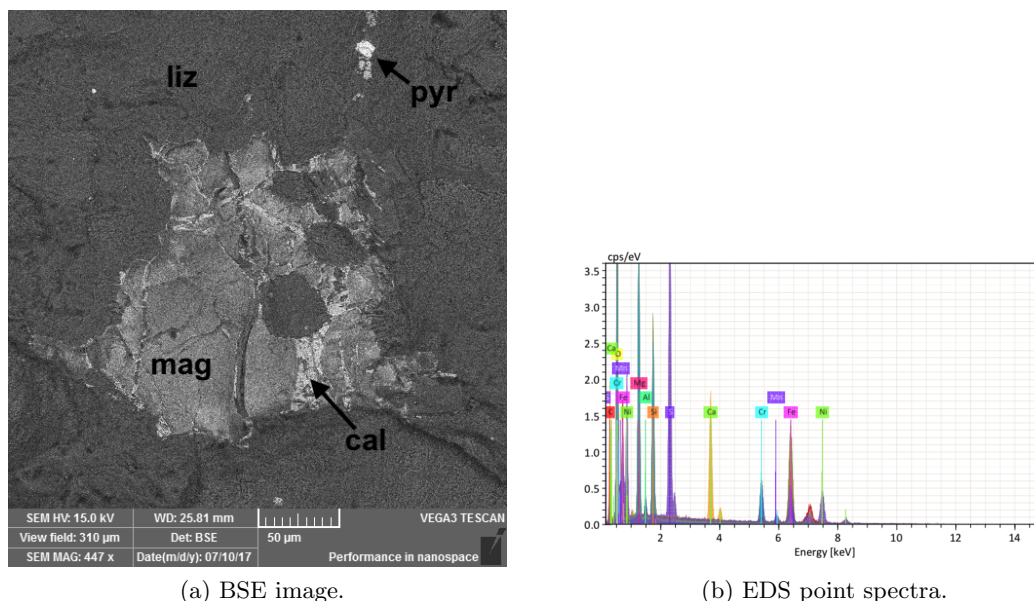


Figure 4.21: BSE image of annotated inclusion in lizardite sample with corresponding EDS point spectra taken in different brightness zones of the BSE image.

fine grained lizardite matrix with minor inclusions, some complicated with more than one mineral phase (Figure 4.21(a)). EDS point spectral analysis (15 kV) of these components confirmed the lizardite composition of the matrix, and identified *S*, *Ca*, *Cr*, *Fe*, and *Ni* in the inclusions. The *Fe* is likely in the form of magnetite (and pyrite), a common iron oxide resulting from serpentinization reactions, and the *S* is likely from pyrite, which has been identified as a secondary mineral in the Mt. Genevre Massif (Lewis and Smewing, 1980). The concentrations of these trace minerals must be low to not appear in the XRD data. The solid sample was pulverized using a combination of the rock hammer and ball mill. The resulting powder sample had a large proportion of very fine particles, which were removed using the method described in section 4.1.7. The magnetite from the sample was removed using the method described in section 4.1.8. The final powder consisted of a small amount of material, which was sorted into #170 (90 μm) and #325 (45 μm) sized sieves, resulting in a mass weighted average particle size of 104 μm. The grain density of the lizardite was measured using the pycnometer to be $2.634 \pm 0.001 \text{ g/cm}^3$.

4.2.7 Dolomite ($\text{CaMg}(\text{CO}_3)_2$)

The dolomite sample used in this research was provided as a solid rock sample by the University of Toronto with unknown provenance. XRD measurements at the ROM identified dolomite to be

the major mineral constituent, with possible traces of calcite present (Figure 4.22). BSE images

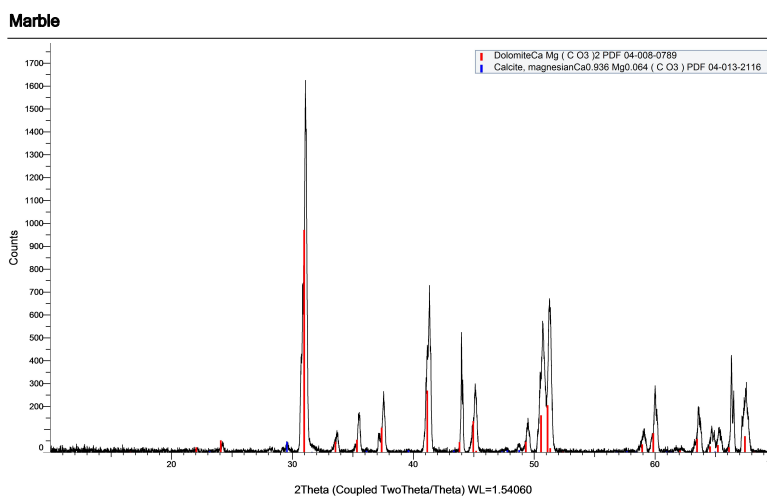
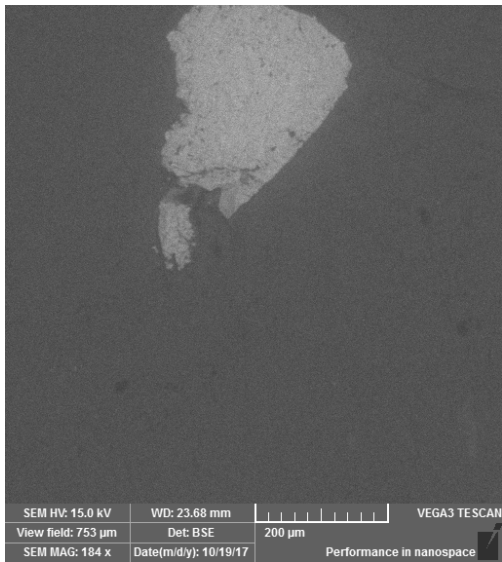


Figure 4.22: XRD spectrum of dolomite sample (labelled marble in the plot) with matching mineral spectrum from ICDD PDF database.

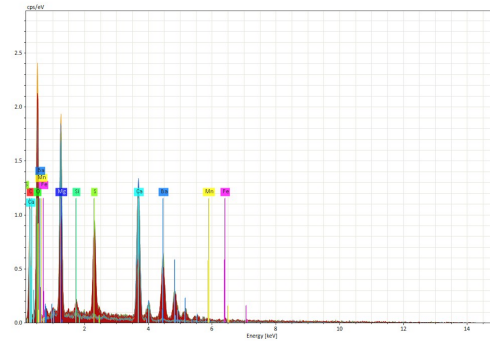
of the solid sample showed a dominantly uniform mineralogy, with some small inclusions present. EDS point spectral analysis (15 kV) of the background and inclusions confirmed that *Mg*, *C*, and *Ca* dominate most of the sample, with *Ba* and *S* dominant in the inclusions (Figure 4.23). The inclusions rich in *Ba* and *S* are likely baryte, and must be small in proportion to the dolomite in the sample since baryte was not recognized in the XRD data. Smaller sections of the larger dolomite sample were removed using the rock saw, and pulverized to powder using a rock hammer and mortar and pestle. The PSD of the sorted powder was fit with a (adjusted) Gaussian distribution with an average particle size of 124 μm . The grain density of the sample was determined to be $2.863 \pm 0.001 \text{ g/cm}^3$ using the pycnometer.

4.2.8 Labradorite ($(Ca, Na)(Al, Si)_4O_8$)

Similar to the dolomite sample, the labradorite sample used in this research was of unknown provenance and provided by the University of Toronto as a solid rock. XRD analysis performed on the sample was matched well by a combination of albite and anorthite spectra, which corresponds with a labradorite feldspar composition (labradorite is 50-70 % anorthite) (Figure 4.24). EDS data



(a) BSE image.



(b) EDS point spectra.

Figure 4.23: BSE image of inclusion in dolomite sample with corresponding EDS point spectra taken in different brightness zones of the BSE image.

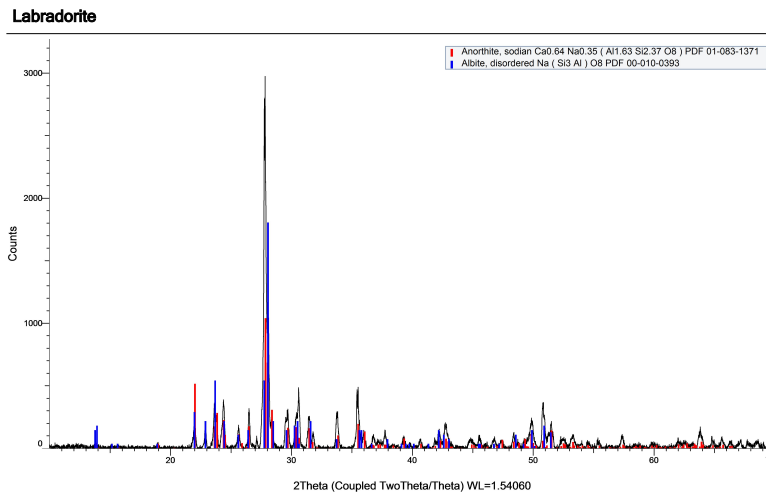


Figure 4.24: XRD spectrum of labradorite sample with matching mineral spectrum from ICDD PDF database.

(10 kV) was collected for a pellet made from the powdered sample, which showed *Si*, *Na*, *Al*, *O*, and *Ca* throughout the roughly 3 mm² spectral mapping area (Figure 4.25). No significant minor

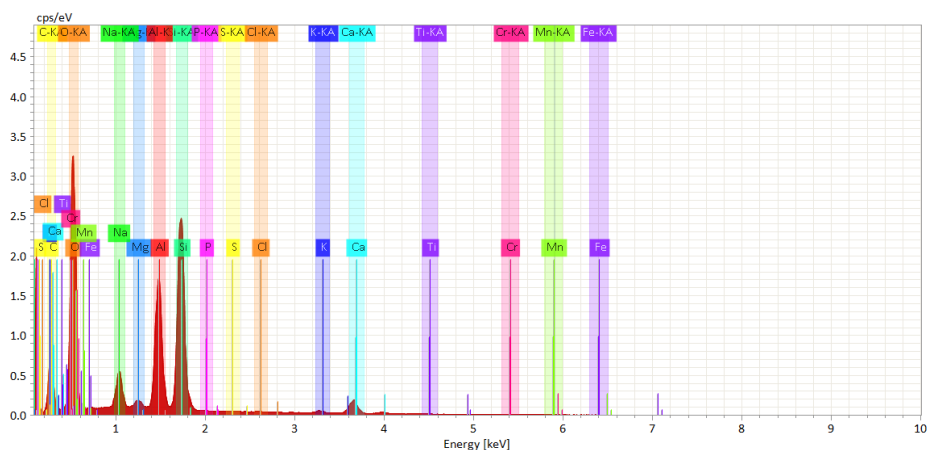


Figure 4.25: EDS spectrum of pelletized labradorite sample.

minerals were identified in the labradorite sample. Sections of the large solid sample were cut using the rock saw, and pulverized to powder using the rock hammer and ball mill. Very fine particles were removed from the resulting powder using the method described in section 4.1.7. The PSD of the leftover material was fit with a (adjusted) Gaussian distribution with an average particle size of 104 μm . The grain density of the sample was measured to be $2.714 \pm 0.001 \text{ g/cm}^3$.

4.2.9 Samples Summary

The samples used in this research have each been described in detail. It is possible to calculate the composition of a sample in weight percent oxides from the EDS data; however, the accuracy is generally very low. Instead, the elemental quantification of the EDS data was used qualitatively to confirm the composition determined by XRD data and to identify any trace mineralogies. Table 4.2 summarizes the main attributes for each sample.

4.3 Oven Drying Samples prior to Permittivity Measurements

It was necessary to oven dry the samples prior to conducting permittivity measurements and volume measurements to remove residual water. Initially, the samples were heated at 250° C for \approx 24 hours prior to measurement. This treatment was applied to the aluminium oxide and forsterite samples without any adverse effects observed in the samples. When the fayalite sample was heated to 250° C the sample underwent a colour change from dark green to brown (Figure 4.26). XRD

Table 4.2: Summary of the samples used in this research.

Sample	Chemical Formula	Minor Minerals	Avg. grain size (μm)	Avg. grain density (g/cm^3)
Aluminium Oxide	Al_2O_3	-	76 – 102	3.948 ± 0.002
Dolomite	$\text{CaMg}(\text{CO}_3)_2$	calcite, baryte	124	2.863 ± 0.001
Labradorite	$(\text{Ca}, \text{Na})(\text{Al}, \text{Si})_4\text{O}_8$	-	104	2.714 ± 0.001
Forsterite	Mg_2SiO_4	antigorite, chromite	146 – 152	3.326 ± 0.001
Fayalite	Fe_2SiO_4	quartz, magnetite	20	4.347 ± 0.003
Antigorite	$\text{Mg}_3\text{Si}_2\text{O}_5(\text{OH})_4$	dolomite, enstatite, chlorite	121 – 164	2.763 ± 0.002
Lizardite	$\text{Mg}_3\text{Si}_2\text{O}_5(\text{OH})_4$	magnetite, pyrite, calcite	104	2.634 ± 0.001

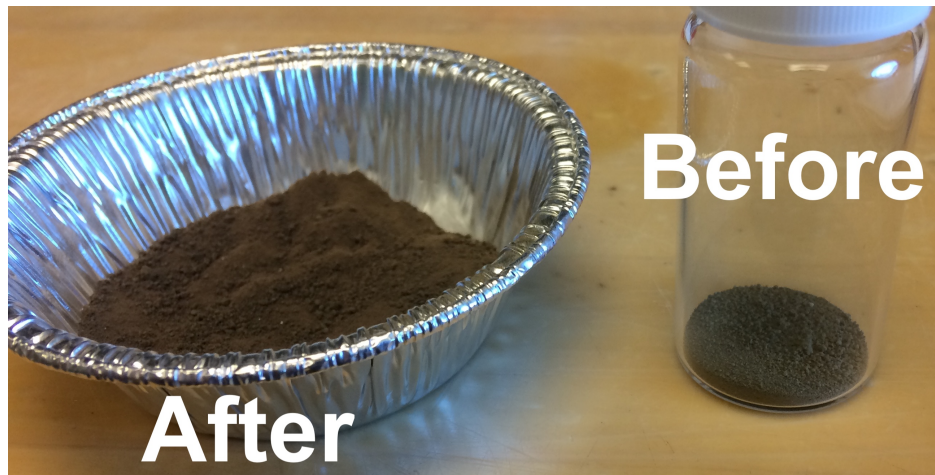


Figure 4.26: Colour change in fayalite sample after heating to 250°C .

data was collected on the fayalite sample before and after the colour change was observed, with no differences between the peak positions in either spectrum, indicating that the sample is still fayalite post-colour change. The width and relative heights of the peaks changed slightly, which indicates that the degree of crystallinity and positions of lattice vacancies changed. New positions for lattice vacancies could describe some of the colour change in the sample. The bulk density of measurements post-colour change were somewhat greater than those pre-colour change, suggesting some change occurred in the sample. A reasonable hypothesis is that the sample underwent some heat-induced oxidation of Fe^{2+} to Fe^{3+} . Shannon et al. (1991) noted that darker colours in fayalite are indicative of oxidized iron and higher permittivities. Since the XRD data confirmed the mineralogy did not change in the sample, the brown sample post-colour change was still considered fayalite. Fayalite can exist with a range in iron oxidation states, so comparing this sample to the literature is still valid.

As a result of the fayalite oxidation at $250^{\circ}C$, it was desirable to heat the remaining samples at a lower temperature. A loss on ignition (LOI) test was performed on the samples to determine if $115^{\circ}C$ was adequate in removing water from the samples (Figure 4.27). From Figure 4.27 it can be seen

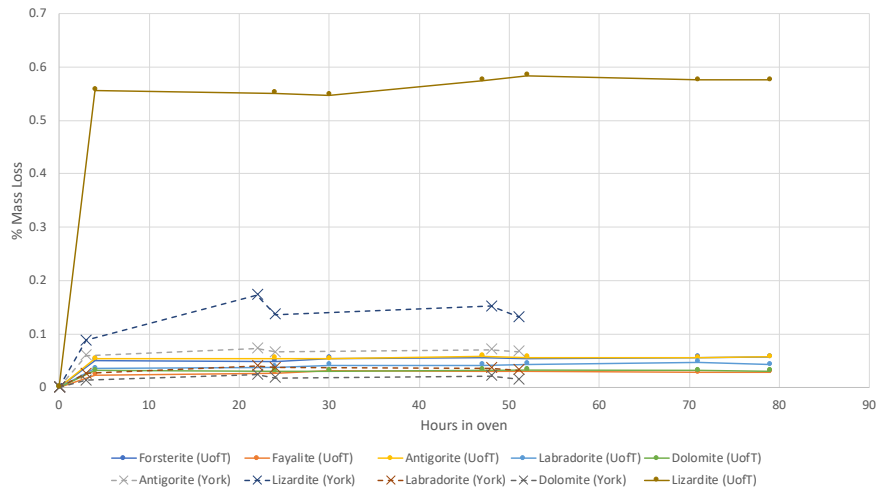


Figure 4.27: Loss on ignition test to determine oven drying time required at $115^{\circ}C$.

that the amount of water removed from the samples levels off very quickly (< 10 hours) when dried at $115^{\circ}C$. The antigorite and lizardite samples had the most amount of water removed due to their clay-like structures and increased water retention compared to the other samples. The samples in this research were therefore heated at $115^{\circ}C$ for at least 10 hours prior to a permittivity or volume

measurement, often for longer. The samples were either kept in the oven between measurements to reduce their exposure to water vapour or were stored in sealed containers. The careful storage of samples kept moisture levels low in the samples, likely influencing the low mass loss observed during the LOI test.

Chapter 5

Boundary Conditions Model

5.1 Overview

One of the major contributions resulting from the research in this thesis is a model developed to correct the effect of heterogeneities in powder samples at the interface of the sample and coaxial airline during a permittivity measurement. Sotodeh (2014) inferred that porosity at the interface between a powder sample and the coaxial airline conductors is greater than for the areas of the sample surrounded by other particles. This region of elevated porosity is larger for larger particle sizes, making this boundary effect more significant. The boundary effect was confirmed by measuring the porosity of aluminium oxide samples with a range in average grain sizes in the 14 mm and 7 mm coaxial airlines introduced earlier in this thesis. The porosity increased with decreasing coaxial airline diameter and increasing grain size, as predicted by the boundary effect hypothesis. Corrections exist in the literature for accounting for air gaps between a solid sample and the coaxial airline conductors in a permittivity measurement. The research in the current thesis aimed modelling efforts at using mixing theory to adapt the traditional solid air gap correction models to the case of powders and the boundary effect identified by Sotodeh (2014). The resulting work was published in the journal *Advances in Space Research* in 2017 (available online in 2016) (Hickson et al., 2017b). Sections 5.2 - 5.9 of this chapter are taken directly from the pre-print version of the article and discuss the model development and testing in detail. The citations, nomenclature, and abbreviations have been altered in some cases to coincide with the rest of the thesis. Some of the introductory notes are repetitive given the thorough introduction already included in this thesis, but have been left as they provide context for the specific discussion points in the journal article. The last section of this chapter (sections 5.10) includes a short summary describing the results of the model in the context of the rest of the thesis. I attest that I did not perform any of the permittivity measurements discussed in this chapter, and that they are taken directly from

Sotodeh (2014).

5.2 Abstract

Accurate measurements of the dielectric properties of materials are essential in constraining interpretations of radar observations of planetary bodies. For bodies whose surfaces are comprised of regolith this requires an understanding of the behaviour of the bulk permittivity of powders. In this research we measure the effective permittivity of powdered aluminium oxide (or alumina, Al_2O_3) in a 7 mm and 14 mm (diameter) coaxial airline at 7.5 GHz for multiple samples with varying grain size. The solid permittivity of alumina is extracted from these measurements using the Bruggeman (Symmetric) mixing equation. We develop a model to account for heterogeneity within the airline, specifically in regards to local variation in porosity. The results of the model show good correlation to experimental data and effectively correct for grain size effects on the measured bulk permittivity. We show that particle shape can have a significant impact on the output of the model and can be accounted for by modelling particles as ellipsoids rather than perfect spheres, where the depolarization factor must be measured and averaged for a specific sample batch.

5.3 Introduction

Active remote sensing techniques in the microwave regime are used in observing planetary bodies through terrestrial/orbiting radar and GPR. The reflectivity and penetration depth of a radar signal incident on a non-conducting surface are largely determined by those materials' dielectric response at a given frequency (Griffiths, 1999; Feynman et al., 1979). For planetary bodies whose surfaces consist of regolith material, such as the Moon and asteroids, properties of that regolith may be extracted from a radar return if the effective permittivity of the regolith is known (Carrier et al., 1991). Polarimetric radar is used to measure the degrees of circular/linear polarizations received from a surface which are sensitive to a variety of target features including subsurface structure, surface roughness, regolith thickness, bulk density, and composition (Carter et al., 2011). Models that derive these features from radar data intrinsically make assumptions about physical characteristics of the target that greatly affect the returned signal properties, such as the dielectric permittivity, introducing large sources of uncertainty to interpretations. To overcome this, radar images of planetary bodies are often compared with terrestrial analogues (Carter et al., 2011); however, this is not appropriate for bodies for which no adequate terrestrial analogues exist, such as asteroids. A corre-

lation between circular polarization ratio and visible-infrared taxonomic class has been identified in near-Earth asteroids that would be better understood if the bulk (effective) dielectric properties as a function of mineralogical composition were known (Benner et al., 2008). Providing information on the dielectric permittivity of regolith materials is therefore relevant for missions to asteroids such as 101955 Benu, the target of NASA's Origins-Spectral Interpretation-Resource Identification-Security-Regolith Explorer (*OSIRIS-REx*) mission. To constrain the analysis of radar data on planetary bodies, specifically asteroids, laboratory measurements are needed to better understand the dielectric permittivity of regolith materials (Nolan et al., 2013; Carter et al., 2011).

A popular and effective approach for measuring the permittivity of any dielectric material is the transmission line method utilizing a coaxial airline and network analyzer (Chen et al., 2004). This technique has the advantage of broadband measurement, being relatively inexpensive, and recently has been shown to have the capability of measuring powdered samples (Grosvenor Jr, 1993; Stillman and Olhoeft, 2008; Sotodeh, 2014). By measuring powdered samples the effects of grain size distribution, grain shape, and porosity on the effective permittivity can be determined. Measurement techniques for powdered samples have been investigated in the literature (Tuhkala et al., 2013; Ebara et al., 2006); however, the aforementioned effects on the effective permittivity are not well understood. For a powdered sample, the measured value in the transmission line method is the effective permittivity of the sample. The effective permittivity is a combination of each phase within the airline: water adsorbed on grain surfaces, air, and the solid sample. Samples can be oven baked to remove residual moisture, resulting in a two phase mixture of air and solid sample. Electromagnetic mixing theory can be used to extract the permittivity of the solid phase of the mixture (true permittivity of the sample). Many mixing theories are based on the assumption of homogeneity within the sample and uniform particle shape (Sihvola, 1999). These assumptions are not valid when considering a powdered sample in a coaxial airline.

In this research a theoretical model is developed to account for heterogeneity at the boundary of the coaxial airline and shows potential to compensate for particle shape effects. The effective complex permittivity of alumina is measured (using the transmission line method) and input to this model to calculate the real part of the permittivity of solid alumina. While both the real and imaginary parts of relative permittivity affect radar scattering, this paper is focused on using the real part of permittivity measurements to test the validity of the model (similar to the rest of

this thesis, if the word permittivity is used it is referring to the real part unless otherwise stated). Given the results of our experiment, future work will be done applying this model to the dielectric loss. Alumina was chosen for this study as it has well known dielectric properties and is readily available in powdered form at a variety of grain sizes, making it a suitable standard to test the model with. The average grain sizes and porosities of samples measured in this research were chosen to correspond to asteroidal surface regolith material (Shepard et al., 2010; Magri et al., 2001; Clark et al., 2002). Section 5.4 discusses our measurement procedure and presents the raw, unprocessed permittivity data. Section 5.5 describes the model developed in this research to correct the raw data. Section 5.6 discusses the results of processing the data presented in section 5.4 with the technique shown in section 5.5. The corrected permittivity values are compared to results from the literature. Improving the accuracy of measurements of the permittivity of powders will tighten constraints on radar/GPR data and allow more accurate interpretations of planetary datasets.

5.4 Experimental Procedure

5.4.1 Sample Preparation

Seven sample batches of alumina grit with average grain sizes ranging from 76 μm to 940 μm supplied by Kramer Industries, Inc. were used in the experiment. The particle size distribution for each sample conform to ANSI B47-12-2001 grit size grading standards. The samples were oven baked at a constant temperature of 200 ° C for 48 hours prior to measurement to evaporate residual moisture. The mass of the sample before and after oven baking was measured using a digital scale within ± 1 mg (Sotodeh, 2014). The volume of each airline was measured with a hole gauge micrometer within ± 0.25 mm to calculate the bulk density of each sample. The sample bulk density and specific gravity were used to calculate the porosity within the coaxial airline for a given measurement. A custom airline filling fixture was created to vibrate the airline and ensure maximum and uniform particle packing density. Tests run on the filling/vibrating procedure showed porosity in the sample holder reaches an asymptotic limit after a given vibration time. By vibrating the airline throughout the filling process there is no suspected gradient in porosity along the airline's length. Each sample's complex permittivity was measured in a 7 mm diameter (HP 85051B, 10 cm length) and 14 mm diameter (GR 900-LZ, 15 cm length) coaxial airline connected to an Agilent E5071C-280 ENA series vector network analyzer. A full two-port short, open, through, and load (SOTL) calibration of the network analyzer was completed before all measurements to

reduce systematic errors following the manufacturer’s instructions (Technologies, 2011; Sotodeh, 2014). The complex permittivity of each sample was calculated from the S-parameters measured by the network analyzer using the non-iterative algorithm outlined in Boughriet et al. (1997).

5.4.2 Measurement Results

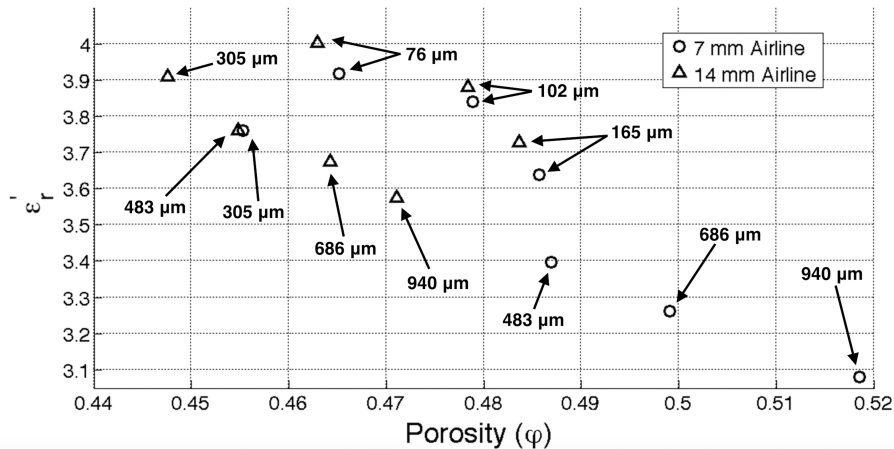


Figure 5.1: Effective (real) permittivity of alumina measured with 7 mm and 14 mm airlines at 7.5 GHz ($\Delta\epsilon_r \approx 0.015$, $\Delta\phi \approx 0.001$). Annotated text refers to average grain size of measured sample (Sotodeh, 2014).

The permittivity measured for each sample at 7.5 GHz is presented in Figure 5.1 as a function of porosity within the sample. At this frequency the wavelength of the exciting electric field (in free space) is 4 cm, which is large enough compared to the particle sizes and airline dimensions to permit homogenization of the dielectric behaviour of the powder (Sihvola, 1999). It is worth noting that this is a broadband measurement technique and the same procedure that is used in this research can be applied at other frequencies, given the frequency is low enough ($\lambda \gg$ particle size) to permit homogenization of the powder under test. In general it is observed in Figure 5.1 that the measured effective permittivity decreases with increasing grain size and porosity. There are two distinct trends in the data corresponding to smaller grain sizes (76 μm , 102 μm , and 165 μm) versus larger grain sizes. We suggest this to be a result of batch processing of the different samples producing two distinct sets of particle shapes, as will be discussed in section 5.6. The measured values for the permittivity of alumina are much lower (3-4) than the values found in the literature (9-10, see Table 1) due to the contribution of the air phase in the powder to the measured effective permittivity. As the permittivity of air is roughly $\epsilon_{\text{air}} \approx 1$, this lowers the measured effective permittivity of the sample, especially at higher porosities.

5.5 Revised Mixing Model

5.5.1 Boundary Conditions

A physical explanation for some of the observed trends in Figure 5.1 is that there are conditions at the boundary of the sample holder (interface between sample and conductor) that are different from those within the bulk sample. Particles pack more densely in the bulk of the sample, whereas grains along the conductor interface have more pore space around them (Figure 5.2). At microwave frequencies used in radar applications, porosity has a profound effect on the dielectric properties of a powder, as seen in section 5.4. Characterizing this heterogeneity is important in calculating the permittivity of the solid material from effective permittivity measurements. This characterization will allow better modelling of the porosity of asteroid regolith from radar returns. In our model,

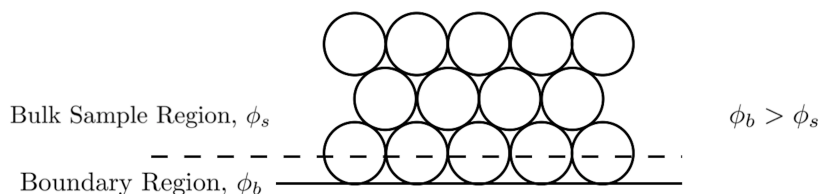


Figure 5.2: Geometry for spherical particles of powder in airline at conductor interface.

we treat the particles as spheres and treat the curved sample/conductor boundary as flat. The volume of the airline can then be divided into two distinct regions with two distinct porosities: the dominating region consisting of the bulk sample material (with porosity denoted as ϕ_s) and another smaller region consisting of particles contacting the surfaces of the conductors (with porosity denoted as ϕ_b , Figure 5.2). The extent of each region within the airline is determined by the grain size of the sample being measured. The boundary region extends radially one half grain size into the airline from the conductor (for both inner and outer conductors in the airline) as shown in Figure 5.2. This particular division is chosen because it defines the transition from one porosity to another.

To constrain the porosities of each region the densest possible packing of spheres for each geometry is considered. For the bulk sample region this porosity limit is given by the Kepler Conjecture which corresponds to a porosity of $\phi_s = 0.25952$ (Hales, 2005). The lower limit on porosity, or highest packing density, in the boundary region can be calculated for unit spheres ($r_{\text{sphere}} = 1, l_{\text{cube}} = w_{\text{cube}} = h_{\text{cube}} = 2$) the following way:

$$V_{\text{sphere}} = \frac{1}{2} \left(\frac{4}{3} \pi r^3 \right) = 2.094$$

$$V_{\text{cube}} = \frac{1}{2} lwh = 4$$

$$V_{\text{void}} = V_{\text{cube}} - V_{\text{sphere}} = 1.905$$

$$\phi_b = \frac{V_{\text{void}}}{V_{\text{cube}}} = 0.47625$$

Thus it can be shown that the constant of proportionality, here called β , between porosities in each region for this limiting case is:

$$\phi_b = \beta \phi_s, \text{ where } \beta = 1.835 \quad (5.1)$$

The volume weighted porosities in each region are related to the total porosity that is recorded during each measurement of a powder sample, ϕ_{tot} by:

$$\phi_{tot} = \phi_s \left(\frac{V_s}{V_{tot}} \right) + \phi_b \left(\frac{V_b}{V_{tot}} \right) \quad (5.2)$$

By combining equations (5.1) and (5.2) the bulk sample region porosity can be calculated from the total porosity:

$$\phi_s = \frac{\phi_{tot} V_{tot}}{\beta V_b + V_s} \quad (5.3)$$

The boundary region porosity can be calculated by combining the result of equation (5.3) with equation (5.2).

5.5.2 Modelling and Mixing

The coaxial capacitor model (Baker-Jarvis et al., 1993), typically used for solid sample air gap correction, can be used to represent the bulk sample and boundary regions in the airline (Figure 5.3). In Figure 5.3 D_1 is the diameter of the inner conductor, D_2 is the diameter of the inner boundary region, D_3 is the diameter of the outer boundary region, and D_4 is the diameter of the outer conductor. The regions bounded by $D_1 - D_2$ (Inner Boundary Region), $D_2 - D_3$ (Bulk Sample Region), and $D_3 - D_4$ (Outer Boundary Region) (Figure 5.3) represent the entire volume of the airline and are modelled as capacitors in series. The capacitance, C_n , of each region can be used

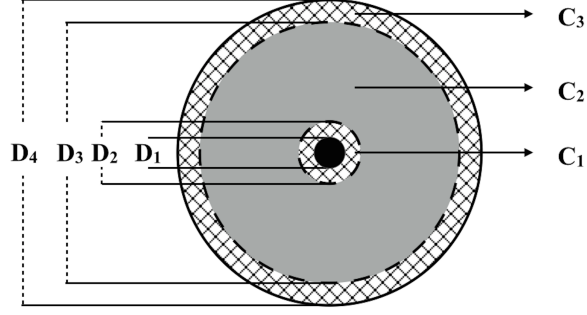


Figure 5.3: Cross section of coaxial airline showing the sample region (C_2) and boundary regions (C_1, C_3). For ‘7 mm’ airline $D_1 = 0.30404$ cm and $D_4 = 0.69926$ cm. For ‘14 mm’ airline $D_1 = 0.62052$ cm and $D_4 = 1.42824$ cm. The values for D_2 and D_3 are dependent on the average grain size of the sample being measured as discussed in section 3.1.

to calculate the effective measured (total) capacitance, C_m , through the following equation:

$$\frac{1}{C_m} = \sum_{n=1}^{n=3} \frac{1}{C_n} \quad (5.4)$$

The capacitance in each region can be rewritten in terms of the effective permittivity of the region, the length of the airline, L , and the bounds on the region. For the total (measured) capacitance this expression is:

$$C_m = \frac{2\pi\epsilon_m L}{\ln\left(\frac{D_4}{D_1}\right)} \quad (5.5)$$

Substituting equation (5.5) into (5.4) yields:

$$\frac{\ln\left(\frac{D_4}{D_1}\right)}{2\pi\epsilon_m L} = \frac{\ln\left(\frac{D_2}{D_1}\right)}{2\pi\epsilon_{ib} L} + \frac{\ln\left(\frac{D_3}{D_2}\right)}{2\pi\epsilon_s L} + \frac{\ln\left(\frac{D_4}{D_3}\right)}{2\pi\epsilon_{ob} L} \quad (5.6)$$

where ϵ_m is the measured effective permittivity, ϵ_{ib} is the effective permittivity in the region $D_1 - D_2$, ϵ_s is the effective permittivity in the region $D_2 - D_3$, and ϵ_{ob} is the effective permittivity in the region $D_3 - D_4$. Assuming that the porosity is the same for both the inner and outer boundary regions (and thus the effective permittivity is the same), $\epsilon_{ib} = \epsilon_{ob} = \epsilon_b$, equation (5.6) can be rewritten to express ϵ_m as:

$$\epsilon_m = \frac{\epsilon_s \epsilon_b \ln\left(\frac{D_4}{D_1}\right)}{\epsilon_s \left[\ln\left(\frac{D_2}{D_1}\right) + \ln\left(\frac{D_4}{D_3}\right) \right] + \epsilon_b \ln\left(\frac{D_3}{D_2}\right)} \quad (5.7)$$

Mixing equations can be used to approximate the effective permittivity of a mixture, or in this case a powder, for each region, ϵ_s and ϵ_b . For any mixing equation the effective permittivity is determined by the permittivity of the components, in this case solid alumina and air, and the volume fraction of each phase, in this case a proxy for porosity. Therefore the permittivity of alumina can be calculated by inverse mixing theory using the experimentally measured effective permittivity of the mixture, the permittivity of air ($\epsilon_{\text{air}} \approx 1$), and a value for porosity. If the space within the coaxial airline is considered homogeneous then the total porosity of a measurement can be used to calculate the total effective permittivity (Figure 5.4a). For the remainder of this paper this scenario will be labelled “Classical Mixing”. If the space within the coaxial airline is considered divided into a bulk sample and boundary region then the effective permittivity of each region can be calculated using the porosity of each region as shown in section 5.5, and the total effective permittivity of the entire space within the airline given by equation (5.7) (Figure 5.4b). For the remainder of this paper this scenario will be labelled “Model Mixing”. To test the

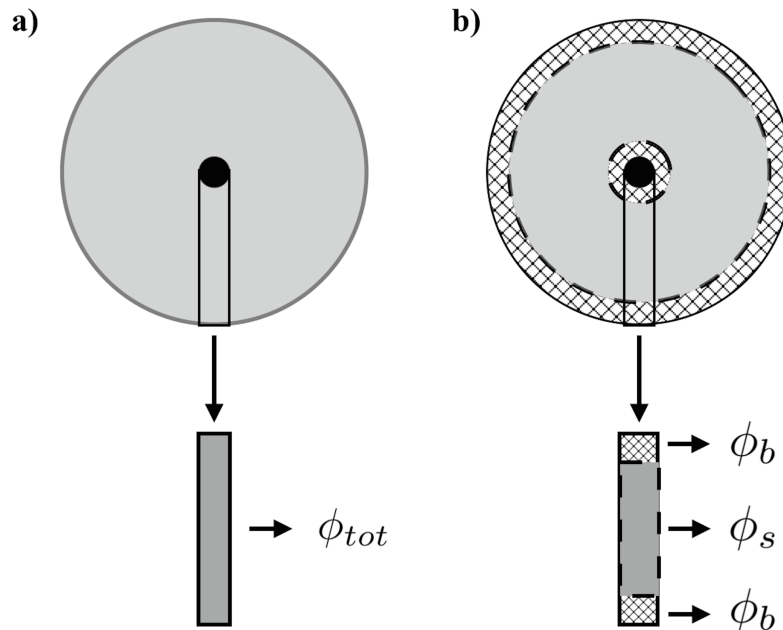


Figure 5.4: Cross section of coaxial airline with radial component cross section for **a)** Classical Mixing Scenario **b)** Model Mixing Scenario.

validity of our model we are interested in the relative change when calculating the permittivity of alumina considering the classical mixing scenario versus the model mixing scenario. Therefore to focus on the model results we will narrow our discussion to the use of one mixing equation. For this discussion, the result of using the Bruggeman symmetric equation, otherwise known as

the Effective Medium Approximation, was chosen as it gave the most realistic results (Bruggeman, 1935; Sihvola, 1999). This equation has the advantage of treating the air phase and solid phase of the powder symmetrically, where the permittivity of air is taken to be $\epsilon_{\text{air}} = 1.0$, as well as being a widely accepted and implemented approximation (Sihvola, 1999). Furthermore, contrary to many mixing equations that are derived empirically, the Bruggeman formula has a theoretical foundation that is appropriate under our sample conditions and allows particle shape to be included in modelling. The results of applying the same method with different mixing equations are given in section (appendix) 5.9. The effective permittivity of each region in the model mixing scenario is calculated according to the Bruggeman equation as (Zhang, 2007; Sihvola, 1999):

$$\gamma_s = (3f_s - 1)\epsilon_i + (2 - 3f_s)\epsilon_e, \quad \epsilon_s = \frac{1}{4}(\gamma_s + \sqrt{\gamma_s^2 + 8\epsilon_i\epsilon_e}) \quad (5.8)$$

$$\gamma_b = (3f_b - 1)\epsilon_i + (2 - 3f_b)\epsilon_e, \quad \epsilon_b = \frac{1}{4}(\gamma_b + \sqrt{\gamma_b^2 + 8\epsilon_i\epsilon_e}) \quad (5.9)$$

In equations (5.8) and (5.9) the inclusion permittivity, ϵ_i , is the true permittivity of solid alumina, the environment permittivity, ϵ_e , is the air phase of the mixture ($\epsilon_e = \epsilon_{\text{air}}$), and the volume fraction in each region is $f = 1 - \phi$.

5.6 Application of Model to Measured Data

Substituting equations (5.8) and (5.9) into (5.7) allows the effective permittivity of the entire airline, ϵ_m , to be calculated for the model mixing scenario. The values for D_1, D_2, D_3 , and D_4 as well as f_b and f_s can be determined for a sample by applying the constraints discussed in section 5.5. Different values of ϵ_i used in equations (5.8) and (5.9) result in different values of ϵ_m calculated in (5.7). Iterating through possible values of ϵ_i from 0 – 100 in (5.8) and (5.9) results in various calculations of ϵ_m which are compared with the experimental results from section 5.4. Those values of ϵ_i that result in a modelled effective permittivity for the entire airline that coincide with the measured effective permittivity values from Figure 5.1 are taken as the true permittivity of alumina. For each measurement the permittivity predicted by the model mixing scenario that calculate the effective permittivity within a tolerance of 0.0005 to the experimentally measured effective permittivity is shown in Figure 5.5. For comparison, the permittivity predicted by the classical mixing scenario applied to the experimental measurements is also shown in Figure 5.5. In this calculation the same iteration through possible values of ϵ_i was conducted, however the volume of the airline

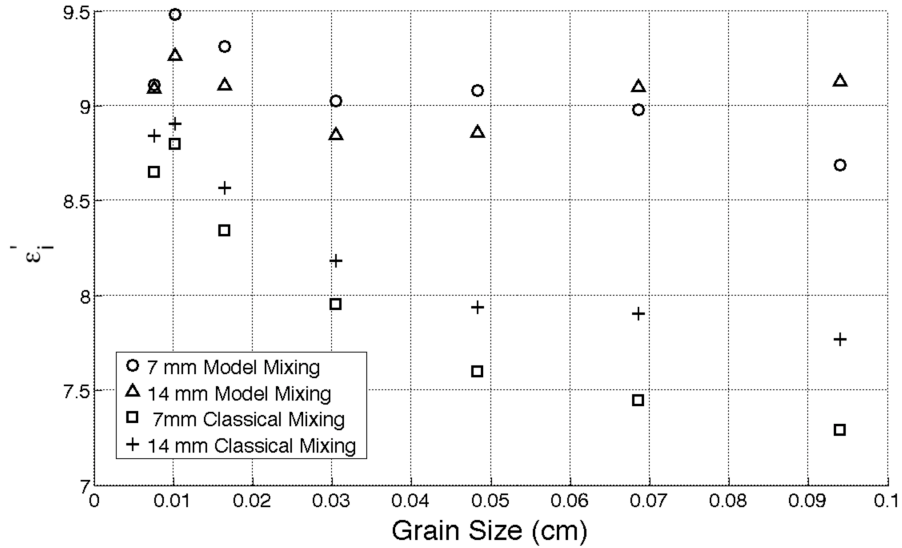


Figure 5.5: Output of model mixing scenario and classical mixing scenario results plotted vs. average grain size of sample measurement (data grouped by coaxial airline used). Smaller grain sizes ($76 \mu\text{m}$, $102 \mu\text{m}$, $165 \mu\text{m}$)

was assumed homogeneous with constant porosity throughout (Figure 5.4.a). Figure 5.5 shows the permittivity of alumina that has been extracted from the raw data presented in section 5.4 from the classical mixing scenario as well as from the model mixing scenario developed in section 3.

To interpret Figure 5.5 accurately it should be noted that since the permittivity of solid alumina is constant regardless of grain size, an ideal distribution of data would be a horizontal line centered at the value of the true permittivity. The trend of measured effective permittivity decreasing with increasing grain size observed in Figure 5.1 is also seen in Figure 5.5 as the permittivity of alumina predicted by the classical mixing scenario also decreases with increasing grain size. The permittivity predicted by the model mixing scenario is in better agreement across the various samples and indicate a reduction in the grain size effects on effective permittivity measurements. It should be noted, however, that samples with different grain sizes were also measured at different porosities, which may be influencing the results of Figure 5.5. The same data in Figure 5.5 is therefore presented in Figure 5.6 as a function of porosity. In Figure 5.6 the permittivity calculated from the classical mixing scenario decreases with increasing porosity, as observed experimentally in Figure 5.1. The permittivity calculated by the model mixing scenario does not follow this trend and furthermore largely removes the differences observed experimentally between the measured permittivity of small grain sizes versus large grain sizes. When looking at the smaller grain sizes in Figure 5.5, however,

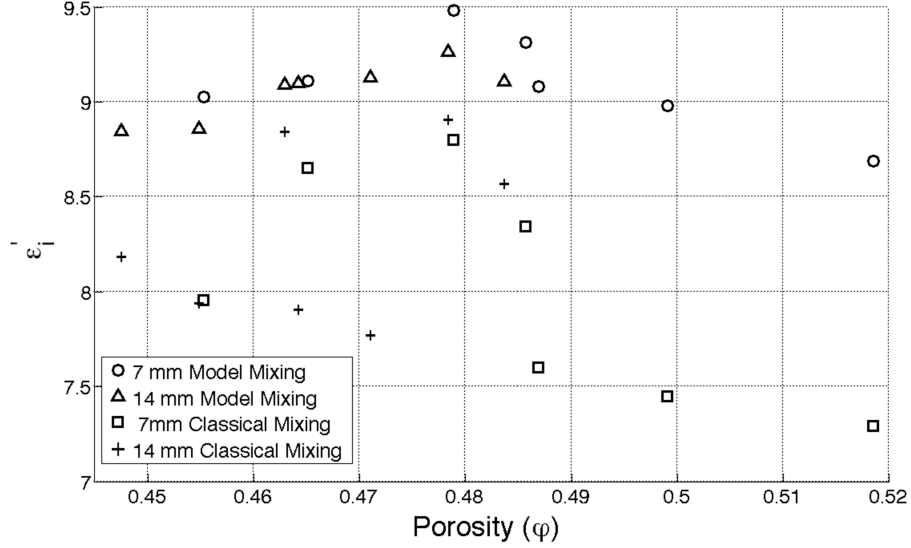


Figure 5.6: Output of model mixing scenario and classical mixing scenario results plotted vs. porosity of sample measurement (data grouped by coaxial airline used)

it is apparent that the values of the permittivity resulting from the model mixing scenario are higher than those of the remaining larger grain sized samples.

To characterize any physical differences between the small grain size samples and large grain size samples, the alumina grains were observed under microscope (Figure 5.7). Representative samples are shown in Figure 5.7 that highlight an observation that the smaller grain sizes (76 μm , 102 μm , and 165 μm) have lower sphericity with angular corners compared with the larger grain sizes which have higher sphericity with rounded corners. As a result, modelling the alumina grains as spheres in equations (5.8) and (5.9) is inappropriate for smaller grain sizes. To test this hypothesis, the same modelling procedure is undertaken with equations (5.8) and (5.9) modified for smaller grain size sample particle shapes to be represented as needles (ellipsoids with depolarization factors $N = (0, \frac{1}{2}, \frac{1}{2})$) while the larger grain size particle shapes represented as spheres (Figure 5.8). The depolarization factor of an inclusion is a shape parameter that represents how the internal electric field changes with particle shape, ultimately affecting the polarizability and dielectric properties of a mixture (Sihvola, 2007). The Bruggeman equation is rewritten to include this depolarization factor in the following way (Sihvola, 1999):

$$\epsilon_{eff} = \epsilon_e + \frac{f}{3}(\epsilon_i - \epsilon_e) \sum_{j=x,y,z} \frac{\epsilon_{eff}}{\epsilon_{eff} + N_j(\epsilon_i - \epsilon_{eff})} \quad (5.10)$$

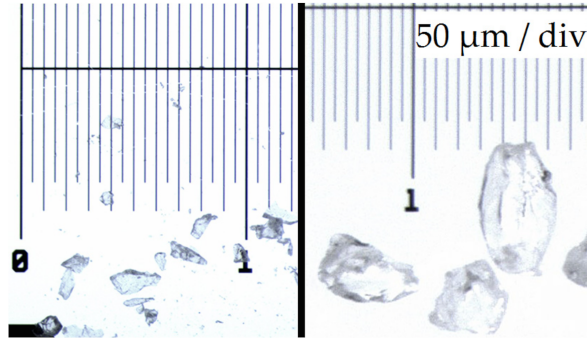


Figure 5.7: 76 μm (left) and 305 μm (right) alumina grain shapes (Sotodeh, 2014)

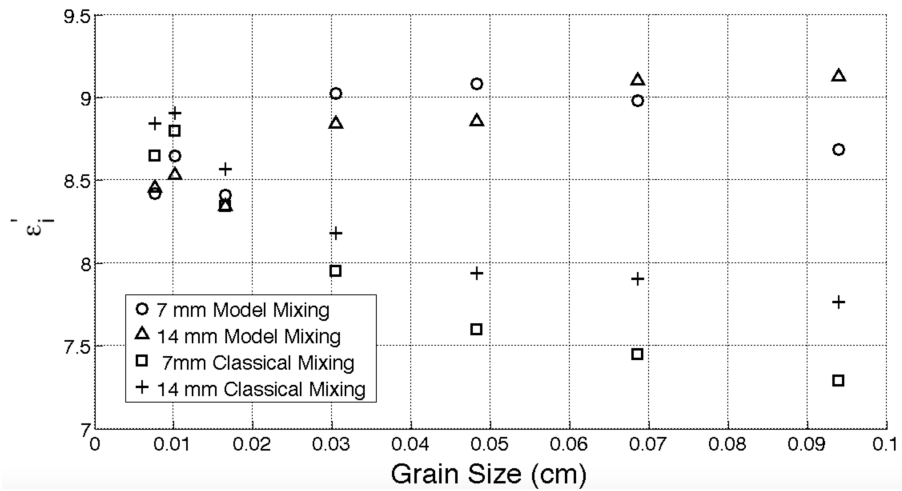


Figure 5.8: Output of model mixing scenario and classical mixing scenario results plotted vs. average grain size of sample measurement (data grouped by coaxial airline used). Smaller grain sizes (76 μm , 102 μm , 165 μm) modelled as needles.

This change in the modelling parameters had the effect of lowering the calculated value of the permittivity of alumina for the smaller grain size samples as desired. However, the new permittivity calculated is lower than the values predicted for the larger grain size samples, effectively overcompensating for particle shape effects. From this it can be inferred that the grain shape for the smaller grain size samples is not perfectly spheroidal or needle-like and is rather somewhere in-between. This is also true of the larger grain sized samples that are not perfectly spherical but somewhat elliptical (Figure 5.7). We deduce that the manufacturing process for a specific sample batch determines the ellipticity of the grains in that sample. This can be accounted for in the Bruggeman mixing equation by measuring the three semi-axes of several representative grains of a sample and determining the average depolarization factor for the grains of that sample (Sihvola, 1999). Furthermore there is a range both in size and shape for particles in a given sample batch which influences the geometry assumed in Figure 5.2, the porosity of the airline, and the mixing equation used in modelling.

An interesting observation in Figures 5.5, 5.6, and 5.8 is the difference in the permittivity calculated for samples with identical grain size but measured in different sized airlines. Since the extent of the boundary region in a given airline is determined by the grain size of the sample being measured, the effects discussed in section 5.5 are more pronounced in airlines with smaller diameters. For a given grain size, the boundary region will occupy a larger proportion of the total volume of the 7 mm airline than in the 14 mm airline. This can be seen in the classical mixing results in Figure 5.5. The model mixing results, however, do not seem to have an obvious correlation between airline dimensions and permittivity. The quantitative differences in permittivities calculated for a given grain size in different airlines is on the order of the uncertainty associated with environmental fluctuations in a given transmission line measurement. In developing this model further these sources of measurement uncertainty (such as relative humidity in the laboratory) need to be eliminated to isolate sources of error in the model. We are currently developing the instrumentation and methodology necessary to make permittivity measurements in a coaxial airline isolated in an environment chamber capable of controlling air pressure (subsequently humidity) and temperature. The permittivity of alumina output from the model mixing scenario and classical mixing scenario have been compared to the values found in other relevant experiments for comparison (Table 5.1). Table 5.1 shows that our model results better reflect the values for the permittivity of aluminium oxide found in other experiments. The standard deviation of the model results are less than half of

Table 5.1: Permittivity of alumina: results from this study (spherical particle shapes) compared to results in the literature

Source	ϵ_i
(Young and Frederikse, 1973)	9.34
(Gershon et al., 2001)	8.82, 9.22
(Rajab et al., 2008)	9.164, 9.424
(Tuhkala et al., 2013)	9.8
Model Mixing Avg ϵ_i	9.07
Classical Mixing Avg ϵ_i	8.15
Model Mixing STDEV, σ	0.199
Classical Mixing STDEV, σ	0.538

the standard deviation of the classical mixing results and therefore show more consistency in the calculated permittivity.

5.7 Conclusion

Air gap correction is well characterized for measurements of permittivity for solid samples using the transmission line method. Currently, no such correction exists to address the increased porosity at boundaries of a sample holder when measuring permittivity of granular samples, nor is magnitude of the systematic error possible by these boundary effects understood. Applying constraints on the porosity and extent of this boundary region allows mixing equations to be used to represent the volume of the sample holder as a series of layered capacitors so the same air gap correction may be applied. This method shows an increase in accuracy when correcting measurements of the permittivity of powdered aluminium oxide compared with a classical mixing approach. The magnitude of the differences between our model approach and classical mixing increases with increasing grain sizes. Our model highlights the large source of error introduced in measurements of powders using the transmission line method at the boundaries of the sample holder. The boundary conditions discussed are even more pronounced for granular materials with a high permittivity and should be taken into consideration for more accurate modelling. By improving non-destructive electrical measurement techniques for powders we are establishing a method that can be applied to samples returned from missions to asteroids such as NASA's *OSIRIS-REx* mission and JAXA's *Hayabusa2* mission. These ground-truth measurements combined with measurements from asteroid analogues will help to constrain the dielectric properties of the broader asteroid population and improve the interpretation of radar observations.

5.8 Acknowledgements

This work was funded in part by the Canadian Space Agency (CSA) and the Natural Sciences and Engineering Research Council of Canada (NSERC).

5.9 Appendix

The results of our study are dependent on the choice of mixing equation used in calculating the permittivity of alumina from experimental data in both the classical mixing and model mixing scenarios (Figure 5.4). The most realistic results were attained through the use of the Bruggeman Symmetric formula as is discussed at length in this paper. For comparison, the result of our model used with several other mixing equations is given here. The data are presented as a function of sample grain size for comparison with Figure 5.5. It is worth noting that the Looyenga-Landau-Lifshitz equation gave similar results to the Bruggeman equation, however does not consider particle shape and therefore was not used for discussion.

5.9.1 Maxwell Garnett

Otherwise known as Clausius-Mossotti, Lorenz-Lorenz, Rayleigh Mixing Formula (Sihvola, 1999; Maxwell Garnett, 1904)

$$\epsilon_{eff} = \epsilon_e + 3f\epsilon_e \frac{\epsilon_i - \epsilon_e}{\epsilon_i + 2\epsilon_e - f(\epsilon_i - \epsilon_e)}$$

5.9.2 Inverse Maxwell Garnett

Same equation as Maxwell Garnett with variable changes: Sihvola (1999)

$$\epsilon_e \rightarrow \epsilon_i$$

$$\epsilon_i \rightarrow \epsilon_e$$

$$f \rightarrow 1 - f$$

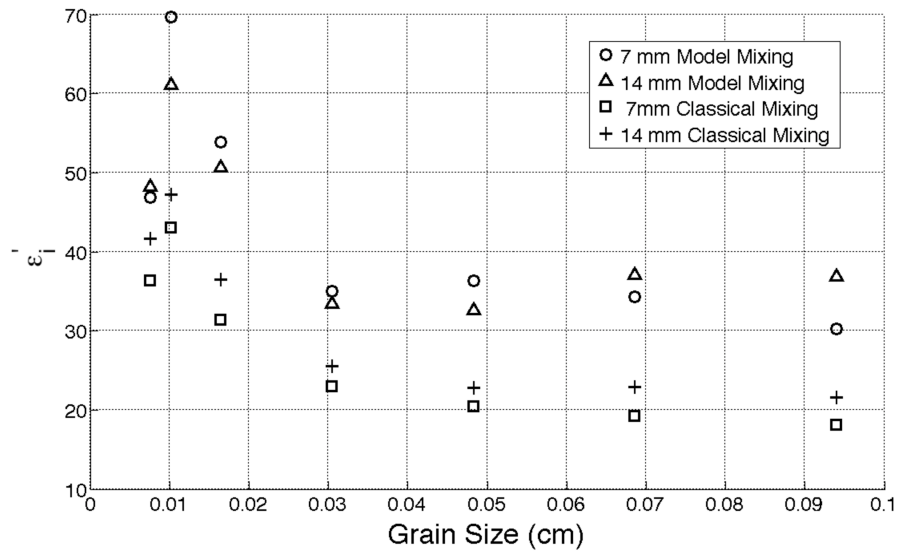


Figure 5.9: Study Results (Figure 5.5) derived using the Maxwell-Garnett equation.

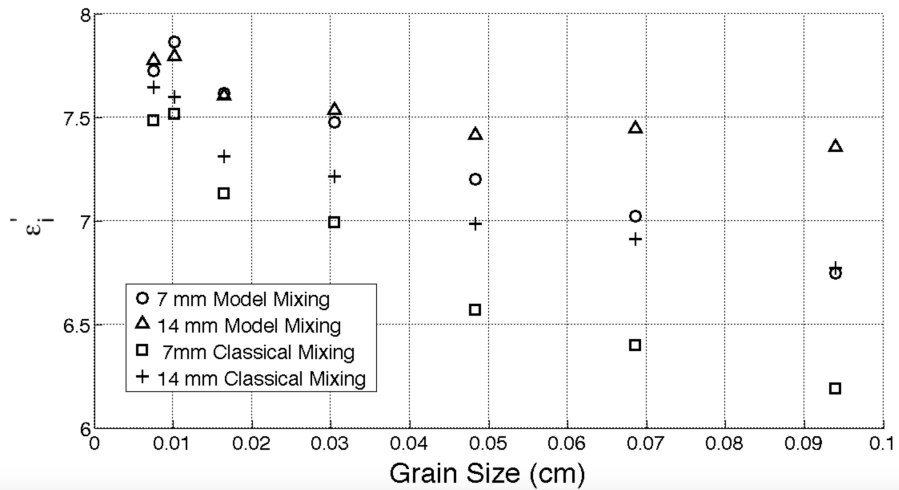


Figure 5.10: Study Results (Figure 5.5) derived using the Inverse Maxwell Garnett equation.

5.9.3 Coherent Potential

(Sihvola, 1999)

$$\epsilon_{eff} = \epsilon_e + f(\epsilon_i - \epsilon_e) \frac{3\epsilon_{eff}}{3\epsilon_{eff} + (1-f)(\epsilon_i - \epsilon_e)}$$

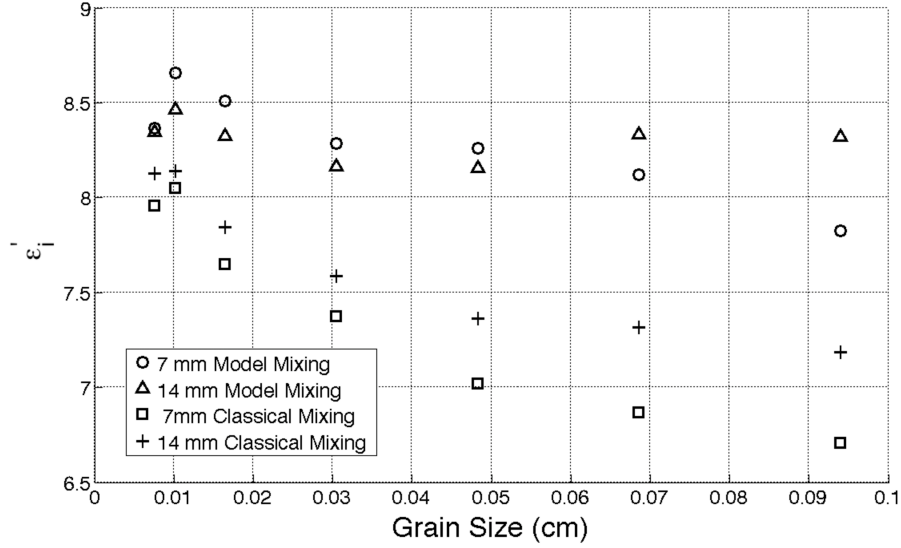


Figure 5.11: Study Results (Figure 5.5) derived using the Coherent Potential equation.

5.9.4 Lichtenecker

(Sihvola, 1999; Lichtenecker, 1926)

$$\epsilon_{eff} = \epsilon_i^f \epsilon_e^{1-f}$$

5.9.5 Looyenga

(Sihvola, 1999; Looyenga, 1965)

$$\epsilon_{eff}^{\frac{1}{3}} = f\epsilon_i^{\frac{1}{3}} + (1-f)\epsilon_e^{\frac{1}{3}}$$

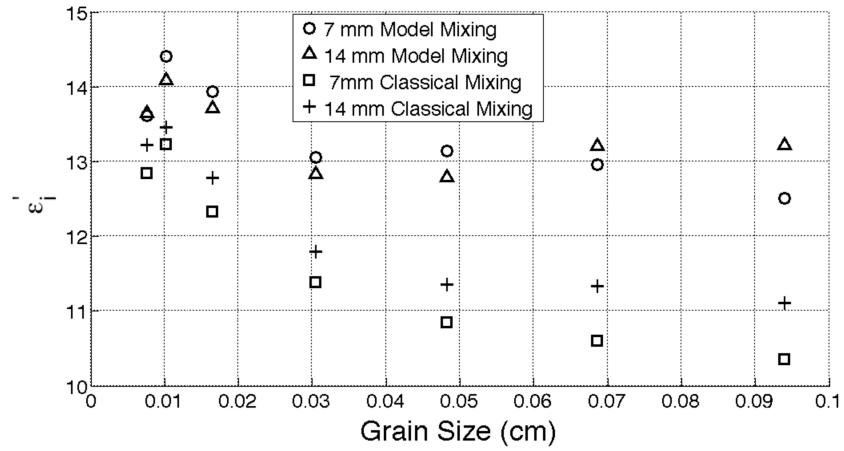


Figure 5.12: Study Results (Figure 5.5) derived using the Lichtenecker equation.

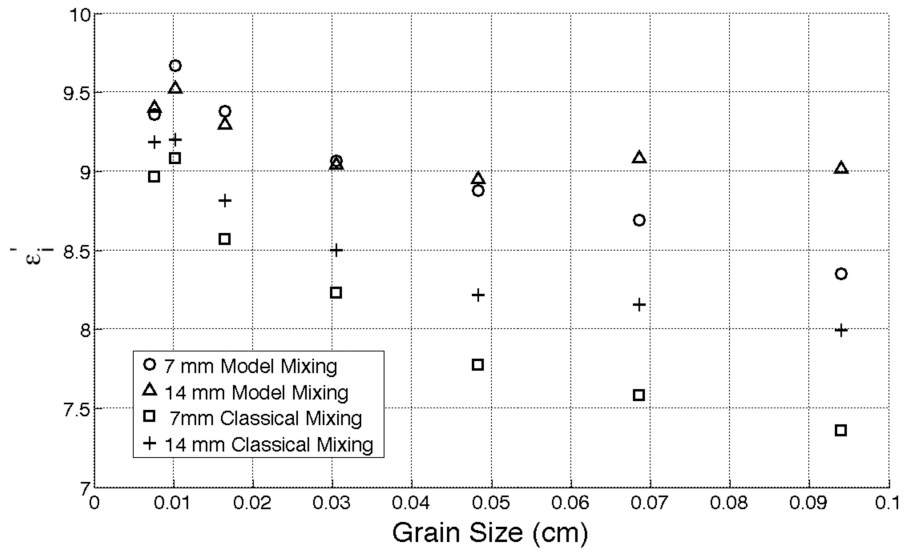


Figure 5.13: Study Results (Figure 5.5) derived using the Looyenga-Landau-Lifshitz equation.

5.10 Summary

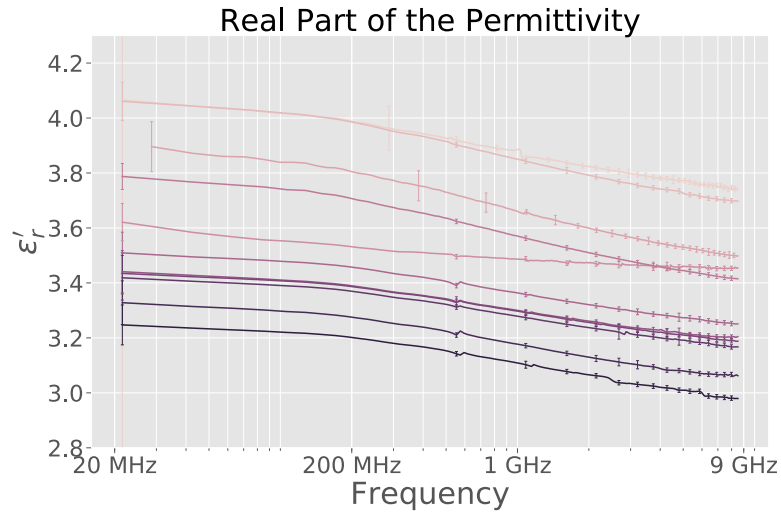
The above discussion highlighted the boundary effects in the coaxial airline during the measurement of the permittivity of a powder sample and provided a model to account for these effects when applying mixing theory. As was shown, the boundary effects are more pronounced for larger grain sizes, which is why the average grain size of samples measured in the research presented in this thesis was kept $< 200 \mu\text{m}$. Although the model showed good results with the aluminium oxide dataset, the influence of PSD on the model was not tested. A broad PSD would imply that voids between larger particles could be filled with smaller particles, and would change the local porosity. This is an opportunity for future work to expand on that presented in this thesis. The boundary conditions model is applied throughout the remainder of this thesis to the experimental results obtained.

Chapter 6

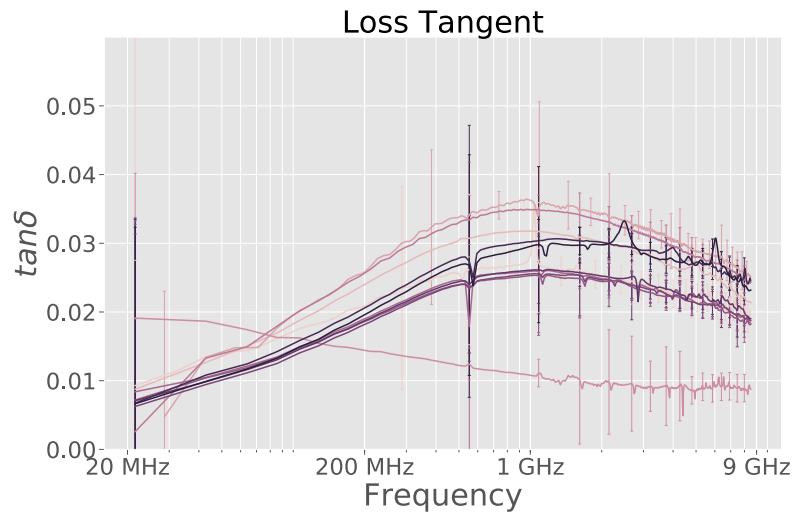
Permittivity Measurements and Mixing Theory Analysis

6.1 Permittivity Measurement Results

The permittivity of each powdered sample was measured using the methodology described in chapter 3, incrementally adding silica aerogel to the samples between measurements so that the measurements spanned a range of porosities. Figures 6.1 - 6.7 show the complex permittivity measured for each sample grouped by sample. In Figures 6.1 - 6.7 the data is plotted with errorbars every 25 data points, with the error calculated using the Type A and Type B uncertainty in *permittivitycalc* (Boivin and Hickson, 2018). The Type A error for powder permittivity measurements described in this thesis is only applicable for a set of permittivity measurements, and cannot be applied to any one measurement. The effects of higher order modes in the measured data above the cutoff frequency is minimal in the real part of the permittivity, but can be clearly identified in the loss tangent measurements. In general the samples are low-loss with resonance spikes present in each dataset, being more pronounced in the loss tangent. The lizardite and antigorite samples display the highest loss tangents which is characteristic of their phyllosilicate mineralogy and structural water in the form of a hydroxyl group (OH^-). Due to the lack of significant relaxation peaks and loss mechanisms at the frequencies measured, every sample except the aluminium oxide sample is frequency independent (see section 6.1.1 for discussion of aluminium oxide dispersion). There are some broader spikes in the loss tangent data (Figures 6.3 and 6.7) that are thought to be the result of imperfect coaxial connections, washer placement, or minor calibration errors. The real part of the permittivity is largely unaffected (within the plotted errorbars) by these errors. Furthermore, these sources of error are accounted for in the Type A uncertainty for powder measurements reported for the frequency-averaged permittivities of the powder samples as discussed in

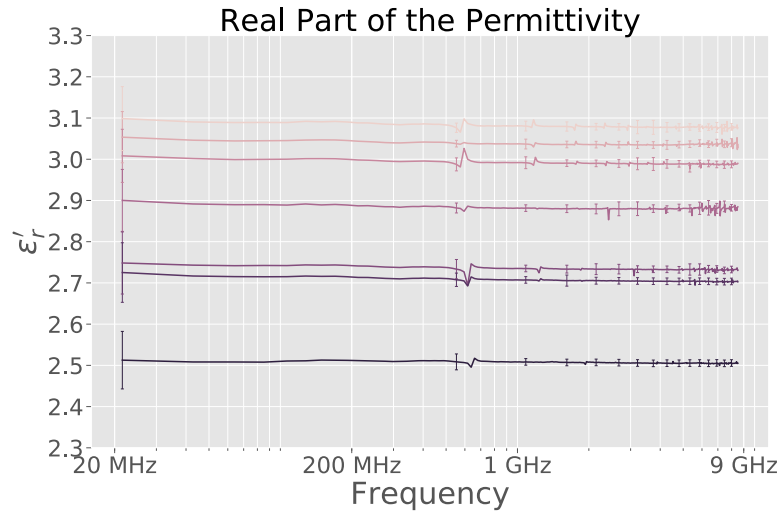


(a) Real part of the permittivity.

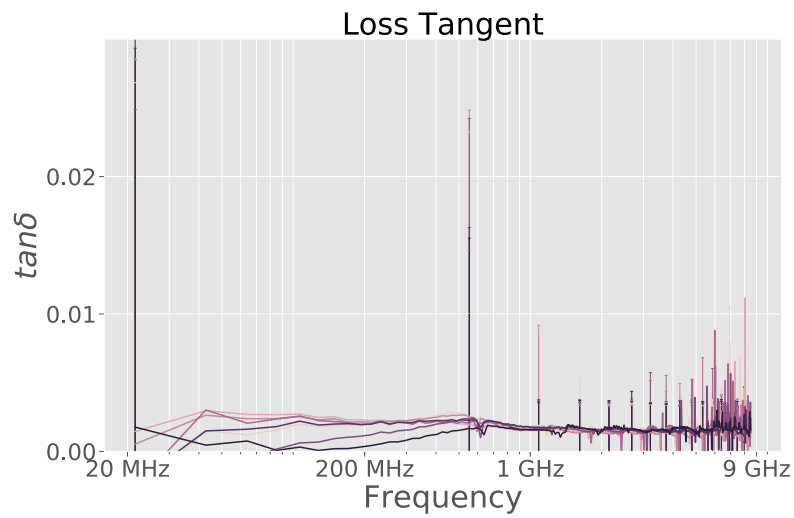


(b) Loss tangent.

Figure 6.1: Dataset of permittivity measurements of the aluminium oxide sample.

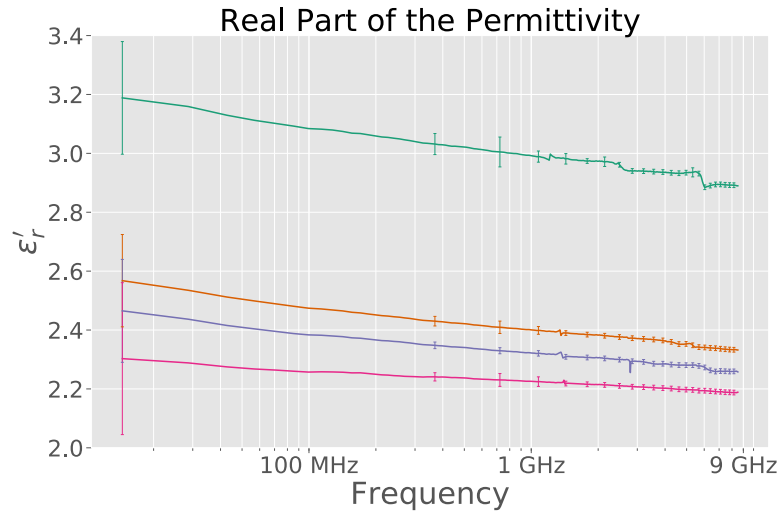


(a) Real part of the permittivity.

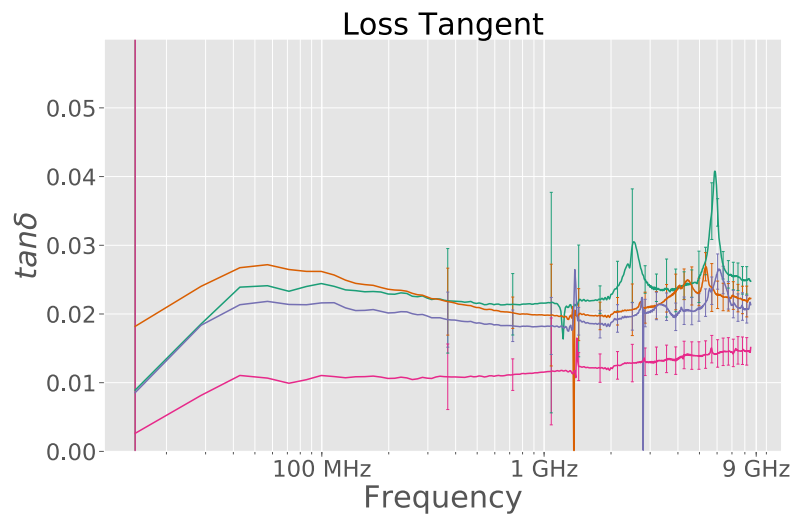


(b) Loss tangent.

Figure 6.2: Dataset of permittivity measurements of the forsterite sample.

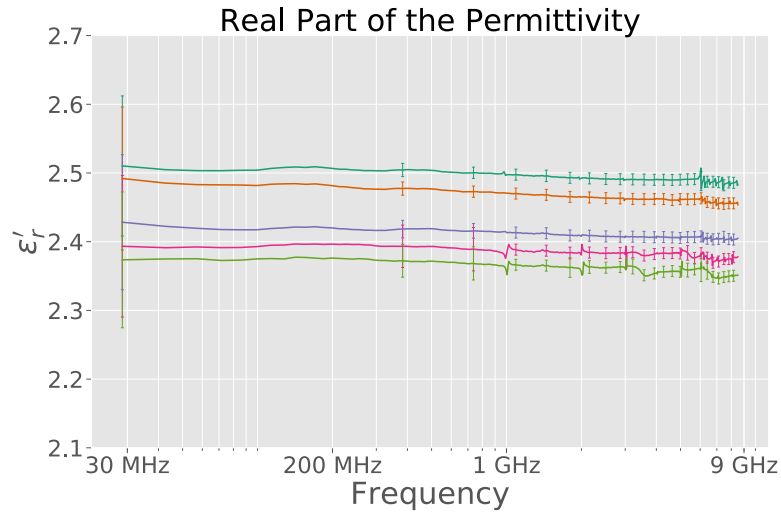


(a) Real part of the permittivity.

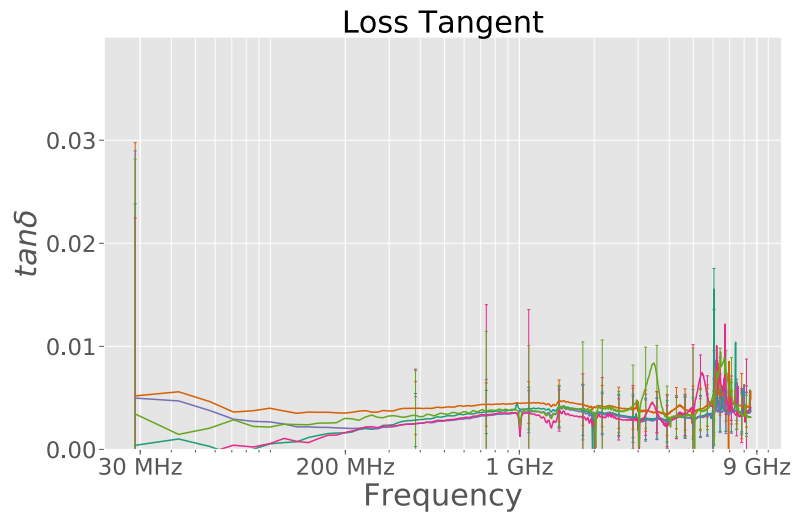


(b) Loss tangent.

Figure 6.3: Dataset of permittivity measurements of the lizardite sample.

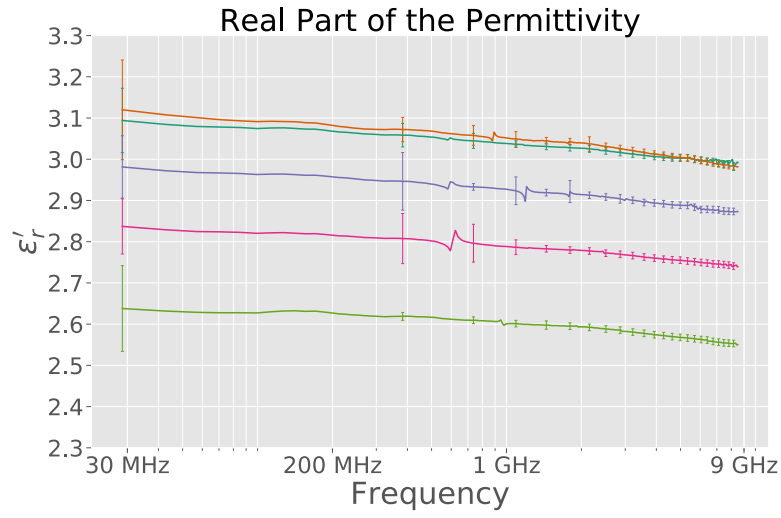


(a) Real part of the permittivity.

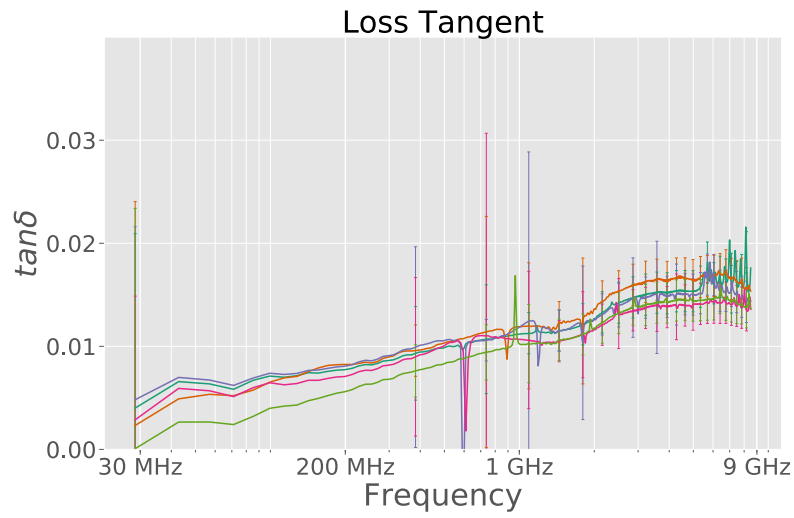


(b) Loss tangent.

Figure 6.4: Dataset of permittivity measurements of the fayalite sample.

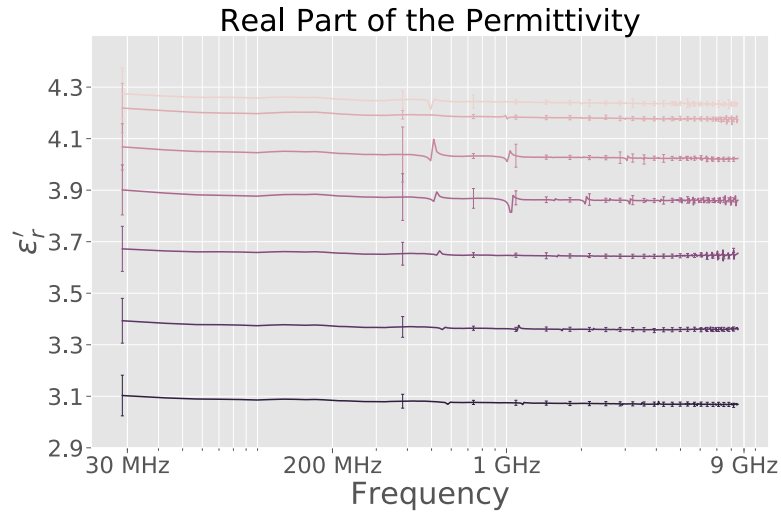


(a) Real part of the permittivity.

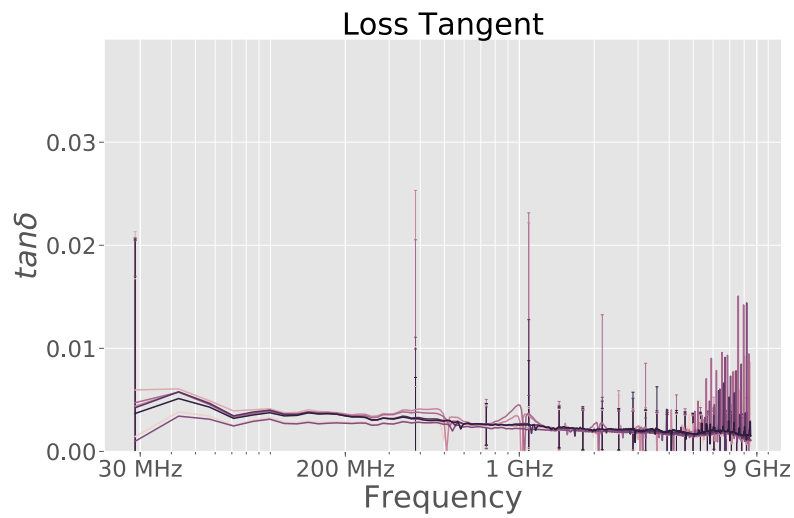


(b) Loss tangent.

Figure 6.5: Dataset of permittivity measurements of the antigorite sample.

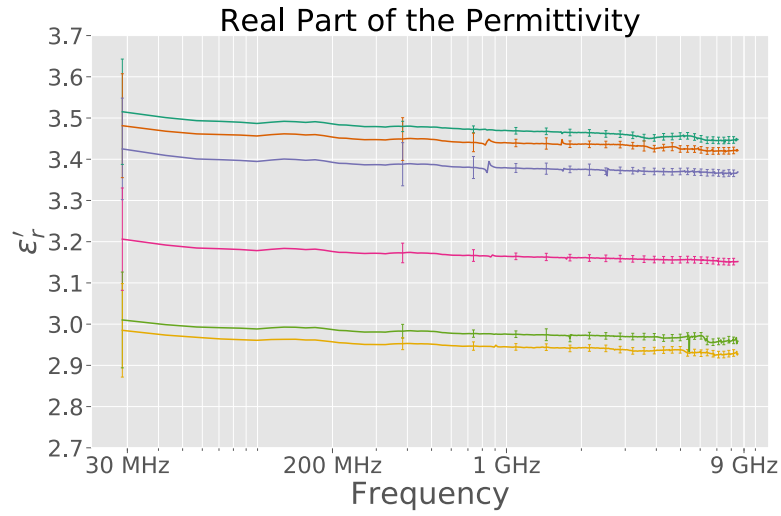


(a) Real part of the permittivity.

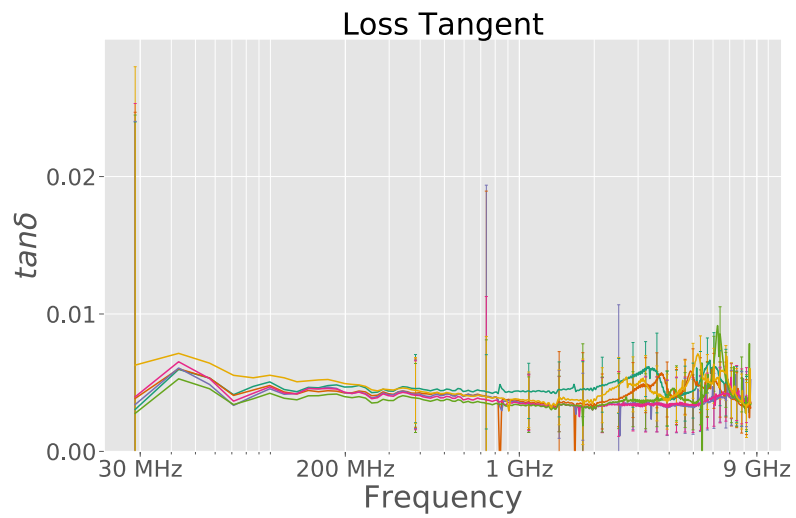


(b) Loss tangent.

Figure 6.6: Dataset of permittivity measurements of the dolomite sample.



(a) Real part of the permittivity.



(b) Loss tangent.

Figure 6.7: Dataset of permittivity measurements of the labradorite sample.

section 3.9.2. It is difficult to eliminate all sources of measurement error for any one permittivity measurement, let alone for a large set of data as is presented in this thesis. The analysis of the data is focused on the real part of the permittivity by averaging across frequency and reporting the Type A uncertainty for powder samples (section 3.9.2). The range in permittivities between measurements of a given sample are a result of the differences in porosity of each sample measurement. The frequency-averaged permittivity of each measurement was extracted from the datasets and is considered representative of the permittivity of the measurement from 1 - 8.5 GHz (Tables 6.1 and 6.2, with the error reported as the Type A uncertainty for powder permittivity measurements (section 3.9.2)). The Type A uncertainty for powder samples reported in Tables 6.1 and 6.2 is different for each sample owing to the different sample properties, and describes the repeatability of measurements for a given sample.

Table 6.1: Frequency-averaged permittivities, $\langle \epsilon'_r \rangle$, of aluminium oxide, dolomite, and labradorite measurements.

Sample Description	Effective permittivity $\langle \epsilon'_r \rangle$	Bulk Density, ρ_{bd} (g/cm³)
Aluminium Oxide	3.78 ± 0.08	2.054 ± 0.002
Aluminium Oxide	3.73 ± 0.08	1.957 ± 0.002
Aluminium Oxide	3.54 ± 0.08	1.832 ± 0.002
Aluminium Oxide	3.46 ± 0.08	1.811 ± 0.002
Aluminium Oxide	3.45 ± 0.08	1.783 ± 0.002
Aluminium Oxide & silica aerogel	3.28 ± 0.08	1.774 ± 0.002
Aluminium Oxide & silica aerogel	3.22 ± 0.08	1.758 ± 0.002
Aluminium Oxide & silica aerogel	3.22 ± 0.08	1.731 ± 0.002
Aluminium Oxide & silica aerogel	3.20 ± 0.08	1.713 ± 0.002
Aluminium Oxide & silica aerogel	3.09 ± 0.08	1.619 ± 0.002
Aluminium Oxide & silica aerogel	3.01 ± 0.08	1.566 ± 0.001
Dolomite	4.2 ± 0.3	1.961 ± 0.002
Dolomite	4.2 ± 0.3	1.922 ± 0.002
Dolomite	4.0 ± 0.3	1.867 ± 0.002
Dolomite	3.9 ± 0.3	1.805 ± 0.002
Dolomite & silica aerogel	3.6 ± 0.3	1.719 ± 0.002
Dolomite & silica aerogel	3.4 ± 0.3	1.600 ± 0.002
Dolomite & silica aerogel	3.1 ± 0.3	1.456 ± 0.001
Labradorite	3.45 ± 0.09	1.726 ± 0.002
Labradorite	3.43 ± 0.09	1.700 ± 0.002
Labradorite	3.37 ± 0.09	1.677 ± 0.002
Labradorite & silica aerogel	3.16 ± 0.09	1.587 ± 0.002
Labradorite & silica aerogel	2.97 ± 0.09	1.486 ± 0.001
Labradorite & silica aerogel	2.93 ± 0.09	1.468 ± 0.001

Table 6.2: Frequency-averaged permittivities, $\langle \epsilon'_r \rangle$, of forsterite, fayalite, and antigorite measurements

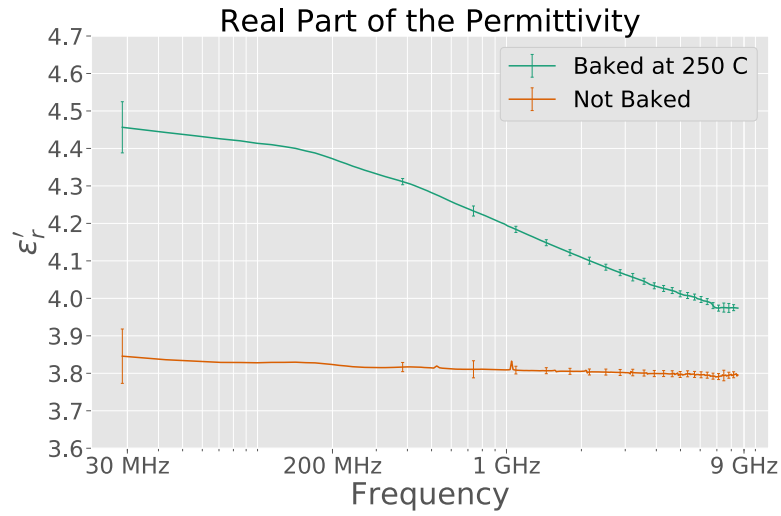
Sample Description	Effective permittivity $\langle \epsilon'_r \rangle$	Bulk Density, ρ_{bd} (g/cm³)
Forsterite	3.08 ± 0.01	1.743 ± 0.002
Forsterite	3.04 ± 0.01	1.724 ± 0.002
Forsterite	2.99 ± 0.01	1.698 ± 0.002
Forsterite & silica aerogel	2.88 ± 0.01	1.638 ± 0.002
Forsterite & silica aerogel	2.73 ± 0.01	1.553 ± 0.001
Forsterite & silica aerogel	2.70 ± 0.01	1.518 ± 0.001
Forsterite & silica aerogel	2.51 ± 0.01	1.393 ± 0.001
Fayalite & silica aerogel	2.49 ± 0.01	1.587 ± 0.002
Fayalite & silica aerogel	2.46 ± 0.01	1.566 ± 0.001
Fayalite & silica aerogel	2.41 ± 0.01	1.525 ± 0.001
Fayalite	2.38 ± 0.01	1.488 ± 0.001
Fayalite*	2.35 ± 0.01	1.469 ± 0.001
Antigorite	3.00 ± 0.03	1.562 ± 0.001
Antigorite	3.00 ± 0.03	1.537 ± 0.001
Antigorite	2.89 ± 0.03	1.505 ± 0.001
Antigorite	2.76 ± 0.03	1.423 ± 0.001
Antigorite & silica aerogel	2.57 ± 0.03	1.274 ± 0.001
Lizardite & silica aerogel	2.92 ± 0.06	1.451 ± 0.001
Lizardite & silica aerogel	2.34 ± 0.06	1.138 ± 0.001
Lizardite & silica aerogel	2.27 ± 0.06	1.100 ± 0.001
Lizardite & silica aerogel	2.19 ± 0.06	1.062 ± 0.001

*Sample prior to oxidation

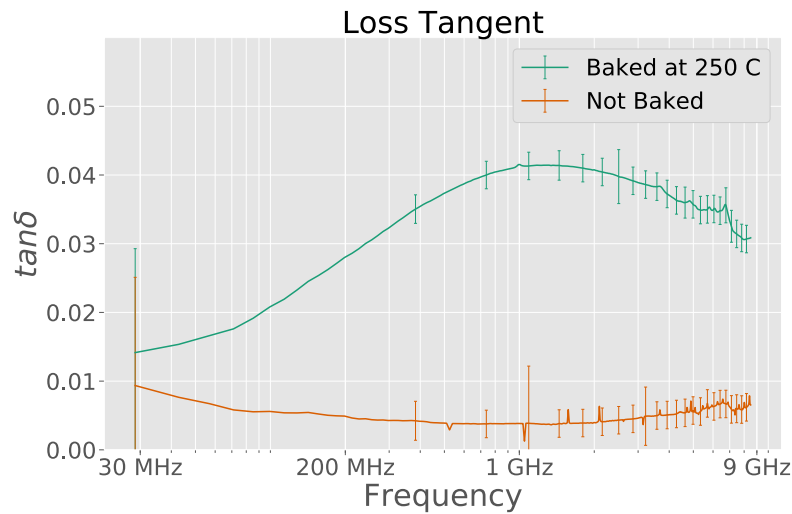
6.1.1 Aluminium Oxide Dispersion

The permittivity measurement dataset for the aluminium oxide sample shows the most significant dispersion with a broad relaxation peak visually identifiable in the loss tangent (Figure 6.1). One measurement, however, does not contain this relaxation peak and displays the low loss behaviour that is expected of aluminium oxide. At first, this discrepancy was attributed to water retention in the samples; however, this did not seem likely since the samples for measurements showing the relaxation peak were oven dried at 250° C and were measured in the environment chamber. In further contradiction to this hypothesis, the sample measurement that does not show the relaxation peak was oven dried at 115° C. If water is responsible for the relaxation, the dispersion behaviour should be reversed (assuming water would more likely be left in the sample if dried at a lower temperature) for these samples. A simple experiment to test if water was responsible for the relaxation peak was performed. A 76 µm average grain size aluminium oxide sample was oven dried at 250° C for 36 hours and its permittivity was measured under ambient conditions. Another 76 µm average grain size aluminium oxide sample from the same overall sample batch was not oven dried,

and its permittivity was measured under the same conditions and for the same calibration. The results of these measurements are shown in Figures 6.8 and 6.9. In Figure 6.8, the sample that



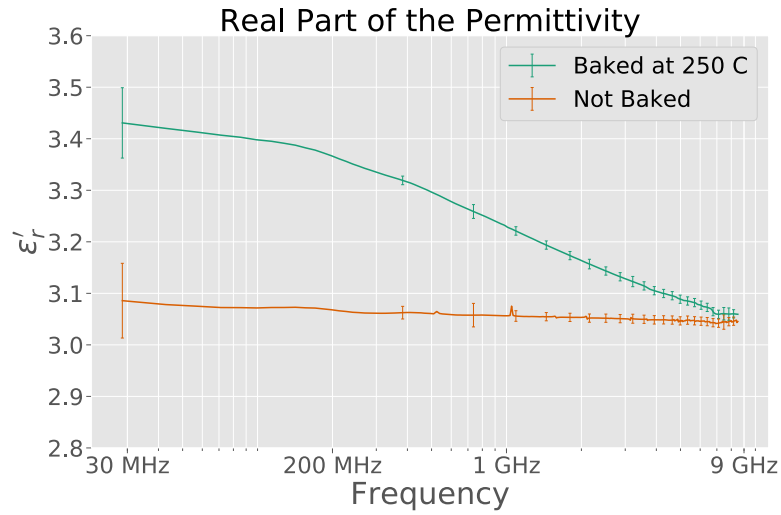
(a) Real part of the permittivity.



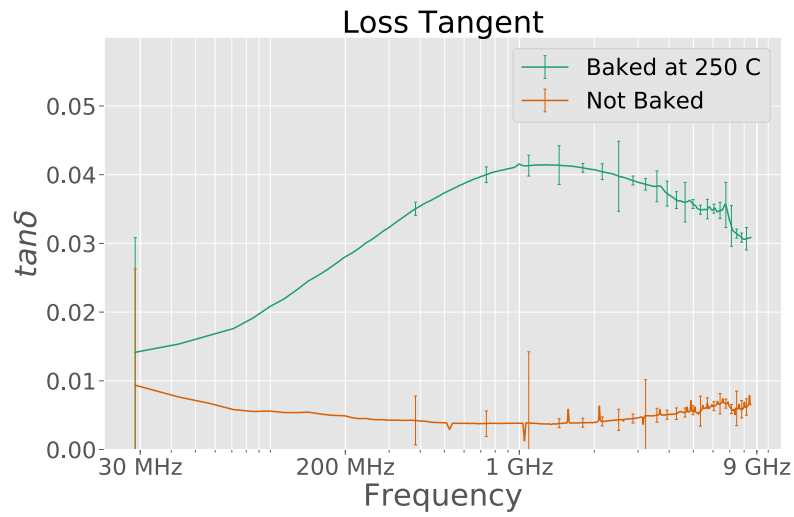
(b) Loss tangent.

Figure 6.8: Permittivity measurements of two $76 \mu\text{m}$ average grain size aluminium oxide, one oven dried at 250°C and the other not oven dried.

was oven dried at 250°C shows the relaxation peak and the sample that was not oven dried shows



(a) Real part of the permittivity.



(b) Loss tangent.

Figure 6.9: Permittivity measurements of two $76 \mu\text{m}$ average grain size aluminium oxide, one oven dried at 250°C and the other not oven dried. Data normalized to a bulk density of $\rho_{\text{bd}} = 1.60 \text{ g/cm}^3$ using the fitted LLL equation.

no relaxation peak. The relaxation peak is most likely not a result of water, since the sample that was oven dried at 250° C is assumed to have retained less water in the sample than the sample that was not oven dried. Instead, this seems to be the result of some alteration of the aluminium oxide sample that is occurring when heated. Courtney (1970) measured the loss tangent of hot-pressed alumina (aluminium oxide) and observed an increase with temperature up to 130° C, although the frequency of measurement for this observation was not specified. Geyer (1990) discussed observed increases in the loss tangent of alumina above 450° C at 1 MHz, although this frequency is well below the relaxation observed in the current data. Krupka et al. (1998) measured an increase in the loss tangent of alumina with temperature up to 150° C at 7.53 GHz. Westphal and Sils (1972) measured the loss tangent of various forms of alumina and observed a broad relaxation peak around 10 GHz at temperatures from 25° – 350° C. Tallan and Detwiler (1963) measured anomalous dispersion in permittivity measurements of single crystal sapphire (aluminium oxide) at temperatures greater than 200° C and frequencies below 10⁴ Hz. The authors attribute the relaxation to interfacial polarization caused by the estimated 10 μm thick electrical double layer at the crystal surface.

In regards to the current research, the sample that was oven dried at 250° C was measured when the sample had been out of the oven for 2 hours (no water was re-adsorbed by the sample as it was filled into the coaxial airline and left on the mass balance to observe any mass change over this time) and re-equilibrated to room temperature. An increase in the loss tangent with increasing temperature is fairly standard for materials; however, in the case of the current measurement the sample was at room temperature. The interfacial polarization observed by Tallan and Detwiler (1963) in their measurements occurs at much lower frequencies than the observed relaxation in the current research. It is unsure as to the physical mechanism responsible for the observed relaxation peak in the permittivity measurements of aluminium oxide. It is possible that some sort of phase transition between alumina polymorphs occurred, although this does not seem likely at such a low temperature. Figure 6.9 shows the data from Figure 6.8 normalized to a bulk density of 1.60 g/cm³. In Figure 6.9 the high frequency data (real part) for either sample is in good agreement, indicating that the relaxation is not significantly affecting the real part of the permittivity that is of interest to the mixing analysis. The frequency-averaged permittivities for the normalized (to a bulk density of 1.60 g/cm³ using the optimized LLL equation) measurements are $\langle \epsilon'_r \rangle = 3.10 \pm 0.08$ and $\langle \epsilon'_r \rangle = 3.05 \pm 0.08$ for the sample oven dried at 250° C and not dried respectively. These permittivities are equivalent to each other within the Type A uncertainty for powder samples

calculated for the frequency-averaged permittivities of the aluminium oxide sample. Based on this, the real part of the permittivity measured for the aluminium oxide samples that show the relaxation peak is considered equivalent to that measured for aluminium oxide samples that do not show the relaxation peak. The dispersive aluminium oxide measurements are fit (using the Python package *LMFIT* (Newville et al., 2014)) with the Havriliak-Negami and Cole-Cole relaxation models in Figures 6.10 and 6.11. The fitting parameters for these models are given in Table 6.3.

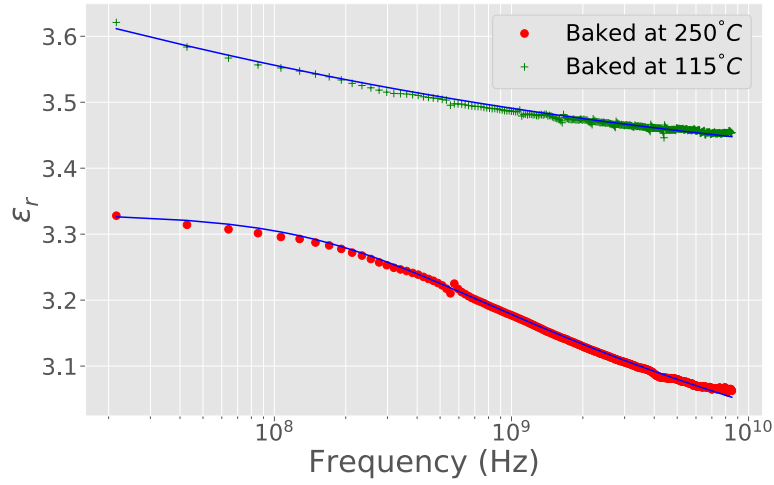
Table 6.3: Fitting parameters for Havriliak-Negami and Cole-Cole model fits to aluminium oxide data from Figures 6.10 and 6.11 (Maximum value of $\tau = 5.0 \times 10^{-7}$ s applied). Note the samples were measured at different bulk densities.

Fitting Parameter	Havriliak-Negami Model		Cole-Cole Model	
	Oven Baked 250° C	Oven Baked 115° C	Oven Baked 250° C	Oven Baked 115° C
$\epsilon'_{r,s}$	3.332	4.240	3.384	4.241
$\epsilon'_{r,\infty}$	2.795	3.362	2.937	3.362
τ	7.261×10^{-10} s	4.983×10^{-7} s	1.166×10^{-10} s	5.000×10^{-07} s
α	0.846	0.214	0.501	0.214
β	0.222	1	-	-

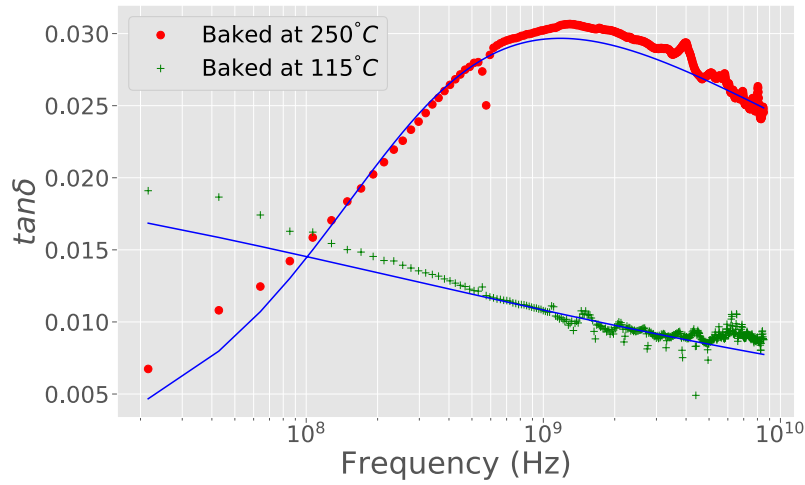
The Havriliak-Negami (HN) model fit the data better than the Cole-Cole (CC) model (lower root-mean-square-error, RMSE), although the frequency of the relaxation peak in the CC model, $f = 1.36$ GHz, matches the observed peak better. The data used to fit these models is not the same as in Figure 6.8, but is instead permittivity measurements of aluminium oxide samples that were heated at 250° C and 115° C and measured in the environment chamber. The relaxation peak was generally not seen in any aluminium oxide measurements heated at 115° C, unless that sample had experienced prolonged exposure at this temperature.

6.2 Fitting mixing theories to data

Tables 6.1 and 6.2 list the frequency-averaged measured (effective, since the sample is considered a mixture) permittivity of each sample at different bulk densities. This data is plotted in Figure 6.12 as a function of bulk density, and in Figure 6.13 as a function of volume fraction of powder ($1 - \text{porosity}$, or $1 - \phi$), where the measured grain density of a given sample is used to convert between bulk density and volume fraction. The grouping of the sample datasets relative to one another changes when viewed as a function of bulk density and volume fraction. The lizardite and antigorite datasets plot close to one another in both cases, as would be expected since they are mineral polymorphs with similar chemical compositions and grain densities. The functional form

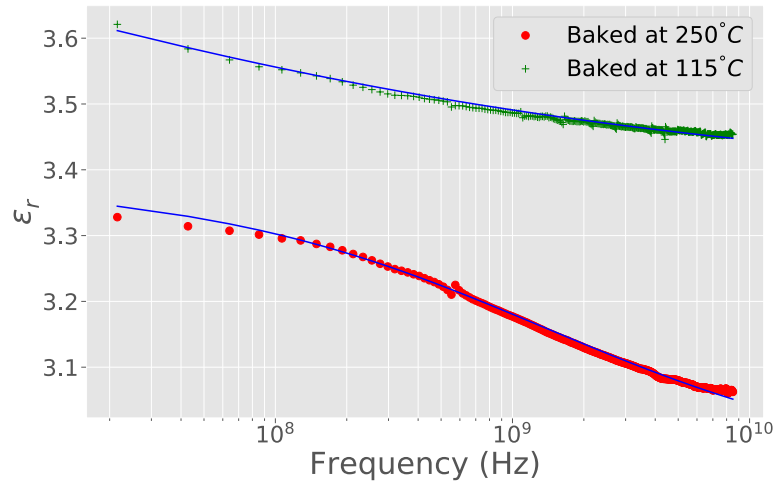


(a) Real part of the permittivity.

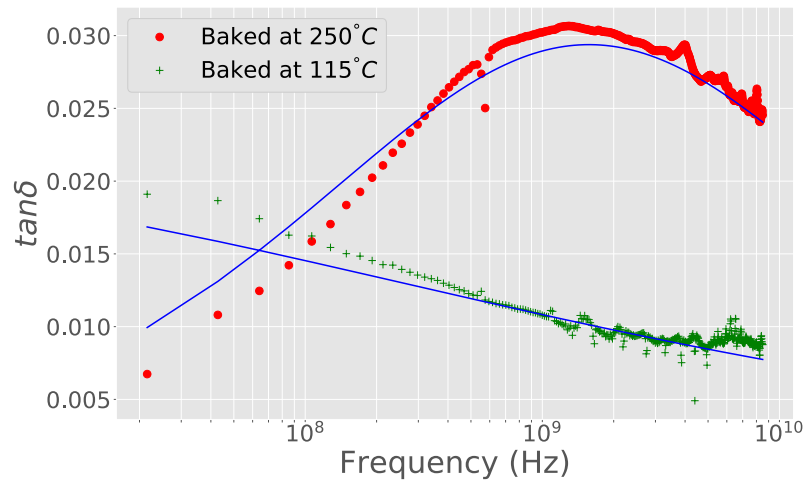


(b) Loss tangent.

Figure 6.10: Permittivity measurements of two 76 μm average grain size aluminium oxide, one oven dried at 250° C and the other oven dried at 115° C fitted with the Havriliak-Negami relaxation model (Maximum value of $\tau = 5.0 \times 10^{-7}$ s applied).



(a) Real part of the permittivity.



(b) Loss tangent.

Figure 6.11: Permittivity measurements of two $76 \mu\text{m}$ average grain size aluminium oxide, one oven dried at 250°C and the other oven dried at 115°C fitted with the Cole-Cole relaxation model.

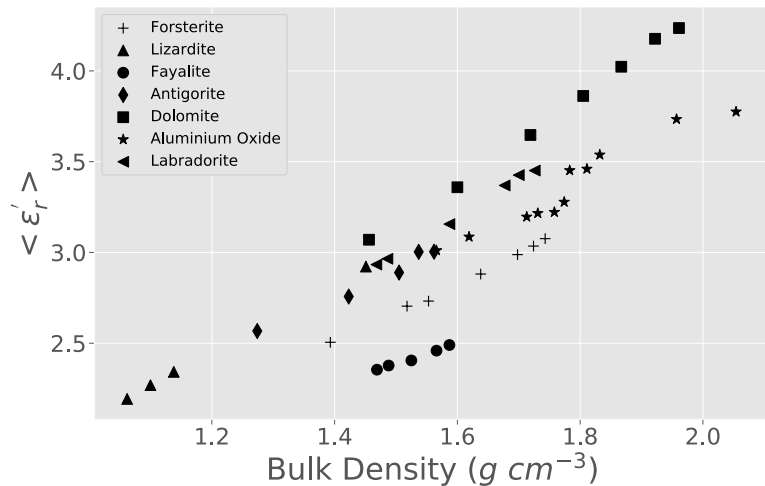


Figure 6.12: Frequency-averaged permittivity as a function of bulk density.

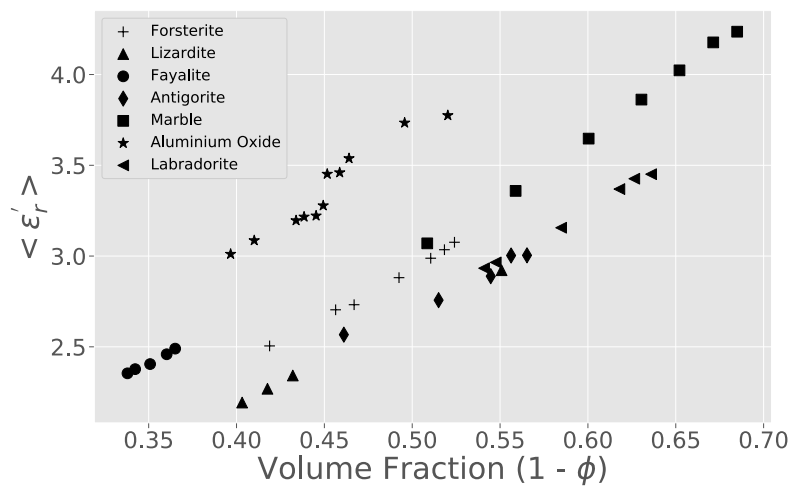
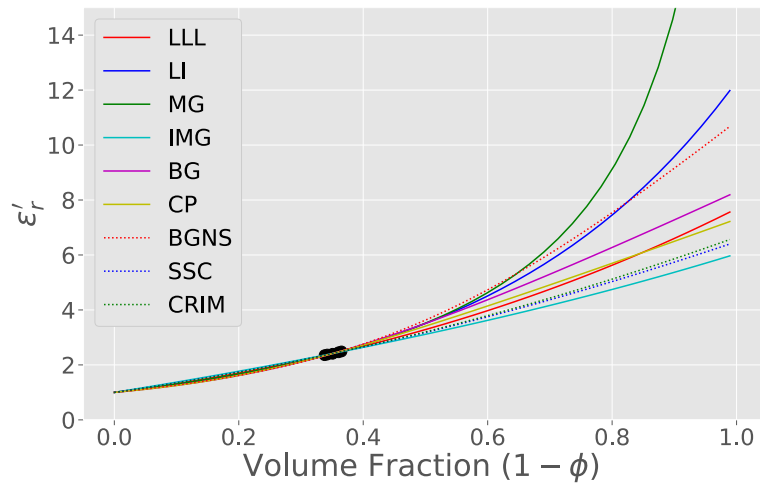


Figure 6.13: Frequency-averaged permittivity as a function of volume fraction ($1 - \phi$).

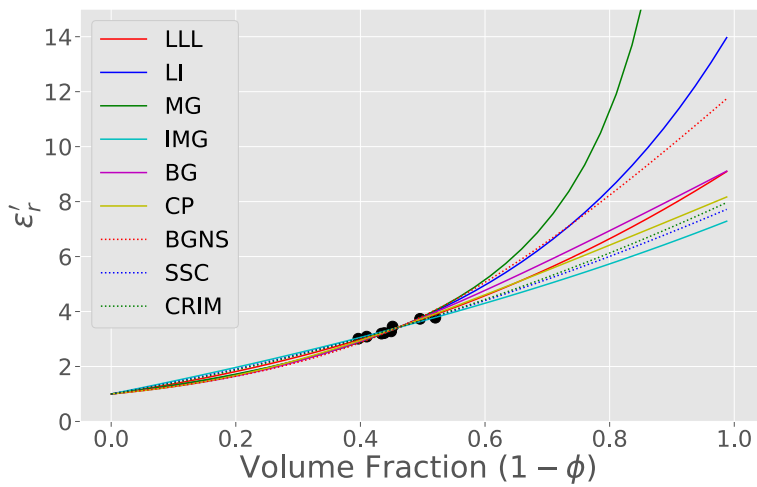
of each of the two-phase mixing equations from Table 2.1 is bounded by the permittivities of each mixture phase and their relative proportions. For powder permittivity measurements one phase is air with a permittivity of 1. The porosity, and therefore also the volume fraction of powder sample, is known for each permittivity measurement through the measured bulk density and grain density of the sample. As a result there is only one free parameter with which to fit a mixing model to powder measurements of a given sample, which is the permittivity of individual grains, or the solid permittivity, of that sample. A non-linear least squares regression was performed of each sample dataset for each mixing equation to determine the solid permittivity that provides the best fit for that mixing model. The Python package *LMFIT*, utilizing the Levenberg-Marquadt method, was used to do this (Newville et al., 2014). It was found that almost any mixing model could fit the powder permittivity measurements, as long as the solid permittivity of the sample was derived through least squares regression analysis. Figure 6.14 shows the result of applying this regression analysis for each mixing equation to the fayalite and aluminium oxide datasets. The goodness of the fits can be judged by the RMSE between the predicted and observed (measured) permittivity, and was generally constant across all fitted mixing models for all samples. This fact highlights the ambiguity of numerous studies in experimentally verifying mixing theories, since any mixing theory has the potential to fit a set of data. Another metric besides the goodness of fit of a mixing model is thus required to compare the accuracy of the different models.

6.3 Comparison to the literature

The free parameter that was optimized in the regression for each mixing model was the solid permittivity assumed for a given sample. This provides a metric with which to compare the accuracy of each fitted mixing model. If a mixing model is fitted to a sample dataset with a solid permittivity that is physically unrealistic for that sample, the model is then also unrealistic and inaccurate in describing the mixing behaviour of that sample. To compare the accuracy of each mixing model it is then necessary to know what the solid permittivity of each sample is. The data presented in Tables 6.4 - 6.9 summarize the results of dielectric experiments in the literature on solid samples (single crystal, or densified samples) that are the closest match to the samples used in the current research. If the papers presented numerous measurements of the same sample, either the average of the measurements were taken or the measurement corresponding to the purest sample, or sample with a composition closest to those in this research, was chosen. The measurement method



(a) Fayalite dataset.



(b) Aluminium oxide dataset.

Figure 6.14: Regression of mixing models for fayalite and aluminium oxide datasets. The data points are the frequency-averaged permittivity, $\langle \epsilon'_r \rangle$, for each measurement.

is listed in Tables 6.4 - 6.9 if provided in the study.

Table 6.4: Solid aluminium oxide permittivity measurements from the literature.

Aluminium Oxide			
Reference	ϵ_r'	Frequency	Method
(Young and Frederikse, 1973)	10.44	10 Hz - 8 GHz	-
(von Hippel, 1954)	9.58	10 Hz - 300 MHz	-
(Carmichael, 1982)	12.1	Radio	-
(Gershon et al., 2001)	9.02	1 - 4 GHz	Resonant Cavity
(Rajab et al., 2008)	9.424	17 GHz	Resonant Cavity
(Robertson, 2000)	9	-	-
(Tuhkala et al., 2013)	9.8	4.5 GHz	Open Ended Coaxial Resonator
(Bussey et al., 1964)	9.42	8.6 - 9.2 GHz	Waveguide/Resonator ¹
(Penn et al., 1997)	9.5	10 GHz	Resonant Cavity
(Webb and Church, 1986)	9.1	100 MHz - 1 GHz	Coaxial liquid immersion
(Olhoeft, 1981)	12.6	1 MHz	-
(Olhoeft, 1981)	9.2	1 MHz	3-Terminal Sample Holder
(Krupka et al., 1998)	10.1	5.4 - 7.53 GHz	Resonant Cavity
(Courtney, 1970)	9.74	9.905 - 12.223 GHz	Dielectric Post Resonator
(Westphal and Sils, 1972)	10.07	3 GHz	-
(Church et al., 1988)	9.81	915 MHz	Coaxial Liquid Immersion
(Sharif, 1995)	12.66	10 GHz	Waveguide Transmission Line
(Plaßmann and Schulz, 2009)	9.8	-	-
(Rosenholtz and Smith, 1936)	5.35	60 Hz	-
(Fontanella et al., 1974)	10.154	1 GHz	Capacitance Bridge

¹Short Circuited Waveguide, Resonant Cavity, H_{011} Resonator

Table 6.5: Solid dolomite permittivity measurements from the literature.

Dolomite			
Reference	ϵ_r'	Frequency	Method
(Fensler et al., 1962) ¹	9.84	420 MHz - 1.8 GHz	Waveguide
(Bapna and Joshi, 2013) ²	4.18	8.8 - 12.2 GHz	Waveguide
(Sengwa and Soni, 2005) ²	6.86	10.1 GHz	Waveguide
(Olhoeft, 1981) ³	7.3	1 MHz	3-Terminal Sample Holder
(Olhoeft, 1981)	7.4	1 MHz	3-Terminal Sample Holder
(Church et al., 1988)	7.26	915 MHz	Coaxial Liquid Immersion
(Pervin, 2015)	6.63	10 MHz - 3 GHz	Coaxial Probe
(Shen et al., 1985) ⁴	6.82	0.8 - 1.2 GHz	Coaxial Transmission Line
(Rosenholtz and Smith, 1936)	8.45	60 Hz	-
(Ulaby et al., 1988)	6.67	1 - 16 GHz	Resonant Cavity
(Carmichael, 1982)	7.4	-	-

¹ White Marble

² White Marble (high Mg content)

³ Marble Dolomitic

⁴ Dolomite with 5.9 - 6.6% porosity

Table 6.6: Solid fayalite permittivity measurements from the literature.

Fayalite			
Reference	ϵ_r'	Frequency	Method
(Geyer, 1990)	5.77	10 GHz	-
(Shannon et al., 1991)	8.77	1 MHz	Parallel Plate Capacitor
(Olhoeft, 1981)	6.8	1 MHz	3-Terminal Sample Holder
(Takei, 1978)	10.35	1 MHz	-
(Suwa, 1964)	14.65	1 MHz	-
(Xiao, 1985)	12.33	9.4 GHz	-

Table 6.7: Solid forsterite permittivity measurements from the literature.

Forsterite			
Reference	ϵ_r'	Frequency	Method
(Shannon et al., 1991) ¹	7.27	1 MHz	Parallel Plate Capacitor
(Davis et al., 1988) ²	8.12	600 kHz	Impedance Analyzer
(Cygan and Lasaga, 1986) ³	7.26	1 MHz	Capacitance Bridge
(Ghosh and Das, 1979)	6.5	100 kHz - 25 MHz	-
(Shannon, 1990)	7.00	-	-
(Saint-Amant, 1968) ⁴	6.4	high frequency limit	-
(Saint-Amant and Strangway, 1970) ⁴	8.2	1 MHz	Capacitance Bridge
(Rosenholtz and Smith, 1936) ⁵	6.77	60 Hz	-
(Ulaby et al., 1988) ⁴	6.10	1 - 16 GHz	Resonant Cavity
(Campbell and Ulrichs, 1969) ⁴	6.15	450 MHz, 35 GHz	Waveguide/Resonant Cavity
(Olhoeft, 1981) ⁵	7.3	1 MHz	3-Terminal Sample Holder
(Olhoeft, 1981)	6.8	1 MHz	-
(Xiao, 1985) ⁵	8.36	9.4 GHz	-

¹ $Mg_{1.80}Fe_{0.22}SiO_4$

² $Mg_{1.86}Fe_{0.14}SiO_4$

³ Synthetic

⁴ Dunite

⁵ Olivine

Table 6.8: Solid labradorite permittivity measurements from the literature.

Labradorite			
Reference	ϵ_r'	Frequency	Method
(Rosenholtz and Smith, 1936)	6.98	60 Hz	-
(Olhoeft, 1981)	6.57	1 MHz	3-Terminal Sample Holder
(Zheng et al., 2005) ¹	6.21	9.37 GHz	Resonant Cavity

¹ Anorthosite

Table 6.9: Solid serpentine permittivity measurements from the literature. There were not enough experiments found differentiating between the types of serpentine, and so the analysis of the lizardite and antigorite samples was combined.

Serpentine (Lizardite/Antigorite)			
Reference	ϵ'_r	Frequency	Method
(Rosenholtz and Smith, 1936)	11.48	60 Hz	-
(Campbell and Ulrichs, 1969)	6.55	450 MHz, 35 GHz	Waveguide/Resonant Cavity
(Telford et al., 1990)	6.6	> 100 MHz	-
(Olhoeft, 1981)	12.87	1 MHz	3-Terminal Sample Holder

The averaging of multiple measurements from a given study is important especially for single crystal measurements, since the crystal orientation will affect the measured permittivity (anisotropy). For a particulate sample, it is assumed that the average crystal grain orientation is random, and that the effective single crystal solid permittivity will then be an average of the values for various orientations. Some samples, like aluminium oxide, have many measurements in the literature of standard materials, whereas other natural samples, like labradorite, lizardite and antigorite, have fewer measurements that are of samples with varying composition. Further complicating the matter is that the literature measurements span a range of frequencies. The permittivity measurements presented in this thesis showed little to no dispersion, indicating that this frequency bias is minimized. The moisture content was not constant across all experiments from the literature and may have a significant impact on the measurements, especially for the serpentine samples and for measurements at lower frequencies where interfacial polarization can occur. The methodology and accuracy across the experiments is also varied, in part owing to the historical and technological context of each study.

Considering these biases in the literature measurements, a direct comparison with the solid permittivity values derived through the mixing analysis should be done carefully. To facilitate this comparison, the mean, $\langle \epsilon'_r \rangle$ (this is the same symbol as the frequency-averaged measured permittivity for the samples; in either case the angled brackets are denoting an average), and standard deviation, $S_{\langle \epsilon'_r \rangle}$, were calculated from the literature measurements for each sample. The Student's t -distribution 95% confidence interval, $t_{0.05, n-1} \frac{S_{\langle \epsilon'_r \rangle}}{\sqrt{n}}$, for each mean was then calculated in order to account for smaller datasets. Here $t_{0.05, n-1}$ is the t -value for 95% confidence and $n - 1$ degrees of freedom, where n is the number of literature measurements for a given sample. This confidence interval was then used as the error for the mean permittivity value calculated from the literature

measurements for a given sample, so that the mean value is calculated as: $\langle \epsilon'_r \rangle \pm t_{0.05, n-1} \frac{S_{\langle \epsilon'_r \rangle}}{\sqrt{n}}$. The mean permittivity value and associated error calculated from the literature measurements for each sample used in this research is summarized in Table 6.10. The values in Table 6.10 can now

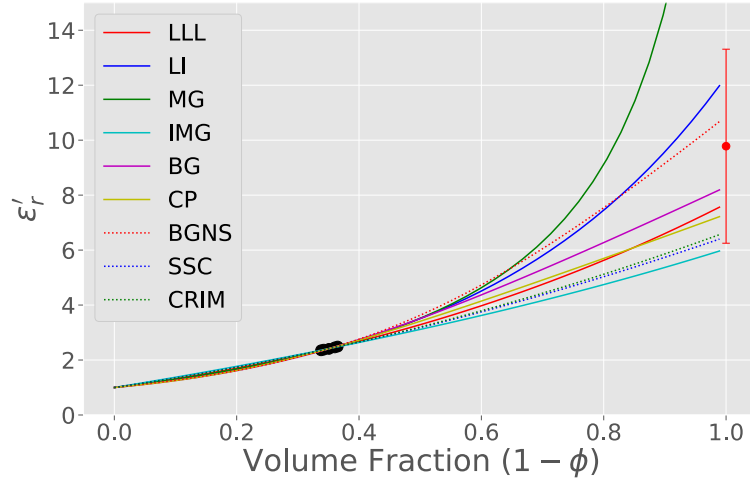
Table 6.10: Mean solid permittivity from the literature with t-distribution 95% confidence intervals.

Sample	$\langle \epsilon'_r \rangle$	$t_{0.05, n-1} \frac{S_{\langle \epsilon'_r \rangle}}{\sqrt{n}}$
Aluminium Oxide	9.84 ±	0.71
Dolomite	7.16 ±	0.92
Fayalite	9.78 ±	3.53
Forsterite	7.09 ±	0.46
Labradorite	6.59 ±	0.96
Serpentine	9.38 ±	5.22

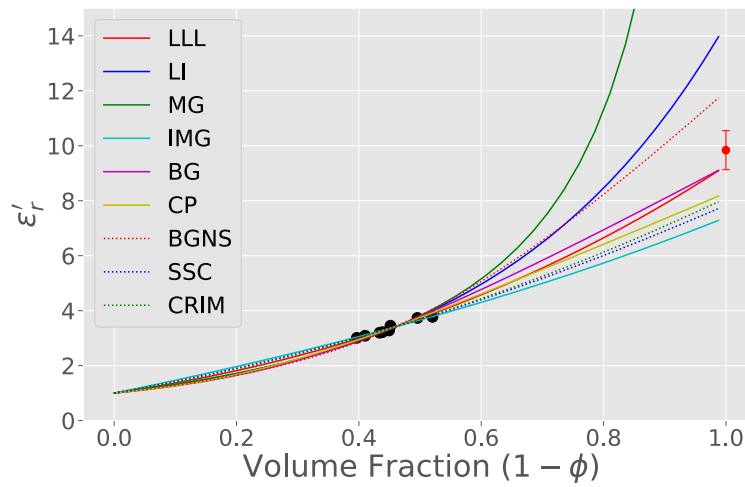
be compared with the solid permittivities resulting from the mixing regression of the powder permittivity measurements presented in this thesis. The same regression analysis from Figure 6.14 is plotted in Figure 6.15 along with the mean solid permittivity from the literature. The large uncertainty in the mean solid permittivity from the literature for the fayalite sample (Figure 6.15(a)) makes it difficult to compare the accuracies of the mixing equations. The lower uncertainty for the aluminium oxide sample (Figure 6.15(b)) makes this comparison easier, and it can clearly be seen that the LLL and BG theories model the dataset with the most accurate solid permittivity. The RMSE between the solid permittivities resulting from regression analysis and the mean solid permittivities from the literature provides a way of quantifying the accuracy of each mixing theory. A weighted RMSE (WRMSE) was applied instead, so that the mean values with lower uncertainty are weighted higher using the uncertainty in the mean solid permittivity from the literature as weights:

$$WRMSE = \sqrt{\sum_{i=1}^N w_i (\langle \epsilon'_{r_i} \rangle - \widehat{\epsilon}'_r)^2} \quad (6.1)$$

In equation (6.1), $\langle \epsilon'_{r_i} \rangle$ is the mean solid permittivity from the literature of the i^{th} sample, $\widehat{\epsilon}'_r$ is the solid permittivity of the i^{th} sample derived for a given mixing equation by fitting the equation to the sample dataset, N is the total number of different samples, and w_i is the weight of the i^{th} sample. The weight for a given sample is the inverse of the squared uncertainty in the mean, $w_i = 1 / (t_{0.05, n-1} \frac{S_{\langle \epsilon'_{r_i} \rangle}}{\sqrt{n}})^2$, where the 95% confidence interval is converted to a percentage of the mean (similar results are obtained if the denominator isn't squared). The weights are normalized so



(a) Fayalite dataset



(b) Aluminium oxide dataset

Figure 6.15: Regression of mixing models for fayalite and aluminium oxide datasets. Mean solid permittivity from the literature measurements are plotted at 100% volume fraction (ideal zero porosity) with the t-distribution 95% confidence intervals as error bars. The data points are the frequency-averaged permittivity, $\langle \epsilon'_r \rangle$, for each measurement.

that $\sum_{i=1}^N w_i = 1$. The WRMSE between the solid permittivity mixing model predictions and mean literature values is shown in Figure 6.16, where each mixing model is applied both with and without coaxial boundary conditions applied (chapter 5). Consideration of the boundary conditions in the

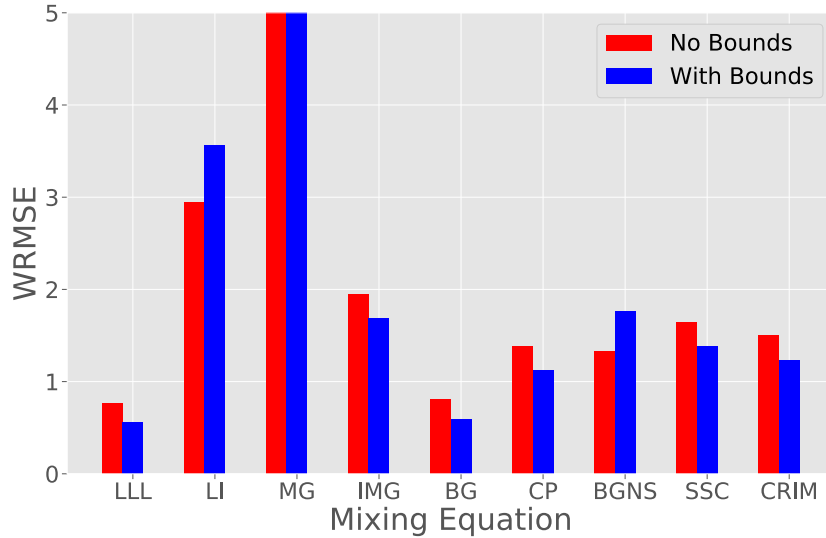


Figure 6.16: WRMSE (equation (6.1)) for each mixing theory prediction compared with literature values across all samples.

mixing modelling increases the solid permittivity required for a given mixing model to fit a dataset because the increased porosity at the sample/conductor interface is taken into account. As a result, models that generally over-predicted the solid permittivity when compared to the mean literature values show an increase of WRMSE when boundary conditions are considered, and models that under-predicted show a decrease of WRMSE. Figure 6.16 shows the LLL and BG equations to have the lowest WRMSE across all samples and are therefore the most accurate models for these samples. This is consistent with the literature review in chapter 2 on the application of mixing theory presented in Tables 2.2 - 2.4, where 56% of studies on dry materials in the GHz range found the LLL and BG models to describe their data best. The permittivity contrast between mixture phases for all of the powder measurements presented in this thesis was $\frac{\epsilon_i}{\epsilon_e} < 10$, and the range of volume fractions of solid inclusions was roughly 0.3 - 0.7. These parameters are consistent with the theoretical assumptions of the LLL and BG mixing models. For dry, particulate minerals, the LLL and BG mixing models most accurately describe the change in the real part of the permittivity across all porosities, up to the solid grain density of a given mineral.

6.3.1 Comparison to Resonant Cavity Measurements

The permittivity of the solid dolomite and labradorite samples was measured in a split cylinder resonator by Brian Tsai prior to the incorporation of either sample into this research. For these measurements, the sample is machined to a flat surface (shape doesn't matter, only size) roughly 1 mm in width and is placed between two cylinder halves. The sample displaces the characteristic resonant frequency of the resonator and the complex permittivity of the sample is calculated from the the shift in frequency. The samples were prepared using an Isomet 4000 Linear Precision Saw and polished with sand paper of increasing grading from 180 - 600 grit to ensure the sides of the sample were as smooth as possible. The samples had to be cut in stages using the saw, resulting in non-uniform topography. To account for this, the dolomite and labradorite samples were each measured five times in the resonator at different orientations. The uneven sample surfaces caused the displacement between the two cylinder halves to vary between measurements. The average thickness of the dolomite and labradorite sample was 1.42 ± 0.03 mm and 2.47 ± 0.02 mm respectively. The average of the five permittivity measurements for each sample was 4.85 ± 0.09 and 5.66 ± 0.06 . The dolomite sample showed a distinct wedge shape, introducing visible air gaps between the cylinder halves and increasing the standard deviation in the measured thickness and permittivity. The labradorite sample was more even throughout and about 1 mm thicker. Air gaps for the thinner dolomite sample therefore impacted the measurement more than for the labradorite sample, as the range in measured thicknesses was roughly 5.6% of the average sample thickness, compared with just 2% for the labradorite sample. Although the standard deviation of the sample thickness is incorporated into the error analysis for the measured permittivity, the effects of the relative amount of air and sample between the cylinder halves is not considered, and so the error in the measured permittivity of the samples is greater than reported, especially for the dolomite sample.

The labradorite sample measured permittivity of 5.66 ± 0.06 is in agreement with the literature value of 6.59 ± 0.96 , whereas the dolomite sample measured permittivity of 4.85 ± 0.09 is not consistent with the literature value of 7.16 ± 0.92 . It is likely that the measurement of the solid dolomite permittivity was significantly affected by air gaps, which lowered the measured permittivity. The resonant cavity permittivity measurement of the solid labradorite sample is plotted along with the powder measurements and mean literature value in Figure 6.17. Since the resonant cavity

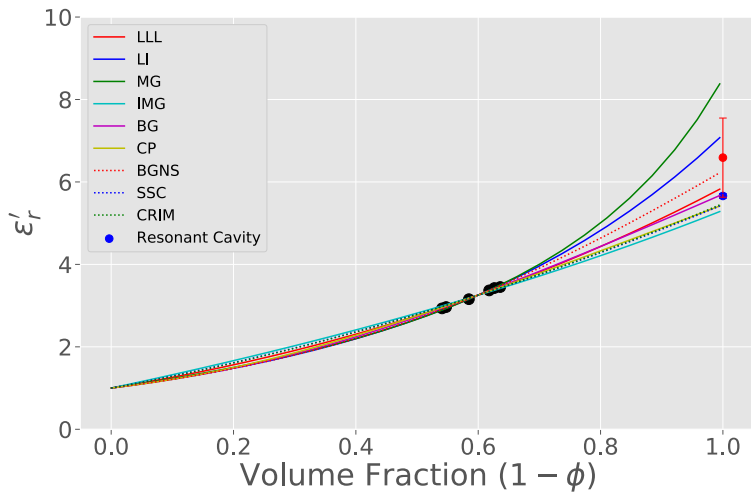


Figure 6.17: Regression of mixing models for labradorite dataset compared with mean literature value and resonant cavity solid sample measurement from Brian Tsai.

measurement is of the same labradorite sample as the powder measurements, the resonant cavity measurement is a better representation of the solid permittivity for the labradorite sample than the mean literature value, which averages measurements from a range in labradorite compositions. The permittivity contrast in the powder mixture is relatively low, and so the mixing model predictions are closer together than for higher contrast mixtures. The BG mixing model predicts a solid permittivity for the labradorite sample of 5.70 (5.79 when coaxial boundary conditions applied), within 0.71% of the resonant cavity measurement (2.3% with coaxial boundary conditions). The LLL, SSC, CP, CRIM, and IMG predictions are all within 3-5% of the resonant cavity measurement.

6.4 Modelling Permittivity of Solid Mineral Samples (Solid Permittivity)

The correlation of the permittivity of a dry geologic powder (or any substance) with porosity has been identified by many researchers. The previous section described how this correlation can be modelled accurately using the LLL and BG equations and an appropriate value for the solid permittivity of a given material. The variation of the solid permittivity between different minerals is not as well studied. Chemical composition has been proposed as a mechanism controlling the

loss tangents of minerals, although this correlation has not been extensively studied (Olhoeft and Strangway, 1975). It was found in the current research that the solid permittivities required to fit the sample datasets for a given mixing equation correlated well with the grain density of the samples. Figure 6.18 shows the solid permittivities resulting from fitting the BG equation to the sample datasets plotted as a function of the grain densities of each sample. The data in Figure 6.18 is fit well by a linear equation with an intercept of 1, corresponding to a permittivity of 1 at zero density, or ideal vacuum. The same analysis as in Figure 6.18 for almost every other mixing

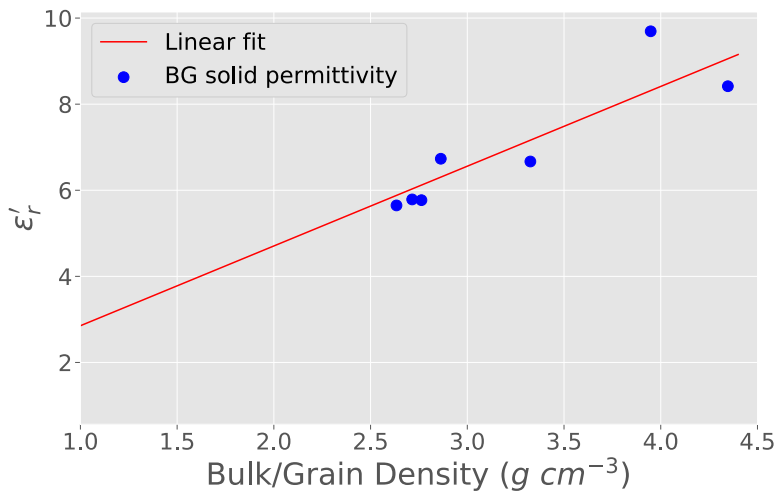


Figure 6.18: Solid permittivities used to fit the BG mixing model (with boundary conditions) to the sample permittivity measurements plotted against the grain density of each sample. The data is fitted with a linear model.

equation resulted in a similar linear correlation between solid permittivity and grain density. Figure 6.19 shows the Pearson correlation coefficient (R^2) calculated for the best linear fit (constrained to have an intercept of 1) through the solid permittivities used for each mixing model fit to the sample datasets. The linear correlation is relatively strong for each mixing equation, but is the strongest for the BG equation. This has some implications for understanding the solid permittivity of minerals since the BG equation was shown to fit the sample datasets with the most accurate solid permittivities. The equation for the line that fits the solid permittivities resulting from the BG (boundary corrected) fit to the sample dataset is $\epsilon'_r = 1.85\rho_s + 1$. This turns out to be exactly the same in the case of the LLL (boundary corrected) fit, which is not surprising given the similar

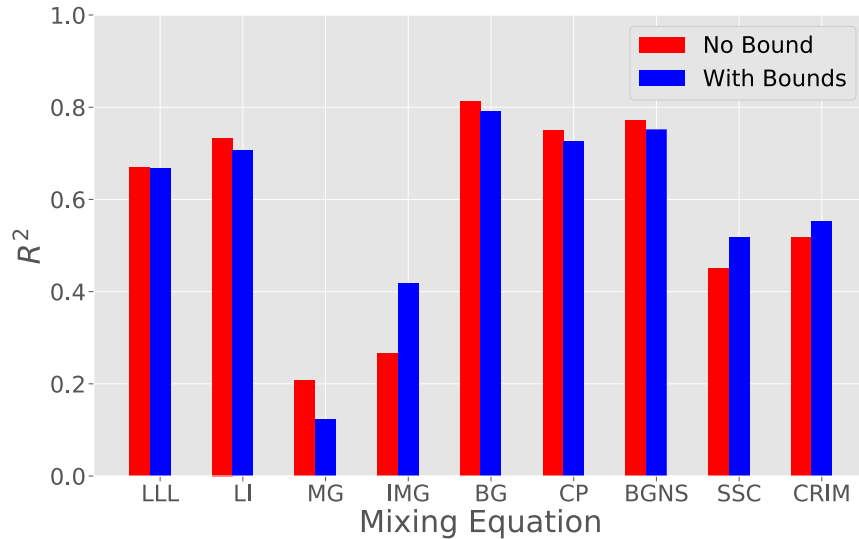


Figure 6.19: Pearson correlation coefficient for linear fits derived from solid permittivities used for each mixing model (with and without boundary conditions applied).

behaviour of the two models. This equation is similar to the model fit from Ulaby et al. (1988), where the linear equation $\epsilon'_r = 1.86\rho_s + 1$ was found to model measurements of 80 rock samples in resonant cavities from 1 - 16 GHz well. Ulaby et al. (1988) found their data to be modelled just as well using a slightly altered version of the Olhoeft and Strangway (1975) empirical model. In the current research, it was found that when plotting the measurements from Ulaby et al. (1988) over the BG solid permittivity values, the measurements of metamorphic and igneous rocks matched well with the linear fit and the measurements of sedimentary rocks plotted below the linear fit, closer to the measurements of the powder samples presented in this thesis (Figure 6.20). It is reasonable to assume that the sedimentary rocks used in Ulaby et al. (1988) had substantial porosity, causing their measured permittivity to be more similar to powdered mineral samples than to solid mineral samples. The metamorphic and igneous rock samples had less porosity and behaved similar to the BG predicted solid permittivity of the samples presented in this thesis. This analysis implies that the dielectric behaviour of geologic materials is different for low and high porosity regimes. In this view, to predict the permittivity of some solid mineral, the linear equation $\epsilon'_r = 1.85\rho_s + 1$ should be used, and to then predict the permittivity of some powder of that mineral, the BG or LLL equations should be used to extrapolate from that solid permittivity to the effective permittivity at the porosity of that powder. The linear equation used to predict solid permittivities is entirely

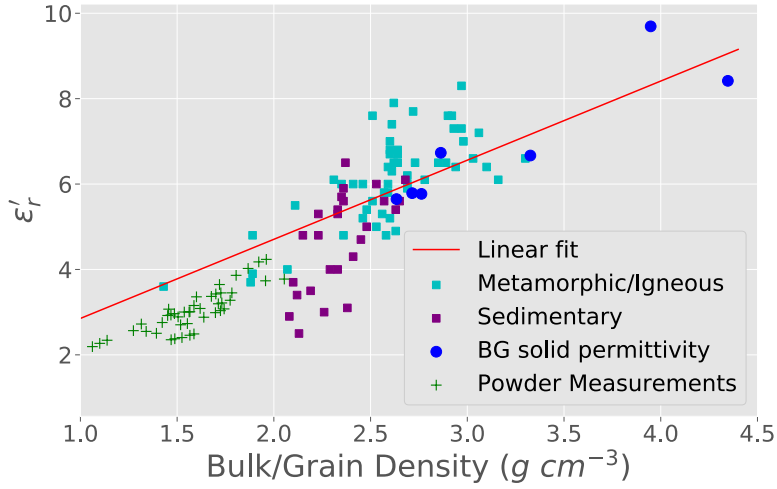


Figure 6.20: Solid permittivities used to fit the BG mixing model (with boundary conditions) to the sample permittivity measurements compared with the sample permittivity measurements and results from Ulaby et al. (1988) separated by rock type.

empirical, unlike the application of mixing theory applied to the powder permittivities. Intuitively, the denser the rock, the more atoms, ions, and molecules available in a given volume with which to be polarized, and therefore the greater the potential for polarizability.

6.4.1 Additivity Rule of Ionic/Molecular Polarizability

It is intuitive that the properties of a molecule are a function of the properties of the atoms and ions that make up that molecule. Additivity rules apply to some of these properties, such as mass, stating that the molecular property is the additive properties of the atoms and ions contained in that molecule. The additivity rule of molecular polarizabilities (ARMP) is a theory stating that the molecular (dielectric) polarizability, α_D , of a complex substance can be determined by the additive dielectric polarizabilities of fundamental molecular constituents (Shannon, 1993; Cygan and Lasaga, 1986; Tuhkala et al., 2017; Blair and Thakkar, 2014):

$$\alpha_D(M_2M'X_4) = 2\alpha_D(MX) + \alpha_D(M'X_2) \quad (6.2)$$

The additivity of molecular properties, or in this case polarizability, can be extended further, where these simpler molecular compounds (and thus the more complex substances) can be described by

the polarizabilities of individual ions through the additivity rule of ionic polarizability (ARIP):

$$\alpha_D(M_2M'X_4) = 2\alpha_D(M^{2+}) + \alpha_D(M'^{4+}) + 4\alpha_D(X^-) \quad (6.3)$$

Using measurements from the literature of the real part of the permittivity and molecular volume for 129 oxides and 25 fluorides, Shannon (1993) used the ARIP and Clausius-Mossotti (CM, equation (2.15)) theories to derive the polarizabilities of 61 ions through least squares regression (Figure 6.21). Ionic polarizability is typically correlated with ionic radii and atomic number, as electrons

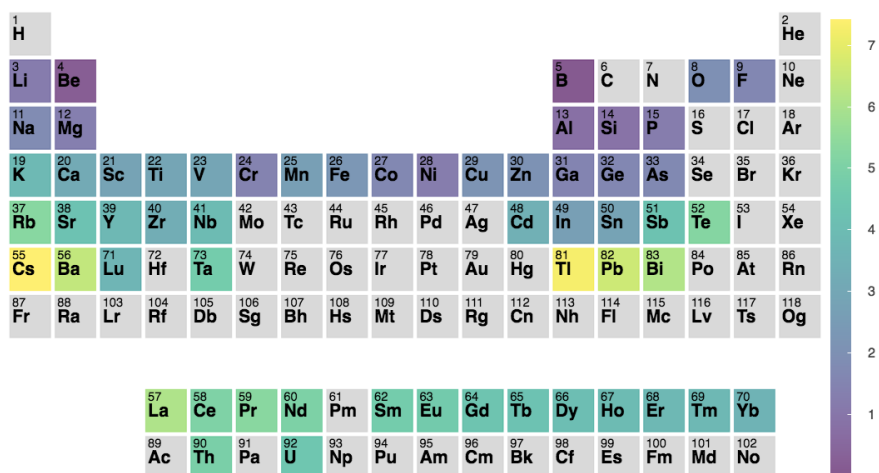


Figure 6.21: Ionic polarizabilities (\AA^3) derived in Shannon (1993).

farther from the atomic nucleus are less tightly bound. The permittivities of the solid mineral samples (or solid permittivities of the mineral samples) in this research were calculated using the ionic dielectric polarizabilities from Shannon (1993), the ARIP and CM equations, and the chemical composition of the minerals from Table 4.2. The (unit) crystal volumes for each mineral were taken from Gaines et al. (1997). Figure 6.22a) shows the results of the solid permittivities calculated this way compared with the mean values from the literature. Within the error bars for the mean values from the literature, the ARIP/CM predictions are generally consistent with the literature. Although the error bars are large for some samples (serpentine and fayalite), the ARIP/CM predictions assume a pure mineral composition, which is generally not true of the samples in this research. This discrepancy is not accounted for in the error bars for the ARIP/CM predictions (error bars calculated from propagated uncertainty in ionic polarizabilities from Shannon (1993)). The solid permittivities for the samples resulting from the LLL fit to the sample datasets is compared with the mean values from the literature in Figure 6.22b). Figures 6.22a) and 6.22b) show that the LLL

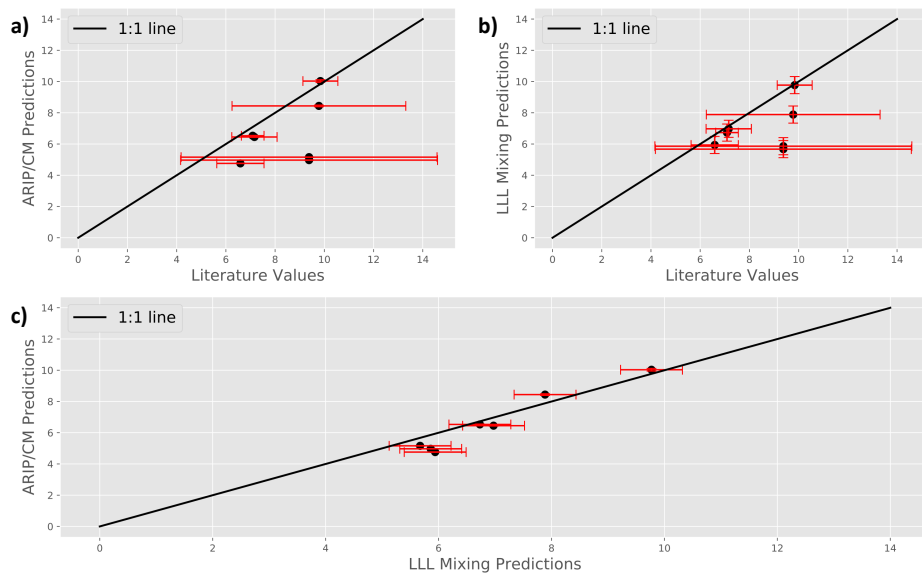


Figure 6.22: **a)** Solid permittivities for the samples predicted using the theoretical ARIP and CM models (ARIP/CM Predictions) compared to the mean values from the literature (Literature Values). **b)** Solid permittivities for the samples predicted by the LLL fit to the sample permittivity measurements (LLL Mixing Predictions) compared to the mean values from the literature (Literature Values). The error bars for the mixing predictions are the WRMSE for the LLL mixing model predictions compared with the mean literature values. **c)** Solid permittivities for the samples predicted by the the ARIP and CM theories (ARIP/CM Predictions) compared to the those predicted by the LLL fit to the sample permittivity measurements (LLL Mixing Predictions). $R^2 = 0.87$.

mixing model predictions match closely with the ARIP/CM predictions for the solid permittivities of the samples. Figure 6.22c) compares the ARIP/CM and LLL mixing predictions for the solid permittivities of the samples, and shows that the two models are in excellent agreement with a correlation of $R^2 = 0.87$. Given the variable mineralogic composition within the samples used in this research, the correspondence between the LLL mixing predictions, based on actual material measurements, and the ARIP/CM predictions, based on theoretical pure mineral properties, is exceptional.

6.5 Empirical Methods

The above results rely on knowing the mineralogical composition of a geologic powder in order to predict the permittivity for that material. The Olhoeft and Strangway (1975) empirical equation for the effective permittivity as a function of bulk density for a geologic material, $\epsilon'_r = 1.93\rho^{\text{bd}}$, requires no *a priori* information about the composition of the material. This equation was derived from the regression of permittivity measurements of lunar regolith samples, but has been shown to also be valid in predicting the permittivity of terrestrial geologic samples (Ulaby et al., 1988; Campbell, 2002). Figure 6.23 shows the version of this equation from Ulaby et al. (1990), $\epsilon'_r = 1.96\rho^{\text{bd}}$, derived through a regression of permittivity measurements of terrestrial geologic samples, plotted with the permittivity measurements of the mineral powder samples from the current research (the Ulaby et al. (1990) equation is used instead of the Olhoeft and Strangway (1975) equation since it was derived from terrestrial samples, such as those used in the research presented in this thesis). Since this equation was derived from regression of permittivity measurements of a range of minerals, it is not surprising that it predicts an effective permittivity for the powder mineral samples that is essentially an average of the actual measurements. If the mineral composition of a geologic powder is unknown, this empirical model is therefore a good prediction for the permittivity of that powder. As shown in Figure 6.14, any mixing model can be fit to a set of permittivity measurements. The goodness of fit of the empirical model of Olhoeft and Strangway (1975) to lunar regolith permittivity measurements, based on the LI mixing theory, should be the same for any other type of empirical model based on a different mixing theory. One of the attractive features of the Olhoeft and Strangway (1975) empirical equation is its simplicity. A similar empirical equation that predicts the effective permittivity of a geologic powder from bulk density can be written according to the LLL mixing theory:

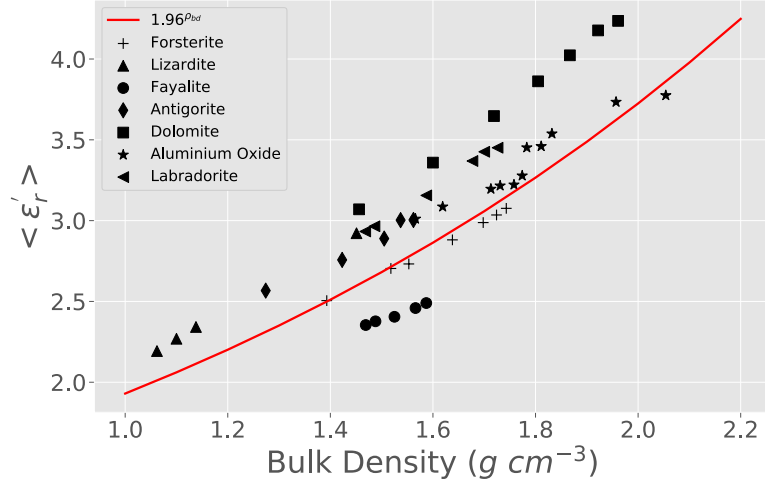


Figure 6.23: Ulaby et al. (1990) empirical equation, $\epsilon'_r = 1.96 \rho_{bd}$, plotted with the frequency-averaged mineral powder permittivity measurements, $\langle \epsilon'_r \rangle$, from the current research.

$$\epsilon'_r = (\rho_{bd} \alpha + 1)^3 \quad (6.4)$$

$$\alpha = \frac{1}{\rho_s} (\epsilon_s^{1/3} - 1) \quad (6.5)$$

In (6.5), ϵ_s refers to the real part of the solid permittivity of whatever mineral, or put another way, the permittivity of whatever solid (single crystal) mineral the particular geologic sample is made up of (and will throughout the remainder of this thesis). In the same way that the constant, a , in the Olhoeft and Strangway (1975) empirical equation ($\epsilon'_r = a \rho_{bd}$) is related to the LI mixing theory according to $a = \epsilon_s^{1/\rho_s}$, the constant α in equation (6.4) is related to the LLL mixing theory according to equation (6.5). Figure 6.24 shows the results of fitting (using *LMFIT* (Newville et al., 2014)) the Olhoeft and Strangway (1975) empirical equation ($\epsilon'_r = a \rho_{bd}$), as well as fitting equation (6.4), to the lunar regolith permittivity measurements compiled in Carrier et al. (1991). The dataset in Carrier et al. (1991) is relatively large and spans permittivity measurements from several different studies. The measurements from Carrier et al. (1991) used for the regression in Figure 6.24 are restricted to only those measurements that were carried out in vacuum, so that it can be certain that the permittivity measurements are truly representative of the samples. The

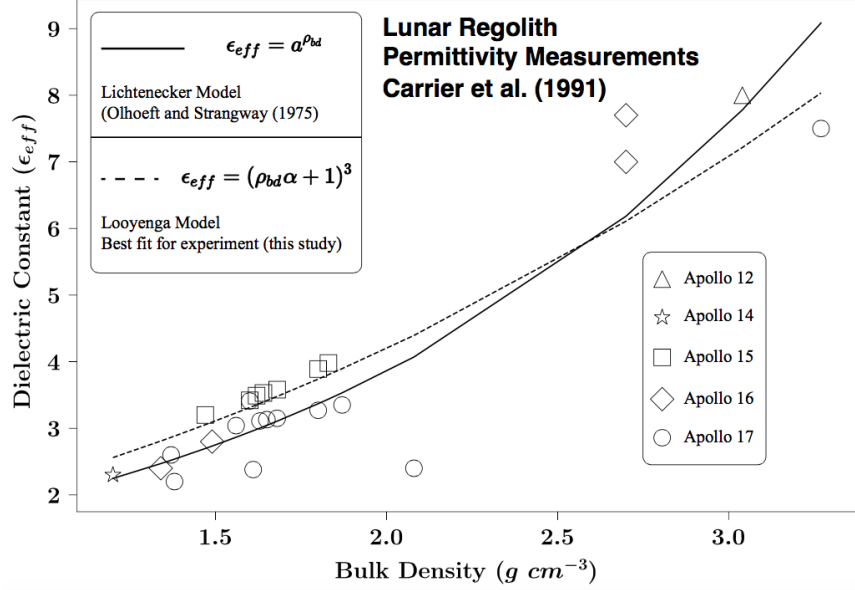


Figure 6.24: Figure taken from Hickson et al. (2017a) $\epsilon_{eff} \equiv \epsilon'_r$. Olhoeft and Strangway (1975) empirical equation, $\epsilon'_r = a^{\rho_{bd}}$, and equation (6.4) fit to lunar regolith permittivity measurements from Carrier et al. (1991).

measurements are also differentiated on the basis of which *Apollo* mission collected the regolith samples used for a given permittivity measurement. The Olhoeft and Strangway (1975) empirical equation fit the data with a value of $a = 1.96$ and an RMSE of 0.6723, whereas equation (6.4) fit the data with a value of $\alpha = 0.307$ and an RMSE of 0.6930. The goodness of fit of either equation, based on the RMSE, is fairly equal. Carrier et al. (1991) suggest a value of $\rho_s = 3.1 \text{ g/cm}^3$ to represent the average grain density of lunar regolith. At this grain density, the fit for the Olhoeft and Strangway (1975) empirical equation ($a = 1.96$) corresponds to a solid permittivity of 8.11 for the lunar regolith. Similarly, the fit for equation (6.4) corresponds to a solid permittivity of 7.42. The mineralogy and composition of the lunar regolith across all of the samples used to derive these numbers is varied, and so these empirical fits represent an average of these properties.

To isolate the influence of composition and mineralogy on the permittivity measurements of lunar regolith from Carrier et al. (1991), the same regression as in Figure 6.24 was carried out separately for the samples collected during the *Apollo* 15, 16, and 17 missions. Due to the smaller datasets, all of the measurements for each mission were used in the regression, not just those taken in vacuum. Table 6.11 shows the results of the regression for the Olhoeft and Strangway (1975) empirical equation, and for equation (6.4), as well as the average TiO_2 and FeO weight percent oxides for each sample from Carrier et al. (1991). The values for the constants a and α in Table 6.11 de-

Table 6.11: Regression analysis of *Apollo* 15, 16, and 17 mission lunar regolith sample permittivity measurements presented in Carrier et al. (1991).

NASA <i>Apollo</i> Mission	$\epsilon'_r = a^{\rho_{bd}}$	$\epsilon'_r = (\rho_{bd}\alpha + 1)^3$	<i>TiO</i> ₂ wt. %	<i>FeO</i> wt. %
<i>Apollo</i> 15	$a = 1.89$	$\alpha = 0.283$	5.39	13.19
<i>Apollo</i> 16	$a = 2.01$	$\alpha = 0.310$	0.6	4.90
<i>Apollo</i> 17	$a = 1.90$	$\alpha = 0.282$	1.42	15.52

Table 6.12: Solid density (g/cm³) measurements of regolith samples returned in *Apollo* missions 15, 16, and 17 with references.

<i>Apollo</i> 15	<i>Apollo</i> 16	<i>Apollo</i> 17
3.24 (Carrier et al., 1991)	2.5 (Lin et al., 1992)	3.51 (Carrier et al., 1991)
3.0 (Carrier et al., 1991)	2.79 (Robens et al., 2007)	3.44 (Carrier et al., 1991)
3.1 (Carrier et al., 1991)	2.709 - 2.751 (Jeanloz and Ahrens, 1978)	3.07 (Carrier et al., 1991)
		3.05 (Carrier et al., 1991)
Avg. = 3.11	Avg. = 2.69	Avg. = 3.27

rived through regression of the lunar regolith permittivity measurements show a correlation with the average *TiO*₂ and *FeO* concentrations in the samples. The regression results are similar for *Apollo* missions 15 and 17, which have similar *TiO*₂ and *FeO* concentrations, but not for *Apollo* 16. *Apollo* missions 15 and 17 were carried out at lunar sites closer to the mare regions of the Moon when compared to the *Apollo* 16 mission, which is reflected in the higher concentrations of *TiO*₂ and *FeO*. *TiO*₂ and *FeO* are dense mineral oxides, and increase the average grain density of a regolith mixture that is otherwise composed of less dense minerals such as plagioclase. The grain density of regolith grains returned during *Apollo* missions 15, 16, and 17 have been measured by various authors and are summarized in Table 6.12. Using the values for the constants a and α calculated through regression and listed in Table 6.11, as well as the average grain density measured for regolith samples returned for the *Apollo* 15, 16, and 17 missions listed in Table 6.12, the solid permittivity (ϵ_s) of the regolith material predicted by the Olhoeft and Strangway (1975) equation, equation (6.4), and the linear fit from section 6.4 ($\epsilon'_r = 1.85\rho_s + 1$) for each mission is calculated and presented in Table 6.13. Using any of the three equations in Table 6.13 to calculate the solid permittivity of the lunar regolith, the calculated solid permittivity shows correlation with the *TiO*₂ and *FeO* concentrations and grain density measured for the samples returned by each *Apollo* mission. The solid permittivity predicted by the linear equation $\epsilon_s = 1.85\rho_s + 1$ is very similar to that derived for the empirical LLL equation that was fit to the datasets by regression. The variation in fitting empirical models to permittivity measurements of lunar regolith samples is largely explained by the variation in grain density of the samples, which is likely caused by the

Table 6.13: Calculated solid permittivity for lunar regolith returned during the *Apollo* 15, 16, and 17 missions using the data in Tables 6.11 and 6.12. The solid permittivity is calculated using the Olhoeft and Strangway (1975) equation ($\epsilon_s = a^{\rho_s}$), equation (6.4) ($\epsilon_s = (\rho_s \alpha + 1)^3$), and the linear equation $\epsilon_s = 1.85\rho_s + 1$ defined in section 6.4.

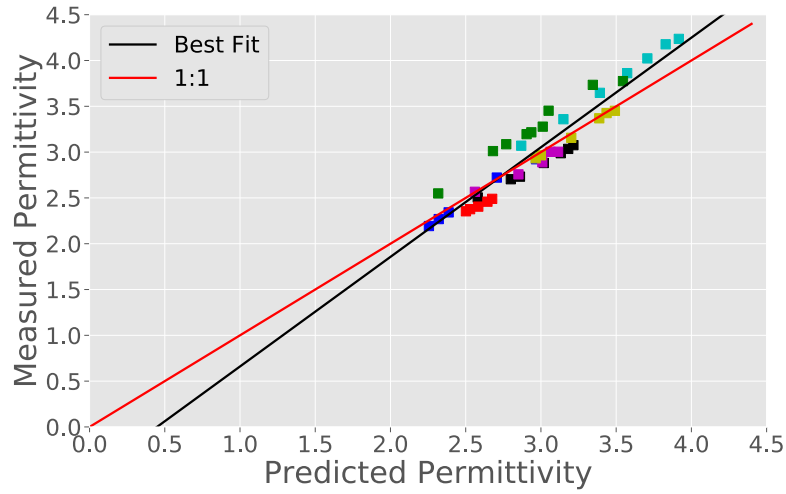
NASA <i>Apollo</i> Mission	$\epsilon_s = a^{\rho_s}$	$\epsilon_s = (\rho_s \alpha + 1)^3$	$\epsilon_s = 1.85\rho_s + 1$
<i>Apollo</i> 15	7.28	6.64	6.75
<i>Apollo</i> 16	6.52	6.16	5.98
<i>Apollo</i> 17	8.19	7.10	7.05

differences in TiO_2 and FeO concentrations. Using the general empirical equations, such as the Olhoeft and Strangway (1975) equation $\epsilon'_r = a^{\rho_{bd}}$ or equation (6.4) to fit the *Apollo* lunar regolith sample permittivity measurements will result in an average fit that does not consider variation in composition or mineralogy between the samples. Different empirical equations (given by values of a and α in Table 6.11) provide better fits to the individual datasets from each *Apollo* missions by taking into consideration the specific composition and mineralogy. The application of the linear equation $\epsilon_s = 1.85\rho_s + 1$ and LLL mixing theory to fit the measurements is comparable in accuracy, and does not require any regression of the dataset.

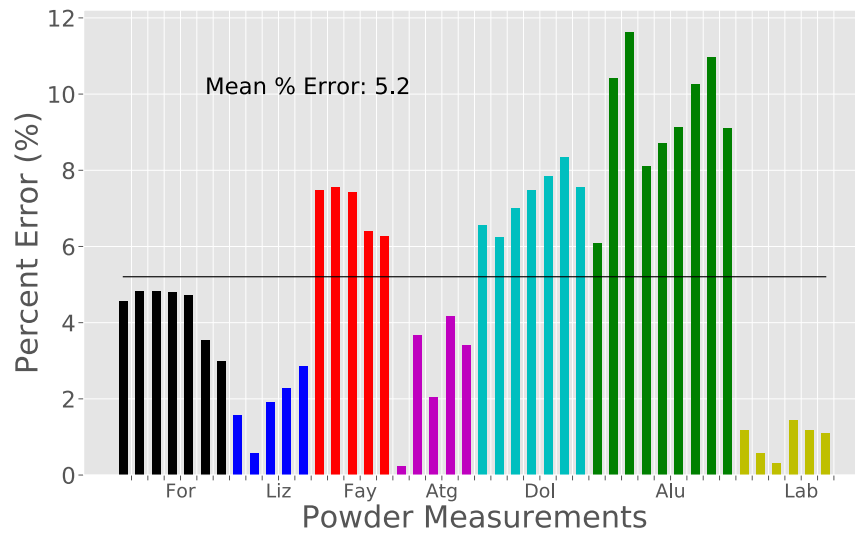
The frequency-averaged measured permittivity across all samples (Tables 6.1 and 6.2) was compared with predictions from the two types of empirical equations discussed. Figure 6.25 shows the results of using $\epsilon_s = 1.85\rho_s + 1$ (with the measured grain densities of each sample) to calculate a solid permittivity for each sample, and then using that as input to the LLL mixing theory (with boundary conditions) to predict the powder permittivity measurements. Figure 6.26 shows the results of predicting the powder permittivity measurements directly from $\epsilon'_r = 1.96^{\rho_{bd}}$. The predicted permittivities are more accurate using the method for Figure 6.25, which takes the variation in grain densities between the samples into consideration.

6.6 Summary

This chapter has described the results of measurements of the permittivity of several powdered silicate, phyllosilicate, carbonate, and oxide mineral samples. These measurements were used to compare the accuracy of the mixing theories presented in chapter 2 against similar permittivity measurements from the literature that were consolidated into average permittivities for the solid phase (single crystal) of each mineral sample. The LLL and BG mixing theories were shown to model the powder permittivity measurements with the most accurate solid permittivities. The

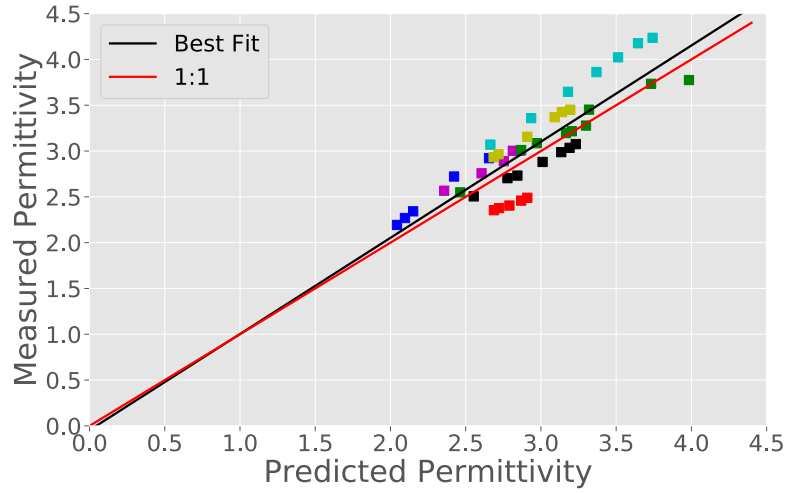


(a) Measured vs. Predicted.

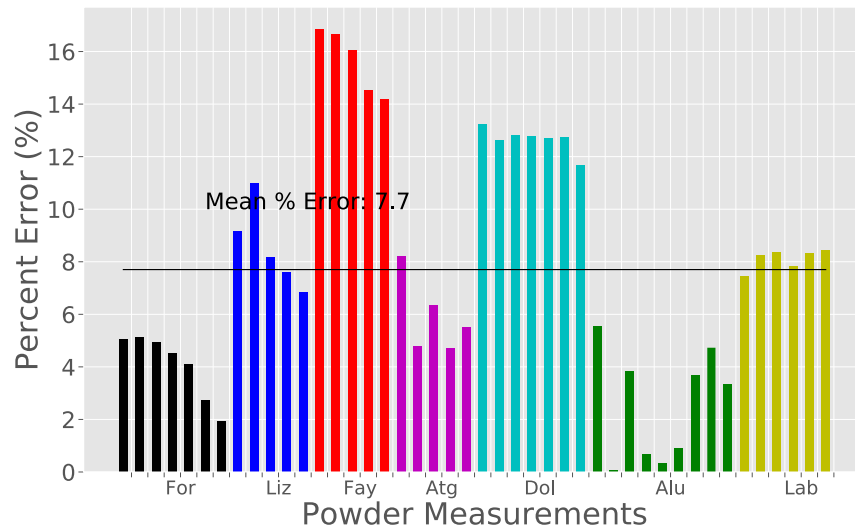


(b) Errors.

Figure 6.25: Comparison of measured permittivities across all samples with permittivities predicted from measured grain densities using $\epsilon_s = 1.85\rho_{bd} + 1$ to predict solid permittivities, and then using these as inputs to the LLL model (with boundary conditions). R^2 for 1:1 line is 0.85.



(a) Measured vs. Predicted.



(b) Errors.

Figure 6.26: Comparison of measured permittivities across all samples with permittivities predicted from the Ulaby et al. (1990) equation $\epsilon'_r = 1.96^{\rho_{bd}}$. R^2 for 1:1 line is 0.71.

BGNS, SSC, and CRIM models also showed good agreement with the average literature values, and the LI and MG models were in poor agreement. This result is significant considering the widespread application of the LI and MG models in planetary radar applications. The combination of the ARIP and CM theories were shown to also predict solid permittivities for each mineral sample that matched well with the average values from the literature. Then it was shown that the LLL mixing predictions (and therefore also the BG mixing predictions) were very similar to the ARIP/CM predictions for the solid permittivities of each mineral sample. The correspondence between the LLL mixing model predictions and theoretical ARIP/CM predictions for the solid permittivity of the samples in this research explains the change in dielectric characteristics of geologic materials in the low and high porosity regimes, representing a kind of dielectric hierarchy (Figure 6.27). The application of these theories allows the length-scale dependent prediction of the

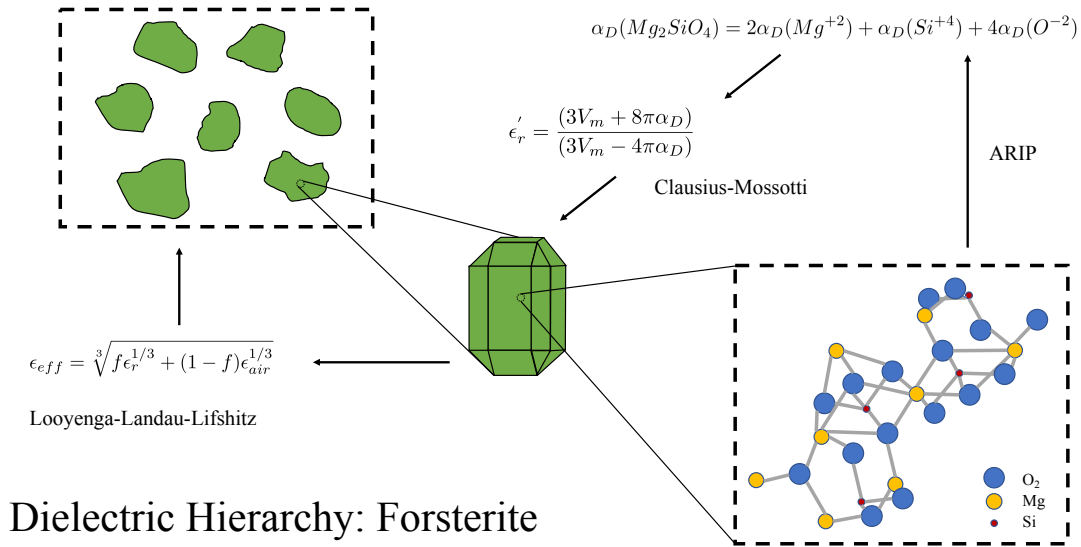


Figure 6.27: The accurate modelling of the permittivity of the mineral samples in this research is dependent on the length-scale considered: at high porosity (e.g a bulk powder of that mineral) the LLL mixing model was shown to be accurate, and at low porosity (e.g a single mineral grain) the ARIP/CM theories were shown to be accurate. This describes a hierarchical system depending on the length-scale and type of material (single grain or bulk powder) considered. This figure is a graphical depiction of these different models for the forsterite mineral.

permittivity of a given mineral, for both the solid grains of a mineral and a bulk powder. Only the mineral composition is required to apply the ARIP/CM theories to predict the solid permittivity of some mineral, which can then be used as input to the LLL mixing model to predict the effective permittivity of some bulk powder of that mineral.

The accuracy of empirical models for the effective permittivity of a geologic powder was also considered in this chapter. It was shown that the Olhoeft and Strangway (1975) empirical equation, based on the LI mixing theory, that was used to model lunar regolith permittivity measurements can be replaced by any other empirical equation based on a different mixing theory. The empirical equation (6.4) based off of the LLL mixing theory was shown to model lunar regolith permittivity measurements to similar accuracy when compared with the Olhoeft and Strangway (1975) model. For both the lunar regolith permittivity measurement dataset and the permittivity measurement dataset from the current research, the sequential application of the linear equation $\epsilon_s = 1.85\rho_s + 1$ and the LLL mixing theory was shown to be more accurate in predicting the permittivity measurements than in applying any one kind of empirical equation. The most accurate modelling of powder permittivities is then dependent on the amount of information known about the sample. If the composition is known, the ARIP/CM theories can be used to calculate the solid permittivity. If the average grain density is known, the linear equation $\epsilon_s = 1.85\rho_s + 1$ can be used. From either of these estimates of solid permittivity, the LLL or BG mixing theories can be used to extrapolate to the desired powder porosity. Otherwise, the application of an entirely empirical equation, such as $\epsilon'_r = a\rho^{bd}$, can be used.

Determination of olivine or serpentine end-member compositions from radar data does not seem possible, based on the above discussion. The differences in the solid permittivities is largely due to the difference in grain densities. Since multiple minerals can share a similar grain density, this does not help in determining specific olivine or serpentine concentrations.

Chapter 7

Applications to Asteroid Radar

Modelling

7.1 Incorporating mixing analysis into asteroid radar model

The permittivity measurements and modelling that have been discussed in this thesis have been performed with the ultimate goal of applying any insights gained to modelling the surface properties of planetary radar targets, specifically asteroids. Magri et al. (1999, 2001) developed an asteroid radar model that calculates the Fresnel power reflection coefficient, R_{fp} , from radar observations of asteroids. In this model, the quasi-specular radar albedo, $\hat{\sigma}_{OC,qs}$, is estimated from the ratio of the circular polarization ratio (CPR), μ_C , to the diffuse circular polarization ratio, $\mu_{C,diff}$:

$$\hat{\sigma}_{OC,qs} = \hat{\sigma}_{OC} \left(1 - \frac{\mu_C}{\mu_{C,diff}} \right) \quad (7.1)$$

The diffuse circular polarization ratio, $\mu_{C,diff}$, is the circular polarization ratio of the component of the radar echo due to diffuse scattering alone. Harmon and Ostro (1985) summarized the diffuse radar scattering properties of the Moon, Venus, Mercury, and Mars, both derived in their study and from the literature. Magri et al. (2001) assume a value of $\mu_{C,diff} = 0.50 \pm 0.15$ for their model, which is the 2 sigma interval that encompasses the span of values reported in Harmon and Ostro (1985). Garvin et al. (1985) used the equation for Fresnel reflectivity at normal incidence (1.55) and a modified version of the Olhoeft and Strangway (1975) empirical equation to estimate the bulk density of the Venusian surface from the *Pioneer* mission radar mapper data. Magri et al. (2001) adapted this model from Garvin et al. (1985) to include their equation for the quasi-specular radar albedo (7.1) and Fresnel reflectivity (using equation (1.8)) to arrive at the following model predicting the bulk density of asteroid surfaces from radar observations:

$$\rho_{\text{bd}} = \left(\frac{2}{\ln[a]} \right) \ln \left[\frac{1 + \sqrt{\frac{\hat{\sigma}_{\text{OC}}}{g} \left(1 - \frac{\mu_{\text{C}}}{\mu_{\text{C, diff}}}\right)}}{1 - \sqrt{\frac{\hat{\sigma}_{\text{OC}}}{g} \left(1 - \frac{\mu_{\text{C}}}{\mu_{\text{C, diff}}}\right)}} \right] \quad (7.2)$$

In equation (7.2), a is a constant representing the value chosen for the base of the exponential in the Olhoeft and Strangway (1975) empirical equation $\epsilon'_r = a^{\rho_{\text{bd}}}$. Garvin et al. (1985) chose a value of $a = 1.87$, which was then adopted by Magri et al. (2001) in their model. Magri et al. (2001) then tried to constrain their model using the grain density of the regolith on asteroid 433 Eros measured by NASA's *NEAR-Shoemaker* mission. As was shown in the previous chapter, the grain density of a geologic material is correlated with the solid permittivity of that material and influences any empirical mixing models for the permittivity of a powder of that material. The use of the empirical equation $\epsilon'_r = a^{\rho_{\text{bd}}}$ with $a = 1.87$ is only valid for a narrow range in grain density of a material, and so intrinsically assumes a grain density for the material attempting to be modelled, and therefore cannot be applied to material of a different grain density, invalidating the constraints using the grain density of 433 Eros applied by Magri et al. (2001). Nolan et al. (2013) used equation (7.2) to model the bulk density in the near surface of NEA 101955 Bennu using Arecibo S-band radar data in support of NASA's *OSIRIS-REx* mission. Nolan et al. (2013) calculated the bulk density within the radar penetration depth (within the upper 1 m of the surface) to be $\rho_{\text{bd}} = 1.65 \text{ g/cm}^3$.

The results of the mixing analysis in this thesis can be incorporated into the Magri et al. (2001) asteroid radar model to improve the bulk density estimates of asteroid surfaces from radar observations. If the estimation of the Fresnel reflectivity is treated the same as in Magri et al. (1999, 2001), equation (7.2) can be modified to incorporate the LLL mixing equation as opposed to the LI mixing equation:

$$\rho_{\text{bd}} = \frac{1}{\alpha} \left(\left[\frac{1 + \sqrt{\frac{\hat{\sigma}_{\text{OC}}}{g} \left(1 - \frac{\mu_{\text{C}}}{\mu_{\text{C, diff}}}\right)}}{1 - \sqrt{\frac{\hat{\sigma}_{\text{OC}}}{g} \left(1 - \frac{\mu_{\text{C}}}{\mu_{\text{C, diff}}}\right)}} \right]^{2/3} - 1 \right) \quad (7.3)$$

In equation (7.3), α is a constant similar to a in equation (7.2), that is determined according to the LLL mixing theory to be $\alpha = \frac{1}{\rho_{\text{s}}}(\epsilon_{\text{s}}^{1/3} - 1)$. The value of α in equation (7.3) can thus be calculated for specific mineralogies expected for a given asteroid surface. In a paper published from the preliminary research presented in this thesis, the bulk density in the near surface of 101955 Bennu and 25143 Itokawa (the asteroid visited by JAXA's *Hayabusa* mission) were calculated using (7.3)

to be $1.27 \pm 0.33 \text{ g/cm}^3$ and $1.68 \pm 0.53 \text{ g/cm}^3$ respectively (Hickson et al., 2018). This calculation used a value of α that was estimated using the grain densities of meteorite analogues for either asteroid, CI/CM carbonaceous chondrites for Bennu and LL ordinary chondrites for Itokawa, and assuming a solid permittivity of $\epsilon'_r = 6.5 \pm 0.71$.

Planetary regolith consists of lithic fragments of a range of mineral compositions, glasses, agglutinates, and space weathered material. Furthermore the chemical composition of asteroid regolith is only loosely constrained and remains relatively unknown. As such, an application of the ARIP/CM theories to estimate the solid permittivity of individual regolith grains is not feasible. The correlation of solid permittivity with grain density discussed in the previous chapter, $\epsilon'_r = 1.85\rho_s + 1$ is relevant here instead. This linear equation was derived from the accurate BG and LLL mixing equation fits to the powder permittivity measurements presented in this thesis, as well as the average grain density measured for each sample. The measured grain density for each sample represents an average of the grain densities for each mineral contained in that sample. Therefore, the linear equation $\epsilon'_r = 1.85\rho_s + 1$ holds for mixtures of multiple minerals, albeit with one dominant mineralogy. This linear equation can be incorporated into equation (7.3) by calculating the constant α according to:

$$\alpha = \frac{\sqrt[3]{1.85\rho_s + 1} - 1}{\rho_s} \quad (7.4)$$

Using equations (7.3) and (7.4), the bulk density within the radar penetration depth of an asteroid can be calculated from radar observations and an estimate of the average grain density of the regolith material. The applications of these two equations represent the applications of the LLL mixing theory and the linear equation $\epsilon'_r = 1.85\rho_s + 1$ for determining solid permittivity.

7.2 Modelling Asteroid Regolith Porosity

The asteroid radar model (equations (7.3) and (7.4)) described in section 7.1 can be applied to any asteroid that has been observed by radar. Based on the radar scattering assumptions in the portion of the model incorporated from Magri et al. (2001), the model is better suited to asteroids with low CPR. To test the accuracy of the model, the model is applied to seven asteroids that either have been, or currently are, targeted by robotic spacecraft missions. Table 7.1 lists these asteroids, the relevant data for each asteroid and the resulting bulk density estimates using the

asteroid radar model (equations (7.3) and (7.4)). In applying the asteroid radar model (equations

Table 7.1: Asteroids for which the asteroid radar model (equations (7.3) and (7.4)) are applied with required input data and references.

Asteroid	Spectral Type	Meteorite Analogue	ρ_s (g/cm ³)	Radar Data	ρ_{bd} (g/cm ³)
101955 Bennu	B-type (Clark et al., 2011; DeMeo et al., 2009)	CI/CM (Lauretta et al., 2015)	2.68 ± 0.04 (Consolmagno et al., 2008)	$\hat{\sigma}_{OC} = 0.12 \pm 0.04$ $\mu_C = 0.18 \pm 0.03$ (Nolan et al., 2013)	1.36 ± 0.33
253 Mathilde	C-type (Yeomans et al., 1997)	CM (Consolmagno et al., 2008)	2.90 ± 0.08 (Consolmagno et al., 2008)	$\hat{\sigma}_{OC} = 0.072 \pm 0.022$ $\mu_C = 0.08 \pm 0.02$ (Magri et al., 2007)	1.21 ± 0.24
433 Eros	Sw-type (DeMeo et al., 2009)	L (Consolmagno et al., 2008)	3.75 ± 0.1 (Magri et al., 2001)	$\hat{\sigma}_{OC} = 0.25 \pm 0.09$ $\mu_C = 0.28 \pm 0.06$ (Magri et al., 2001)	1.95 ± 0.76
21 Lutetia	Xc-type (DeMeo et al., 2009)	CO, CV, CK, En (Coradini et al., 2011; Barucci et al., 2015)	3.54 ± 0.05	$\hat{\sigma}_{OC} = 0.19 \pm 0.07$ $\mu_C = 0.22 \pm 0.07$ (Magri et al., 2007)	1.86 ± 0.62
25143 Itokawa	S-type (Yoshikawa et al., 2015)	LL (Yoshikawa et al., 2015)	3.54 ± 0.13 (Consolmagno et al., 2008)	$\hat{\sigma}_{OC} = 0.16 \pm 0.05$ $\mu_C = 0.26 \pm 0.04$ (Ostro et al., 2004)	1.52 ± 0.46
4 Vesta	V-type (DeMeo et al., 2009)	HED (De Sanctis et al., 2012)	3.44 ± 0.12 (Consolmagno et al., 2008)	$\hat{\sigma}_{OC} = 0.12 \pm 0.04$ $\mu_C = 0.28 \pm 0.05$ (Magri et al., 2007)	1.19 ± 0.40
4179 Toutatis	Sq-type (DeMeo et al., 2009)	L (Reddy et al., 2012)	3.56 ± 0.1 (Consolmagno et al., 2008)	$\hat{\sigma}_{OC} = 0.23 \pm 0.3$ $\mu_C = 0.21 \pm 0.03$ (Nolan et al., 2013)	2.17 ± 0.42

(7.3) and (7.4)) to the asteroids listed in Table 7.1, several assumptions were made. The diffuse circular polarization ratio and backscatter gain were assumed to be the same as in Magri et al. (2001), $\mu_{C,diff} = 0.5 \pm 0.15$ and $g = 1.2 \pm 0.1$ respectively. The grain density of 101955 Bennu was taken as the average of averages for CI and CM carbonaceous chondrites from Consolmagno et al. (2008). The grain density of 433 Eros was taken from Magri et al. (2001) instead of the average for measured L-chondrite falls from Consolmagno et al. (2008), since Magri et al. (2001) note that terrestrial weathering lowers the grain density of meteorites, and so a more appropriate value for pristine L-chondrite material is the highest measured grain density for the L-chondrite falls. The grain density of 21 Lutetia is an average of the average grain densities of CO, CV, and CK carbonaceous chondrites and the average grain density of Enstatite chondrites from Consolmagno et al. (2008), since the meteorite analogue is relatively unknown for this asteroid and may span

these meteorite types (Coradini et al., 2011; Barucci et al., 2015). The grain density of 4 Vesta is assumed equal to the bulk density of the overall asteroid from Consolmagno et al. (2008), since the average of the Howardite, Eucrite, and Diogenite (HED) grain densities from Consolmagno et al. (2008) is lower than the bulk density (which is physically impossible).

The space missions that are associated with each of the asteroids in Table 7.1 have been described already in chapter 1 section 1.1. The mass and volume of each asteroid is known with high accuracy as a result of each of these missions, which allows calculation of the bulk density of the entire body. With the grain densities in Table 7.1, the bulk porosity (entire body) for each asteroid in Table 7.1 can be calculated. Similarly, the porosity in the near surface (within the radar penetration depth) can be calculated from the near surface bulk density estimates in Table 7.1. Figure 7.1 compares the near surface bulk porosity for the asteroids in Table 7.1 calculated using the Magri et al. (1999) model (equation (7.2), $a = 1.87$, specified according to the Magri et al. (1999) study as opposed to the Magri et al. (2001) study to clarify that the Eros-calibrated model was not used) and the asteroid radar model from this thesis (equations (7.3) and (7.4)), as well as the bulk porosity for the entire asteroid calculated from bulk density values in the literature (see references in chapter 1 section 1.1). Figure 7.1 shows that both the Magri et al. (1999) radar model and the radar model from this thesis (equations (7.3) and (7.4)) produce very similar results. This is likely a result of the overall good fit of the Olhoeft and Strangway (1975) empirical model to powder permittivities of geologic materials that is used in the Magri et al. (1999) radar model. Despite the inaccurate theoretical assumptions contained in this model, the empirical fit still provides a good estimate of permittivity from bulk density, and therefore also a good estimate of bulk density from radar data. The asteroid radar model from this thesis (equations (7.3) and (7.4)) is based on the LLL mixing theory that was shown to accurately model the powder permittivity measurements presented in this thesis under the theoretical constraints of the theory. The variation in mineral composition in asteroid regoliths is taken into account in this model by incorporating the linear correlation of grain density and solid permittivity observed in this thesis. Therefore, the use of the asteroid radar model in this research (equations (7.3) and (7.4)) is more accurate, and theoretically sound than the Magri et al. (1999) model. Figure 7.1 also shows that the near-surface porosity is significantly greater than the overall bulk porosity for asteroids 433 Eros, 21 Lutetia, and 4 Vesta. This suggests the presence of a porous regolith covering each body, which has been inferred from spacecraft observations. Asteroid radar models are therefore useful in determining if there is a

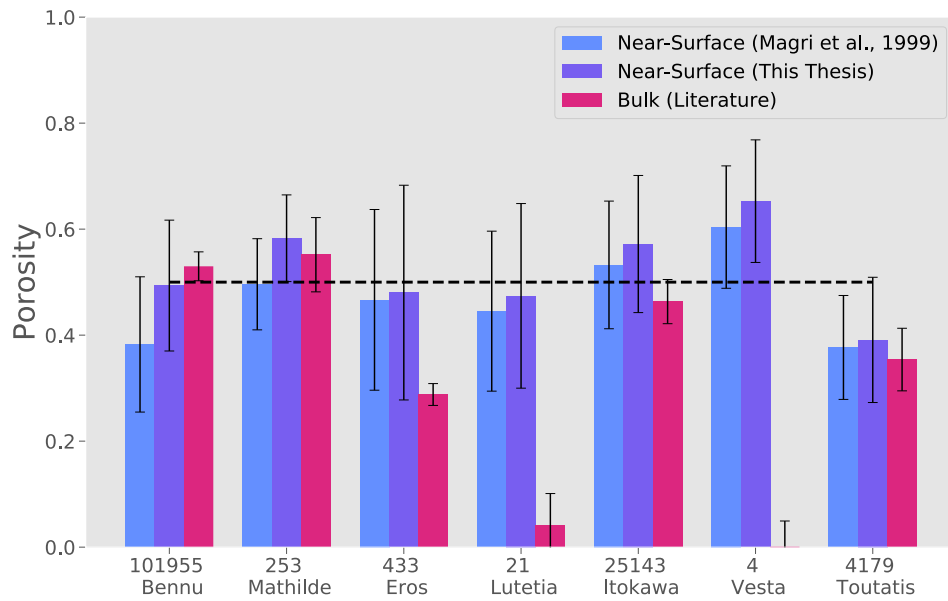


Figure 7.1: Near-surface porosity of asteroids visited by robotic spacecraft calculated using two asteroid radar models (this thesis, and (Magri et al., 1999)) compared with the bulk porosity for the entire asteroid. The dashed line is 50% porosity.

regolith component to an asteroid surface. The near-surface porosity for each asteroid considered in Table 7.1 and Figure 7.1 are all close to 50% porosity, which is the average lunar regolith porosity within the first 30 cm of the lunar surface (Carrier et al., 1991). This agreement implies similar upper regolith properties among these asteroids and the Moon. A preliminary conclusion from this is that the regolith formation mechanisms on the Moon and asteroids are similar. Considering the range in size, composition, and histories of each body this is an interesting observation. Regolith is generally thought to form from meteoroid bombardment and solar irradiation of surface material, breaking the material down and accumulating more regolith over time. Based on Figure 7.1, this mechanism seems relatively independent of the composition, size, and evolutionary history for a given airless body in the solar system. Asteroid regolith formation is generally assumed to be analogous to lunar regolith formation, due a lack of independent data. These results contribute an independent validation of this assumption. Confirming the presence of and porosity of the regolith of asteroids may also shed light on the interior structures of asteroids, and the interaction between the surface and the interior. Most of the sources of uncertainty in the asteroid radar model from this thesis (equations (7.3) and (7.4)) is in estimating the Fresnel reflectivity from asteroid radar observations. Continued research efforts into improving radar scattering models and our understanding of the roles of surface roughness and composition on radar interactions with planetary surfaces will help to reduce these ambiguities.

Chapter 8

Conclusions and Future Work

8.1 Conclusion

In this thesis, the dielectric properties of powdered geologic material have been determined experimentally in order to better understand the interaction of radar signals with planetary regoliths on airless bodies. The experimental design implemented by Sotodeh (2014) at York University was greatly expanded upon for these purposes. A custom environment chamber was designed and built to isolate samples from atmospheric humidity during a permittivity measurement. Temperature variation was also added to the experimental setup using heating tape and an accompanying temperature controller. Silica aerogel was utilized for the first time to increase the range of densities in which a powdered material's permittivity could be measured. The software and methodology used to complete a permittivity measurement using the coaxial transmission line method was refined to concise scripts and procedures that are readily available for use by other researchers in the field. A model was developed to account for the boundary effects observed in coaxial airline permittivity measurements of powdered material, and was shown to accurately describe these effects. This model can be adapted by other researchers to correct this effect in their data, and highlighted that these effects are minimized for smaller grain sized samples. An extensive review of electromagnetic mixing theory was carried out in order to provide context for the experimental results obtained in this thesis. Seven different geologic samples were powdered, processed, and characterized using a variety of techniques to determine their structures and compositions. The permittivity of each sample was measured for a range of porosities. This allowed a subsequent analysis into modelling these measurements with a variety of mixing theories, with the accuracy of a given model fit determined by the correspondence to other experimental work in the literature. The Looyenga-Landau-Lifshitz (LLL) and Bruggeman (Symmetric) (BG) theories were shown to most accurately describe the change in the dry, non-conducting, non-magnetic geologic powder samples measured in this thesis,

which is consistent with the theoretical assumptions in either theory's derivation. The permittivity of the solid phase for each sample, or solid permittivity, predicted by either theory showed a strong linear correlation with the grain density of each sample. This correlation was described by a linear equation, which was also identified in similar experimental work in this field. The solid permittivity was also shown to be accurately predicted by the additivity rule of ionic polarizability (ARIP) and Clausius-Mossotti (CM) theories. The accuracy of either the LLL/BG models or ARIP/CM models depends on the length-scale of the dielectric mixture in question, describing a dielectric hierarchical system. These mixing results were incorporated into an existing asteroid radar model for use in predicting the bulk density and porosity of near-surface regolith material on radar observed asteroid surfaces. This model was applied to seven asteroids visited by robotic space exploration missions which measured the bulk (entire body) properties of the asteroids with exceptional accuracy. A comparison of the surface and bulk (entire body) porosity of each asteroid revealed that some asteroids are more homogeneous than others. The so called rubble-pile asteroids had a surface porosity that was similar to the value for the bulk (entire body) asteroid, whereas for some asteroids the surface porosity was significantly greater than that for the bulk (entire body) asteroid. The application and use of the asteroid radar model in this thesis was shown to be a useful tool in analyzing surface properties of asteroids, and can potentially be used to constrain other asteroidal properties such as internal structure.

Radar is an integral type of remote sensing observation that is extensively used to survey the natural universe. This thesis focused on radar observations from large telescopes such as Arecibo Observatory and Goldstone Solar System Radar, but many other forms of radar are applied in planetary science studies. NASA's *Mars 2020* mission to Mars will include the RIMFAX ground-penetrating radar (GPR) instrument, which will collect subsurface radar profiles from 150 - 1200 MHz along the rover's ground track. Similarly, the ESA-Roscosmos *ExoMars Rover* mission to Mars will include the WISDOM GPR instrument, operating from 0.5 - 3 GHz. The CNSA has included a GPR instrument on the *Chang'e 3* and *Chang'e 4* missions to the Moon. ESA's *JUICE* mission and NASA's *Europa Clipper* mission to the Jovian system will include RIME and REASON, which are orbiting radar sounding instruments. Continued funding and support for planetary radar will extend and improve future radar observations of asteroids performed primarily by Arecibo Observatory. These radar studies span a wide range of types of planetary bodies, surface-atmosphere interactions, chemistry, surface topography, and radar signal parameters. This is a profound oppor-

tunity to utilize radar observations to their fullest extent, to extract more information from data that will facilitate a deeper analysis of the properties of our solar system. Experimental research and modelling like that presented in this thesis will support these space missions, and expand our collective understanding of planetary science.

8.2 Future Work

The experimental methodology developed in this research can be used to measure the permittivity of other types of materials relevant to planetary radar. While this thesis was only concerned with dry, non-magnetic, non-conducting geologic material, these assumptions are not valid for bodies with appreciable atmospheres, such as Mars, or regoliths with significant volatile content. Iron oxides, such as magnetite and hematite, possess magnetic permeabilities above unity and must also be taken into account for more accurate characterization of the electromagnetic response of planetary regolith. High circular polarization ratios (CPRs) are associated with permanently shadowed regions in the polar areas of Mercury and the Moon, and are thought to be a result of ice mixed in the regolith. Permittivity measurements of rock/ice analogue mixtures would support the study of these types of surfaces. Although most samples in this thesis were dispersionless, characterizing the above materials over a range of frequencies is important since radar systems operate in a range in frequencies, with orbiting radars typically in the 1-10 MHz range and GPR's typically in the 100 MHz - GHz range. The frequency and temperature dependence of the observed aluminium oxide relaxation in this thesis could be investigated by sequential measurements of aluminium oxide at increasing temperatures. The validity of the LLL and BG mixing models was confirmed for dry, non-magnetic, and non-conducting geologic materials in this thesis; however, this accuracy should decrease as the material properties deviate from these assumptions. Permittivity experiments on magnetic and conducting materials should then also investigate the accuracy of the different mixing theories in modelling the measurements. Based on the mixing review completed in this thesis, an educated guess would be that the BGNS or SSC models would be more appropriate in the case of conducting materials. The methodology applied to test the accuracies of the different mixing theories in modelling the permittivity measurements in this thesis is novel, and can be used in future research applying mixing theory. The boundary conditions model that was developed in this thesis did not consider the effects of the particle size distribution (PSD) on the model results. The amount of void space in a powder is dependent on the PSD, and so future experiments using

the coaxial transmission line method should attempt to account for this factor when considering boundary effects. In particular, the method of characterization of the PSD could be improved from mechanical sieving, for instance, by using petrographic microscope images. The asteroid radar model developed in this thesis makes use of the experimentally verified mixing models analyzed in this thesis, but is only as accurate as the estimations for the Fresnel reflectivity from radar data. Radar scattering models are applied to estimate the Fresnel reflectivity, and need to be improved for the inversion of radar data for surface properties to increase in accuracy. NASA's *OSIRIS-REx* and JAXA's *Hayabusa2* missions, as well as future space missions to asteroids, provide the opportunity to ground truth asteroid radar model predictions, and can help refine these models as well as radar scattering models.

Chapter 9

References

- Adam, S. and Packard, H. (1969). *Microwave theory and applications*. Prentice-Hall Upper Saddle River, NJ, USA:.
- Adams, R., Perger, W., Rose, W., and Kostinski, A. (1996). Measurements of the complex dielectric constant of volcanic ash from 4 to 19 GHz. *Journal of Geophysical Research: Solid Earth*, 101(B4):8175–8185.
- Baker-Jarvis, J., Janezic, M., Grosvenor Jr, J., and Geyer, R. (1993). Transmission/Reflection and Short-Circuit Line Methods for Measuring Permittivity and Permeability. Technical Report NIST Technical Note 1355-R, National Institute of Standards and Technology.
- Baker-Jarvis, J., Janezic, M., Riddle, B., Johnk, R., Holloway, C., Geyer, R., and Grosvenor, C. (2005). Measuring the Permittivity and Permeability of Lossy Materials: Solids, Liquids, Metals, and negative-Index Materials. Technical Report NIST Technical Note 1536, National Institute of Standards and Technology.
- Baker-Jarvis, J., Vanzura, E., and Kissick, W. (1990). Improved technique for determining complex permittivity with the Transmission/Reflection method. *IEEE Transactions on microwave theory and techniques*, 38(8):1096–1103.
- Balanis, C. (1989). *Advanced Engineering Electromagnetics*. John Wiley & Sons.
- Banhegyi, G. (1988). Numerical analysis of complex dielectric mixture formulae. *Colloid and Polymer Science*, 266(1):11–28.
- Bapna, P. and Joshi, S. (2013). Measurement of dielectric properties of various marble stones of Mewar region of Rajasthan at X-band microwave frequencies. *International Journal of Engineering and Innovative Technology (IJEIT)*, 2:180–186.

- Barmatz, M., Steinfeld, D., Winterhalter, D., Rickman, D., Gustafson, R., Butts, D., and Weinstein, M. (2012). Microwave permittivity and permeability measurements on lunar simulants. *43rd Lunar and Planetary Science Conference*, Abstract 1050.
- Barucci, M., Fulchignoni, M., Ji, J., Marchi, S., and Thomas, N. (2015). The flybys of asteroids (2867) steins, (21) lutetia, and (4179) toutatis. *Asteroids IV*, 1:433–450.
- Benadda, M., Carru, J., Amoureux, J., Castelain, M., and Chapoton, A. (1982). Experimental and theoretical study of the dielectric properties of 1-cyanoadamantane; spectrum of the compact crystal from measurements on powder. *Journal of Physics D: Applied Physics*, 15(8):1477.
- Benner, L., Busch, M., Giorgini, J., Taylor, P., and Margot, J. (2015). Radar observations of near-Earth and main-belt asteroids. *Asteroids IV*, 1:165–182.
- Benner, L., Ostro, S., Magri, C., Nolan, M., Howell, E., Giorgini, J., Jurgens, R., Margot, J., Taylor, P., Busch, M., and Shepard, M. (2008). Near-Earth asteroid surface roughness depends on compositional class. *Icarus*, 198(2):294–304.
- Birchak, J., Gardner, C., Hipp, J., and Victor, J. (1974). High dielectric constant microwave probes for sensing soil moisture. *Proceedings of the IEEE*, 62(1):93–98.
- Blair, S. and Thakkar, A. (2014). Additive models for the molecular polarizability and volume. *Chemical Physics Letters*, 610:163–166.
- Boivin, A. and Hickson, D. (2018). permittivitycalc. doi:10.5281/zenodo.1469776. v0.5.0.
- Boivin, A., Hickson, D., Tsai, C.-A., Cunje, A., Ghent, R., and Daly, M. (2018). Broadband measurements of the complex permittivity of carbonaceous asteroid regolith analog materials. *Journal of Geophysical Research: Planets*.
- Böttcher, C. and Bordewijk, P. (1978). *Theory of Electric Polarization*, volume 2. Elsevier Science Ltd.
- Boughriet, A.-H., Legrand, C., and Chapoton, A. (1997). Noniterative stable transmission/reflection method for low-loss material complex permittivity determination. *IEEE Transactions on Microwave Theory and Techniques*, 45(1):52–57.
- Boyle, M. (1985). The electrical properties of heterogeneous mixtures containing an oriented spheroidal dispersed phase. *Colloid and Polymer Science*, 263(1):51–57.

- Brosseau, C. (2006). Modelling and simulation of dielectric heterostructures: A physical survey from an historical perspective. *Journal of Physics D: Applied Physics*, 39(7):1277–1294.
- Brouet, Y., Becerra, P., Sabouroux, P., Pommerol, A., and Thomas, N. (2019). A laboratory-based dielectric model for the radar sounding of the martian subsurface. *Icarus*, 321:960–973.
- Brouet, Y., Levasseur-Regourd, A., Encrenaz, P., and Gulkis, S. (2014). Permittivity of porous granular matter, in relation with Rosetta cometary mission. *Planetary and Space Science*, 103:143–152.
- Brouet, Y., Levasseur-Regourd, A., Sabouroux, P., Encrenaz, P., Thomas, N., Heggy, E., and Kofman, W. (2015). Permittivity measurements of porous matter in support of investigations of the surface and interior of 67P/Churyumov-Gerasimenko. *Astronomy & Astrophysics*, 583:A39.
- Brouet, Y., Neves, L., Sabouroux, P., Levasseur-Regourd, A., Poch, O., Encrenaz, P., Pommerol, A., Thomas, N., and Kofman, W. (2016). Characterization of the permittivity of controlled porous water ice-dust mixtures to support the radar exploration of icy bodies. *Journal of Geophysical Research: Planets*, 121(12):2426–2443.
- Browning, L., Jr, H. M., and Zolensky, M. (1996). Correlated alteration effects in CM carbonaceous chondrites. *Geochimica et Cosmochimica Acta*, 60(14):2621–2633.
- Bruggeman, V. D. (1935). Berechnung cerschiedener physikalisher Konstanten von heterogenen Substanzen. I. Dielektrizitätskonstanten und Leitfähigkeiten der Mischkörper aus isotropen Substanzen. *Annalen der physik*, 416(7):636–664.
- Bruker Nano GmbH (2011). Introduction to EDS analysis: Reference Manual. Technical Report DOC-M82-EXX053, Bruker Nano GmbH.
- Bus, S. and Binzel, R. (2002). Phase II of the Small Main-Belt Asteroid Spectroscopic Survey: A Feature-Based Taxonomy. *Icarus*, 158(1):146–177.
- Bussey, H. (1979). Microwave dielectric measurements of lunar soil with a coaxial line resonator method. *Lunar and Planetary Science Conference Proceedings*, 10th:2175–2182.
- Bussey, H., Gray, J., Bamberger, E., Rushton, E., Russell, G., Petley, B., and Morris, D. (1964). International comparison of dielectric measurements. *IEEE Transactions on Instrumentation and Measurement*, 13(4):305–311.

- Cabot Corporation (2017). *Enova Aerogel IC3100 Datasheet*. Cabot Corporation. <http://www.buyaerogel.com/product/enova-aerogel-ic3100/>.
- Calame, J. (2008). Dielectric permittivity simulation of random irregularly shaped particle composites and approximation using modified dielectric mixing laws. *Journal of Applied Physics*, 104(11):114108.
- Calame, J., Birman, A., Carmel, Y., Gershon, D., Levush, B., Sorokin, A., Semenov, V., Dadon, D., Martin, L., and Rosen, M. (1996). A dielectric mixing law for porous ceramics based on fractal boundaries. *Journal of applied physics*, 80(7):3992–4000.
- Campbell, B. (2002). *Radar remote sensing of planetary surfaces*. Cambridge University Press.
- Campbell, B. (2016). Planetary Geology with Imaging Radar: Insights from Earth-based Lunar Studies, 2001–2015. *Publications of the Astronomical Society of the Pacific*, 128(964):20pp.
- Campbell, M. and Ulrichs, J. (1969). Electrical properties of rocks and their significance for lunar radar observations. *Journal of Geophysical Research*, 74(25):5867–5881.
- Carmichael, R. (1982). *Handbook of Physical Properties of Rocks*, volume 1. CRC Press, Inc.
- Carrier, W., Olhoeft, G., and Mendell, W. (1991). Physical properties of the lunar surface. *Lunar sourcebook*, pages 475–594.
- Carter, L., Campbell, D., and Campbell, B. (2011). Geologic studies of planetary surfaces using radar polarimetric imaging. *Proceedings of the IEEE*, 99(5):770–782.
- Chapman, C. (1996). S-type asteroids, ordinary chondrites, and space weathering: The evidence from Galileo’s fly-bys of Gaspra and Ida. *Meteoritics & Planetary Science*, 31(6):699–725.
- Chen, L. and Hunter, G. (2004). Temperature dependent dielectric properties of Polycrystalline 96% Al_2O_3 . *MRS Online Proceedings Library Archive*, 833.
- Chen, L.-F., Ong, C., Neo, C., Varadan, V., and Varadan, V. (2004). *Microwave Electronics: Measurement and Materials Characterization*. John Wiley & Sons.
- Church, R., Webb, W., and Salsman, J. (1988). Dielectric Properties of Low-Loss Minerals. Technical report, United States Department of the Interior Bureau of Mines.

- Clark, B., Binzel, R., Howell, E., Cloutis, E., Ockert-Bell, M., Christensen, P., Barucci, M., DeMeo, F., Lauretta, D., Connolly, H., Soderberg, A., Hergenrother, C., Lim, L., Emery, J., and Mueller, M. (2011). Asteroid (101955) 1999 RQ36: Spectroscopy from 0.4 to 2.4 μm and meteorite analogs. *Icarus*, 216:462–475.
- Clark, B., Hapke, B., Pieters, C., and Britt, D. (2002). Asteroid space weathering and regolith evolution. *Asteroids III*, pages 585–599.
- Consolmagno, G., Britt, D., and Macke, R. (2008). The significance of meteorite density and porosity. *Chemie der Erde-Geochemistry*, 68(1):1–29.
- Coradini, A., Capaccioni, F., Erard, S., Arnold, G., De Sanctis, M., Filacchione, G., Tosi, F., Barucci, M., Capria, M., Ammannito, E., Grassi, D., Piccioni, G., Giuppi, S., Bellucci, G., Benkhoff, J., Bibring, J., Blanco, A., Blecka, M., Bockelee-Morvan, D., Carraro, F., Carlson, R., Carsenty, U., Cerroni, P., Colangeli, L., Combes, M., Combi, M., Crivisier, J., Drossart, P., Encrenaz, E., Federico, C., Fink, U., Fonti, S., Giacomini, L., Ip, W., Jaumann, R., Kuehrt, E., Langevin, Y., Magni, G., McCord, T., Mennella, V., Mottola, S., Neukum, G., Orofino, V., Palumbo, P., Schade, U., Schmitt, B., Taylor, F., Tiphene, D., and Tozzi, G. (2011). The surface composition and temperature of asteroid 21 Lutetia as observed by Rosetta/VIRTIS. *Science*, 334(6055):492–494.
- Cosenza, P., Ghorbani, A., Camerlynck, C., Rejiba, F., Guérin, R., and Tabbagh, A. (2009). Effective medium theories for modelling the relationships between electromagnetic properties and hydrological variables in geomaterials: a review. *Near Surface Geophysics*, 7(5-6):563–578.
- Courtney, W. (1970). Analysis and Evaluation of a Method of Measuring the Complex Permittivity and Permeability of Microwave Insulators. *IEEE Transactions on Microwave Theory and Techniques*, 18(8):476–485.
- Covey, S., Lewis, J., Metzger, P., and Britt, D. (2018). Developing Carbonaceous Chondrite Asteroid Simulants. In *16th Biennial International Conference on Engineering, Science, Construction, and Operations in Challenging Environments, Cleveland Ohio, USA April 9-12*, pages 8–16. ASCE.
- Cygan, R. and Lasaga, A. (1986). Dielectric and polarization behavior of forsterite at elevated temperatures. *American Mineralogist*, 71(5-6):758–766.

- Davis, A., Leigh, C., Hampton, R., Saunders, G., and Parker, S. (1988). Temperature dependence of the static dielectric constant of naturally occurring monocrystalline forsterite. *Journal of materials science letters*, 7(4):415–416.
- De Sanctis, M., Ammannito, E., Capria, M., Tosi, F., Capaccioni, F., Zambon, F., Carraro, F., Fonte, S., Frigeri, A., Jaumann, R., Magni, G., Marchi, S., McCord, T., McFadden, L., McSween, H., Mittlefehldt, D., Nathues, A., Palomba, E., Pieters, C., Raymond, C., Russell, C., Toplis, M., and Turrini, D. (2012). Spectroscopic characterization of mineralogy and its diversity across Vesta. *Science*, 336(6082):697–700.
- Demeo, F., Alexander, C., Walsh, K., Chapman, C., and Binzel, R. (2015). The Compositional Structure of the Asteroid Belt. *Asteroids IV*, pages 13–41.
- DeMeo, F., Binzel, R., Slivan, S., and Bus, S. (2009). An extension of the bus asteroid taxonomy into the near-infrared. *Icarus*, 202(1):160–180.
- Dobson, M., Ulaby, F., Hallikainen, M., and El-Rayes, M. (1985). Microwave dielectric behavior of wet soil-Part II: Dielectric mixing models. *IEEE Transactions on Geoscience and Remote Sensing*, (1):35–46.
- Dube, D. (1970). Study of Landau-Lifhitz-Looyenga’s formula for dielectric correlation between powder and bulk. *Journal of Physics D: Applied Physics*, 3(11):1648–1652.
- Dube, D. and Parshad, R. (1970). Study of Böttcher’s formula for dielectric correlation between powder and bulk. *Journal of Physics D: Applied Physics*, 3(5):677.
- Ebara, H., Inoue, T., and Hashimoto, O. (2006). Measurement method of complex permittivity and permeability for a powdered material using a waveguide in microwave band. *Science and Technology of Advanced Materials*, 7(1):77.
- ElShafie, A. and Heggy, E. (2013). Dielectric and hardness measurements of planetary analog rocks in support of in-situ subsurface sampling. *Planetary and Space Science*, 86:150–154.
- Feng, S. and Sen, P. (1985). Geometrical model of conductive and dielectric properties of partially saturated rocks. *Journal of Applied Physics*, 58(8):3236–3243.
- Fensler, W., Knott, E., Olte, A., and Siegel, K. (1962). The electromagnetic parameters of selected terrestrial and extraterrestrial rocks and glasses. In *The Moon*, volume 14, pages 545–565.

- Feynman, R., Leighton, R., and Sands, M. (1979). *The Feynman lectures on physics, vol. 2: Mainly electromagnetism and matter*. Addison-Wesley.
- Fontanella, J., Andeen, C., and Schuele, D. (1974). Low-frequency dielectric constants of α -quartz, sapphire, MgF₂, and MgO. *Journal of Applied Physics*, 45(7):2852–2854.
- Fujiwara, A., Kawaguchi, J., Yeomans, D., Abe, M., Mukai, T., Okada, T., Saito, J., Yano, H., Yoshikawa, M., Scheeres, D., Barnouin-Jha, O., Cheng, A., Demura, H., Gaskell, R., Hirata, N., Ikeda, H., Kominato, T., Miyamoto, H., Nakamura, A., Nakamura, R., Sasaki, S., and Uesugi, K. (2006). The rubble-pile asteroid Itokawa as observed by Hayabusa. *Science*, 312(5778):1330–1334.
- Gaines, R., Dana, J., and Dana, E. (1997). *Dana's new mineralogy: The system of mineralogy of James Dwight Dana and Edward Salisbury Dana*. Wiley.
- Garvin, J., Head, J., Pettengill, G., and Zisk, S. (1985). Venus global radar reflectivity and correlations with elevation. *Journal of Geophysical Research*, 90:6859–6871.
- Gershon, D., Calame, J., and Birnboim, A. (2001). Complex permittivity measurements and mixing laws of porous alumina. *Journal of Applied Physics*, 89(12):8117–8120.
- Geyer, R. (1990). Dielectric Characterization and Reference Materials. Technical report, United States Department of Commerce National Institute of Standards and Technology (NIST).
- Ghosh, P. and Das, A. (1979). Preparation and characterization of forsterite and measurement of its dielectric constant and loss factor in the frequency range of 100 kc/s to 25 mc/s. *Transactions of the Indian Ceramic Society*, 38(3):89–95.
- Gladstone, J. and Dale, T. (1863). XIV. Researches on the refraction, dispersion, and sensitiveness of liquids. *Philosophical Transactions of the Royal Society of London*, (153):317–343.
- Goncharenko, A. (2003). Generalizations of the Bruggeman equation and a concept of shape-distributed particle composites. *Physical review E*, 68(4):041108.
- Goncharenko, A., Lozovski, V., and Venger, E. (2000). Lichtenecker's equation: applicability and limitations. *Optics Communications*, 174(1):19–32.
- Griffiths, D. (1999). *Introduction to Electrodynamics, Vol 4*. Prentic Hall.

- Grosvenor Jr, J. (1993). Nist measurement service for electromagnetic characterization of materials. Technical report, National Institute of Standards and Technology.
- Gurav, J., Jung, I.-K., Park, H.-H., Kang, E., and Nadargi, D. (2010). Silica aerogel: synthesis and applications. *Journal of Nanomaterials*, 2010:11pp.
- Hagfors, T. (1964). Backscattering from an Undulating Surface with Applications to Radar Returns from the Moon. *Journal of Geophysical Research*, 69(18):3779–3784.
- Hales, T. (2005). A proof of the Kepler conjecture. *Annals of mathematics*, pages 1065–1185.
- Hanai, T. (1960). Theory of the dielectric dispersion due to the interfacial polarization and its application to emulsions. *Kolloid-Zeitschrift*, 171(1):23–31.
- Harmon, J. and Ostro, S. (1985). Mars: Dual-polarization radar observations with extended coverage. *Icarus*, 62(1):110–128.
- Hashin, Z. and Shtrikman, S. (1962). A variational approach to the theory of the effective magnetic permeability of multiphase materials. *Journal of applied Physics*, 33(10):3125–3131.
- Heggy, E., Palmer, E., Kofman, W., Clifford, S., Richter, K., and Hérique, A. (2012). Radar properties of comets: Parametric dielectric modeling of Comet 67P/Churyumov–Gerasimenko. *Icarus*, 221(2):925–939.
- Heggy, E. and Paillou, P., Ruffié, G., Malezieux, J., Costard, F., and Grandjean, G. (2001). On water detection in the Martian subsurface using sounding radar. *Icarus*, 154(2):244–257.
- Hérique, A., Kofman, W., Beck, P., Bonal, L., Buttarazzi, I., Heggy, E., Lasue, J., Lvasseur-Regourd, A., Quirico, E., and Zine, S. (2017). Cosmochemical implications of CONSERT permittivity characterization of 67P/CG. *Monthly Notices of the Royal Astronomical Society*, 462(Suppl.1):S516–S532.
- Hickson, D., Boivin, A., Daly, M., Ghent, R., Nolan, M., Tait, K., Cunje, A., and Tsai, C. (2018). Near surface bulk density estimates of NEAs from radar observations and permittivity measurements of powdered geologic material. *Icarus*, 306.
- Hickson, D., Boivin, A., Daly, M., Ghent, R., Nolan, M., Tait, K., Cunje, A., and Tsai, C.-A. (2017a). Constraining Bulk Densities of near-Earth Asteroid Surfaces from Radar Observations

- Using Laboratory Measurements of Permittivity. *2017 AGU Fall Meeting Poster Presentation*, Abstract P13B-1963.
- Hickson, D., Sotodeh, S., Daly, M., Ghent, R., and Nolan, M. (2017b). Improvements on effective permittivity measurements of powdered alumina: Implications for bulk permittivity properties of asteroid regoliths. *Advances in Space Research*, 59(1):472–482.
- Howard, K., Benedix, G., Bland, P., and Cressey, G. (2009). Modal mineralogy of CM2 chondrites by X-ray diffraction (PSD-XRD). Part 1: Total phyllosilicate abundance and the degree of aqueous alteration. *Geochimica et Cosmochimica Acta*, 73(15):4576–4589.
- Hrubesh, L. and Pekala, R. (1994). Dielectric properties and electronic applications of aerogels. In *Sol-Gel Processing and Applications*, pages 363–367.
- Huang, J., Ji, J., Ye, P., Wang, X., Yan, J., Meng, L., Wang, S., Li, C., Li, Y., Qiao, D., Zhao, W., Zhao, Y., Zhang, T., Liu, P., Jiang, Y., Rao, W., Li, S., Huang, C., Ip, W.-H., Hu, S., Zhu, M., Yu, L., Zou, Y., Tang, X., Li, J., Zhao, H., Huang, H., Jiang, X., and Bai, J. (2013). The ginger-shaped asteroid 4179 toutatis: New observations from a successful flyby of Chang’e-2. *Scientific reports*, 3:3411.
- Hudson, R. and Ostro, S. (1994). Shape of Asteroid 4769 Castalia (1989 PB) from Inversion of Radar Images. *Science*, 263(5149):940–943.
- Huss, G., Rubin, A., and Grossman, J. (2006). Thermal Metamorphism in Chondrites. *Meteorites and the Early Solar System II*, pages 567–586.
- Hutchison, R. (2004). *Meteorites: A Petrologic, Chemical and Isotopic Synthesis*. Cambridge University Press.
- ISO/IEC GUIDE 98-3 (2008). Uncertainty of measurements - Part 3: Guide to the Expression of Uncertainty in Measurement (GUM: 1995). Technical report, Geneva, Switzerland: International Organisation for Standardisation.
- Jeanloz, R. and Ahrens, T. (1978). The equation of state of a lunar anorthosite: 60025. In *Lunar and Planetary Science Conference Proceedings*, volume 9, pages 2789–2803.
- Johnson, R. and Poeter, E. (2005). Iterative use of the Bruggeman-Hanai-Sen mixing model to determine water saturations in sand. *Geophysics*, 70(5):K33–K38.

- Jones, S. (2006). Aerogel: space exploration applications. *Journal of Sol-Gel Science and Technology*, 40(2-3):351–357.
- Jylhä, L. (2008). *Modeling of electrical properties of composites*. PhD thesis, Helsinki University of Technology.
- Jylhä, L. and Sihvola, A. (2007). Equation for the effective permittivity of particle-filled composites for material design applications. *Journal of Physics D: Applied Physics*, 40(16):4966.
- Kameyama, K. and Miyamoto, T. (2008). Measurement of solid phase permittivity for volcanic soils by time domain reflectometry. *European journal of soil science*, 59(6):1253–1259.
- Kärkkäinen, K., Sihvola, A., and Nikoskinen, K. (2000). Effective permittivity of mixtures: Numerical validation by the FDTD method. *IEEE Transactions on Geoscience and Remote Sensing*, 38(3):1303–1308.
- Kärkkäinen, K., Sihvola, A., and Nikoskinen, K. (2001). Analysis of a three-dimensional dielectric mixture with finite difference method. *IEEE Transactions on Geoscience and Remote Sensing*, 39(5):1013–1018.
- Keller, H., Barbieri, C., Koschny, D., Lamy, P., Rickman, H., Rodrigo, R., Sierks, H., A’Hearn, M., Angrilli, F., Barucci, M., Bertaux, J.-L., Cremonese, G., Da Deppo, V., Davidsson, B., De Cecco, M., Debei, S., Fornasier, S., Fulle, M., Groussin, O., Gutierrez, P., Hviid, S., Ip, W.-H., Jorda, L., Knollenberg, J., Kramm, J., Kührt, E., Küppers, M., Lara, L.-M., Lazzarin, M., Lopez Moreno, J., Marzari, F., Michalik, H., Naletto, G., Sabau, L., Thomas, N., Wenzel, K.-P., Bertini, I., Besse, S., Ferri, F., Kaasalainen, M., Lowry, S., Marchi, S., Mottola, S., Sabolo, W., Schröder, S., Spjuth, S., and Vernazza, P. (2010). E-type asteroid (2867) Steins as imaged by OSIRIS on board Rosetta. *Science*, 327(5962):190–193.
- Kenyon, W. (1984). Texture effects on megahertz dielectric properties of calcite rock samples. *Journal of Applied Physics*, 55(8):3153–3159.
- KeysightTechnologies (2014a). *Applying Error Correction to Network Analyzer Measurements*. Keysight Technologies, USA. Literature Number: 5965-7709E.
- KeysightTechnologies (2014b). *Signal Integrity Analysis Series Part 3: The ABCs of De-Embedding*. Keysight Technologies, USA. Literature Number: 5989-5765EN.

- KeysightTechnologies (2016). *Keysight E5071C ENA Network Analyzer Data Sheet*. Keysight Technologies, USA. Literature Number: 5989-5479EN.
- Kiley, E., Yakovlev, V., Ishizaki, K., and Vaucher, S. (2012). Applicability study of classical and contemporary models for effective complex permittivity of metal powders. *Journal of Microwave Power and Electromagnetic Energy*, 46(1):26–38.
- Knight, R. and Nur, A. (1987). The dielectric constant of sandstones, 60 kHz to 4 MHz. *Geophysics*, 52(5):644–654.
- Knoll, M. (1996). *A Petrophysical Basis for Ground Penetrating Radar and Very Early Time Electromagnetics: Electrical Properties of Sand-Clay Mixtures*. PhD thesis, University of British Columbia.
- Kofman, W., Herique, A., Barbin, Y., Barriot, J., Ciarletti, V., Clifford, S., Edenhofer, P., Elachi, C., Eyraud, C., Goutail, J., Heggy, E., Jorda, L., Lasue, J., Lévassieur-Regourd, A., Nielsen, E., Pasquero, P., Preusker, F., Puget, P., Plettmeier, D., Rogez, Y., Sierks, H., Statz, C., Svedhem, H., Williams, I., Zine, S., and Van Zyl, J. (2015). Properties of the 67P/Churyumov-Gerasimenko interior revealed by CONSERT radar. *Science*, 349(6247).
- Krupka, J., Derzakowski, K., Riddle, B., and Baker-Jarvis, J. (1998). A dielectric resonator for measurements of complex permittivity of low loss dielectric materials as a function of temperature. *Measurement Science and Technology*, 9(10):1751–1756.
- Lafuente, B., Downs, R., and N., S. (2015). The power of databases: The RRUFF project. In *Highlights in Mineralogical Crystallography*, pages 1–30.
- Landau, L. and Lifshitz, E. (1960). *Electrodynamics of continuous media*. Oxford Pergamon Press.
- Landauer, R. (1978). Electrical conductivity in inhomogeneous media. *AIP Conference Proceedings*, 40(1978):2–45.
- Lauretta, D., Balram-Knutson, S., Beshore, E., Boynton, W., d’Aubigny, C., DellaGiustina, D., Enos, H., Golish, D., Hergenrother, C., Howell, E., Bennett, C., Morton, E., Nolan, M., Rizk, B., Roper, H., Bartels, A., Bos, B., Dworkin, J., Highsmith, D., Lorenz, D., Lim, L., Mink, R., Moreau, M., Nuth, J., Reuter, D., Simon, A., Bierhaus, E., Bryan, B., Ballouz, R., Barnouin, O., Binzel, R., Bottke, W., Hamilton, V., Walsh, K., Chesley, S., Christensen, P., Clark, B., Connolly,

- H., Crombie, M., Daly, M., Emery, J., McCoy, T., McMahon, J., Scheeres, D., Messenger, S., Nakamura-Messenger, K., Righter, K., and Sandord, S. (2017). OSIRIS-REx: sample return from asteroid (101955) Bennu. *Space Science Reviews*, 212(1-2):925–984.
- Lauretta, D., Bartels, A., Barucci, M., Bierhaus, E., Binzel, R., Bottke, W., Campins, H., Chesley, S., Clark, B., Clark, B., Cloutis, E., Connolly, H., Crombie, M., Delbo, M., Dworkin, J., Emery, J., Glavin, D., Hamilton, V., Hergenrother, C., Johnson, C., Keller, L., Michel, P., Nolan, M., Sandford, S., Scheeres, D., Simon, A., Sutter, B., Vokrouhlicky, D., and Walsh, K. (2015). The OSIRIS-REx target asteroid (101955) Bennu: Constraints on its physical, geological, and dynamical nature from astronomical observations. *Meteoritics & Planetary Science*, 50(4):834–849.
- Leão, T., Perfect, E., and Tyner, J. (2015). Evaluation of Lichtenecker’s Mixing Model for Predicting Effective Permittivity of Soils at 50 MHz. *Transactions of the ASABE*, 58(1):83–91.
- Lemmon, E., McLinden, M., and D.G., F. (2017). Thermophysical properties of fluid systems. In *P. Linstrom & W. Mallard (Eds.), NIST Chem. Webbook, NIST Stand. Ref. Database Number 69*, page 20899. Gaithersburg MD: National Institute of Standards and Technology.
- Lewis, A. and Smewing, J. (1980). The Montgenevre ophiolite (Hautes Alpes, France): Meta—morphism and trace-element geochemistry of the volcanic sequence. *Chemical Geology*, 28:291–306.
- Lichtenecker, K. (1926). Die Dielektrizitätskonstante natürlicher und künstlicher Mischkörper. *Physikalische Zeitschrift*, 27(4):115–158.
- Lichtenecker, K. and Rother, K. (1931). Die herleitung des logarithmischen mischungsgesetzes aus allgemeinen prinzipien der stationären stroemung. *Physikalische Zeitschrift*, 32:255–260.
- Lin, T., Love, H., and Stark, D. (1992). Physical properties of concrete made with Apollo 16 lunar soil sample. In *Lunar Bases and Space Activities of the 21st Century*, pages 483–487.
- Looyenga, H. (1965). Dielectric constants of heterogeneous mixtures. *Physica*, 31(3):401–406.
- Lymer, E. (2017). Laser-Induced Fluorescence Spectroscopy as a Non-Destructive Technique for Mineral and Organic Detection in Carbonaceous Chondrites. Master’s thesis, York University.

- Magri, C., Nolan, M., Ostro, S., and Giorgini, J. (2007). A radar survey of main-belt asteroids: Arecibo observations of 55 objects during 1999–2003. *Icarus*, 186(1):126–151.
- Magri, C., Ostro, S., Rosema, K., Thomas, M., Mitchell, D., Campbell, D., Chandler, J., Shapiro, I., Giorgini, J., and Yeomans, D. (1999). Mainbelt asteroids: Results of Arecibo and Goldstone radar observations of 37 objects during 1980–1995. *Icarus*, 140(2):379–407.
- Magri, C. and Consolmagno, G., Ostrch, S., Benner, L., and Beeney, B. (2001). Radar constraints on asteroid regolith properties using 433 eros as ground truth. *Meteoritics & Planetary Science*, 36(12):1697–1709.
- Malik, S., Khan, K., Shamim, A., Suleman, M., and Mateen, A. (1988). Determination of dielectric constant of marble by the application of Looyenga’s equation. *Journal of materials science letters*, 7(4):368–370.
- Mamunya, Y., Muzychenko, Y., Pissis, P., Lebedev, E., and Shut, M. (2001). Processing, structure, and electrical properties of metal-filled polymers. *Journal of Macromolecular Science, Part B*, 40(3-4):591–602.
- Martinez, A. and Brynes, A. (2001). *Modeling dielectric-constant values of geologic materials: An aid to ground-penetrating radar data collection and interpretation*, volume 247. Kansas Geological Survey Lawrence, Kansas.
- Maxwell Garnett, J. (1904). Colours in Metal Glasses and in Metallic Films. *Trans. of the Royal Society of London*, 203:385–420.
- McCullom, T. and Jakosky, B. (1993). Interpretation of planetary radar observations: The relationship between actual and inferred slope distributions. *Journal of Geophysical Research: Planets*, 98(E1):1173–1184.
- McCoy, T., Scott, E., Jones, R., Keil, K., and Taylor, G. (1991). Composition of chondrule silicates in LL3-5 chondrites and implications for their nebular history and parent body metamorphism. *Geochimica et Cosmochimica Acta*, 55(2):601–619.
- McSween Jr, H., Binzel, R., De Sanctis, M., Ammannito, E., Prettyman, T., Beck, A., Reddy, V., Le Corre, L., Gaffey, M., McCord, T., Raymond, C., Russell, C., and the Dawn Science Team (2013). Dawn; the Vesta–HED connection; and the geologic context for eucrites, diogenites, and howardites. *Meteoritics & Planetary Science*, 48(11):2090–2104.

- Merrill, W., Diaz, R., LoRe, M., Squires, M., and Alexopoulos, N. (1999). Effective medium theories for artificial materials composed of multiple sizes of spherical inclusions in a host continuum. *IEEE Transactions on antennas and propagation*, 47(1):142–148.
- Metzger, P., Britt, D., Covey, S., Schultz, C., Cannon, K., Grossman, K., Mantovani, J., and Mueller, R. (2019). Measuring the fidelity of asteroid regolith and cobble simulants. *Icarus*, 321:632–646.
- Mitchell, D., Ostro, S., Hudson, R., Rosema, K., Campbell, D., Velez, R., Chandler, J., Shapiro, I., Giorgini, J., and Yeomans, D. (1996). Radar Observations of Asteroids 1 Ceres, 2 Pallas, and 4 Vesta. *Icarus*, 124:113–133.
- Napijalo, M., Nikolić, Z., Dojčilović, J., Napijalo, M., and Novaković, L. (1998). Temperature dependence of electric permittivity of linear dielectrics with ionic and polar covalent bonds. *Journal of Physics and Chemistry of solids*, 59(8):1255–1258.
- Neelakantaswamy, P., Chowdari, B., and Rajaratnam, A. (1983). Estimation of permittivity of a compact crystal by dielectric measurements on its powder: A stochastic mixture model for the powder-dielectric. *Journal of Physics D: Applied Physics*, 16(9):1785.
- Neelakantaswamy, P., Turkman, R., and Sarkar, T. (1985). Complex permittivity of a dielectric mixture: corrected version of Lichtenecker’s logarithmic law of mixing. *Electronics Letters*, 21(7):270–271.
- Nelson, S. (1992). Estimation of permittivities of solids from measurements on pulverized or granular materials. *Dielectric Properties of Heterogeneous Materials: Progress in Electromagnetics Research*, 6:231–271.
- Nelson, S. (2005). Density-permittivity relationships for powdered and granular materials. *IEEE Transactions on Instrumentation and Measurement*, 54(5):2033–2040.
- Nelson, S. and Bartley, P. (1998). Open-ended coaxial-line permittivity measurements on pulverized materials. *IEEE Transactions on Instrumentation and Measurement*, 47(1):133–137.
- Nelson, S. and Bartley Jr, P. (2000). Measuring frequency-and temperature-dependent dielectric properties of food materials. *Transactions of the ASAE*, 43(6):1733.

- Nelson, S., Lindroth, D., and Blake, R. (1989). Dielectric properties of selected minerals at 1 to 22 GHz. *Geophysics*, 54(10):1344–1349.
- Newville, M., Ingargiola, A., Stensitzki, T., and Allen, D. (2014). LMFIT: non-linear least-square minimization and curve-fitting for Python. doi: 10.5281/zenodo.11813. v0.8.0.
- Nicolson, A. and Ross, G. (1970). Measurement of the intrinsic properties of materials by time-domain techniques. *IEEE Trans. Instrum. Meas*, 19(4):377–382.
- Nolan, M., Magri, C., Howell, E., Benner, L., Giorgini, J., Hergenrother, C., Hudson, R., Lauretta, D., Margot, J., Ostro, S., and Scheeres, D. (2013). Shape model and surface properties of the OSIRIS-REx target Asteroid (101955) Bennu from radar and lightcurve observations. *Icarus*, 226(1):629–640.
- Oguchi, T., Udagawa, M., Nanba, N., Maki, M., and Ishimine, Y. (2009). Measurements of dielectric constant of volcanic ash erupted from five volcanoes in Japan. *IEEE Transactions on Geoscience and Remote Sensing*, 47(4):1089–1096.
- Olhoeft, G. (1981). Electrical Properties of Rocks. In *Physical Properties of Rocks and Minerals, CINDAS Data Series on Material Properties II-2*. Hemisphere Publishing Corporation.
- Olhoeft, G. (1987). Electrical properties from 10^{-3} to 10^9 HZ— Physics and chemistry. In *AIP conference proceedings*, volume 154, pages 281–298.
- Olhoeft, G. and Strangway, D. (1975). Dielectric properties of the first 100 meters of the Moon. *Earth and Planetary Science Letters*, 24(3):394–404.
- Ostro, S. (1993). Planetary Radar Astronomy. *Reviews of Modern Physics*, 65(4):1235–1279.
- Ostro, S., Benner, L., Nolan, M., Magri, C., Giorgini, J., Scheeres, D., Broschart, S., Kaasalainen, M., Vokrouhlický, D., Chesley, S., Margot, J., Jurgens, R., Rose, R., Yeomans, D., Suzuki, S., and De Jong, E. (2004). Radar observations of asteroid 25143 Itokawa (1998 SF36). *Meteoritics & Planetary Science*, 39(3):407–424.
- Ostro, S., Campbell, D., and Shapiro, I. (1985). Mainbelt asteroids: Dual-polarization radar observations. *Science*, 229(4712):442–446.
- Palmer, E., Heggy, E., Capria, M., and Tosi, F. (2015). Dielectric properties of Asteroid Vesta’s surface as constrained by Dawn VIR observations. *Icarus*, 262:93–101.

- Park, C.-H., Behrendt, A., LeDrew, E., and Wulfmeyer, V. (2017). New approach for calculating the effective dielectric constant of the moist soil for microwaves. *Remote Sensing*, 9(7):732.
- Parker, M. (1973). *Radio-wave Scattering from Rough Surfaces and the Estimation of Surface Shape*. PhD thesis, Stanford University.
- Pätzold, M., Andert, T., Asmar, S., Anderson, J., Barriot, J.-P., Bird, M., Häusler, B., Hahn, M., Tellmann, S., Sierks, H., Lamy, P., and Weiss, B. (2011). Asteroid 21 Lutetia: Low mass, high density. *Science*, 334(6055):491–492.
- Pekonen, O., Kärkkäinen, K., Sihvola, A., and Nikoskinen, K. (1999). Numerical testing of dielectric mixing rules by FDTD method. *Journal of Electromagnetic Waves and Applications*, 13(1):67–87.
- Penn, S., Alford, N., Templeton, A., Wang, X., Xu, M., Reece, M., and Schrapel, K. (1997). Effect of porosity and grain size on the microwave dielectric properties of sintered alumina. *Journal of the American Ceramic Society*, 80(7):1885–1888.
- Pervin, S. (2015). Investigation of dielectric properties of rocks and minerals for GPR data interpretation. Master’s thesis, University of Alberta.
- Platzmann, W. and Schulz, D. (2009). Handbuch Elektrotechnik Grundlagen und Anwendungen für Elektrotechniker. *Kapitel*, 2:338.
- Plonus, M. (1978). *Applied Electromagnetics*. McGraw-Hill.
- Plug, W., Bruining, J., Slob, E., and Goritti, A. (2006). Numerical validation of various mixing rules used for up-scaled geo-physical properties. In *Proc. of CMWR XVI, Copenhagen*.
- Pulido-Gaytán, M., Reynoso-Hernández, J., Loo-Yau, J., Zárate-de Landa, A., and del Carmen Maya-Sánchez, M. (2015). Generalized theory of the thru-reflect-match calibration technique. *IEEE Transactions on Microwave Theory and Techniques*, 63(5):1693–1699.
- Rajab, K., Naftaly, M., Linfield, E., Nino, J., Arenas, D., Tanner, D., Mittra, R., and Lanagan, M. (2008). Broadband Dielectric Characterization of Aluminum Oxide (Al₂O₃). *Journal of Microelectronics and Electronic Packaging*, 5(1):101–106.
- Reddy, V., Sanchez, J., Gaffey, M., Abell, P., Le Corre, L., and Hardersen, P. (2012). Composition of near-Earth Asteroid (4179) Toutatis. *Icarus*, 221(2):1177–1179.

- Reynolds, J. and Hough, J. (1957). Formulae for Dielectric Constant of Mixtures. *Proc. Phys. Soc. B*, 70(769).
- Robens, E., Bischoff, A., Schreiber, A., Dabrowski, A., and Unger, K. (2007). Investigation of surface properties of lunar regolith: Part I. *Applied Surface Science*, 253(13):5709–5714.
- Robertson, J. (2000). Band offsets of wide-band-gap oxides and implications for future electronic devices. *Journal of Vacuum Science & Technology B: Microelectronics and Nanometer Structures Processing, Measurement, and Phenomena*, 18(3):1785–1791.
- Robinson, D. and Friedman, S. (2003). A method for measuring the solid particle permittivity or electrical conductivity of rocks, sediments, and granular materials. *Journal of Geophysical Research: Solid Earth*, 108(B2).
- Robinson, D. and Friedman, S. (2005). Electrical conductivity and dielectric permittivity of sphere packings: Measurements and modelling of cubic lattices, randomly packed monosize spheres and multi-size mixtures. *Physica A: Statistical Mechanics and its Applications*, 358(2-4):447–465.
- Rogers, A., Macfarlane, D., and Robertson, D. (2011). Complex permittivity of volcanic rock and ash at millimeter wave frequencies. *IEEE Geoscience and Remote Sensing Letters*, 8(2):298–302.
- Rosenholtz, J. and Smith, D. (1936). The dielectric constant of mineral powders. *American Mineralogist: Journal of Earth and Planetary Materials*, 21(2):115–120.
- Rubin, A., Trigo-Rodríguez, J., Huber, H., and Wasson, J. (2007). Progressive aqueous alteration of CM carbonaceous chondrites. *Geochimica et Cosmochimica Acta*, 71(9):2361–2382.
- Russell, C., McSween, H., Jaumann, R., and Raymond, C. (2015). The Dawn Mission to Vesta and Ceres. *Asteroids IV*, pages 419–432.
- Russell, C., Raymond, C., Ammannito, E., Buczkowski, D., De Sanctis, M., Hiesinger, H., Jaumann, R., Konopliv, A., McSween, H., Nathues, A., Park, R., Pieters, C., Prettyman, T., McCord, T., McFadden, L., Mottola, S., Zuber, M., Joy, S., Polanskey, C., Rayman, M., Castillo-Rogez, J., Chi, P., Combe, J., Ermakov, A., Fu, R., Hoffmann, M., Jia, Y., Kind, S., Lawrence, D., Li, J.-Y., Marchi, S., Preusker, F., Roatsch, T., Ruesch, O., Schenk, P., Vilarreal, M., and Yamashita, N. (2016). Dawn arrives at Ceres: Exploration of a small, volatile-rich world. *Science*, 353(6303):1008–1010.

- Rust, A., Russell, J., and Knight, R. (1999). Dielectric constant as a predictor of porosity in dry volcanic rocks. *Journal of Volcanology and Geothermal Research*, 91(1):79–96.
- Rytting, D. (2001). Network analyzer accuracy overview. In *ARFTG Conference Digest-Fall, 58th*, volume 40, pages 1–13.
- Saint-Amant, M. (1968). Frequency and temperature dependence of dielectric properties of some common rocks. Master’s thesis, Massachusetts Institute of Technology.
- Saint-Amant, M. and Strangway, D. (1970). Dielectric properties of dry, geologic materials. *Geophysics*, 35(4):624–645.
- Semenov, A. (2018). On applicability of differential mixing rules for statistically homogeneous and isotropic dispersions. *Journal of Physics Communications*, 2(3):035045.
- Sen, P., Scala, C., and Cohen, M. (1981). A self-similar model for sedimentary rocks with application to the dielectric constant of fused glass beads. *Geophysics*, 46(5):781–795.
- Sengwa, R. and Soni, A. (2005). Dielectric dispersion and microwave dielectric study of marbles in support of radar investigations. *Indian Journal of Pure & Applied Physics*, 43:777–782.
- Shannon, R. (1990). Factors determining the dielectric constants of oxides and fluorides. In *Chemistry of Electronic Ceramic Materials. Proc. Int. Conf. Chemistry of Electronic Ceramic Materials Jackson, 17-22 August 1990*, pages 457–469.
- Shannon, R. (1993). Dielectric polarizabilities of ions in oxides and fluorides. *Journal of Applied physics*, 73(1):348–366.
- Shannon, R., Subramanian, M., Hosoya, S., and Rossman, G. (1991). Dielectric constants of tephroite, fayalite and olivine and the oxide additivity rule. *Physics and chemistry of minerals*, 18(1):1–6.
- Sharif, S. (1995). Chemical and mineral composition of dust and its effect on the dielectric constant. *IEEE Transactions on Geoscience and remote sensing*, 33(2):353–359.
- Sheen, J., Hong, Z.-W., Su, C.-W., and Chen, H.-C. (2010). Microwave measurements of dielectric constants by exponential and logarithmic mixture equations. *Progress In Electromagnetics Research*, 100:13–26.

- Shen, L., Savre, W., Price, J., and Athavale, K. (1985). Dielectric properties of reservoir rocks at ultra-high frequencies. *Geophysics*, 50(4):692–704.
- Shepard, M., Clark, B., Ockert-Bell, M., Nolan, M., Howell, E., Magri, C., Giorgini, J., Benner, L., Ostro, S., Harris, A., Warner, B., Stephens, R., and Mueller, M. (2010). A radar survey of M-and X-class asteroids II. Summary and synthesis. *Icarus*, 208(1):221–237.
- Shutko, A. and Reutov, E. (1982). Mixture formulas applied in estimation of dielectric and radiative characteristics of soils and grounds at microwave frequencies. *IEEE Transactions on Geoscience and Remote Sensing*, (1):29–32.
- Sihvola, A. (1989). Self-consistency aspects of dielectric mixing theories. *IEEE Transactions on Geoscience and Remote Sensing*, 27(4):403–415.
- Sihvola, A. (1999). *Electromagnetic Mixing Formulas and Applications*. Number 47. IET: Electromagnetic Wave Series.
- Sihvola, A. (2007). Dielectric polarization and particle shape effects. *Journal of Nanomaterials*, 2007(1):5–5.
- Sihvola, A., Kettunen, H., and Wallén, H. (2013). Mixtures and composite particles: Correspondence of effective description. In *Electromagnetic Theory (EMTS), Proceedings of 2013 URSI International Symposium on*, pages 908–911.
- Simpkin, R. (2010). Derivation of Lichtenecker’s logarithmic mixture formula from Maxwell’s equations. *IEEE Trans. on Microwave Theory and Techniques*, 58(3):545–550.
- Simpson, R. and Tyler, G. (1982). Radar Scattering Laws for the Lunar Surface. *IEEE Transactions on Antennas and Propagation*, 30(3):438–449.
- Soleimani Dorcheh, A. and Abbasi, M. (2008). Silica aerogel; synthesis, properties and characterization. *Journal of Materials Processing Technology*, 199(1):10–26.
- Sotodeh, S. (2014). Effective Broadband Measurements of the Permittivity of Geological Materials. Master’s thesis, York University.
- Stillman, D. (2006). *Frequency and Temperature Dependence in Electromagnetic Properties of Martian Analog Minerals*. PhD thesis, Colorado School of Mines.

- Stillman, D., Grimm, R., and Dec, S. (2010). Low-Frequency Electrical Properties of Ice- Silicate Mixtures. *The Journal of Physical Chemistry B*, 114(18):6065–6073.
- Stillman, D. and Olhoeft, G. (2008). Frequency and temperature dependence in electromagnetic properties of Martian analog minerals. *Journal of Geophysical Research: Planets*, 113(E9).
- Suwa, K. (1964). Mineralogy of fayalite, with special reference to its thermal and thermodynamical properties. *The Journal of earth sciences, Nagoya University*, 12(2):129–146.
- Takei, H. (1978). Growth of fayalite (Fe_2SiO_4) single crystals by the floating-zone method. *Journal of Crystal Growth*, 43(4):463–468.
- Takir, D., Emery, J., Mcswen, H., Hibbitts, C., Clark, R., Pearson, N., and Wang, A. (2013). Nature and degree of aqueous alteration in CM and CI carbonaceous chondrites. *Meteoritics & Planetary Science*, 48(9):1618–1637.
- Tallan, N. and Detwiler, D. (1963). An Anomalous Dissipation Factor Maximum in Sapphire. *Journal of Applied Physics*, 34(6):1650–1656.
- Technologies, A. (2011). *Agilent Vector Network Analyzer Receiver, Dynamic Accuracy: Specifications and Uncertainties*. Agilent Technologies, USA. Literature Number: N5247-90003.
- Telford, W., Geldart, L., and Sheriff, R. (1990). Electrical Properties of Rocks and Minerals. In *Applied Geophysics, 2nd Edition*. Cambridge University Press.
- Thompson, T., Ustinov, E., and Heggy, E. (2011). Modeling radar scattering from icy lunar regoliths at 13 cm and 4 cm wavelengths. *Journal of Geophysical Research: Planets*, 116(E1).
- Tomeoka, K. and Buseck, P. (1985). Indicators of aqueous alteration in CM carbonaceous chondrites: Microtextures of a layered mineral containing Fe, S, O and Ni. *Geochimica et Cosmochimica Acta*, 49(10):2149–2163.
- Tsai, C., Ghent, R., Boivin, A., and Hickson, D. (2019). Discrimination of Dispersive Materials From Radar Signals Using Q^* . *Ground Penetrating Radar*, 2(1):26–50.
- Tuhkala, M., Juuti, J., and Jantunen, H. (2013). Method to characterize dielectric properties of powdery substances. *Journal of Applied Physics*, 114(1):014108–1–014108–8.

- Tuhkala, M., Teirikangas, M., and Juuti, J. (2017). Modeling of Microwave Dielectric Properties of Composites. In *Microwave Materials and Applications, 2 Volume Set*, page 53. John Wiley & Sons.
- Ulaby, F., Bengal, T., Dobson, M., East, J., Garvin, J., and Evans, D. (1990). Microwave dielectric properties of dry rocks. *IEEE Transactions on Geoscience and Remote Sensing*, 28(3):325–336.
- Ulaby, F., Bengal, T., East, J., Dobson, M., Garvin, J., and Evans, D. (1988). Microwave Dielectric Spectrum of Rocks. Technical report, The University of Michigan College of Engineering.
- Unified Abrasives Manufacturers' Association (2018). Abrasives 101. <https://uama.org/abrasives-101/>. Accessed: 2019-02-14.
- van Beek, L. (1967). Dielectric Behaviour of Heterogeneous Systems. *Progress in Dielectrics, Vol. 7*, pages 69–114.
- von Hippel, A. (1954). *Dielectric materials and applications*. Technology Press of M.I.T. and John Wiley and Sons.
- Watanabe, S., Tsuda, Y., Yoshikawa, M., Tanaka, S., Saiki, T., and Nakazawa, S. (2017). Hayabusa2 mission overview. *Space Science Reviews*, 208(1-4):3–16.
- Webb, W. and Church, R. (1986). Measurement of Dielectric Properties of Minerals at Microwave Frequencies. Technical report, United States Department of the Interior Bureau of Mines.
- Weir, W. (1974). Automatic measurement of complex dielectric constant and permeability at microwave frequencies. *Proceedings of the IEEE*, 62(1):33–36.
- Westphal, W. and Sils, A. (1972). Dielectric constant and loss data. Technical report, Massachusetts Institute of Technology.
- Wollensack, M., Hoffmann, J., Rufenacht, J., and Zeier, M. (2012). VNA Tools II: S-parameter uncertainty calculation. In *Microwave Measurement Conference (ARFTG), 2012 79th ARFTG*, pages 1–5. IEEE.
- Xiao, J. (1985). The effects of mineral composition and structure on dielectric constants. *Acta Mineralogica Sinica*, pages 331–337.

- Yeomans, D., Antreasian, P., Barriot, J.-P., Chesley, S., Dunham, D., Farquhar, R., Giorgini, J., Helfrich, C., Konopliv, A., McAdams, J., Miller, J., Owen Jr., W., Scheeres, D., Thomas, P., Veverka, J., and Williams, B. (2000). Radio science results during the NEAR-Shoemaker spacecraft rendezvous with Eros. *Science*, 289(5487):2085–2088.
- Yeomans, D., Barriot, J.-P., Dunham, D., Farquhar, R., Giorgini, J., Helfrich, C., Konopliv, A., McAdams, J., Miller, J., Owen Jr., W., Scheeres, D., Synnott, S., and Williams, B. (1997). Estimating the mass of asteroid 253 Mathilde from tracking data during the NEAR flyby. *Science*, 278(5346):2106–2109.
- Yoshikawa, M., Kawaguchi, J., Fujiwara, A., and Tsuchiyama, A. (2015). Hayabusa sample return mission. *Asteroids IV*, 1:397–418.
- Young, K. and Frederikse, H. (1973). Compilation of the static dielectric constant of inorganic solids. *Journal of Physical and Chemical Reference Data*, 2(2):313–410.
- Zakri, T., Laurent, J.-P., and Vauclin, M. (1998). Theoretical evidence for ‘Lichtenecker’s mixture formulae’ based on the effective medium theory. *Journal of Physics D: Applied Physics*, 31(13):1589.
- Zhang, D. (2007). *Inverse electromagnetic problem for microstructured media*. PhD thesis, University of Utah.
- Zheng, Y., Wang, S., Feng, J., Ouyang, Z., and Li, X. (2005). Measurement of the complex permittivity of dry rocks and minerals: application of polythene dilution method and Lichtenecker’s mixture formulae. *Geophysical Journal International*, 163(3):1195–1202.
- Zolensky, M., Barrett, R., and Browning, L. (1993). Mineralogy and composition of matrix and chondrule rims in carbonaceous chondrites. *Geochimica et Cosmochimica Acta*, 57:3123–3148.

Appendix A

Appendix

A.1 Landau & Lifshitz Derivation

From Landau and Lifshitz (1960):

Consider a mixture in which the electric field is averaged over a volume that is large in comparison with the scale of the inhomogeneities. The mixture itself is homogeneous and isotropic with respect to the average electric field, $\bar{\mathbf{E}}$ (average quantities denoted by bar above variable and vectors by bold variables), and can be described by effective material properties, such as dielectric permittivity. We can write for the effective permittivity:

$$\bar{\mathbf{D}} = \epsilon_{eff} \bar{\mathbf{E}} \tag{A.1}$$

The assumption is made that all of the particles, or inhomogeneities, of the mixture are isotropic and have small differences in permittivity. We can write expressions for the local electric field, \mathbf{E} , and local permittivity, ϵ , as:

$$\mathbf{E} = \bar{\mathbf{E}} + \delta\mathbf{E}$$

$$\epsilon = \bar{\epsilon} + \delta\epsilon$$

where

$$\bar{\epsilon} = \frac{1}{V} \int \epsilon dV$$

is the volume averaged permittivity. Substituting the local fields in to (A.1) and averaging over the mixture results in:

$$\bar{\mathbf{D}} = \overline{(\bar{\epsilon} + \delta\epsilon)(\bar{\mathbf{E}} + \delta\mathbf{E})}$$

Expanding the above equation results in:

$$\bar{\mathbf{D}} = \overline{\bar{\epsilon}\bar{\mathbf{E}}} + \overline{\bar{\epsilon}\delta\mathbf{E}} + \overline{\delta\epsilon\bar{\mathbf{E}}} + \overline{\delta\epsilon\delta\mathbf{E}}$$

Here the second and third term are equal to zero, since the average of the random fluctuations $\delta\epsilon$ and $\delta\mathbf{E}$ are inherently zero, and we can write:

$$\bar{\mathbf{D}} = \bar{\epsilon}\bar{\mathbf{E}} + \overline{\delta\epsilon\delta\mathbf{E}} \quad (\text{A.2})$$

Since the mixture in question is a dielectric, we know that the free charge, ρ_f , must be zero, and we can write the divergence of the electric flux as: $\text{div}\mathbf{D} = 0$ (the notation here is to match Landau & Lifshitz, and is equivalent to $\text{div}\mathbf{D} \equiv \nabla \cdot \mathbf{D}$). We can take the expression for the average electric flux, $\bar{\mathbf{D}}$, and remove the averaging to write:

$$\text{div}[(\bar{\epsilon} + \delta\epsilon)(\bar{\mathbf{E}} + \delta\mathbf{E})] = 0$$

Expanding the above equation results in:

$$\text{div}(\bar{\epsilon}\bar{\mathbf{E}}) + \text{div}(\bar{\epsilon}\delta\mathbf{E}) + \text{div}(\delta\epsilon\bar{\mathbf{E}}) + \text{div}(\delta\epsilon\delta\mathbf{E}) = 0$$

Now we apply the product rule to get:

$$\bar{\epsilon}(\text{div}\bar{\mathbf{E}}) + \bar{\mathbf{E}} \cdot \nabla\bar{\epsilon} + \bar{\epsilon}(\text{div}\delta\mathbf{E}) + \delta\mathbf{E} \cdot \nabla\bar{\epsilon} + \delta\epsilon(\text{div}\bar{\mathbf{E}}) + \bar{\mathbf{E}} \cdot \nabla\delta\epsilon + \delta\epsilon(\text{div}\delta\mathbf{E}) + \delta\mathbf{E} \cdot \nabla\delta\epsilon = 0$$

Removing terms that are second order in $\delta\epsilon$ and $\delta\mathbf{E}$ results in:

$$\bar{\epsilon}(\text{div}\bar{\mathbf{E}}) + \bar{\mathbf{E}} \cdot \nabla\bar{\epsilon} + \bar{\epsilon}(\text{div}\delta\mathbf{E}) + \delta\mathbf{E} \cdot \nabla\bar{\epsilon} + \delta\epsilon(\text{div}\bar{\mathbf{E}}) + \bar{\mathbf{E}} \cdot \nabla\delta\epsilon = 0$$

Since the divergence of a spatially averaged field is zero, and the gradient of an average scalar field is zero, the first, second, fourth, and fifth terms in the above equation will be zero, allowing us to write:

$$\text{div}[(\bar{\epsilon} + \delta\epsilon)(\bar{\mathbf{E}} + \delta\mathbf{E})] = \bar{\epsilon}(\text{div}\delta\mathbf{E}) + \bar{\mathbf{E}} \cdot \nabla\delta\epsilon = 0$$

To arrive at equation (9.4) in Landau & Lifshitz we then take a slightly different approach to what is suggested in the original text. First, we follow the original text by substituting the electric potential, ϕ , for the electric field $\delta\mathbf{E} = -\mathbf{grad}\delta\phi$ (the notation here is similar to the divergence, $\mathbf{grad}\delta\phi = \nabla\phi$) in the above equation:

$$-\bar{\epsilon}(\nabla \cdot \nabla\delta\phi) + \bar{\mathbf{E}} \cdot \nabla\delta\epsilon = 0$$

which can be re-written as:

$$\nabla^2\delta\phi = \frac{1}{\bar{\epsilon}}(\bar{\mathbf{E}} \cdot \nabla\delta\epsilon) \quad (\text{A.3})$$

Here ∇^2 is the Laplacian operator. The following step taken in this derivation is slightly different from Landau and Lifshitz (1960), where we take the Laplacian of both sides of $\delta\mathbf{E} = -\mathbf{grad}\delta\phi$ to arrive at:

$$\nabla^2\delta\mathbf{E} = \nabla^2(-\nabla\delta\phi) \quad (\text{A.4})$$

Next we make use of the identity (for an arbitrary vector field \mathbf{A}) $\nabla \times (\nabla \times \mathbf{A}) = \nabla(\nabla \cdot \mathbf{A}) - \nabla^2\mathbf{A}$ and substitute $-\nabla\delta\phi = \mathbf{A}$:

$$\nabla \times (\nabla \times [-\nabla\delta\phi]) = \nabla(\nabla \cdot [-\nabla\delta\phi]) - \nabla^2(-\nabla\delta\phi)$$

and since the cross product of a gradient is zero we can now write:

$$\nabla(\nabla^2\delta\phi) = \nabla^2(\nabla\delta\phi)$$

Using the above equation we can re-write (A.4) as:

$$\nabla^2\delta\mathbf{E} = -\nabla(\nabla^2\delta\phi)$$

Substituting the expression for $\nabla^2\delta\phi$ from (A.3):

$$\nabla^2 \delta \mathbf{E} = -\nabla \left(\frac{1}{\bar{\epsilon}} \bar{\mathbf{E}} \cdot \nabla \delta \epsilon \right)$$

The above expression can be expanded using the identity (for arbitrary vector fields \mathbf{A} and \mathbf{B})
 $\nabla(\mathbf{A} \cdot \mathbf{B}) = \mathbf{A} \times (\nabla \times \mathbf{B}) + \mathbf{B} \times (\nabla \times \mathbf{A}) + (\mathbf{A} \cdot \nabla)\mathbf{B} + (\mathbf{B} \cdot \nabla)\mathbf{A}$:

$$\nabla^2 \delta \mathbf{E} = -\frac{1}{\bar{\epsilon}} [\bar{\mathbf{E}} \times (\nabla \times \nabla \delta \epsilon) + \nabla \delta \epsilon \times (\nabla \times \bar{\mathbf{E}}) + (\bar{\mathbf{E}} \cdot \nabla) \nabla \delta \epsilon + (\nabla \delta \epsilon \cdot \nabla) \bar{\mathbf{E}}]$$

For the terms in the square brackets on the right of the above equation, the first, second, and fourth terms all equal zero since the curl of a gradient is zero and the derivatives of a constant (average) vector field are zero, leaving us with:

$$\nabla^2 \delta \mathbf{E} = -\frac{1}{\bar{\epsilon}} (\bar{\mathbf{E}} \cdot \nabla) \nabla \delta \epsilon \quad (\text{A.5})$$

Equation (A.5) is identical to (9.4) in Landau and Lifshitz (1960), but was arrived at by applying the Laplacian operator to the electric field and potential fluctuations and rearranging. This equation will be used to derive an expression for $\overline{\delta \epsilon \delta \mathbf{E}}$ that can be substituted back into (A.2). The averaging in $\overline{\delta \epsilon \delta \mathbf{E}}$ is completed in two steps, where the first step consists of spatially averaging (A.5) for a given mixture component, or $\delta \epsilon$. This can be done by first looking at the term $(\bar{\mathbf{E}} \cdot \nabla) \nabla$ on the R.H.S of (A.5) and writing it in index notation:

$$(\bar{\mathbf{E}} \cdot \nabla) \nabla = (\mathbf{E}_j \cdot \frac{\partial}{\partial x_j}) \frac{\partial}{\partial x_k}$$

where for 3 dimensional Cartesian space:

$$\mathbf{E}_j \cdot \frac{\partial}{\partial x_j} = \sum_{j=1}^3 \mathbf{E}_j \cdot \frac{\partial}{\partial x_j}$$

Here $j = 1 = x$, $j = 2 = y$, $j = 3 = z$. Expanding the term $(\bar{\mathbf{E}} \cdot \nabla) \nabla$:

$$(E_x \frac{\partial}{\partial x} + E_y \frac{\partial}{\partial y} + E_z \frac{\partial}{\partial z}) (\frac{\partial}{\partial x}, \frac{\partial}{\partial y}, \frac{\partial}{\partial z})$$

The first term is a scalar and the second term is a vector. The multiplication results in a three component vector:

$$\begin{pmatrix} E_x \frac{\partial^2}{\partial x \partial x} + E_y \frac{\partial^2}{\partial x \partial y} + E_z \frac{\partial^2}{\partial x \partial z} \\ E_x \frac{\partial^2}{\partial y \partial x} + E_y \frac{\partial^2}{\partial y \partial y} + E_z \frac{\partial^2}{\partial y \partial z} \\ E_x \frac{\partial^2}{\partial z \partial x} + E_y \frac{\partial^2}{\partial z \partial y} + E_z \frac{\partial^2}{\partial z \partial z} \end{pmatrix}$$

The spatial averaging is essentially an integration, which will affect the operator $\frac{\partial^2}{\partial x_j \partial x_k}$ differently for different values of j and k . Since the mixture medium is isotropic (even function in x , y , and z), if $j \neq k$ the operator will return an odd function that when integrated will cancel itself out. As a result, and since due to isotropy $\frac{\partial}{\partial x} = \frac{\partial}{\partial y} = \frac{\partial}{\partial z}$, we can replace the operator $\frac{\partial^2}{\partial x_j \partial x_k}$ with the following:

$$\frac{\partial^2}{\partial x_j \partial x_k} = \frac{1}{3} \sum_{i=1}^3 \frac{\partial^2}{\partial x_i^2} = \frac{1}{3} \nabla^2$$

We can now write the spatially averaged (A.5):

$$\nabla^2 \overline{\delta \mathbf{E}} = -\frac{1}{3\bar{\epsilon}} \bar{\mathbf{E}} \nabla^2 \delta \epsilon \quad (\text{A.6})$$

Re-writing the above with $-\frac{1}{3\bar{\epsilon}} \bar{\mathbf{E}}$ taken as some constant value, c :

$$\nabla^2 \overline{\delta \mathbf{E}} = c \nabla^2 \delta \epsilon$$

The above implies that $\overline{\delta \mathbf{E}} + f(x, y, z) = c \delta \epsilon$ for some unknown function $f(x, y, z)$, where $\nabla^2 f = 0$. Since we know that the permittivity and electric field are proportional through the electric flux, i.e. $\mathbf{E} \propto \epsilon$, $f(x, y, z)$ must be zero, otherwise $\overline{\delta \mathbf{E}} \propto \delta \epsilon$ would not be true. With this constraint of proportionality, $\overline{\delta \mathbf{E}} \propto \delta \epsilon$, we can say that $\overline{\delta \mathbf{E}} = c \delta \epsilon$, and re-write (A.6) as:

$$\overline{\delta \mathbf{E}} = -\frac{1}{3\bar{\epsilon}} \bar{\mathbf{E}} \delta \epsilon$$

Now we multiply the above by $\delta \epsilon$ and effect the second step of the averaging, which is now over the components of the mixture to obtain:

$$\overline{\delta \epsilon \delta \mathbf{E}} = -\frac{1}{3\bar{\epsilon}} \bar{\mathbf{E}} \overline{\delta \epsilon^2}$$

With the above we have an expression for $\overline{\delta \epsilon \delta \mathbf{E}}$ that can be substituted into (A.2) to get:

$$\bar{\mathbf{D}} = \bar{\epsilon}\bar{\mathbf{E}} + \overline{\delta\epsilon\delta\mathbf{E}} = \bar{\epsilon}\bar{\mathbf{E}} - \frac{1}{3\bar{\epsilon}}\bar{\mathbf{E}}\overline{\delta\epsilon^2}$$

Comparing this with (A.1):

$$\epsilon_{eff}\bar{\mathbf{E}} = \bar{\epsilon}\bar{\mathbf{E}} - \frac{1}{3\bar{\epsilon}}\bar{\mathbf{E}}\overline{\delta\epsilon^2}$$

Cancelling out terms results in:

$$\epsilon_{eff} = \bar{\epsilon} - \frac{1}{3\bar{\epsilon}}\overline{\delta\epsilon^2} \quad (\text{A.7})$$

We now need to substitute for $\delta\epsilon$, which can be done by first defining:

$$\overline{\epsilon^{\frac{1}{3}}} = \overline{(\bar{\epsilon} + \delta\epsilon)^{\frac{1}{3}}}$$

The Taylor expansion at $\delta\epsilon = 0$ for the above equation, ignoring higher than second-order terms, is:

$$\overline{\epsilon^{\frac{1}{3}}} \approx \bar{\epsilon}^{\frac{1}{3}} + \frac{\overline{\delta\epsilon}}{3\bar{\epsilon}^{\frac{2}{3}}} - \frac{\overline{\delta\epsilon^2}}{9\bar{\epsilon}^{\frac{5}{3}}} + \dots$$

The second term on the right is equal to zero since $\overline{\delta\epsilon} = 0$, which allows us to write:

$$\overline{\epsilon^{\frac{1}{3}}} = \bar{\epsilon}^{\frac{1}{3}} \left(1 - \frac{\overline{\delta\epsilon^2}}{9\bar{\epsilon}^2} \right) \quad (\text{A.8})$$

The Taylor expansion at $\overline{\delta\epsilon^2} = 0$ of the cube root of (A.7), ignoring higher than second-order terms, is:

$$\epsilon_{eff}^{\frac{1}{3}} \approx \bar{\epsilon}^{\frac{1}{3}} - \frac{\overline{\delta\epsilon^2}}{9\bar{\epsilon}^{\frac{5}{3}}} - \dots$$

Which can be re-written as:

$$\epsilon_{eff}^{\frac{1}{3}} = \bar{\epsilon}^{\frac{1}{3}} \left(1 - \frac{\overline{\delta\epsilon^2}}{9\bar{\epsilon}^2} \right)$$

The above is equivalent to (A.8), which allows us to write:

$$\epsilon_{eff}^{\frac{1}{3}} = \bar{\epsilon}^{\frac{1}{3}} \quad (\text{A.9})$$

Here $\overline{\epsilon^{\frac{1}{3}}}$ is a weighted average, where the weights are the volume fractions, f_i , of each mixture phase, i of an N phase mixture:

$$\overline{\epsilon^{\frac{1}{3}}} = \frac{\sum_{i=1}^N f_i \epsilon_i^{\frac{1}{3}}}{\sum_{i=1}^N f_i}$$

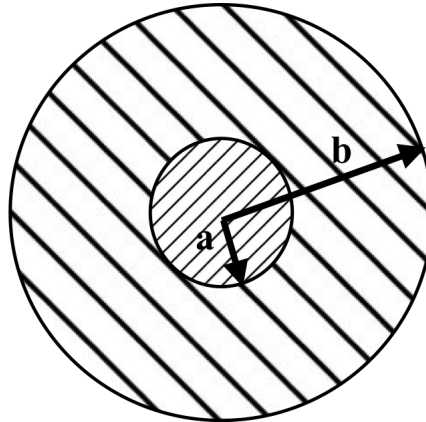
By definition of the volume fractions we know $\sum_{i=1}^N f_i = 1$, and thus we can write:

$$\epsilon_{eff}^{\frac{1}{3}} = \sum_{i=1}^N f_i \epsilon_i^{\frac{1}{3}} \quad (\text{A.10})$$

Equation (A.10) is the Looyenga-Landau-Lifshitz mixing equation and the derivation is complete.

A.2 Looyenga Derivation

Looyenga (1965) produced an alternate derivation arriving at the same result as Landau and Lifshitz. In this derivation, a large spherical (radius b) mixture is considered with an embedded small sphere (radius a) containing inclusions corresponding to similar mixtures with slightly higher and lower effective permittivities:



A Taylor expansion up to second order is used to produce an expression defining the effective permittivity in the large sphere as a volume weighted average of the inclusion permittivities. The BG (and Bottcher, with similar results) model is also used to define the effective permittivity of the small sphere as a function of the inclusion permittivities, ignoring the large sphere. The two expressions are then combined to produce a differential equation, whose solution (with appropriate

boundary conditions) is the LLL equation. The assumptions in this derivation is that the inclusion sizes are small compared to the averaged volumes, and more importantly, that the mixture contains intermediate volume fractions of the phases. Since the model does not consider the polarizability of a single inclusion, at the limit of low volume fractions of either component this model will overestimate the effective permittivity. However, unlike in the MG derivation, the model inherently considers the influences of nearby inclusions. Numerically the LLL and BG equations produce very similar results, with identical values at roughly 43% volume fraction of a given inclusion phase. Below this threshold, the LLL model predicts higher effective permittivities and above this it predicts lower permittivities, relative to the BG model.